SCUOLA
NORMALE
SUPERIORE
PISA

Tesi

Corso di Perfezionamento in Chimica

Spectroscopic Applications of Rare Earth Complexes dependent on Ligands Structure and Lanthanide Ion

Supervisor: Prof. Dr. Lorenzo Di Bari

Candidate: Samuele Lo Piano

Introduction

In the last decades, lanthanide chemistry has received a growing interest from many fields, going from catalysis to the investigation of biological macromolecules, to the use as contrast agents in MRI medical applications, as probes in vivo and for cellular systems as well. Moreover in NMR, taking advantage of the lanthanide induced shift and relaxation (LIS and LIR, respectively) for structural determination.[1] Especially for the latter, lanthanides offer very relevant properties, both for small complexes and biomolecules structural determination, due to their paramagnetic, electronic, optical and luminescent properties.[2] The structural homogeneity along the lanthanide series offer the rare advantage of a safe comparison with blank systems, giving the opportunity of reliable and easily identifiable phenomena, by virtue of the fact that some elements are silent regarding the mentioned properties, while others are not.

The research developed in the present thesis concerns the development of new techniques and methods of structural determination, using lanthanide physical-chemical properties. In particular:

- a new method for the Fermi contact-pseudocontact chemical shift separation;
- a brand-new highlighting of VCD bands through the interaction with metal systems having low-lying electronic states, potentially useful for selective ion-binding pockets structural characterization;
- A new chiral optical-probe selective acute phase proteins α-1-acid glycoprotein and α-1-antitrypsin.

The present thesis is organized in two parts: the first one, including Chapters 1,2, 3 and 4, consists of an introduction, with some basic concepts of lanthanide chemistry, in particular luminescent and paramagnetic properties, Vibrational Circular Dichroism and the state of the art regarding lanthanide magnetic and optical probe development.

Chapter 1 is a brief summary about the physicochemical properties and the main aspects of lanthanides coordination chemistry.

Chapter 2 is an introductive chapter about the analysis of the paramagnetic contributions to NMR, pointing out their chemical shifts and relaxation times influence, highlighting the lanthanide case.

Chapter 3 is an introductive chapter about Vibrational Circular Dichroism. Instrumentation, spectra calculation and current hot applications are briefly introduced.

Chapter 4 is an introductive chapter about Lanthanides probes, both as contrast agents in magnetic resonance imaging, and as luminescent probes for biomedical analysis and cellular imaging, with a close-up on chiral systems and their use in chiroptical techniques.

In Chapter 5 a new method for gaining accurate pseudocontact shifts is presented. These parameters are the basis for structural determination in solution by means of paramagnetic NMR. Separation of pseudocontact (PCS) from Fermi contact (FC) shifts from NMR data can be achieved by means of various methods, briefly reviewed in the first part of the Chapter. One of the most used, because of its simplicity, the so-called Reilley method,[3] has relevant limitations in the case of change of crystal field parameters through the series, as

determined by various processes, primarily axial ligand dynamics, or as a consequence of lanthanide contraction. Actually it faces a break around the middle of the series, known as 'Gadolinium break '.[4] We propose a simple alternative procedure to compensate for any variation (smooth or abrupt) in crystal field parameters. Four examples taken from the literature, plus the complete set of unpublished data for Ln DOTMA are discussed in detail, to illustrate the power and limitation of the conventional Reilley treatment and to demonstrate the power and scope of our alternative approach. The DOTMA case is further studied as well, with detailed structural information, like hydratation along the series and a comparison of the Dipolar terms for the two SAP and TSAP forms along the series and for every single element as well.

In Chapter 6 the case of VCD signal enhancement in complexes containing metals with low-lying electronic state is shortly recapitulated, a potential approach to compensate low signal to noise ratio, 10^{-4} of the corresponding absorption spectrum, characteristic of this technique. Afterwards we discuss our experimental evidences for a few lanthanide C_4 symmetrical complexes: Ln DOTMA, lanthanide-cesium bimetallic camphorate complexes and Ln DOPhA. In the presence of certain elements, mid-IR VCD intensity increases dramatically, while preserving the overall shape. In the last part, the geometrical conditions for this phenomenon, dubbed with the acronym LIVE, are summed up, with speculations about the requirement of the electronic state energy of the lanthanide ion as well.

In Chapter 7 the first specific chiral probe for alpha-glycoprotein and alpha-antrypsin is presented. Their interaction with other serum proteins are studied, but the intensity increase of emission occours only with AGP. Also CPL and CD spectra are acknowledged only in the complex formation with AGP, proving its selectivity for this system, therefore the probe could be potentially used in the determination of anomalous concentrations of AGP in serum, characteristic of pathologic conditions. Some details concerning ECD spectra gave some insight about the actual interaction with the protein binding-site. Also with AAT there is a significative response, although an order of magnitude lower than in the case of AGP.

References

[1] a) I. Bertini, C. Luchinat, G. Parigi *et al. Dalton Trans.* **2008**, 3782. b) I. Bertini, C. Luchinat, *Coord. Chem. Rev.* **1996**, *150*, 1.

[2] a) A. Thibon, V. C. Pierre, *Anal. Bioanal. Chem.* **2009**, *394*, 107. b) C. P. Montgomery, B. S. Murray, E. J. New, R. Pal, D. Parker, *Acc. Chem. Res.* **2009**, *42*, 925.

[3] C.N. Reilley, B.W. Good, *Anal. Chem.* **1975**, *47*, 2110.

[4] a) S. Rigault, C. Piguet, *J. Am. Chem. Soc.* **2000**, *122*, 9304. b) J. K. A. Geschneidner, J.C.G. Bünzli, V.K. Pecharsky (Eds.) *Handbook on the Physics and Chemistry of Rare Earths*, **2003**, Elsevier:Amsterdam, **2003**, pp. 353.

Contents

Theoretical Part

Chapter 1

Fundamental aspects of Lanthanide Chemistry

The *f*-block elements following lanthanum (which generally is included itself) in the periodic table are known as lanthanides, or *lanthanoids*, according to IUPAC recommendation. These elements resemble each other much more closely than do the members of a row of *d*-block metals, with a slight variation of chemical and physical properties along the series. Lanthanide paramagnetism and low-lying electronic states make them very interesting in nuclear magnetic resonance techniques and in optical applications. In this Chapter, we will shortly point out some chemical properties deriving from Lanthanide configuration (Section 1.1) and how they affect the coordinative behavior in rare earth complexes (Section 1.2).

1.1 Electronic configuration and chemical properties

The electronic configuration of lanthanides is characterized by the progressive filling of the inner *4f* orbitals ([Xe]$6s^2 5d^1 4f^n$, where *n* varies between 0, for La, and 14, for Lu). The sum of the outer *6s* and *5d* ionization enthalpies is comparatively low, similar in magnitude to those of the alkali metals, which makes these elements highly electropositive and prone to form cationic species (Table 1.1).

Table 1.1 General chemical properties of rare earth elements.[1]

Element	Symbol	Electronic configuration		Ionic Radius (Å)[3]		E^0 (V)[(a)]	Oxidation
		Atomic (Ln^0)	Ionic (Ln^{3+})	CN[(b)]=6	CN=9		States
Lanthanum	La	[Xe]$6s^2 5d^1$	[Xe]$4f^0$	1.03	1.22	-2.37	3
Cerium	Ce	[Xe]$6s^2 5d^0 4f^2$	[Xe]$4f^1$	1.01	1.20	-2.34	3, 4
Praseodymium	Pr	[Xe]$6s^2 5d^0 4f^3$	[Xe]$4f^2$	0.99	1.18	-2.35	3, 4
Neodymium	Nd	[Xe]$6s^2 5d^0 4f^4$	[Xe]$4f^3$	0.98	1.16	-2.32	2, 3,4
Promethium	Pm	[Xe]$6s^2 5d^0 4f^5$	[Xe]$4f^4$			-2.29	3
Samarium	Sm	[Xe]$6s^2 5d^0 4f^6$	[Xe]$4f^5$	0.96	1.13	-2.30	2, 3
Europium	Eu	[Xe]$6s^2 5d^0 4f^7$	[Xe]$4f^6$	0.95	1.12	-1.99	2, 3
Gadolinium	Gd	[Xe]$6s^2 5d^1 4f^7$	[Xe]$4f^7$	0.94	1.11	-2.29	3
Terbium	Tb	[Xe]$6s^2 5d^0 4f^9$	[Xe]$4f^8$	0.92	1.10	-2.30	3, 4
Dysprosium	Dy	[Xe]$6s^2 5d^0 4f^{10}$	[Xe]$4f^9$	0.91	1.08	-2.29	2, 3, 4
Holmium	Ho	[Xe]$6s^2 5d^0 4f^{11}$	[Xe]$4f^{10}$	0.90	1.07	-2.33	3, 4
Erbium	Er	[Xe]$6s^2 5d^0 4f^{12}$	[Xe]$4f^{11}$	0.89	1.06	-2.31	2, 3
Thulium	Tm	[Xe]$6s^2 5d^0 4f^{13}$	[Xe]$4f^{12}$	0.88	1.05	-2.31	2, 3
Ytterbium	Yb	[Xe]$6s^2 5d^0 4f^{14}$	[Xe]$4f^{13}$	0.87	1.04	-2.22	2, 3
Lutetium	Lu	[Xe]$6s^2 5d^1 4f^{14}$	[Xe]$4f^{14}$	0.86	1.03	-2.30	3

[(a)]For $M^{3+} + 3e^- = M$; [(b)]CN: Coordination Number

The trivalent state Ln(III) is generally the most common oxidation state, although tetravalent (Ln(IV), for Ce, Pr, Nd, Tb, Dy and Ho) and divalent states (Ln(II), for Nd, Sm, Eu, Dy, Er, Tm and Yb) are also known.[2] These *non*-trivalent state are easily reduced or oxidized to the more stable +3 ions; stable complexes in water have been observed only for two species: Ce^{4+} and Eu^{2+}.[1] However, SmI_2 has found very interesting applications in reductive (organic) reactions. Besides that compound, also other Sm(II) salts and complexes, as well as TmI_2, DyI_2 and NdI_2, have been fruitfully employed, as reductive reagents in the same type of synthesis, with satisfactory results.[2d]

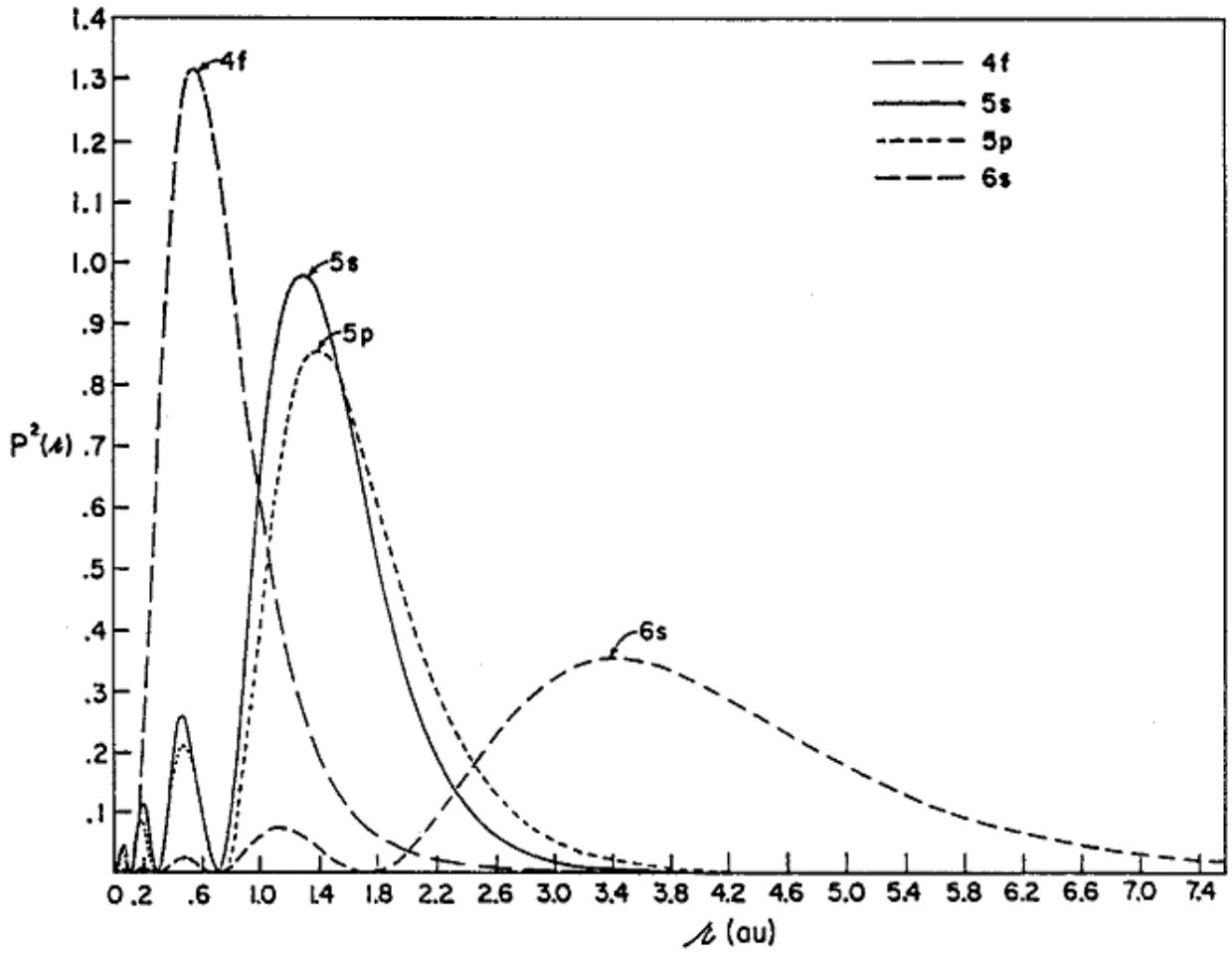

Figure 1.1 Plot of the radial charge density (P^2) of the *4f*-, *5s*-, *5p*-, and *6s*- orbital function for Gd^{3+} ion (radius in atomic units).[3]

Considering this fact, the attention will be focused on Ln(III) complexes, even if Sm(II) and Ce(IV) compounds are of great interest in the application for catalysis and organometallic chemistry.[3]

The electronic configuration for a generic Ln(III) cation is [Xe]$4f^n$ and all the Ln(III) ions are paramagnetic, with the exception of La^{3+} and Lu^{3+}. The *4f* orbital shielding from external fields by the overlying $5s^2$ and $5p^6$ shells (Figure 1.1) makes the states arising from the various $4f^n$ configurations pretty invariant in energy for a given

[1] Albeit the high oxidation power of Ce^{4+} solutions and the sensitivity of Eu^{2+} solutions to the presence of dissolved oxygen.

ion. This is well proved, considering the element ionization energies,[4] optical properties [5] and the magnetic moments of various complexes.[6]

Therefore ligands, as other external field sources, provide a minimal perturbation of the Ln(III) electronic states [3] and can give rise usually to small crystal-field splittings (lifting the degeneracy of spectroscopic terms).

The progressive increase of nuclear charge along the series, due to the poor shielding of *4f* electrons and to relativisitic effect,[7] causes a gradual ionic radius decrease, known as *lanthanide contraction.*[8] The ionic radius of the trivalent ions varies from 1.03 Å in La^{3+} to 0.86 in Lu^{3+} for CN=6, while from 1.22 to 1.03 Å for CN=9 (Table 1.1), values comparable with Ca^{2+} ion radius. This size similarity makes protein binding sites for Ca^{2+} also potentially interesting for Ln^{3+}, offering an interesting tool to study Ln(III)-protein interaction (this will be discussed more in-depth in Chapters 4, 7).

1.2 Coordination chemistry of Ln(III) ions

The electronic configuration of Ln^{3+} directly affects their coordination chemistry: the *4f* electrons are shielded by the 6s and 5p ones and are not available for covalent bonding, owing to their minimal overlap with ligand orbitals, consequently Ln^{3+} give rise to metal-ligand bonds with prevalent ionic (electrostatic) character.[1,3]

Moeller et al. pointed out that, even in the most stable complexes, bond strength is of the same order of magnitude as Ln^{3+}-H_2O interaction.[9] Also bond distance measurements have confirmed the mainly ionic nature of lanthanide bonding. Therefore in lanthanide chemistry, classical aspects of *d*-transition metal chemistry as σ-donation and π-retrodonation, the '18 electrons rule', or the formation of multiple bonds ($Ln = O$ or $Ln \equiv N$) are not observed.

The strong electrostatic character of ligand-metal bonds allows variable coordination numbers and irregular geometries, often not easily described as 'planar', 'tetrahedral' or 'octahedral'. For this reason, lanthanide complexes geometry is hardly predictable and should be experimentally determined. Moreover, ligand arrangement can significantly differ between solution and solid-state, e.g. because of the presence of conformational dynamics, solvent coordination or of crystal packing, hence, specific studies are generally required and XRD structures may be questionable to depict the behaviour in solution. Coordination numbers are usually high reaching 9 for Yb and Lu, and even 11 for the larger La ions.[1,3,10]

According to HSAB classification of Pearson,[11] lanthanides cations are considered as 'hard' *Lewis* acids, showing a strong preference for oxygen donor atoms to nitrogen and sulphur (O >> N > S, F > Cl). This property makes Lanthanides trivalent ions very suited for specific applications in catalysis, like, for instance, carbonyl group activation to nucleophilic attack and many other analogous reactions.[12] Especially triflate salts show very promising uses as catalysts in *green* solvents.[13]

Bond *non*-directionality and CN flexibility are peculiar to rare-earth coordination chemistry, making them suitable elements in catalysis: potentially, smaller activation energy are necessary to reduce or expand the metal centre coordination sphere, allowing an easy substrate binding and product release.

Common polar solvents or contaminants, having oxygen donor atoms, like, for instance, water, alcohols, ethers and DMSO, show a great tendency to compete with ligands for Ln binding, which restricts the choice of the medium for the hypothetical catalyzed reaction and/or poses specific requirements to the structure of ligands able to provide stable complexes.[14]

Chelation is the predominant form of complexation in lanthanide chemistry, because of entropic driving force, arising from the coordination of polydentate ligands, compensating for the competition with the solvent, allowing the formation of stable complexes. The complex stability depends on the number and the nature of donor atoms: chelating *N*-ligands such as ethylendiamine dissociate in water and in oxygenated solvents,[1] but in case the polydentate ligand has *O*- donors (e.g. carboxylates), as in EDTA, there is a great increase in complex stability, with binding constants in water up to 10^{15}-10^{20} M^{-1} (a very important factor for their employment as contrast agents and luminescence bioprobes, as will be described in detail in Chapters 4 and 7). On the contrary with macrocyclic ligands, the entropy loss is compensated by the enthalpic term.

The crystallographic structure of $[La(EDTA)(H_2O)_3]^-$ shows that three water molecules are bound, with an overall CN = 9. The negatively charged carboxylic oxygens are more strongly bound to the metal than neutral water and nitrogens, as it is clear by the shorter crystallographic bond lengths: 2.54 Å for La-O of EDTA, against 2.60 Å for La-O of water, and 2.86 Å for La-N.

Other analogous polydentate ligands were derived by changing the number of pendant arms: HEDTA (*N'*-hydroxyethylethylenediamine-*N, N, N'*-triacetic acid), DTPA (diethylenetriamine-*N, N, N', N', N''*-penta-acetic acid), DCTA (1,2-diaminocyclohexane-*N, N, N', N'* -tetraacetic acid). In particular, DTPA (octadentate with five caboxylate donors) establishes high stability constants in water with all Ln^{3+} ions (≈ 10^{22}): even for this reason Gd DTPA is one of the most used contrast agents in Magnetic Resonance Imaging (MRI).[1] Macrocyclic polydentate ligands derived from DOTA (1,4,7,10-tetraazacyclododecane-1,4,7,10-tetraacetic acid) are used as well for the same application; they will be described in detail in Chapters 4, 5, 6 and 7.

Water is such a strong ligand for Ln^{3+} ions that is often observed in the crystallographic structure of complexes crystallized from solvents having even small traces of it.[15] Considering the difficulty for competing ligands to replace water, lanthanide complexes are generally synthesized starting from anhydrous salts ($LnCl_3$, $Ln(OTf)_3$, $Ln(alcoholates)_3$, etc.), in which anions are more easily replaceable.

In aqueous solutions, Ln^{3+} ions bind several water molecules: the exact number is somewhat controversial, luminescence data have suggested values of 10 for La^{3+}-Nd^{3+}, and 9 for Tb^{3+}-Lu^{3+}.[16] The rate constants for the exchange process in the lanthanide hydratation sphere (eq. 1.1) are approximately estimated to $8 \cdot 10^7$ s^{-1} for La^{3+} - Eu^{3+}, $4 \cdot 10^7$ s^{-1} for Gd^{3+} and $1 \cdot 10^7 s^{-1}$ for Dy^{3+} -Lu^{3+}, and are also affected by the number of water molecules in the coordination sphere.

Increasing pH, hydrolysis of bound water is favored (eq. 1.2), leading to the complete precipitation of $Ln(OH)_3$. Together with hydroxide precipitation, the formation of polymetallic species as $Ln[Ln(OH)_3]^{3+}$ or colloids may be observed: if the lanthanide hydroxyde is desired, a careful control of the precipitation conditions is needed.[17] $Ln(OH)_3$ solubility shows a gradual decrease along the series, in correspondence with ionic radius reduction, passing from $8 \cdot 10^{-6}$ mol/L to $6 \cdot 10^{-7}$mol/L for Lu^{3+}.

$$[Ln(H_2O)_n]^{3+} + H_2O^* \rightleftharpoons [Ln(H_2O)_{n-1}(H_2O^*)]^{3+} + H_2O \qquad (1.1)$$

$$[Ln(H_2O)_n]^{3+} + H_2O \rightleftharpoons [Ln(H_2O)_{n-1}(OH)]^{2+} + H_3O^+ \quad (1.2)$$

References

[1] C. H. Evans, *Biochemistry of Lanthanides,* **1990,** Plenum Press: New York.

[2] a) F. Nief, *Dalton Trans.* **2010**, *39*, 6589 b) G. Meyer, *Angew. Chem. Int. Ed.* **2008**, *47*, 4962. c) M. N. Bochkarev, *Coord. Chem. Rev.* **2004**, *248*, 835. d) M. Szostak, D. J. Procter, *Angew. Chem. Int. Ed.* **2012**, *51*, 2 and references therein.

[3] S. Kobayashi, *Lanthanides: Chemistry and Use in Organic Synthesis*, *Topics in Organometallic Chemistry,* **1999,** Springer-Verlag:Berlin.

[4] J.-C. G. Bünzli, C. R. Choppin, *Lanthanides probes in life, chemical and earth science, theory and practice,* **1989,** Elsevier: Amsterdam.

[5] (a) R. D. Peacock, *Struct. Bonding* **1975,** *22***,** 83. (b) W. T. Carnall, In: K. A. Jr. Gschneider, L. Eyring, *Handbook of the physics and chemistry of rare earths,* **1979**, North-Holland Publishing Company: Amsterdam, (Chapter 24).

[6] T. Moeller in T. Moeller, E. Schleitzer-Rust, *Gmelin handbook of inorganic chemistry, Sc, Y, La-Lu rare elements,* **1980,** part D1, 8thedition; Springer: Berlin, Heidelberg, New York, (Chapter 24).

[7] K. S. Pitzer, *Acc. Chem. Res.* **1979,** *12*, 271.

[8] M. Seitz, A. G. Oliver, *J. Am. Chem. Soc.* **2007,** *129,* 11153 and references therein.

[9] T. Moeller, D. F. Martin, L. C. Thompson, R. Ferrus, G. R. Feistel, W. J. Randall, *Chem. Rev.* **1965**, *65*, 1.

[10] a) J. Lisowski, P. Starynowicz, *Polyhedron* **2000**, *19,* 465; b) S. A. Cotton, *C. R. Chimie* **2005**, *8,* 129.

[11] a) R. G. Pearson, *J. Am. Chem. Soc.* **1963**, *85*, 3533; b) R. G. Pearson, *Hard and Soft Acids and Bases,* **1973,** Dowden, Hutchinson, and Ross: Stroudsburg, PA.

[12] a) M. Shibasaki, in H. Yamamoto *Lewis Acids in Organic Synthesis* **2000**, VCH-Wiley: New York, *Vol. 2*, 911. b) P. G. Steel, *J. Chem. Soc., Perkin Trans. 1*, **2001**, 2727. c) G. K. Veits, J. Read de Alaniz, *Tetrahedron* **2012**, *68*, 2015.

[13] S. Luo, *Mini-Reviews in Organic Chemistry*, **2005**, *2*, 177.

[14] a) L.-W. Yang, S. Liu, E. Wong, S. J. Rettig and C. Orvig, *Inorg. Chem.* **1995**, *34*, 2164. b) C.-Y. Su, B.-S. Kang, X.-Q. Mu, J. Sun, Y.-X. Tong and Z.-N. Chen, *Aust. J. Chem.* **1998**, *51*, 565. c) X.-P. Yang , C.-Y. Su , B.-S. Kang , X.-L. Feng , W.-L. Xiao and H.-Q. Liu, *J. Chem. Soc. Dalton Trans.* **2000**, 3253.

[15] H. Sasai, T. Suzuki, N. Itoh, K. Tanaka, T. Date, K. Okamura, M. Shibasaki, *J. Am. Chem. Soc.* **1993,** *115,* 10372.

[16] W. DeW. Horrocks, D. R. Sudnick, *J. Am. Chem. Soc.* **1979,** *101,* 334.

[17] R. J. Withey, *Can. J. Chem.* **1969,** *47,* 4383.

Chapter 2

NMR of Lanthanide complexes

Except for lanthanum (La^{3+}) and lutetium (Lu^{3+}), having *f*-shell completely empty ($4f^0$, for La^{3+}) and full ($4f^{14}$, for Lu^{3+}) respectively, in all other Ln^{3+} ions, the partial filling of *f*-orbitals gives a variable number of unpaired electrons, which are responsible for molecular paramagnetism.

Irrespective of its origin, this property directly influences the NMR spectrum: the unpaired electrons magnetic moment generates a magnetic field, that may interact with the nuclear magnetic dipole (the so called **hyperfine interaction**), and produces additional contributions to both the NMR chemical shift and the relaxation time of the observed nuclei. The paramagnetic contributions (δ^{para}, R^{para}) are determined by taking the difference between the observed shift and relaxation rate (δ^{obs}, R^{obs}) and those expected for the same nucleus in a diamagnetic complex (δ^{dia}, R^{dia}).[2]

$$\delta^{\mathrm{obs}} = \delta^{\mathrm{para}} + \delta^{\mathrm{dia}} \tag{2.1}$$

$$\delta^{\mathrm{para}} = \delta^{\mathrm{obs}} - \delta^{\mathrm{dia}} \tag{2.2}$$

$$R_1^{\mathrm{para}} = \frac{1}{T_1^{\mathrm{para}}} = \frac{1}{T_1^{\mathrm{obs}}} - \frac{1}{T_1^{\mathrm{dia}}} = R_1^{\mathrm{obs}} - R_1^{\mathrm{dia}} \tag{2.3}$$

$$R_2^{\mathrm{para}} = \frac{1}{T_2^{\mathrm{para}}} = \frac{1}{T_2^{\mathrm{obs}}} - \frac{1}{T_2^{\mathrm{dia}}} = R_2^{\mathrm{obs}} - R_2^{\mathrm{dia}} \tag{2.4}$$

In this chapter we report a brief description of the main aspects of paramagnetic NMR, with particular regard to lanthanides.[1-5]

2.1 The paramagnetic shift

The paramagnetic contribution due to hyperfine interaction can be partitioned in two terms, the *Fermi* or *contact* coupling and the *dipolar* or *pseudocontact* coupling: the first one is related to electron-nucleus spin interaction, when electrons are localized *on* that nucleus. On the contrary, the second one is described by a *long-range* magnetic dipolar coupling, with the anisotropic distribution of the electronic magnetic moment. In the nuclear spin Hamiltonian ($H_{\mathrm{spin}}^{\mathrm{nuc}}$), contact and pseudocontact couplings provide two terms (H_{con} and H_{pc}, respectively) in addition to Zeeman (H_{Zeeman}), chemical shift Hamiltonians (H_{CS}) and scalar coupling (H_{J})

$$H_{\mathrm{spin}}^{\mathrm{nuc}} = H_{\mathrm{Zeeman}} + H_{\mathrm{CS}} + H_J + H_{\mathrm{con}} + H_{\mathrm{pc}} \tag{2.5}$$

[2] The correct diamagnetic reference is not a trivial matter. In most cases the lanthanum complexes are good references for early lanthanides (Ce-Eu), while lutetium complexes are for the late elements (Tb-Yb).

Notwithstanding both terms accounting for the hyperfine interaction describe a spin-spin coupling, they are both proportional to electron spin polarization and, consequently, to the external magnetic field intensity. Therefore they give rise to two additional contributions to the NMR chemical shift: a contact (δ^{con}) and a pseudocontact term (δ^{pc}) term (eq. 2.5)

$$\delta^{\mathrm{para}} = \delta^{\mathrm{con}} + \delta^{\mathrm{pc}} + \delta^{\mathrm{bulk}} \tag{2.6}$$

The additional term δ^{bulk} accounts for the effects derived from the modified magnetic field susceptibility of the whole sample, and it is generally cancelled using a frequency-locked spectrometer together with an appropriate internal reference [2]: for the sake of simplicity, this term will be ruled out in the following discussion.

2.1.1 The Fermi contact shift

As electrons relax orders of magnitude faster than nuclei, the nucleus in each of its M_I energy level only senses an average static magnetic momentum $\langle\mu\rangle = -g_e\mu_B\langle S_Z\rangle$ which results from the slight excess of electron population in the M_S = -1/2 state. The spin density ρ at zero distance from the nucleus, deriving from this electron density difference is the parameter to which contact coupling is proportional (eq. 2.7) [1]

$$\rho = \left|\Psi_{-1/2}(0)\right| - \left|\Psi_{1/2}(0)\right| \tag{2.7}$$

Where $\Psi(0)$ is the MO wavefunction *on* the nucleus. The *p, d, f* orbitals have vanishing electron density on the nucleus, therefore only the *s*-components of MO contribute to the contact coupling. The spin density delocalization can occur either through Fermi hyperfine interaction, or, in alternative, polarization of occupied *s*-containing MO.[3] The contact Hamiltonian describes this kind of coupling, between nuclear and electron spin operators **I** and **S**, respectively, through tensor $\widetilde{\mathbf{A}}$**,** (eq. 2.8)

$$H_{\mathrm{con}} = \mathbf{I}\cdot\widetilde{\mathbf{A}}\cdot\mathbf{S} \tag{2.8}$$

where,

$$\mathbf{I} = \hat{\mathbf{i}}I_x + \hat{\mathbf{j}}I_y + \hat{\mathbf{k}}I_z \tag{2.9}$$

$$\mathbf{S} = \hat{\mathbf{i}}S_x + \hat{\mathbf{j}}S_y + \hat{\mathbf{k}}S_z \tag{2.10}$$

For sufficiently high magnetic field,[3] and by replacing the electron spin term with its expectation value $\langle S_z\rangle$,[4] the contact Hamiltonian becomes [1a,b] (eq. 2.11)

$$H_{\mathrm{con}} = A\, I_z\langle S_z\rangle \tag{2.11}$$

[3] This condition is satisfied when, for any a_k eigenvalue of $\widetilde{\mathbf{A}}$, is $a_k \ll g_e\mu_B B_0$.
[4] This is correct in view of the fast electronic relaxation, with respect to NMR timescale.

Where *A* is the contact coupling constant (eq. 2.12)

$$A = \frac{\mu_0}{3S}\hbar\gamma_I g_e \mu_B \sum_i \rho_i \tag{2.12}$$

and the sum runs over all the *s*-components of the MOs of the molecule, $\hbar$ is the Planck constant, μ_0 is the magnetic permeability in vacuum, μ_B is the Bohr magneton, g_e is the Landé coefficient for the free electron , γ_I is the nuclear magnetiogyric ratio and *S* is the electron-spin quantum number.

Since the nuclear resonance frequency is proportional to the total magnetic field, this mechanism provides a contribution δ^{con} to the paramagnetic shift, which could be derived, calculating the energy difference for the close nuclear levels ($\Delta M_I = \pm 1$); the NMR contact shift becomes

$$\delta^{\mathrm{con}} = \frac{A}{\hbar\gamma_I}\frac{g_e\mu_B S(S+1)}{3kT} \tag{2.13}$$

Eq. predicts a T^{-1} dependence of δ^{con} (as expected for the Curie law) and large contact shifts for strongly paramagnetic complexes possessing efficient spin delocalization.

In close analogy to *J* coupling mechanism, δ^{con} may be anisotropic, as g_e varies with molecular orientation. The propagation of electron spin density from the metal center to the observed nucleus occurs through contiguous electron clouds magnetic polarization (Figure 2.1), and, as stated before, it is enhanced in presence of electron delocalization. In such a way the contact shift may reach the *s*-orbitals of hydrogen or hetero-atoms not directly involved in metal bonding.

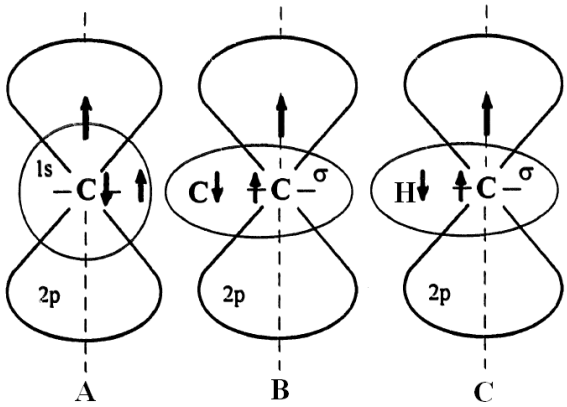

Figure 2.1 Propagation of electronic spin density ρ through polarization of electronic clouds. An unpaired electron, located in a *2p* orbital, may polarize the electronic clouds in *s* or σ orbitals, propagating the spin density ρ onto the nucleus (picture A), or onto the closest nuclei (picture B and C).

The through-bond spin-density propagation is sensitive to ligand backbone conformation and sometimes it allows getting structural information. For instance, in ligands with nitrogen donors, the contact shift may be correlated with the M-N-C-H dihedral angle θ (Figure 2.2),[1] through a relation analogous to the Karplus rule (eq. 2.14)

$$\delta^{\mathrm{con}} = a\cos^2\theta + b\cos\theta + c \qquad (2.14)$$

This simple expression becomes more complicate, changing the donors, the metal, or the ligand complexity.[5] As a consequence, apart from a few cases, obtaining structural information from contact shifts remains a hard matter.

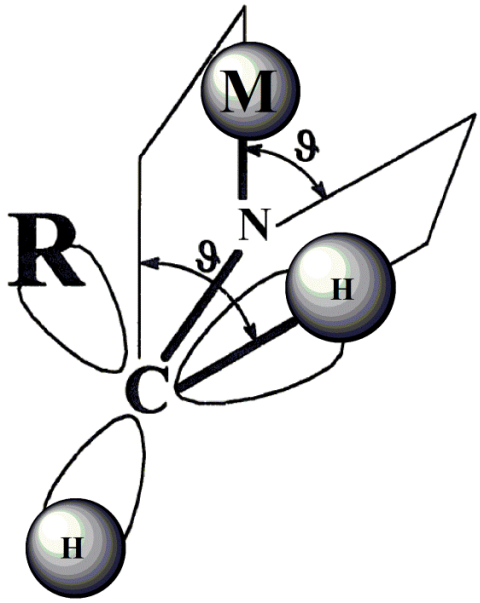

Figure 2.2 Conformational dependence of the proton contact shift in proximity of the metal (M).

2.1.2 The pseudocontact shift

The pseudocontact coupling is due to the through space *dipolar interaction* between electron and nuclear magnetic dipoles. As seen in the previous sections, the static induced magnetic moment results from the difference in population of the various electron spin states created by the external magnetic field. Nuclei sense the sum of the external magnetic field and of the field originated by the electron static magnetic moment. The dipolar interaction between the total magnetic field and nuclei is not completely quenched by molecular rotation as it is for any dipolar interaction between vectors. The anisotropy of the static magnetic moment is responsible for this average residual dipolar interaction, whose effect on the nuclear chemical shift is termed with *pseudocontact shift*. In the classic picture, this is described by dipole-dipole interaction

$$E^{\mathrm{dip}} = -\frac{\mu_0}{4\pi}\left[\frac{3(\boldsymbol{\mu_1}\cdot\boldsymbol{r})(\boldsymbol{\mu_2}\cdot\boldsymbol{r})}{r^5} - \frac{(\boldsymbol{\mu_1}\cdot\boldsymbol{\mu_2})}{r^3}\right] \qquad (2.15)$$

Where $\boldsymbol{\mu_1}$ and $\boldsymbol{\mu_2}$ are the nuclear and electronic dipoles, and **r** is the vector between them.

[5] In case of *d*-transition metals, where metal coordination may involve *s*-donation and *p*-retrodonation, the Karplus type rule may contain also a $\sin^2\theta$ term, or more complicated expressions ([1] and ref. therein).

In quantum mechanics, the dipolar Hamiltonian is introduced

$$H_{\mathrm{dip}} = -\frac{\mu_0}{4\pi}\,\hbar\gamma_I\left[\frac{3(\boldsymbol{\mu}\cdot\boldsymbol{r})\boldsymbol{r}}{r^5}-\frac{\boldsymbol{\mu}}{r^3}\right]\cdot\mathbf{I} == -\frac{\mu_0}{4\pi}\,\hbar\gamma_I\boldsymbol{\mu}\cdot\widetilde{\mathbf{D}}\cdot\mathbf{I} \tag{2.16}$$

with $\mathbf{I}$ the nuclear spin operator, $\boldsymbol{\mu}$ the effective magnetic dipole resulting from electronic distribution and $\widetilde{\mathbf{D}}$ the dipolar tensor

$$\widetilde{\mathbf{D}} = \frac{1}{r^5}\begin{bmatrix} 3x^2-r^2 & 3xy & 3xz \\ 3xy & 3y^2-r^2 & 3yz \\ 3xz & 3yz & 3z^2-r^2 \end{bmatrix} \tag{2.17}$$

For nuclei sufficiently far from the metal, the unpaired electron(s) distribution can be approximated to an electric dipole centered *on* the metal (*Metal-centered point-dipole approximation*), and $\widetilde{\mathbf{D}}$ contains the coordinates of the nucleus with respect to it. Expressing the magnetic dipole $\boldsymbol{\mu}$ in terms of the external field $\mathbf{B_0}$ and the magnetic susceptibility tensor $\tilde{\boldsymbol{\chi}}$

$$\boldsymbol{\mu} = \frac{1}{\mu_0}\tilde{\boldsymbol{\chi}}\cdot\mathbf{B_0} \tag{2.18}$$

and replacing eq. (2.18) in (2.16), we obtain

$$H_{\mathrm{dip}} = -\frac{\hbar\gamma_I}{4\pi}\mathbf{B_0}\cdot(\tilde{\boldsymbol{\chi}}\widetilde{\mathbf{D}})\cdot\mathbf{I} \tag{2.19}$$

This is formally analogue to the diamagnetic term describing the sum of Zeeman and chemical shift Hamiltonians

$$H_{\mathrm{dia}} = H_{\mathrm{Zeeman}} + H_{\mathrm{CS}} = -\hbar\gamma_I\mathbf{B_0}\cdot(\mathbf{1}-\tilde{\boldsymbol{\sigma}})\cdot\mathbf{I} \tag{2.20}$$

where $\tilde{\sigma}$ is the chemical shielding tensor and $\mathbf{1}$ the identity operator. Neglecting H_{con}, the nuclear-spin Hamiltonian, eq. (2.5) can be rewritten

$$H_{\mathrm{spin}}^{\mathrm{nuc}} = -\hbar\gamma_I\mathbf{B_0}\cdot(\mathbf{1}-\tilde{\boldsymbol{\sigma}}+\frac{1}{4\pi}\tilde{\boldsymbol{\chi}}\widetilde{\mathbf{D}})\cdot\mathbf{I} \tag{2.21}$$

For a $\mathbf{B_0}$ aligned along the *z*-axis, and averaging eq. (2.19) for all molecular orientations, the energy difference between levels with $\Delta M_I = \pm 1$ is

$$\Delta E = \hbar\gamma_I\mathbf{B_0}\left(1-\sigma^{\mathrm{iso}}+\frac{1}{12\pi}\mathrm{tr}\{\tilde{\boldsymbol{\chi}}\widetilde{\mathbf{D}}\}\right) \tag{2.22}$$

where σ^{iso} is proportional to the trace of $\tilde{\boldsymbol{\sigma}}$ ($\sigma^{\mathrm{iso}} = \frac{1}{3}(\sigma_{xx}+\sigma_{yy}+\sigma_{zz}) = \frac{1}{3}\mathrm{tr}\{\tilde{\boldsymbol{\sigma}}\}$. The chemical shift is obtained dividing eq. (2.22) the Zeeman energy by $\hbar\gamma_I B_0$

$$\delta = \frac{\Delta E}{\hbar\gamma_I B_0} = 1-\sigma^{\mathrm{iso}}+\frac{1}{12\pi}\mathrm{tr}\{\tilde{\boldsymbol{\chi}}\widetilde{\mathbf{D}}\} \tag{2.23}$$

$$\delta^{\mathrm{dia}} = 1 - \sigma^{\mathrm{iso}} \tag{2.24}$$

$$\delta^{\mathrm{pc}} = \frac{1}{12\pi}\mathrm{tr}\{\tilde{\boldsymbol{\chi}}\tilde{\mathbf{D}}\} \tag{2.25}$$

where the diamagnetic and pseudocontact shifts were made explicit. As $\tilde{\mathbf{D}}$ is a traceless tensor, the isotropic component $\chi^{\mathrm{iso}}\mathbf{1}$ of magnetic susceptibility gives no contribution to δ^{pc}, which depends only on the anisotropic part of the magnetic susceptibility $\tilde{\boldsymbol{\chi}}'$

$$\tilde{\boldsymbol{\chi}}' = \tilde{\boldsymbol{\chi}} - \mathrm{tr}\{\tilde{\boldsymbol{\chi}}\}\mathbf{1} = \tilde{\boldsymbol{\chi}} - \tilde{\chi}^{\mathrm{iso}}\mathbf{1} \tag{2.26}$$

$$\delta^{\mathrm{pc}} = \frac{1}{12\pi}\mathrm{tr}\{(\tilde{\boldsymbol{\chi}}' + \tilde{\chi}^{\mathrm{iso}}\mathbf{1})\tilde{\mathbf{D}}\} = \frac{1}{12\pi}\left[\mathrm{tr}\{\tilde{\boldsymbol{\chi}}, \tilde{\mathbf{D}}\} + \tilde{\chi}^{\mathrm{iso}}\mathrm{tr}\{\tilde{\mathbf{D}}\}\right] = \frac{1}{12\pi}\mathrm{tr}\{\tilde{\boldsymbol{\chi}}'\tilde{\mathbf{D}}\} \tag{2.27}$$

In the metal-centered Cartesian coordinates eq. (2.27) becomes

$$\begin{aligned}\delta^{\mathrm{pc}} = \frac{1}{12\pi}\frac{1}{r^5}[&\chi'_{xx}(3x^2 - r^2) + \chi'_{yy}(3y^2 - r^2) + \chi'_{zz}(3z^2 - r^2) + 6\chi'_{xy}xy + 6\chi'_{xz}xz \\ &+ 6\chi'_{yz}yz]\end{aligned} \tag{2.28}$$

By choosing the coordinate system oriented along the principal axes of $\tilde{\boldsymbol{\chi}}'$, this can be re-written in eq. (2.29)

$$\begin{aligned}\delta^{\mathrm{pc}} &= D_1\frac{3\cos^2\theta - 1}{r^3} + D_2\frac{\sin^2\theta\,\cos 2\gamma}{r^3} \\ D_1 &= \frac{1}{12\pi}\left[\chi'_{zz} - \frac{\chi'_{yy} + \chi'_{xx}}{2}\right] = \frac{1}{12\pi}\left[\frac{3}{2}\chi'_{zz}\right] \\ D_2 &= \frac{1}{12\pi}\left[\frac{3}{2}(\chi'_{yy} + \chi'_{xx})\right]\end{aligned} \tag{2.29}$$

Where the position of the nucleus is described by polar coordinates (*r, θ, φ* in Figure 2.3), and the coefficients D_1 and D_2 contain the principal values of the magnetic anisotropy tensor. For molecules with axial symmetry (C_n with $n \geq 3$), $\chi'_{xx} = \chi'_{yy} = \chi'_{\perp}$, and $\chi'_{zz} = \chi'_{\parallel}$, equation (2.29) simplifies to

$$\begin{aligned}\delta^{\mathrm{pc}} &= D\left[\frac{3\cos^2\theta - 1}{r^3}\right] \\ D &= \frac{\chi'_{\parallel} - \chi'_{\perp}}{12\pi}\end{aligned} \tag{2.30}$$

In both (2.29) and (2.30) the terms $(3\cos^2\theta - 1)/r^3$ and $(\sin^2\theta\cos 2\varphi)/r^3$explicitly contain the coordinates of the observer nucleus, and make pseudocontact shifts a precious information source about the geometry of the complex (these terms are called *geometrical factors*, shortly *GF*). The pseudocontact shift does not depend on the magnetogyric ratio γ_I, therefore is independent of the observed nucleus nature.

Equations (2.28-30) are effective within the limits of the metal-centered point-dipole approximation: if not, the whole electronic orbital distribution should be considered.[6] For *d*-transition metals, significant deviations from point-dipole approximation are estimated for distances lower than 7 Å from the metal.[6] Conversely in lanthanides the inner character of *f*-orbitals strongly reduces this deviation: Golding *et al.* calculated δ^{pc} from

the exact charge distribution in *f*-orbitals, showing that the deviation from point-dipole approximation is negligible for distances larger than 3-4 Å.[6] In the case of f^{13} configuration (Yb^{3+}) in a tetragonal distortion, the error in the metal-nucleus distance calculated by using the point-dipole limit is of the order of $0.6\text{-}2.4 \cdot 10^{-2}$ Å at 2 Å (< 1.5%) and reduces to less than $0.4\text{-}1.5 \cdot 10^{-2}$ Å at 3 Å (< 0.5%).

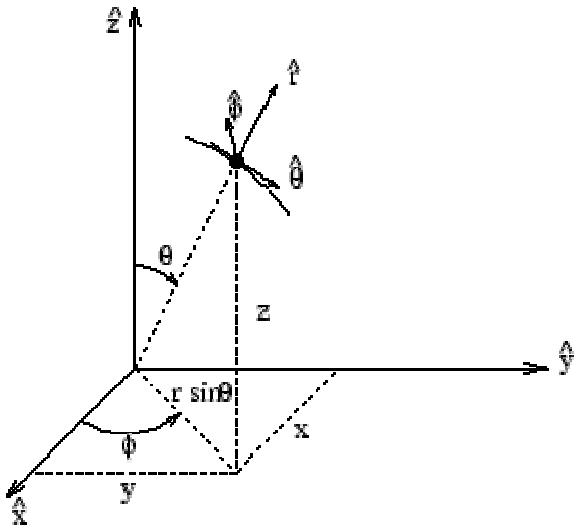

Figure 2.3 Polar coordinate reference system

2.2 The paramagnetic nuclear relaxation

In addition to contributing to the hyperfine shift, the electronic paramagnetism affects also nuclear relaxation. Longitudinal and transverse relaxation times (T_1 and T_2, respectively) are generally shortened by interaction with paramagnetic center, equations (2.3-4), with relaxation rates depending on the nature and on their distance from the observed nucleus. This contribution is often termed as *lanthanide-induced relaxation* (*LIR*). The phenomenon depends both on inner-sphere and outer-sphere mechanisms, which can be divided further into three mechanisms, responsible for paramagnetic nuclear relaxation: the **dipolar**, the **Curie** and (to a lesser extent) the contact mechanism.

- ***The dipolar relaxation mechanism:*** The paramagnetic inner-sphere relaxation may be tracked back to the fluctuating magnetic field produced by the electron magnetic momentum, which induces nuclear spin transitions for nuclei whose magnetic momentum interacts with the electronic magnetic one.[1a,2,7] The electron-nuclear dipolar interaction (2.17-18) depends on the relative position and orientations of the magnetic dipoles, thus, the continuous reorientation of the molecule with respect to the magnetic field, due to molecular tumbling, as well as the electron-spin-state change due to electronic relaxation generate stochastic fluctuations of this interaction, and cause **dipolar relaxation.**

The correlation time τ_C for these fluctuations is a combination of rotational correlation time τ_R,[6] electronic correlation time τ_E,[7] and one derived from chemical exchange τ_M

$$[\textit{dipolar}\ \tau_C] \qquad \tau_C^{-1} = \tau_R^{-1} + \tau_E^{-1} + \tau_M^{-1} \tag{2.31}$$

The relaxation rates are described by the Solomon equations.[7-9]

$$R_1^{\mathrm{dip}} = \frac{1}{T_1^{\mathrm{dip}}} = \frac{2}{15}\left(\frac{\mu_0}{4\pi}\right)^2 \frac{\gamma_I^2 g_e^2 \mu_B^2 S(S+1)}{r^6}\left[\frac{\tau_C}{1+(\omega_I-\omega_S)^2\tau_C^2} + \frac{3\tau_C}{1+\omega_I^2\tau_C^2} + \frac{6\tau_C}{1+(\omega_I+\omega_S)^2\tau_C^2}\right] \tag{2.32}$$

$$R_2^{\mathrm{dip}} = \frac{1}{T_2^{\mathrm{dip}}} = \frac{1}{15}\left(\frac{\mu_0}{4\pi}\right)^2 \frac{\gamma_I^2 g_e^2 \mu_B^2 S(S+1)}{r^6}\left[4\tau_C + \frac{\tau_C}{1+(\omega_I-\omega_S)^2\tau_C^2} + \frac{3\tau_C}{1+\omega_I^2\tau_C^2} + \frac{6\tau_C}{1+(\omega_I+\omega_S)^2\tau_C^2} + \frac{6\tau_C}{1+\omega_S^2\tau_C^2}\right] \tag{2.33}$$

$$R_{1\rho}^{\mathrm{dip}} = \frac{1}{T_{1\rho}^{\mathrm{dip}}} = \frac{1}{15}\left(\frac{\mu_0}{4\pi}\right)^2 \frac{\gamma_I^2 g_e^2 \mu_B^2 S(S+1)}{r^6}\left[\frac{4\tau_C}{1+\omega_B^2\tau_C^2} + \frac{\tau_C}{1+(\omega_I-\omega_S)^2\tau_C^2} + \frac{3\tau_C}{1+\omega_I^2\tau_C^2} + \frac{6\tau_C}{1+(\omega_I+\omega_S)^2\tau_C^2} + \frac{6\tau_C}{1+\omega_S^2\tau_C^2}\right] \tag{2.34}$$

where all constants are the same reported above. The spectral density terms (reported in square brackets) describe the efficiency of the relaxation mechanism as a function of Larmor frequencies and correlation times.

The $R_{1\rho}^{\mathrm{dip}}$ term is the longitudinal relaxation rate in the rotating frame, and ω_B is the nuclear Larmor frequency around the spin-lock radio frequency field $\mathbf{B_1}$. As $|\omega_B^2\tau_C^2| \ll 1$, $R_{1\rho}^{\mathrm{dip}}$ is substantially equal to R_2^{dip} and will be omitted in the following description.[1a,b]

In the fast motion limit ($|\omega_I^2\tau_C^2| \ll 1$ and $|\omega_S^2\tau_C^2| \ll 1$)

$$R_1^{\mathrm{dip}} = R_2^{\mathrm{dip}} = \frac{4}{3}\left(\frac{\mu_0}{4\pi}\right)^2 \frac{\gamma_I^2 g_e^2 \mu_B^2 S(S+1)}{r^6}\tau_C \tag{2.35}$$

The constant $\gamma_I^2 g_e^2 \mu_B^2 S(S+1)/r^6$ is proportional to the square of the nuclear-electron dipolar interaction, and is strongly influenced by the metal-nucleus distance (r^{-6}).

[6] It should be more appropriate to use the term 'reorientational' correlation time, due to full molecular rotation prevention by the frequents hits with the solvent. As 'rotational correlation time' is a very commonly used term, in this work we keep this expression.

[7] The electron correlation time τ_E is related to electronic relaxation. In principle, longitudinal (T_{1E}) and transverse relaxation times (T_{2E}) may be distinguished into $\tau_{E1} = T_{1E}$ and $\tau_{E2} = T_{2E}$. In the present work, we consider fast motion limit for electron, with $T_{1E} = T_{2E}$, and consequently $\tau_E = T_{1E} = T_{2E}$.

- ***The Curie relaxation mechanism*:** the fluctuation of the electronic magnetic dipole averages around an 'effective' magnetic dipole μ arising from the slight difference in population between electronic states, and proportional to the external field $\mathbf{B_0}$ Eq. (2.20). The dipolar interaction between μ and the observed nucleus fluctuates under the effect of molecular tumbling, and is responsible for **Curie relaxation**. As μ is averaged over *S* states, the correlation time here contains only the rotational and exchange terms

$$[Curie\ \tau_C]\ \tau_C^{-1} = \tau_R^{-1} + \tau_M^{-1} \tag{2.36}$$

and the relaxation rates are thus expressed [9-11]

$$R_1^{\text{Curie}} = \frac{1}{T_1^{\text{Curie}}} = \frac{2}{5}\left(\frac{\mu_0}{4\pi}\right)^2 \frac{\gamma_I^2 g_e^4 \mu_B^4 B_0^2 [S(S+1)]^2}{(3kT)^2 r^6} \frac{3\tau_C}{1+\omega_I^2\tau_C^2} \tag{2.37}$$

$$R_2^{\text{Curie}} = \frac{1}{T_2^{\text{Curie}}} = \frac{1}{5}\left(\frac{\mu_0}{4\pi}\right)^2 \frac{\gamma_I^2 g_e^2 \mu_B^4 B_0^2 [S(S+1)]^2}{(3kT)^2 r^6} \left[4\tau_C + \frac{3\tau_C}{1+\omega_I^2\tau_C^2}\right] \tag{2.38}$$

that, in the fast motion limit ($|\omega_I^2\tau_C^2| \ll 1$) become

$$R_1^{\text{Curie}} = \frac{6}{7} R_2^{\text{Curie}} = \frac{6}{5}\left(\frac{\mu_0}{4\pi}\right)^2 \frac{\gamma_I^2 g_e^2 \mu_B^4 B_0^2 [S(S+1)]^2}{(3kT)^2 r^6} \tau_C \tag{2.39}$$

The Curie relaxation rates R_1 and R_2 are never equal, even in the fast motion limit, and significantly increase with external magnetic field ($\propto B_0^2$). This relaxation mechanism is strongly temperature-dependent: in addition to the explicit T^{-2} term, temperature largely influences also τ_R. Magnetic field and temperature dependence in dipolar relaxation mechanism are generally smaller and hardly evaluated, and depend only on the implicit contribution included in τ_C. However Curie-spin contribution is often much smaller than the dipolar one, except for ^{1}H-NMR experiment (large γ_I) performed at high magnetic field (large B_0) and strongly paramagnetic (large g_e) samples.

- ***The contact relaxation mechanism*:** contact interaction also contributes to nuclear relaxation with a contact relaxation term. In this mechanism, correlation time τ_C depends only on electronic and exchange correlation times, as contact interaction is essentially scalar and minimally influenced by molecular orientation

$$[contact\ \tau_C]\ \tau_C^{-1} = \tau_E^{-1} + \tau_M^{-1} \tag{2.40}$$

The expressions for R_1 and R_2 are given by the Bloembergen equations [9,12]

$$R_1^{\text{con}} = \frac{2}{3} S(S+1)\left(\frac{A}{\hbar}\right)^2 \frac{\tau_C}{1+\omega_S^2\tau_C^2} \tag{2.41}$$

$$R_2^{\text{con}} = \frac{1}{3} S(S+1)\left(\frac{A}{\hbar}\right)^2 \left[\tau_C + \frac{\tau_C}{1+\omega_S^2\tau_C^2}\right] \tag{2.42}$$

Where *A* is the coupling constant (2.12). In extreme narrowing condition ($|\omega_S^2 \tau_C^2| \ll 1$) (2.41) and (2.42) simplify in

$$R_1^{\text{con}} = R_2^{\text{con}} = \frac{1}{3} S(S+1) \left(\frac{A}{\hbar}\right)^2 \tau_C \tag{2.43}$$

Apart from donor ligand nuclei themselves, contact relaxation is generally much smaller than dipolar and Curie terms and often may be neglected.[1]

The relative importance of dipolar and Curie mechanism is strongly variable with the nature of the paramagnetic species, magnetic field and electronic and rotational correlation times, and must be evaluated for each specific case. For all relaxation mechanisms reported above, relaxation rates are proportional to the square of magnetogyric ratio (γ_I^2): hence, proton and fluorine are much more affected by relaxation than most heteronuclei (^{13}C, ^{15}N, etc.).

2.3 The case of lanthanides

2.3.1 Paramagnetic shift

Lanthanide ions paramagnetism is due to *4f* orbitals partial filling. In this elements, the total electronic spin angular moment (*S*) and the orbital angular moment (*L*) are strongly coupled by the spin-orbit interactions, so their magnetic properties are better described by the total angular momentum *J* ($|J| = |L \pm S|$).

The equation of the paramagnetic shift and relaxation rates are easily derived replacing the spin quantum numbers *S* with *J*, and the corresponding Landé factor g_e with g_j that contains the orbital contribution. Table 2.1 reports, for each Ln^{3+} ion, the spectroscopic states with the calculated values of *J* and g_j.

The hyperfine **contact shift** in lanthanides is less important than in *d*-transition metals,[1-2,13] because of the inner character of *4f* orbitals. The propagation of the contact coupling occurs through the overlap of the donor orbitals and the outer *6s* orbitals of the metal, which are in turn polarized by *4f* electrons. The contact shift equation (2.15) corrected for the *J* term is

$$\delta^{\text{con}} = \frac{A}{\hbar\gamma_I} \frac{g_j(g_j - 1)\mu_B J(J+1)}{3kT} = -\frac{A}{\hbar\gamma_I B_0} \langle S_z \rangle_J \tag{2.44}$$

where, *A* is described in (2.13-14) and $\langle S_z \rangle_J$ is the expectation value of the electronic spin *z*-component.[8]

Pseudocontact shift is due to magnetic susceptibility anisotropic part (2.22), which is in turn originated by electronic orbital contributions, which arise only when spherical symmetry around the metal is removed, that is only when the lanthanide ion is immersed into ligand crystal-field. Bleaney [14] provided an elegant procedure to derive in a general way δ^{pc} from ligand crystal-field parameters: the crystal-field effect on the electronic spin Hamiltonian $H_{\text{spin}}^{\text{el}}$ is spanned into a sum of *spin-operators* O_k^q of *k* rank, involving J_x, J_y, J_z components

[8] It should be mentioned that the constant *A* contains the electronic Landé factor g_e, which is not replaced by g_j.

$$H_{\text{spin}}^{\text{el}} = \mu_0 g_J \mu_\beta \mathbf{J} \cdot \mathbf{B_0} + \sum_{k,q} A_k^q \langle r^k \rangle \langle J \| k \| J \rangle O_k^q \tag{2.45}$$

where: k = 2, 4, 6, and $0 \leq q \leq k$, $\mu_0 g_J \mu_\beta \mathbf{J} \cdot \mathbf{B_0}$ is the Zeeman term, $\mathbf{B_0}$ is the magnetic field vector, $\mathbf{J}$ is the total angular moment operator, A_k^q is the energy crystal-field coefficient of order q and rank k, $\langle r^k \rangle$ is the average of the k^{th} power of the electronic radius in the *4f* orbitals, and $\langle J \| k \| J \rangle$ are numerical factors calculated for this electron state of each lanthanide ion.

Table 2.1 Electronic properties of lanthanide ions.[1] The spectroscopic states $^{2S+1}L_J(2J+1)$ are referred to the ground state. The pseudocontact shifts (δ^{pc}) are calculated for a nucleus with GF = 1 in an axially symmetric tensor. $\langle S_z \rangle_J$ values are calculated including excited states. Relative linewidths are calculated from (2.53-58) below, using electron correlation times reported in [1], and scaled to Yb linewidth 10 Hz

Ln(III)	$^{2S+1}L_J(2J+1)$	g_J	$\langle S_z \rangle_J$	δ^{PC}	$\delta^{PC}/\langle S_z \rangle_J$	Relative Linewidth
				(ppm)		(Hz)
Ce^{3+}	$^2F_{5/2}(6)$	6/7	0.98	1.6	1.6	2.3
Pr^{3+}	$^3H_4(9)$	4/5	2.97	2.7	0.9	5.2
Nd^{3+}	$^4I_{9/2}(10)$	8/11	4.49	1.0	0.2	5.7
Pm^{3+}	$^5I_4(9)$	3/5	4.01	-0.6	-0.1	2.7
Sm^{3+}	$^6H_{5/2}(6)$	2/7	-0.06	0.2	-3.3	0.2
Eu^{3+}	$^7F_0(1)$	-	-10.68	-1.0	0.1	-
Gd^{3+}	$^8S_{7/2}(8)$	2	-31.50	0.0	0.0	100-10^4
Tb^{3+}	$^7F_6(13)$	3/2	-31.82	20.7	-0.7	109.5
Dy^{3+}	$^6H_{15/2}(16)$	4/3	-28.54	23.8	-0.8	151.0
Ho^{3+}	$^5I_8(17)$	5/4	-22.63	9.4	-0.4	149.0
Er^{3+}	$^4I_{15/2}(16)$	6/5	-15.37	-7.7	0.5	104.3
Tm^{3+}	$^3H_6(13)$	7/6	-8.21	-12.7	1.5	47.1
Yb^{3+}	$^2F_{7/2}(8)$	8/7	-2.59	-5.2	2.0	10.0

From this Hamiltonian the magnetic susceptibility tensor $\boldsymbol{\chi}$ is derived, which is inserted in (2.29) to give

$$\delta^{\text{pc}} = -\frac{\mu_0}{4\pi} \frac{g_j^2 \mu_B^2 J(J+1)(2J-1)(2J+3)}{60(kT)^2} \left[D_Z \frac{3\cos^2\theta - 1}{r^3} + (D_X - D_Y) \frac{\sin^2\theta \cos 2\gamma}{r^3} \right]$$
$$D_X = \langle r^2 \rangle \langle J \| \alpha \| J \rangle (A_2^2 - A_0^2)$$
$$D_Y = \langle r^2 \rangle \langle J \| \alpha \| J \rangle (-A_2^2 - A_0^2)$$
$$D_Z = \langle r^2 \rangle \langle J \| \alpha \| J \rangle (2A_0^2) \tag{2.46}$$

Where D_X, D_Y, D_Z contain crystal-field parameters. Bleaney [14] observed that whilst the magnetic susceptibility isotropic component depends on temperature with T^{-1} (Curie law), the anisotropic part depends on T^{-n} with ($n \geq 2$). He assumed that the ground state multiplet crystal-field energy (ΔE_{CF}) is small compared

to kT so that only crystal-field terms with rank k = 2 can be considered, which gives a temperature dependence on T^{-2}.[9]

Assuming an isostructural series of axially symmetric complexes and considering a reasonable value of $A_0^2\langle r^2\rangle$ = +10 cm^{-1}, for all lanthanides, Bleaney [14] estimated the pseudocontact shift with (2.46) for a nucleus with $(3\cos^2\theta - 1)/r^3$ = 1 (Figure 2.4 and Table 2.1).[10] Notably the strongest shifts are given by Tb^{3+} and Dy^{3+}, opposite in sign with respect to Er^{3+}, Tm^{3+}, and Yb^{3+}.

In Figure 2.4 these shifts are plotted together with the values of $-\langle S_z\rangle_J$ (2.44) in order to show each lanthanide ion tendency to give contact and pseudocontact shift contributions.

The pseudocontact shift T^{-2} dependence proposed by Bleaney is correct under the assumption that *J* manifold crystal-field splitting energy (ΔE_{CF}) is small compared to *kT,* otherwise crystal-filed parameters of rank k = 4, 6 should be considered, which generates additional T^{-n} terms of order higher than 2 (*n* > 2). McGarvey estimated that T^{-3} contributions in $D_1$and D_2 constants (see eq. (2.29)) are not negligible but do not exceed 10% of T^{-2} term.[15] He concluded that contact shift (proportional to T^{-1}) cannot be easily separated from the pseudocontact part (depending on T^{-2} and T^{-3} terms) by simply fitting the shifts trend at variable temperature, because T^{-1}, T^{-2}, and T^{-3} functions have very similar trends in a wide range of temperatures.[15-16] The assumption that crystal-field splitting is small compared to *kT* ($\Delta E_{CF} < kT$) is often not acceptable, as ΔE_{CF} may be much larger than *kT* (ΔE_{CF} > 400 cm^{-1}, see for example the Yb DOTMA and Yb(BINOL)$_3$ cases [17]). More recently, Mironov *et al*. [18] calculated the magnetic susceptibility anisotropy D_1along the lanthanide series, including all crystal-field terms, and for several regular and distorted polyhedrons. These values were compared with those expected from Bleaney's theory, which limits crystal-field terms to A_0^2. It results that, under a qualitative point of view, D_1 trend along Ln^{3+} series, expected from Bleaney (Table 2.1 and Figure 2.4) is still acceptable, but in a quantitative analysis, Bleaney values may show large deviations from those calculated including all crystal-field terms. Mironov also evidenced how D_1 has a remarkable dependence on the geometry of the coordinated polyhedron and is largely influenced by small distortions in ligand arrangement.[18a]

2.3.2 Paramagnetic relaxation

The paramagnetic relaxation contributions, corrected for the spin-orbit effect, and in the absence of chemical exchange, are thus summarized

$$R_1^{\mathrm{dip}} = \frac{2}{15}\left(\frac{\mu_0}{4\pi}\right)^2 \frac{\gamma_I^2 g_J^2 \mu_B^2 J(J+1)}{r^6}\left[\frac{\tau_C}{1+(\omega_I-\omega_S)^2\tau_C^2} + \frac{3\tau_C}{1+\omega_I^2\tau_C^2} + \frac{6\tau_C}{1+(\omega_I+\omega_S)^2\tau_C^2}\right] \qquad (2.47)$$

[9] Eu^{3+} and Sm^{3+} ions do not follow (2.46) because of the presence of excited states differing in *J* from ground state and close in energy to it (see Table 6.1). These excited states give contributions to magnetic susceptibility anisotropy in T^{-n} with $n \geq 2$. Anyway, for all other lanthanide ions, these excited states are far in energy from the ground one, therefore these additional terms can be safely neglected (Ref. [14]).

[10] Other values of the crystal field coefficient, even negative, are equally possible; so data here reported should be considered only for the relative shift magnitude in different lanthanide ions.

$$R_2^{\text{dip}} = \frac{1}{15}\left(\frac{\mu_0}{4\pi}\right)^2 \frac{\gamma_I^2 g_J^2 \mu_B^2 J(J+1)}{r^6}\left[4\tau_C + \frac{\tau_C}{1+(\omega_I-\omega_S)^2\tau_C^2} + \frac{3\tau_C}{1+\omega_I^2\tau_C^2} + \frac{6\tau_C}{1+(\omega_I+\omega_S)^2\tau_C^2} + \frac{6\tau_C}{1+\omega_S^2\tau_C^2}\right] \quad (2.48)$$

$$R_1^{\text{con}} = \frac{2}{3}J(J+1)\left(\frac{A}{\hbar}\right)^2 \frac{\tau_C}{1+\omega_S^2\tau_C^2} \quad (2.49)$$

$$R_2^{\text{con}} = \frac{1}{3}J(J+1)\left(\frac{A}{\hbar}\right)^2 \left[\tau_C + \frac{\tau_C}{1+\omega_S^2\tau_C^2}\right] \quad (2.50)$$

$$R_1^{\text{Curie}} = \frac{2}{5}\left(\frac{\mu_0}{4\pi}\right)^2 \frac{\gamma_I^2 g_J^4 \mu_B^4 B_0^2 [J(J+1)]^2}{(3kT)^2 r^6} \frac{3\tau_C}{1+\omega_I^2\tau_C^2} \quad (2.51)$$

$$R_2^{\text{Curie}} = \frac{1}{5}\left(\frac{\mu_0}{4\pi}\right)^2 \frac{\gamma_I^2 g_J^2 \mu_B^4 B_0^2 [S(S+1)]^2}{(3kT)^2 r^6}\left[4\tau_C + \frac{3\tau_C}{1+\omega_I^2\tau_C^2}\right] \quad (2.52)$$

With the exclusion of donor atoms, contact relaxation is generally negligible in comparison to other terms. For all lanthanide ions, apart from Gd^{3+}, the dipolar mechanism correlation time is dominated by the electronic one τ_E (10^{-12}-10^{-14}) [1,19], which is much smaller than rotational correlation time. The very short value of τ_E is due to the efficient electronic relaxation (Orbach-type process),[20] favored by the presence of several states near in energy to the ground state. This is not the case of Gd^{3+}, for which the ground state is a singlet ($^8S_{7/2}$) without low-lying excited levels, therefore τ_E is considerably higher (10^{-8}-10^{-9}).[21]

In the absence of chemical exchange (or better for $\tau_E \ll \tau_M$), for small molecules ($|\omega_I^2\tau_C^2| \ll 1$ and $|\omega_S^2\tau_C^2| \ll 1$), and for all paramagnetic lanthanides, except Gd^{3+}, equations (2.47)-(2.52) become

$$R_1^{\text{dip}} = R_2^{\text{dip}} = \frac{4}{3}\left(\frac{\mu_0}{4\pi}\right)^2 \frac{\gamma_I^2 g_J^2 \mu_B^2 J(J+1)}{r^6}\tau_E \quad (2.53)$$

$$R_1^{\text{con}} = R_2^{\text{con}} = \frac{2}{3}J(J+1)\left(\frac{A}{\hbar}\right)^2 \tau_E \quad (2.54)$$

$$R_1^{\text{Curie}} = \frac{6}{7}R_2^{\text{Curie}} = \frac{6}{5}\left(\frac{\mu_0}{4\pi}\right)^2 \frac{\gamma_I^2 g_J^2 \mu_B^4 B_0^2 [J(J+1)]^2}{(3kT)^2 r^6}\tau_E \quad (2.55)$$

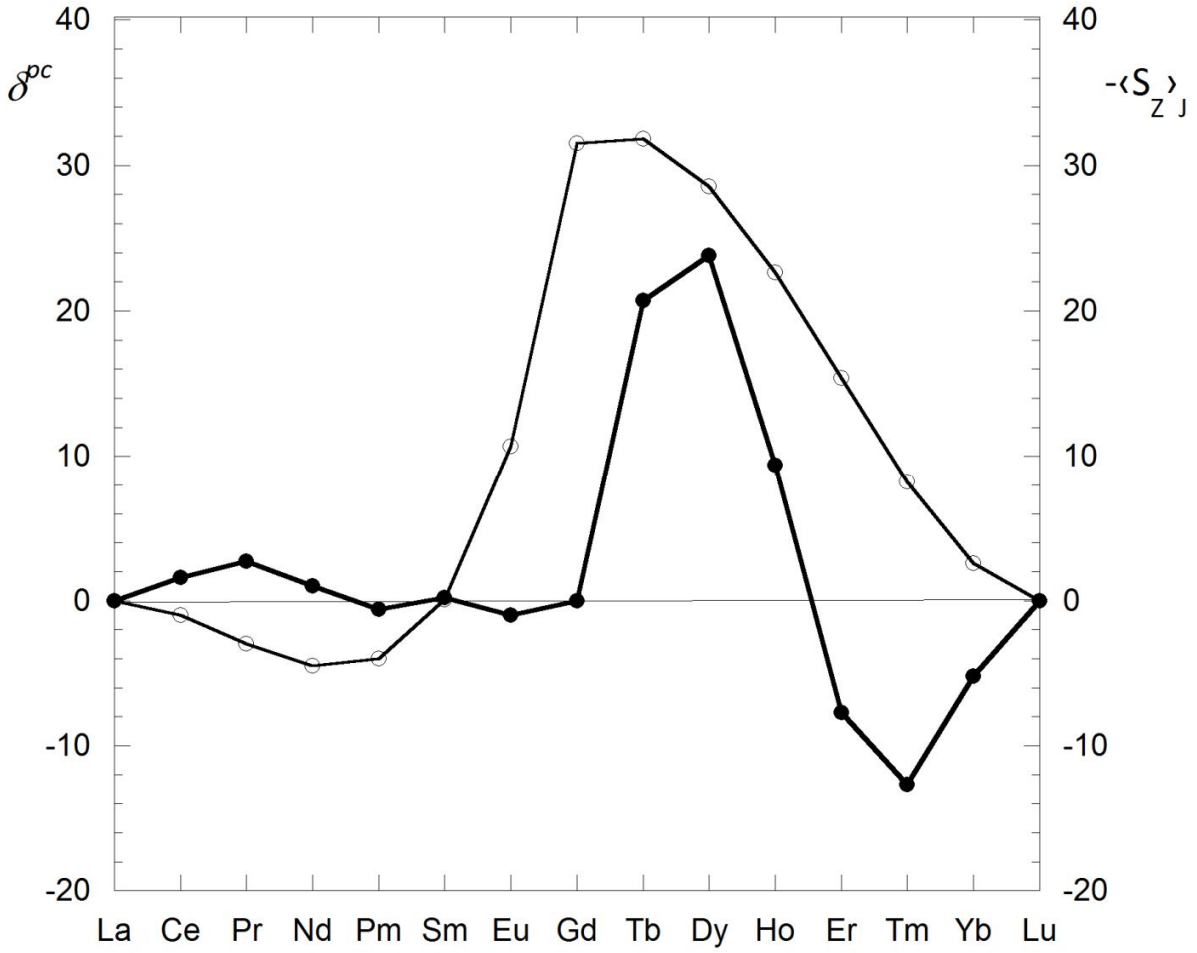

Figure 2.4 Relative contributions of pseudocontact (δ^{pc}, filled dots) and contact terms ($-\langle S_z \rangle_J$, empty dots), along the Ln(III) series, as reported in Table 2.1.[1,14]

References

[1] (a) I. Bertini, C. Luchinat, *Coord. Chem. Rev.* **1996**, *150*, 29. (b) I. Bertini, C. Luchinat, G. Parigi, *Solution NMR of Paramagnetic Molecules* **2001**, Elsevier: Amsterdam. (c) I. Bertini, C. Luchinat, G. Parigi, *Prog. Nucl. Magn. Res. Spec.* **2002**, *40*, 249.

[2] J. A. Peters, J. Huskens, D. J. Raber, *Prog. Nucl. Magn. Reson. Spec.* **1996**, *28*, 283.

[3] C. Piguet, C. F. G. C. Geraldes, in *Handbook on the Physics and Chemistry of Rare Earths;* K. A. Jr. Gschneider, J.-C. G. Bünzli, V. K. Pecharsky, Eds. **2003**, Elsevier: Amsterdam. Vol. 33, 353.

[4] R. R. Sharp, *Nuc. Magn. Reson.* **2005**, *34*, 553.

[5] L. Di Bari, P. Salvadori, *Coord. Chem. Rev.* **2005**, *249*, 285.

[6] M. R. Golding, R. O. Pascual, B. R. McGarvey, *J. Magn. Res.* **1982**, *46*, 30.

[7] I. Solomon, *Phys. Rev.* **1955**, *99*, 559.

[8] A. Abragam, *The Principles of Nuclear Magnetism,* **1961**, Oxford University Press: Oxford.

[9] S. H. Koenig, *J. Magn. Reson.* **1982**, *47*, 441.

[10] M. Guéron, *J. Magn. Res.* **1975**, *19*, 58.

[11] A. J. Vega, D. Fiat, *Mol. Phys.***1976**, *31*, 347.

[12] N. Bloemberg, *J. Chem. Phys.* **1957**, *27*, 575.

[13] J. A. Peters, M. S. Nieuwenhuizen, D. J. Raber, *J. Magn. Res.* **1985**, *65*, 417.

[14] B. Bleaney, *J. Magn. Res.* **1972**, *8*, 91.

[15] B. R. McGarvey, *J. Magn. Res.* **1979**, *33*, 445.

[16] M. D. Kemple, B. D. Ray, K. B. Lipkowitz, F. Prendergast, B. D. N. Rao, *J. Am. Chem. Soc.* **1988**, *110*, 8275.

[17] a) L. Di Bari, G. Pintacuda, P. Salvadori, *J. Am. Chem. Soc.* **2000**, *122*, 557. b) L. Di Bari, M. Lelli, G. Pintacuda, G. Pescitelli, F. Marchetti, P. Salvadori, *J. Am. Chem. Soc.* **2003**, *125*, 5549.

[18] (a) V. S. Mironov, Y. G. Galayametdinov, A. Ceulemans, C. Goerller-Walrand, K. Binnemans, *J. Chem. Phys.* **2002**, *116*, 4673. (b) V. S. Mironov, Y. G. Galayametdinov, A. Ceulemans, C. Goerller-Walrand, K. Binnemans, *Chem. Phys. Lett.* **2001**, *345*, 132.

[19] (a) B. M. Alsaadi, F. J. C. Rosotti, R. J. P. Williams, *J. Chem. Soc. Dalton Trans.* **1980**, 2151. (b) S. K. Misra, U. Orhum, *Solid State Commun.* **1987**, *63*, 867. (c) V. M. Malhotra, H. A. Buckmaster, J. M. Dixon, *J. Phys. C: Solid State Phys.* **1980**, *13*, 3921. (d) I. Bertini, F. Capozzi, C. Luchinat, G. Nicastro, Z. Xia, *J. Phys. Chem.* **1993**, *97*, 6351. (e) S. Aime, M. Botta, G. Ermondi, *Inorg. Chem.* **1992**, *31*, 4291.

[20] R. Orbach, *Proc. R. Soc. London* **1961**, *SER. A264,* 458.

[21] (a) G. P. Vishnevskaya, B. M. Kozyrev, *J. Struct. Chem.* **1966**, *7*, 20. (b) A. Hudson, J. W. E. Lewis, *Trans. Faraday Soc.* **1970**, *66*, 1297. (c) S. H. Koenig, *Magn. Reson. Med.* **1991**, *22*, 183. (d) G. Hernandez, M. Tweedle, R. G. Bryant, *Inorg. Chem.* **1990**, *29*, 5109. (e) S. Aime, L. Barbero, M. Botta, *Magn. Res. Imaging* **1991**, *9*, 843.

Chapter 3

Vibrational Circular Dichroism

Vibrational circular dichroism (VCD) is the differential absorbance of left and right circulary polarized light of a vibrational transition in the infrared (IR) fingerprint spectral region.[1] Since its discovery in the seventies [2] and the accompanying theoretical developments,[3] VCD has matured into a major research area in physical and analytical chemistry, especially in the past decade. The advent of the first commercial Fourier transform (FT) IR-VCD spectrometer in 1997 and the implementation of density functional theory (DFT) calculations of VCD intensities into the Gaussian suite of programs in 1996, and into other electronic structure software packages later on, have triggered a flourish of VCD related applications. Today, VCD is a very successful spectroscopic technique, especially for mid-size chiral molecules absolute configuration determination.[4]

The advantageous utility of VCD is rooted in the abundance of spectral information manifested through numerous, well-resolved peaks in the mid-IR region (typically, 900-2000 cm^{-1}). Also, its high information-content stems from the fact that transition taking place during vibrational excitation are commonly 10^2-10^3 times faster than bond rotations, hence allowing the intrinsic conformational structure of a molecule to be determined. Nevertheless, the disadvantages associated with VCD are mainly due to its empirical implementation. Specifically, a requirement for relatively high sample quantity (around 10 mg, at least) or longer signal-collection periods (more than 1 h, generally), due to low signal to noise ratio (commonly $\Delta A/A$ is around 10^{-4}-10^{-6}) could preclude recording of VCD spectra for rare and labile natural products. When obtaining the VCD spectrum, one should be mindful of solubility of a chiral molecule in typically used IR-silent solvents (CCl_4, $CHCl_3$, CH_2Cl_2, CS_2), so that the combination of the concentration and pathlength can provide acceptable IR absorption intensities. More than one combination of pathlength and concentration might be necessary to optimize this parameter in the whole detectable frequency-window. Deuterated solvents could be used as well, in order to shift the relative absorption frequency out of the inquired range and minimize the blind regions. In case of low solubility in apolar or low polar solvents, D_2O or DMSO-d_6 could be used, even though these solvents could participate in hydrogen bonds network and severely affect and modify bands patterns and shape for the vibrations involved in this kind of interactions.

Compared to X-ray crystallography, probably the other most authoritative AC determination tool (when applicable), VCD offers the advantage of not requiring a single crystal of satisfactory size and can be performed directly in solution. So far, no cases of wrong configuration assignment by VCD and DFT analysis, in comparison to other AC techniques determination have been established.[4i] On the contrary, VCD uncovered a few errors in AC assignments by other methods, including X-ray crystallography.[5] Another key advantage of VCD, as an optical spectroscopic method, is the ability to record separate signals from individual conformers, which is not possible by other techniques, notably NMR, due to their slow response to structural changes. The DFT theoretical simulation, requiring a complete analysis of the dominant conformers, combined with the VCD

measurements, makes possible to determine in the same process both AC and the major conformations of chiral molecules.[6][11]

The development of the VCD experimental and theoretical techniques has been accompanied by new possible applications, such as the study of conformational landscape of flexible chiral molecules and hydrogen (H)-bonded chiral complexes, in order to understand solvent effects and chiral recognition: this issue is extremely intriguing, as studying intermolecular *H*-bonding interactions between chiral biomolecules and water is a prerequisite to the understanding the chemistry of life.[8]

In this Chapter we focus on the latest advances of new VCD applications (Section 3.3), along with a brief review of the basic experimental techniques (Section 3.1) and theoretical methods (Section 3.2).

3.1 VCD Instrumentation and Recent Technique Developments

VCD instrumentation has experienced significant growth from its earlier days as a scanning grating instrument.[9] Such a grating spectrometer, which works fine for collecting data in a narrow spectral range of one or two key signature bands, may be inferior compared to an FTIR instrument where a broad range of spectral frequencies can be covered simultaneously. The first FTIR-VCD spectrometer was demonstrated in 1979 by Nafie and co-workers, who placed a photoelastic modulator (PEM) before a sample in an FTIR spectrometer to generate alternating right and left circularly polarized IR light in order to detect the differential absorption.[10] A block diagram of the optical-electronic layout of such an FTIR-VCD spectrometer is shown in Fig. 3.1.[4a] The first commercial VCD spectrometer was marketed by Bomem/BioTools, Inc. in 1997, based on the design from Nafie's laboratory. At present, major FTIR companies, such as Bruker, Thermo Scientific, and Jasco, provide either VCD modules or stand-alone instrumentation. Nowadays, the vast majority of VCD spectrometers in operation around the world are FTIR-VCD spectrometers which take advantage of the high-throughput and multiplex characteristics associated with FTIR spectroscopy.

Compared to a typical electronic CD (ECD) signal, a VCD signal is usually quite weak, about 10^4–10^6 times lower than the intensity of the corresponding vibrational absorption (VA) band. As such, it is considerably more difficult to obtain good quality VCD spectra. Substantial efforts have been devoted over the years to improve the performance of VCD instruments, noticeably by Nafie and co-workers.[11] One primary concern in VCD measurements is the occurrence of optical artifacts which can interfere with the small VCD intensities. In the absence of chirality in a sample, one expects the VCD spectrum to be zero (with low level of noise) across the whole spectral range measured. In practice, this may not be the case because of strain and other imperfections of the optical components employed in the measurement. These can modify the beam polarization state and result in so called baseline artifacts.[11a] For instance, the VCD spectra in the CH-stretching region of camphor in CCl_4 measured using several different versions of FTIR-VCD spectrometers was studied in a recent paper.[12] Several approaches in order to remove baseline artifacts were implemented, starting from the simplest operation: measuring the VCD spectrum of the opposite enantiomer of a chiral sample under identical

[11] Recently Taniguchi and Monde [7] have successfully applied the excitonic coupling method to the absolute configuration assignment of bicarbonylic compounds, bypassing the need of theoretical simulations. It has been the first time that this approach, widely used in ECD, has been extended to VCD.

conditions and then obtain the spectrum by subtracting the two raw spectra and dividing the difference spectrum by two. Actually, this procedure is considered the best way to obtain the 'true' VCD spectrum. Alternatively, one can measure the racemic mixture under identical conditions and subtract it from the raw spectrum of the chiral sample. Very often neither the opposite enantiomer nor the racemic mixture is available, and in this case, the common practice is to correct the baseline by subtracting the solvent VCD spectrum measured under the same experimental condition, to reduce at least the baseline artifacts.

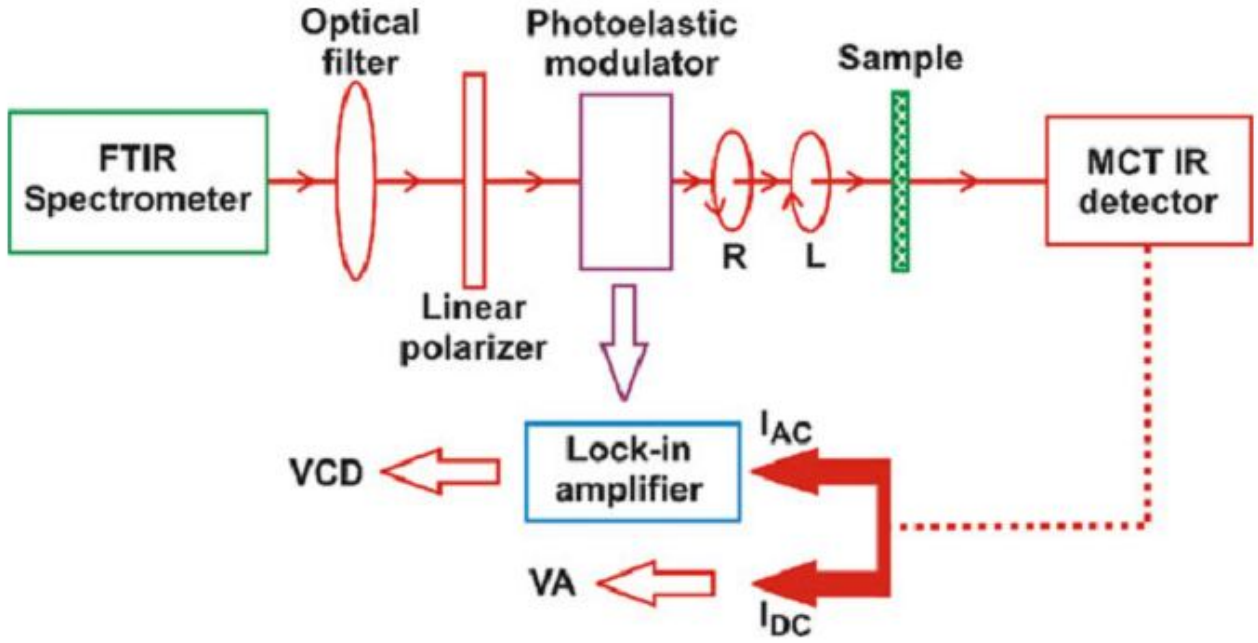

Figure 3.1 Block diagram of the optical-electronic layout of an FTIR-VCD spectrometer

Significant improvements in baseline stability and artifact suppression were reported in 2000 with a dual-PEM FTIR-VCD spectrometer.[11a] This dual polarization modulation (DPM) method involves adding a second PEM between the sample and the detector, in addition to the first PEM which is placed right before the sample in a standard single polarization modulation (SPM) spectrometer. More recently, Cao *et al.* added a rotating half-wave plate (RHWP) to the optical train to suppress further the linear birefringence (LB) effects associated with the sample cell in a DPM setup.[12] Their method is based on Hug's virtual enantiomer method, originally proposed for Raman Optical Activity (ROA).[13] With such a setup, these authors achieved basically the same artifact suppression as when using the opposite enantiomer. In addition to improving the sensitivity of FTIR-VCD instruments, efforts have also been made to extend the VCD operation into near IR region to as high as 10.000 cm^{-1} [14a,b],[12] for instance by incorporating a dual light source into the DPM FTIR-VCD spectrometer.[14c] Currently, such an instrument is available commercially from Bomen/Biotools Inc.

A few scanning dispersive VCD instruments are still in use for biological applications in the mid-IR region.[16] In 2009, a newly designed and optimized dispersive VCD instrument was reported.[16a] This instrument offers

[12] This region is potentially a source of very important structural information. For more detail, see the review by S. Abbate *et al.* [15]

the possibility to improve signal-to-noise (S/N) ratios, above all in the structural studies of peptides/proteins, especially in the amide I region signals are better quality than standard commercial FTIR-VCD spectrometers.[17]

Besides the continuous improvements of FTIR-VCD instruments described above, some exciting new developments related to VCD measurements have been reported in recent years. These include the development of matrix isolation FTIR VCD instruments and of laser based real time VCD spectrometers. These new developments are associated with brand new applications and research directions, such as combining the matrix isolation technique with VCD spectroscopy to probe conformationally flexible chiral molecules and H-bonded chiral molecular complexes, and using femtosecond laser VCD instruments to record time resolved VCD spectra, for monitoring fast chemical reactions or folding and unfolding events of peptides and proteins in solution. These will be discussed in more detail in Section 3.3.

3.2 VCD theory and calculations

The developments of the quantum mechanical calculations of VCD have been summarized before in a number of review articles and books.[3j-k,4a] In this section, we briefly describe the basic terms involved, a few key milestones in the development, and the current status. Vibrational Absorption Intensity is proportional to the electric dipole strength. In the harmonic approximation, D_{01}^{i}, the dipole strength for the *i*-th normal mode of a fundamental vibrational transition (0 → 1) can be expressed as

$$D_{01}^{i} = \left|\bar{\mu}_{01}^{i}\right|^{2} = \left|\langle\psi_0|\bar{\mu}|\psi_1^{i}\rangle\right|^{2} = \frac{\hbar}{2\omega_i}\left|\frac{\partial\bar{\mu}}{\partial Q_i}\right|_0^{2} \tag{3.1}$$

Here ψ_0 is the ground vibrational wavefunction and ψ_1^i is the wavefunction corresponding to the first excited vibrational state of the *i*-th normal mode; $\bar{\mu}$ is the electric dipole moment operator; Q_i is the normal coordinate for the *i*-th vibrational mode; the subscript '0' at derivative indicates that the term is evaluated at the equilibrium geometry. The related rotational strength or VCD intensity is determined by the dot product between the electric dipole and magnetic dipole transition moment vectors, as given in eq. (3.2):

$$R_{01}^{i} = \langle\psi_0|\bar{\mu}|\psi_1^{i}\rangle \cdot \mathrm{Im}\langle\psi_1^{i}|\bar{m}|\psi_0\rangle = \bar{\mu}_{01}^{i} \cdot \mathrm{Im}[\bar{m}_{01}^{i}] = 2\hbar\left(\frac{\partial\bar{\mu}}{\partial Q_i}\right)_0 \cdot \left(\frac{\partial\bar{m}}{\partial\dot{Q}_i}\right)_0 \tag{3.2}$$

The new term $\langle\psi_1^i|\bar{m}|\psi_0\rangle$ is the corresponding magnetic dipole transition moment and $\dot{Q}_i$ is the time derivative of Q_i. The vector $\mathrm{Im}\langle\psi_1^i|\bar{m}|\psi_0\rangle$ is real since $\langle\psi_1^i|\bar{m}|\psi_0\rangle$ is purely imaginary. Thus, a prediction of rotational strength requires the calculations of the transition moments of both electric dipole moment operator and magnetic dipole moment ones. Although the calculation of electric dipole transition moments of vibrational transitions within the Born–Oppenheimer (BO) approximation is straightforward, this is not the case for magnetic dipole transition moments. The electronic contribution to a vibrational magnetic dipole transition

moment vanishes within the BO approximation[13].[18] At this stage of theory development, a good number of approximate quantum mechanical methods, such as localized molecular orbital,[19] vibronic coupling,[3l,20] nuclear electric shielding tensor,[21] and localized orbital-local origin [22] methods, were proposed to calculate VCD intensities. The quality of the predicting power of these methods was not nearly satisfactory and further efforts were put into developing a better approximation to evaluate the electronic contribution to a vibrational magnetic dipole transition moment.

Using the so-called magnetic field perturbation method, Buckingham together with his co-workers [3b] and Stephens [3c] resolved this problem independently by including corrections to the BO approximation. In this approach, the electronic contribution to a vibrational magnetic dipole transition moment can be expressed in a simple form involving only adiabatic electronic wave functions of the ground electronic state. Specifically, it is necessary to calculate the ground state wavefunction as a function of nuclear displacement and of applied magnetic field. With this method, the electronic part of magnetic dipole moment derivative can be written as eq. 3.3 [3j]

$$\left(\frac{\partial m_\alpha^{el}}{\partial \dot{Q}_\iota}\right)_0 = -2\hbar \mathrm{Im}\left\langle \frac{\partial \psi_0}{\partial B_\alpha} \middle| \frac{\partial \psi_0}{\partial Q_i} \right\rangle \tag{3.3}$$

where $\partial\psi_0/\partial B_\alpha$ is the derivative of the wave function with respect to the αth component of the magnetic field and $\partial\psi_0/\partial Q_i$ is the derivative with respect to the *i*th normal coordinate. An analytic procedure for evaluating the normal coordinate derivatives of electric dipole moment was developed in the mid-80s.[23] Subsequent efforts were directed at finding an analytic procedure for evaluating the normal coordinate derivatives of the magnetic dipole moment. The implementation of magnetic field perturbation theory with DFT for VCD predictions was realized in 1996.[24] Since then, it has been used to simulate many good quality VCD spectra for comparison with the associated experimental data to determine the molecular conformations and ACs of a wide range of chiral molecules.[3j-k, 4a-d]

Equation (3.2) can be rewritten as (3.4) below where the sign of R_{01}^i is determined by the angle $\xi(i)$ between the vectors $\bar{\mu}_{01}^i$ and $\mathrm{Im}[\bar{m}_{01}^i]$:

$$\cos\xi(i) = \frac{\bar{\mu}_{01}^i \cdot \mathrm{Im}[\bar{m}_{01}^i]}{|\bar{\mu}_{01}^i||\mathrm{Im}[\bar{m}_{01}^i]|} = \frac{R_{01}^i}{|\bar{\mu}_{01}^i||\mathrm{Im}[\bar{m}_{01}^i]|} \tag{3.4}$$

For a certain vibrational mode, if $\xi(i) > 90°$, then $R_{01}^i < 0$, and if $\xi(i) < 90°$, then $R_{01}^i > 0$. However, when $\xi(i)$ is close to 90° even a small perturbation (be it experimental or theoretical), such as solvent, concentration, functional, or basis set can make it larger than 90°. This results in a change of VCD sign. Recently, Baerends *et al.* systemically investigated the effects of small perturbations on the sign of R_{01}^i.[25] They classify the vibrational modes as either robust where $\xi(i)$ is far from 90° or non-robust where $\xi(i)$ is very close to 90°. These authors advocate the use of only robust modes for AC determinations since their VCD signs are not sensitive to small perturbations either of computational or experimental nature and as a result should be predicted correctly by DFT calculations. How well this works in practice has yet to be tested, since current VCD

[13] In particular, the vibronic coupling theory [3f, 3l] represents the first attempt to introduce corrections to the BO approximation.

assignments rely largely on an overall pattern recognition in both VA and VCD spectra, rather than one or two peaks.[4i] A potential challenge is to assign confidently an observed VCD peak as robust taking into consideration possible overlap of vibrational bands in the experimental spectra and the somewhat limited accuracy of harmonic frequency predictions.

3.3 VCD Applications

Probably the most important application of VCD is the determination of the absolute configuration of chiral compounds. Recently, He *et al.* published an excellent review on the topic, with plenty of examples, mostly about biologically active compounds.[6]

Another hot topic concerns the *H*-bonding interactions of chiral molecules in solution, very important are those with water, especially in life sciences. The structural aspects of water surrounding a chiral molecule and the fundamental role of water in many important biological processes remain subject of intense debate.[26] To model VA and VCD measurements of biological molecules, such as proteins, peptides, sugars and amino acids, it is necessary to take into account the important intermolecular interactions, such as solute–solvent and solute–solute *H*-bonding, accurately.[27] Considered that water is an achiral molecule, why should there be such VCD features in its bending mode region? The answer is that some of the water molecules are explicitly *H*-bonded to a chiral solute and therefore become optically active as part of the super *H*-bonded chiral complexes. This phenomenon is termed *induced solvent chirality* or *chirality transfer*. The *induced solvent chirality* is due exclusively to the explicit intermolecular *H*-bonding interactions between a chiral solute molecule and water molecules. Consequently, these spectral features contain important information about the number of water molecules that are explicitly *H*-bonded to the chiral solute molecule and the specific binding sites. This region is called chirality transfer spectral window which allows one an exclusive view to the chiral solute–water *H*-bonding networks in solution.

Self-aggregation of chiral molecules containing both *H*-bond donor and acceptor functional groups, capable of forming strong intra- and intermolecular *H*-bonds, has also been studied by VCD. The case of glycidol [28], lactic acid [29], serine and its derivatives [30] clearly showed the utility of VCD in order to determine intermolecular interactions in solution.

Another promising application, consisting in VCD intensity enhancement in metal complexes containing chiral ligands, will be treated more extensively in Chapter 6.

Recently, Bürgi and co-workers [31] have reported a series of conformational investigations of chiral ligands absorbed on gold nanoparticles using VCD spectroscopy complemented with DFT calculations, which resulted in a powerful spectroscopic tool for conformational studies of condensed matter.

The Matrix isolation technique has been successfully applied to model the solvent–solute interactions for highly flexible chiral molecules. Since VCD is sensitive to torsional angles, consequently the corresponding VCD bands of different conformers have often opposite signs. In addition, strong solute–solvent or solute–solute *H*-bonding interactions can not only shift the band positions, but also modify the band intensities and alter the conformational distributions. More importantly, the dominant species contributing to the observed chiroptical

measurements may no longer be the isolated chiral solute molecules, but rather clusters of solute with solvent molecules or solute self-aggregates. All these effects together may lead to broad, featureless spectra which make it difficult, or impossible, to extract the information contained in them. In the vast majority of VCD studies, the interpretations rely on the calculations of isolated target molecules. Theoretical VCD modeling that takes into account the solvent–solute interactions has yet to be fully developed. Therefore it is strongly desirable to have a spectroscopic technique where one can control spectral contributions of different species and resolve spectral signatures of different conformers in order to test and to benchmark the corresponding theoretical modeling. The coupling of matrix isolation and VCD techniques provides such an opportunity.[32] Matrix isolation is a promising technique that has been fruitfully used to supply a wealth of structural and dynamical information of several molecular systems, especially for amino acids and other simple molecules. Because of the very low temperature achieved using this technique, one has the advantages of minimum interference from an almost non-interacting rare gas matrix and substantially better sensitivity and resolution for the VCD spectra. A further bonus with a matrix is that the absolute intensity and the S/N ratio obtained are about an order of magnitude larger.

In order to perform real time VCD measurements, instrument modifications have been developed, such as substituting the FTIR module with a white light source with a femtosecond laser. The ultimate goal here is to detect transient VCD signals and other related vibrational optical activities (VOA) in order to monitor, for example, the folding and unfolding events of polypeptides in solution. Bonmarin and Helbing [33] recently reported a picosecond time resolved VCD spectrometer, which was based on the blueprint of a similar set-up for ECD measurements.[34] A femtosecond IR pulse with a 200 cm^{-1} bandwidth (FWHM) was split into a reference and a probe beam where the latter passed through a wire grid linear polarizer and a PEM before impinging onto a standard sample cell, the same as used in the regular FTIR-VCD experiments. The IR laser signals from both beams were recorded by two MCT IR detectors. The laser pulses were synchronized with the reference frequency of the PEM so that the opposite circularly polarized light was generated in two sequential laser pulses. The intensity of each laser pulse was measured individually using gated amplifiers. Samples spectra studied showed, by varying the delay time on the picosecond scale between the pump and probe beams, a transient VCD responses, having recognizable differences from the static spectra. This first proof-of-principle experiment [33] demonstrates the feasibility of following fast time scale structural changes using VCD spectroscopy.

References

[1] a) L. D. Barron, *Molecular light scattering and optical activity, 2nd edn.* **2004**, Cambridge Press University: Cambridge. b) P. L. Polavarapu, *Vibrational spectra: principles and applications with emphasis on optical activity*, **1998**, Elsevier: New York. c) L.A. Nafie, *Vibrational optical activity: principles and applications*, **2011**, John Wiley & Sons: Chichester. d) P.J. Stephens, F. J. Devlin and J. R. Cheeseman, *VCD Spectroscopy for Organic Chemists*, **2012**, CRC Press: Boca Raton.

[2] a) G. Holzwarth, E. C. Hsu, H. S. Mosher, *J. Am. Chem. Soc.* **1974**, *96*, 251. b) L. A. Nafie, J. C. Cheng, P. J. Stephens, *J. Am. Chem. Soc.* **1975**, *97*, 3842.

[3] a) P. A. Galwas, *On the distribution of optical polarization in molecules*, **1983**, PhD Thesis, University of Cambridge: Cambridge. b) A. D. Buckingham, P. W. Fowler, P. A. Galwas, *Chem. Phys.* **1987**, *112*, 1. c) P. J. Stephens, *J. Phys. Chem.* **1985**, *89*, 748. d) P. J. Stephens, M. A. Lowe, *Annu. Rev. Phys. Chem.* **1985**, *36*, 213. e) P. J. Stephens, *J. Phys. Chem.* **1987**,

91, 1712. f) L. A. Nafie, *J. Chem. Phys.* **1983**, *79*, 4950. g) L. A. Nafie, *J. Chem. Phys.* **1992**, *96,* 5687. h) L. A. Nafie, *J. Phys. Chem. A,* **1997**, *101*, 7826. i) T. B. Freedman, M-L Shih, E. Lee, L. A. Nafie, *J.Am. Chem. Soc.* **1997**, *119*, 10620. j) P. J. Stephens, F. J. Devlin, *Chirality,* **2000**, *12*, 172. k) P. L. Polavarapu, *Int. J. Quantum Chem.* **2006,** *106*, 1089. l) L. A. Nafie, T. B. Freedman, *J. Chem. Phys.* **1983**, *78*, 7108.

[4] a) T. B. Freedman, X. L. Cao, R. K. Dukor and L.A. Nafie, *Chirality,* **2003**, *15*, 743. b) P. L. Polavarapu, J. He, *Anal. Chem.* **2004**, *76*, 61. c) P. L. Polavarapu, *Chem Rec* **2007**, *7*, 125. d) P. J. Stephens, F. J. Devlin, J. J. Pan, *Chirality* **2008**, *20*, 643. e) P. J. Stephens, F. J. Devlin, A. Aamouche, *Determination of the structures of chiral molecules using vibrational circular dichroism spectroscopy.* In: J. M. Hicks (ed.) Chirality: physical chemistry. ACS Symposium Series, vol. 810, Chap. 2, **2002**, Oxford University Press: New York, pp. 18 – 33. f) G. C. Yang, T. Ha, E. Fan, W. Shi, T. L. Lowary and Y. Xu, *Chirality,* **2010**, *22*, 734. g) G. C. Yang, Y. Xu, J. B. Hou, *Chem. Eur. J.* **2010**, *16*, 2518. h) H. Sato, Y. Mori, Y. Fukuda, *Inorg. Chem.* **2009**, *48*, 4354. i) L. A. Nafie, *Nat. Prod. Commun.* **2008**, *3*, 451.

[5] a) T. Brotin, D. Cavagnat, J. P. Dutasta, T. Buffeteau, *J. Am. Chem. Soc.* **2006**, *128*, 5533. b) F. J. Devlin, P. J. Stephens, P. Besse, *Tetr. Asym.* **2005**, *16*, 1557. c) A. Aamouche, F. J. Devlin, P. J. Stephens, *J. Am. Chem. Soc.* **2000**, *122*, 2346. VCD has been used also to decide between two conflicting reports of AC by X-ray crystallography: A. B. Dyatkin, T. B. Freedman, X. Cao, R. K. Dukor, B. E. Maryanoff, C. A. Maryanoff, J. M. Matthews, R. D. Shah and L. A. Nafie, *Chirality* **2002**, *14*, 215.

[6] Y. He, B. Wang, R. K. Dukor, L. A. Nafie, *App. Spect.* **2011**, *65*, 699.

[7] T. Taniguchi, K. Monde, *J. Am. Chem. Soc.* **2012**, *134*, 3695.

[8] G. A. Jeffrey, W. Saenger, *Hydrogen bonding in biological structures,* **1991**, Springer-Verlag: Berlin.

[9] a) L. A. Nafie, T. A. Keiderling, P. J. Stephens, *J. Am. Chem. Soc.* **1976**, *98*, 2715. b) L. A Nafie, *Polarization modulation FTIR spectroscopy.* In: Mackenzie MW (ed) Advances in applied FTIR spectroscopy, **1988**, Wiley: New York, pp 67–104. c) L. A. Nafie, F. Long, T. B. Freedman *et al. The determination of enantiomeric purity and absolute configuration by vibrational circular dichroism spectroscopy.* In: J. A. de Haseth (ed.) Fourier transform spectroscopy: 11th International Conference, vol. 430, American Institute of Physics, **1998** Woodbury: New York, pp 432–434. d) R. K. Dukor, L. A. Nafie, *Vibrational optical activity of pharmaceuticals and biomolecules.* In: R. A. Meyers (ed) Encyclopaedia of analytical chemistry: instrumentation and applications, **2000**, Wiley: Chichester, UK, pp 662–676.

[10] a) L. A. Nafie, M. Diem, *Appl. Spectrosc.* **1979**, *33*, 130. b) L. A Nafie, M. Diem, D. W. Vidrine, *J. Am. Chem. Soc.* **1979**, *101*, 496. c) E. D. Lipp, C. G. Zimba, L. A. Nafie, *Chem. Phys. Lett.* **1982**, *90*, 1.

[11] a) L. A. Nafie, *Appl. Spectrosc.* **2000**, *54*, 1634. b) P. Malon, T. A. Keiderling, *Appl. Spectrosc.* **1988**, *42*, 32. c) P. L. Polavarapu, *Appl. Spectrosc.* **1989**, *43*, 1295. d) P. Malon, T. A. Keiderling, *Appl. Spectrosc.* **1996**, *50*, 669. e) P. Malon, T. A. Keiderling, *Appl. Opt.* **1997**, *36*, 6141.

[12] X. L. Cao, R. K. Dukor, L. A. Nafie, *Theor. Chem. Acc.* **2008**, *119*, 69.

[13] W. Hug, *Appl. Spectrosc.* **2003**, *57*, 1.

[14] a) X. L. Cao, D. R. Shah, R. K. Dukor, C. Guo, T. B. Freedman, L. A. Nafie, *Appl. Spectrosc.* **2004**, *58*, 1057. b) C. Guo, R. D. Shah, R. K. Dukor, T. B. Freedman, X. Cao, L. A. Nafie, *Vib. Spectr.* **2006***, 42*, 254. c) L. A. Nafie, H. Bujis, A. Rilling *et al. Appl. Spectrosc.* **2004**, *58*, 647.

[15] S. Abbate, E. Castiglioni, F. Gangemi, G. Gangemi, C. Longhi, *Chirality,* **2010**, *21*, E242.

[16] a) T. A. Keiderling, J. Kubelka, J. Hilario, *Vibr. Spectr. Biol. Polym. Mat.* **2006**, 253. b) A. Lakhani, P. Malon, T. A. Keiderling, *Appl. Spectr.* **2009**, *63*, 755.

[17] M. Losada, X. Yu, *Phys. Chem. Chem. Phys.* **2007**, *9*, 3127.

[18] a) N. V. Cohan, H. F. Hameka, *J Am Chem Soc* **1966**, *88*, 2136. b) T. R. Faulkner, C. Marcott, A. Moscowitz, J. Overend, *J. Am. Chem. Soc.* **1977**, *99*, 8160.

[19] a) L. A. Nafie, T. H. Walnut, *Chem. Phys. Lett.* **1977**, *49*, 441. b) T. H. Walnut, L. A. Nafie, *J. Chem. Phys.* **1977**, *67,* 1501.

[20] a) R. Dutler, A. Rauk, *J. Am. Chem. Soc.* **1989**, *111*, 6957. b) D. Yang, A. Rauk, *J. Chem. Phys.* **1992**, *97*, 6517.

[21] a) K. L. C. Hunt, R. A. Harris, *J. Chem. Phys.* **1991**, *94*, 6995. b) P. Lazzeretti, M. Malagoli, R. Zanasi, *Chem. Phys. Lett.* **1991**, *179*, 297.

[22] A. E. Hansen, P. J. Stephens, T. D. Bouman, *J. Phys. Chem.* **1991**, *95*, 4255.

[23] a) R. D. Amos, *Chem. Phys. Lett.* **1984**, *108,* 185. b) Y. Yamaguchi, M. Frisch, J. Gaw, H. F. Schaefer, and J. S. Binkley, *J. Chem. Phys.* **1986**, *84*, 2262.

[24] J. R. Cheeseman, M. J. Frisch, F. J. Devlin, *Chem. Phys. Lett.* **1996**, *252*, 211.

[25] a) V. P. Nicu, J. Neugebauer, E. J. Baerends, *J. Phys. Chem. A*, **2008**, *112*, 6978. b) V. P. Nicu, E. J. Baerends, *Phys Chem Chem Phys* **2009**, *11*, 6107.

[26] a) C. Y. Ruan, V. A. Lobastov, F. Vigliotti, S. Chen, A. H. Zewail, *et al. Science* **2004**, *304*, 80. b) P. Wernet, D. Nordlund, U. Bergmann, M. Cavalleri, M. Odelius *et al. Science* **2004**, *304,* 995. c) J. D. Smith, C. D. Cappa, K. R. Wilson, B. M. Messer, R. C. Cohen, and R. J. Saykally, *Science* **2004**, *304*, 851. d) R. Bukowski, K. Szalewicz, G. C. Groenenboom, A. Van der Avoid, *Science* **2007**, *307*, 1249.

[27] a) K. Jalkanen, S. Suhai, *Chem. Phys.* **1996**, *208*, 81. b) V. W. Jurgensen, K. Jalkanen, *Phys. Biol.* **2006**, *3*, S63.

[28] G. C. Yang, Y. Xu, *Phys. Chem. Chem. Phys.* **2008,** *10,* 6787.

[29] M. Losada, H. Tran, Y. Xu, *J. Chem. Phys.* **2008**, *128*, 14508.

[30] a) M. R. Poopari, Z. Dezhahang, G. Yang, Y. Xu, *ChemPhysChem,* **2012**, *13*, 2310. b) P. Zhu, G. Yang, M. R. Poopari, Z. Bie, Y. Xu, *ChemPhysChem,* **2012**, *13*, 1272.

[31] a) C. Gautier, T. Bürgi , *Chem. Comm.* **2005**, 5393. b) C. Gautier, T. Bürgi , *J. Am. Chem. Soc.* **2006**, *128*, 11079. d) C. Gautier, T. Bürgi , *J. Phys. Chem. C.* **2010**, *114,* 15897.

[32] a) D. W. Schlosser, F. Devlin, K. Jalkanen *et al. Chem. Phys. Lett.* **1982**, *88*, 286. b) P. L. Polavarapu, B. A. Hess, L. J. Schaad, *J. Phys. Chem.* **1985**, *82*, 1705. c) M. A. Lowe, J. S. Alper, R. Kawiecki *et al. J. Phys. Chem.* **1986**, *90*, 41. d) G. Tarczay, G. Magyarfalvi, E. Vass, *Angew. Chem. Int. Ed.* **2006**, *45*, 1775. e) X. Qu, M. Citra, N. Ragunathan, Proceedings of the 9th International Conference on Fourier Transform Spectroscopy, **1993**, SPIE vol. *2089*, p 142. f) G. Tarczay, S. Gobi, E. Vass, G. Magyarfalvi, *Vibr. Spec.* **2009**, *50*, 21. g) G. Pohl, A. Perczel, E. Vass, Elemer, G. Magyarfalvi, G. Tarczay, *Tetrahedron* **2008**, *64*, 2126. h) G. Pohl, A. Perczel, E. Vass, Elemer, G. Magyarfalvi, G. Tarczay, *Phys. Chem. Chem. Phys.* **2007**, *9*, 4698. i) K. Shin-ya, H. Sugeta, S. Shin, Y. Hamada, Y. Katsumoto, K. Ohno, *J. Phys. Chem. A* **2007**, *111*, 8598. i) S. Go bi, E. Vass, G. Magyarfalvia, G. Tarczay, *Phys. Chem. Chem. Phys.***2011**, *13*, 13972.

[33] M. Bonmarin, J. Helbing, *Optics Lett.* **2008**, *33*, 2086.

[34] a) X. Xie, J. D. Simon, *J. Am. Chem. Soc.* **1990**, *112*, 7802. b) X. Xie, J. D. Simon, *J. Opt. Soc. Am. B,* **1990**, *7*, 1673. c) X. Xie, J. D. Simon, *Rev. Sci. Instrument* **1989**, *60*, 2614.

Chapter 4

Lanthanide probes for Biomedical Analysis and Imaging

Lanthanides have a very peculiar electronic structure, which is the cause of their unusual reactivity and spectroscopic properties, compared to the other transition metals, as already seen in Chapter 1; it is possible to take advantage of some of these peculiarities, using trivalent lanthanide ions Ln(III) in magnetic resonance or luminescence spectroscopy. These properties were exploited in particular for the development of new reporters for molecular imaging, protein and other biomolecules monitoring, etc. Especially in two applications Ln(III) complexes were fruitfully employed: Contrast Agents in Magnetic Resonance Imaging and Optical Bioprobes in Luminescence Spectroscopy.

These applications will be briefly reviewed in the following Sections 4.1 and 4.2.

4.1 Lanthanide-Based Contrast Agents for Magnetic Resonance Imaging

Magnetic resonance imaging (MRI) is based on the principles of nuclear magnetic resonance (NMR), whereby images are generated by spatially encoding the NMR signal coming from nuclei (e.g. protons) present in the object to be imaged through the application of time-dependent, magnetic field gradients.[1] The medical imaging technique is used in radiology to visualize detailed internal structures, most commonly taking advantage of the different relaxation rates of water protons in different tissues. It is a very powerful technique: it can penetrate deep into tissues, provides excellent soft tissues contrast with submillimeter resolution on clinical scanners and does not employ ionizing radiation (like γ- and *X*-ray imaging). The image contrast can be further enhanced by administration of MRI *Contrast Agents* (CAs). CAs cause a dramatic increase of the water proton relaxation rates, thus providing physiological information which add up to the impressive anatomical resolution commonly obtained in the uncontrasted images. CAs are widely used clinically, some applications are, for instance, assess organ perfusion, disruption of the blood–brain barrier, occurrence of abnormalities in kidney clearance, and circulation issues. MRI CAs are not directly visualized in the image, only their effect is observed: contrast is affected by the variation that the CA causes on water protons relaxation times, and consequently on the intensity of NMR signals.[2,3] This is due to the fact that a tissue might have either higher affinity for the CA or higher vascularity than another one. Diseased tissues, such as tumors, are metabolically different from healthy tissues and have a much higher uptake of the CAs, resulting in a higher contrast in MRI images. Paramagnetism is the property used to reduce proton T_1 and/or T_2,, which leads to'T_1 agents' or 'T_2 agents'. The efficiency of MRI CAs is measured in terms of their R_1 and R_2 relaxivity values, which indicate their ability to decrease, respectively, the T_1 and T_2 relaxation times of the water protons per unit (mM) concentration of metal ion. T_1-weighted images give positive image contrast, as the image signal intensity increase at the tissue site where the CA concentrates. T_2-weighted images give negative contrast, due to the fact that increased transverse relaxation leads to signal depression or disappearance.

Among *positive* T_1 agents,[4] attention has been primarily focused on Gd(III) both for its high paramagnetism (seven unpaired electrons) and for its favourable properties in terms of electronic relaxation.[5] This metal does not possess any known physiological function in mammalians, and its administration as a free ion is strongly toxic even at low doses (10–20 μmol kg^{-1}).[14] For this reason, it is necessary to use ligands that form very stable chelates with the lanthanide ion.[2,3]

Lanthanides display very high affinity for polyaminocarboxylic acids, either linear or cyclic, thus forming very stable complexes (up to log K_{ML} > 20): several Gd(III)-based CA have been approved for clinical use (Figure 4.1)

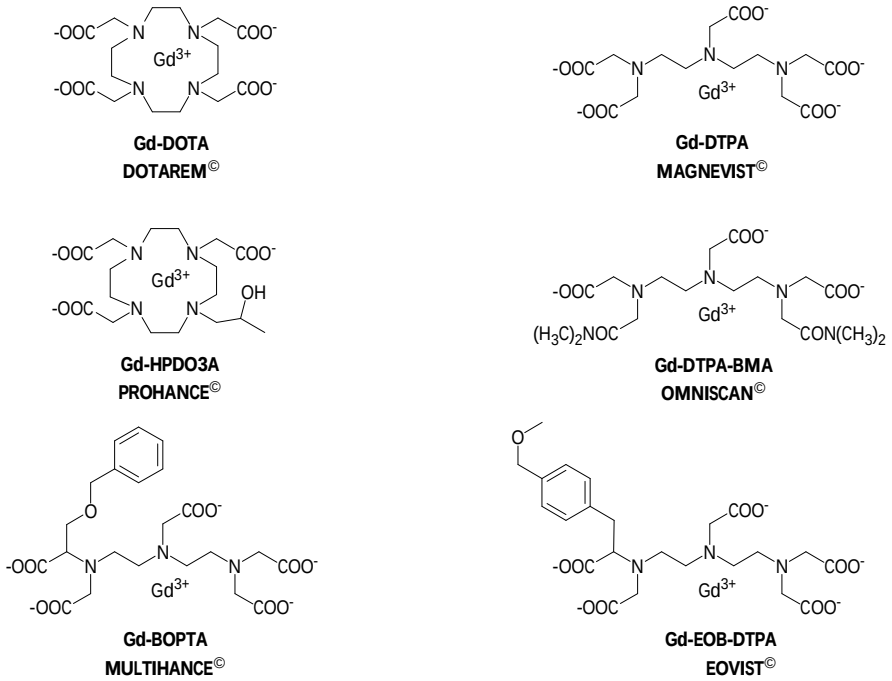

Figure 4.1 Some of the Gd(III) based MRI contrast agents mostly used currently in clinical practice

Paramagnetic Mn(II) chelate, Iron(III) oxide or Gadolinium-based nanoparticles [6] have also been considered for this role.

Besides high thermodynamic stability and kinetic inertness, a Gd-complex, to be considered as a potential CA, should have at least one water molecule coordinated to the metal ion in fast exchange with the bulk water. In fact, it is the exchange with the solvent water molecules that allows to affect the relaxation process of all protons present in the region in which the CA distributes. The Gd(III) chelate efficiency is commonly evaluated in vitro by the measure of its relaxivity (R_1), that, for commercial CAs is 2.5–3.5 mM^{-1} s^{-1} (at 20MHz and 39 °C, for the complexes shown in Figure 4.1). The observed longitudinal relaxation rate (R_1^{obs}) of the water protons in an aqueous solution containing the paramagnetic complex is the sum of two contributions (Eq. (4.1)) [7]: (i) the paramagnetic one, relative to the exchange of water molecules from the inner coordination sphere of the metal ion with bulk water (R_{1p}^{is}); (ii) the magnetic one relative to the contribution of water molecules that

[14] Besides undesirable biodistribution (accumulating in bones, liver or spleen), Gd^{3+} undergoes a rapid hydrolysis at physiological pH, producing insoluble $Gd(OH)_3$.

diffuse in the outer coordination sphere of the paramagnetic center (R_{1p}^{os}).[15] Sometimes, also a third paramagnetic contribution is taken in account, that is due to the presence of mobile protons or water molecules (normally bound to the chelate through hydrogen bonds) in the second coordination sphere of the metal [9]:

$$R_1^{obs} = R_{1p}^{is} + R_{1p}^{os} \tag{4.1}$$

The inner sphere contribution is directly proportional to the molar concentration of the paramagnetic complex, to the number of water molecules coordinated to the paramagnetic center, q, and inversely proportional to the sum of the mean residence lifetime, τ_M, of the coordinated water protons and their relaxation time, T_{1M} (Eq. (4.2)), the latter parameter inversely proportional to the sixth power of the distance between the metal center and the coordinated water proton (as derivable from Eq. 4.2.):

$$R_{1p}^{is} = \frac{q[\mathrm{C}]}{55.5(T_{1\mathrm{M}} + \tau_{\mathrm{M}})} \tag{4.2}$$

The hydration number q represents a scaling factor in the equation that defines inner sphere relaxivity and then a higher number of coordinated water molecules ($q > 1$) provides a clear advantage in terms of efficiency. The use of hepta- or hexadentate ligands would in principle result in Gd(III) complexes with 2- and 3-coordinated water molecules respectively, but the decrease of the denticity of the ligands is likely to be accompanied by a decrease of their thermodynamic stability and an increase in their toxicity. Furthermore, systems with $q = 2$ may suffer a 'quenching' effect upon interacting with endogeneous anions or with proteins, as donor atoms from lactate or Asp or Glu residues may replace the coordinated water molecules.[10] However, sufficiently inert heptadentate Gd(III)-chelates have been developed recently[11-13] (Figure 4.2), showing an increase in relaxivity R_1^{obs} of up to a factor two.

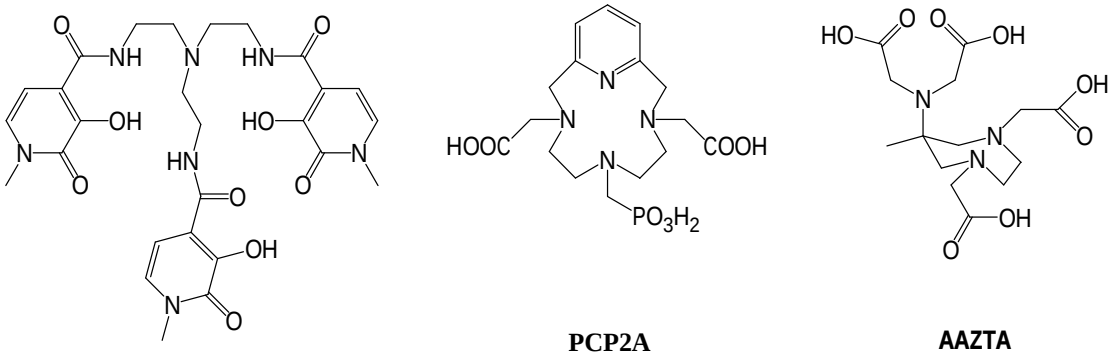

Figure 4.2 Schematic representation of the three heptadentate ligands.

[15] Sessoli *et al.* [8] have shown very recently that the complete model is more complicated, shedding doubts on the assumption that the orientation of the M-O_{water} corresponds to the anisotropy axis and that the apical water molecules lie in the cone of highest susceptibility, at least for the Dy DOTA complex. It is likely that this affects the mechanism of contrast since the labile water molecule modifies the magnetic anisotropy of the lanthanide ion. A simple magneto-structural correlations based on the coordination environment can fail to predict, even approximately, the correct magnetic anisotropy of anisotropic lanthanide ions in a low-symmetry environment.

Other approaches have been investigated in order to increase relaxivity, such as forming a non-covalent adduct between the complex and a slowly tumbling system, through the coupling of the Gd-water vector to its tumbling motion, like human serum albumin (HSA): several modified Gd(III) have been designed to this end.[14-16] Different strategies have been explored in the literature in order to achieve this goal, with the most various systems.[16b-c] For instance, dendritic gadolinium complexes [16d,e] have been very efficacious: placing the metal ion at the barycenter of the molecule have the consequence that it will lie upon the axis of any reorentational motion, and therefore its motion coupling will be markedly improved. In case of glycoconjugate dendrimers, also the contribution of the second water sphere to the relaxation increase is considerable.[16e]

Gd(III) chelates can be entrapped in cells incubated in culture media basically through two mechanisms: I) via pinocytosis; II) via phagocytosis.

Through selective functionalization, it is also possible to target specific epitopes on cellular membranes, several systems have been developed: Gd-containing polymerized liposome,[17] Gd-loaded apoferritin,[18] biotinilated Gd complexes,[19] etc.

Besides Gd, other lanthanides having high inducing chemical shift power, typically Dy and Tm, opposite in sign, (See Table 2.1), have found a special application as *Chemical Exchange saturation transfer agents* (CEST): a CEST agent is a molecule possessing exchangeable protons (-NH, -OH, even coordinated H_2O, etc.) that resonates at a chemical shift that is different from the bulk water signal, which happens when their exchange with the bulk water protons is slow on the NMR timescale. This occurs when $\Delta\omega \geq k_{ex}$, where k_{ex} is the exchange rate of the process and $\Delta\omega$ is the difference in frequency between the chemical environments. When this condition is fulfilled, radio frequency pulses applied at an appropriate frequency and power level can saturate the exchangeable protons of the CEST agent. These protons will then transfer into the bulk water pool and lead to a reduction of its equilibrium magnetization, with a resulting decrease of its signal intensity. Therefore, this water saturation process is caused by chemical exchange. CEST agents can be used to switch the image contrast 'on' and 'off' by changing the irradiation parameters.

According to the value of the lanthanide constant C_J (Table 2.1), some paramagnetic complexes may display large $\Delta\omega$ values for the exchanging proton resonance. In particular, Ln^{3+} complexes having at least a coordinated water molecule could undergo slow exchange (on the paramagnetic NMR scale) with the bulk water, and with very large $\Delta\omega$ values, related to that. A good saturation transfer (ST) effect has been reported by irradiating the metal-bound water protons of Eu^{3+} chelates resonating at 50 ppm downfield from the bulk water.[20] The same effect can be obtained with slow exchanging amide protons of Ln^{3+} complexes, e.g. tetraamide DOTA derivatives,[21] even though a fast relaxation may reduce saturation transfer efficiency.

4.2 Lanthanide-Based Luminescent Probes for Biomedical Analysis and Cellular Imaging

A key challenge in cell biology and biochemistry research lies in gaining greater understanding about the structure and function of biological systems through methods that involve minimal perturbation of the system. The development of emissive optical probes is essential to the progress in such direction. Following excitation

of the probe, emitted photons may be observed by spectroscopy or microscopy and encode information in their energy, lifetime, and polarization.

Trivalent lanthanide ions, Ln(III), present another alternative to organic luminescent stains in view of their properties, part of them has already been introduced in Chapter 1 but will be further analyzed herein. The first staining of biological cells with lanthanides dates back to 1969 when bacterial smears (*Escherichia coli* cell walls) were treated with water/ethanol solutions of europium thenoyltrifluoroacetonate, henceforth appearing as bright red spots under mercury lamp illumination.[22]

The first demonstration of sensitized lanthanide luminescence was due to the efforts of Weissman,[23] who found out that europium fluroscence could be trigged by the organic ligand excitation. Salicylaldehyde and other various systems have been studied, correlating qualitatively the sensitization efficiency to the ligand nature, temperature and solvent.

It has long been appreciated that lanthanide(III) complexes (Ln = Sm, Eu, Tb, Dy, Nd, Er and Yb are the most used ions, in particular the first four ones)[16,17] offer several distinct advantages as optical probes. First, they possess large Stokes shifts, due to the big energy separation between the absorption of the antenna, the sensitizing organic chromophore, and the emission of the lanthanide, thus avoiding concentration-dependent self-absorption problems (Figure 4.3a). Consequently, the response varies linearly with the concentration of the complex over several orders of magnitude. Second, their emission spectra are characterized by very narrow bands, as already seen in Chapter 1, which are poorly sensitive to certain environmental and coordination changes, e.g. to oxygen quenching, due to the involvement of shielded *4f* electrons (Fig. 4.3b). Hence the similarity of the coordination chemistry of lanthanide ions means that the metal ion may be changed within common ligand structure, without significant variation in the chemical stability of the complex.[18] It is possible also to use multiple lanthanide probes, since the emission spectra of lanthanides do not overlap with one another, therefore the response of each probe is a function solely of the target analyte, and is unaffected by the presence of another lanthanide probe. Lastly, lanthanide emissions are Laporte forbidden and are therefore characterized by extremely long luminescence lifetimes, in the millisecond range for europium and terbium and the microsecond range for samarium and dysprosium, several orders of magnitude longer than organic dyes. These very long luminescence lifetimes allow for the use of time-gated acquisition methods to enhance signal/noise, minimizing interference from light scattering or autofluorescence,[25,26] ideal conditions for the detection of an analyte in a complex biological medium such as a cell. In this type of experiment, a delay is set between the excitation pulse and the detection window (Figure 4.3c). The time gate allows the background luminescencet to decay to zero before measuring the luminescence of the complex. Consequently, the luminescence intensity is a function only of the concentrations of the lanthanide probe and

[16] Also Gd^{3+} would have an efficient excited state population, however the emission in the UV range limits seriously its possible use in this application, due to all the possible absorption and emission interference by other species in this wavelength range.

[17] Nd, Er and Yb show emissions in the Near Infrared range.

[18] Most work has focused on emissive complexes of Eu(III) and Tb(III), because the excited states of these ions are less sensitive to vibrational quenching by energy transfer to OH (i.e., nearby or coordinated water molecules), NH, or CH oscillators.[24] On the contrary, Dy^{3+} and Sm^{3+} suffer this limitation, even if their employment is still possible, e.g. when it is necessary to elucidate trends based on variation of ionic radii.

its targeted analyte, and is unaffected by the presence of any other dye in the medium. Hence, time gating facilitates the intracellular spatial and quantitative determination of the concentration of a desired analyte.

A direct consequence of the symmetry-forbidden nature of the *f-f* transitions is their extremely low molar extinction coefficients for direct excitation. This problem is resolved by incorporating a sensitizing moiety, an antenna or chromophore, into the ligand structure. The role of this antenna is to absorb energy from UV-visible radiation and to transfer it to the lanthanide ion (Figure 4.3d). First, the antenna is excited from its ground state to its singlet excited state. This is followed by intersystem crossing to the antenna's triplet state and intramolecular energy transfer from the antenna to the excited state of the the lanthanide. The latter then emits light in the visible range: 545 nm for Tb and 611 to 618 nm for Eu. The absence of degeneracy of the Eu(III) $^5D_0$ excited state means that europium emission spectra are the simplest and the most amenable to interpretation. Similarly, indirect excitation of erbium, neodymium and ytterbium via the triplet state of a nearby antenna results in luminescence in the near-infrared region with a long luminescence lifetime (1530 nm $^4I_{13/2} \rightarrow {}^4I_{15/2}$ transition for Er, 1060 nm $^4F_{3/2} \rightarrow {}^4I_J$ transition for Nd, 980 nm $^2F_{5/2} \rightarrow {}^2F_{7/2}$ transition for Yb).[27] As is apparent from the Jablonski diagram (Fig. 4.3e), the quantum yield of sensitized Eu^{3+} luminescence is dependent on five parameters:

1)The energy of the S_1 excited state, initially populated. It should lie less than 29 000 cm^{-1} (>340 nm) above the ground state, in order to maximize the quantum yield, minimizing the coexcitation of endogenous chromophores and the distruction of biological materials (another advantage is the possibility to use nonquartz optics, in this range of radiation energy);

2) The efficiency by which the triplet excited state of the antenna is populated, which depends on the chromophore selection: tipically a heterocyclic or aromatic moiety is required, that possesses a small singlet-triplet energy gap (<7000 cm^{-1} = 84 kJ mol^{-1});

3) The energy of the triplet excited state of the antenna relative to the ^5D excited state of the lanthanide ion. For intramolecular energy transfer to occur, the triplet excited state of the antenna must be higher in energy than the excited ^5D state of the lanthanide. Direct fluorescence from the antenna is observed if the triplet state of the antenna is too high or too low in energy. Furthermore, when the triplet state of the antenna is too close in energy to the ^5D state of the lanthanide, back energy transfer from the lanthanide to the antenna ensues with a consequent decrease in lanthanide emission. Generally the optimal energy difference between the triplet of the antenna and the Eu $^5D_0$ or Tb $^5D_4$ states, the light-emissive ones, should be 2000 - 3500 cm^{-1}. A typical system strategy is outlined in Figure 4.4;

4) The distance separating the antenna from the lanthanide ion. The efficiency of Förster energy transfer [27] from the antenna to the lanthanide follows an r^6 dependence;

5) The number of coordinated water molecules. Since the fourth overtone of the water O–H oscillator is lower in energy than the ^5D states of Eu and Tb, energy transfer from the excited state of the lanthanide to coordinated water molecules can significantly reduce the quantum yield of the metal luminescence.

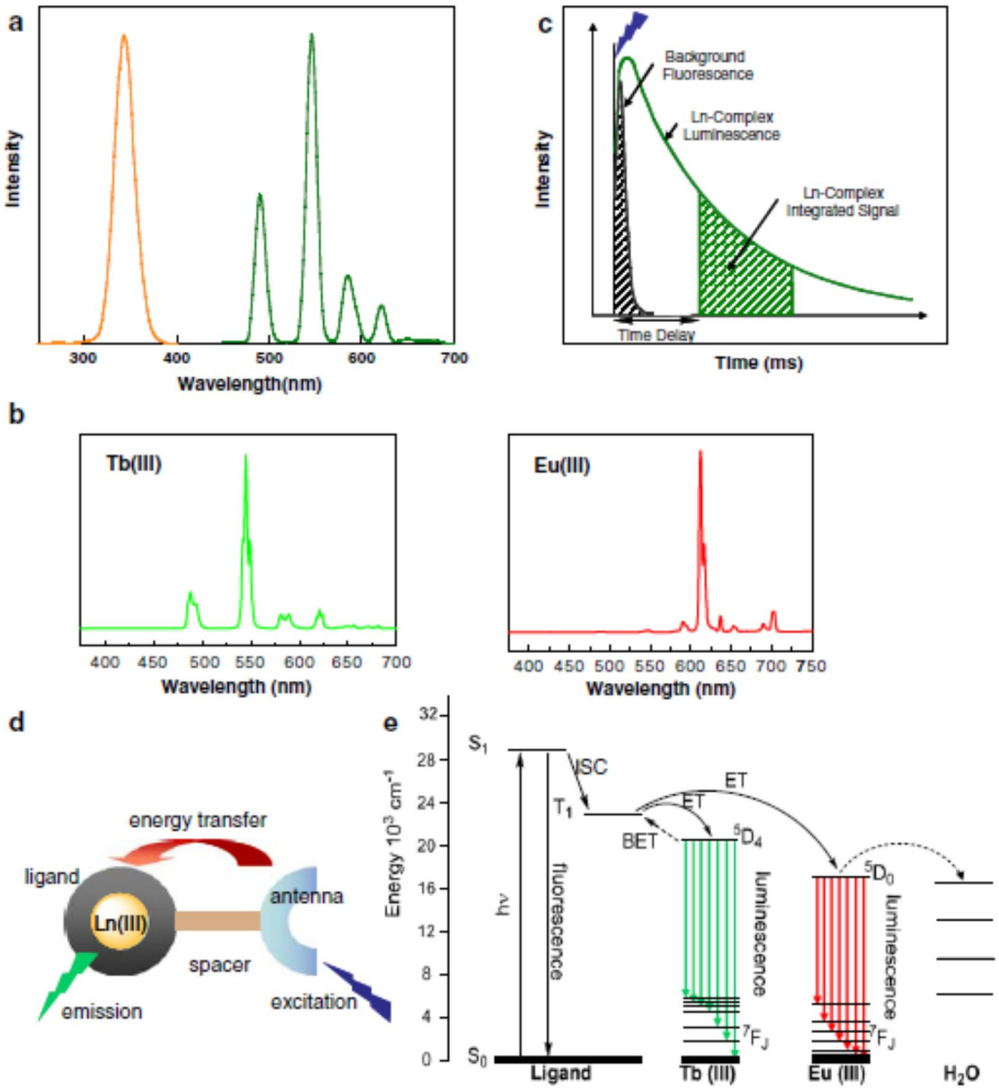

Figure 4.3 Principles of lanthanide luminescence. **a**) representative Stokes shift between the absorption of an antenna (orange) and the emission of a lanthanide (green), **b**) characteristic narrow emission of a terbium and a europium complex, **c**) principle of time-gated spectroscopy, **d**) indirect excitation of a lanthanide via an antenna, **e**) simplified Jablonski diagram showing the main energy flow paths during sensitization of lanthanide luminescence via its antenna.

A further requirement, as for CAs in MRI, is the thermodynamic stability and the kinetic inertness of the compounds.

Taking advantage of the parameters listed above, it's possible to design bioprobes, modulating their emission, depending on external stimuli, affecting these variables and therefore the quantum yield of the emission process. The possible approaches have been recently reviewed by Thibon and Pierre [30] and include several possible modulation strategies:

- variation of the distance between the antenna and the lanthanide in response to a certain analyte, affecting the complex conformation or structure;

- variation of the number of the coordination water molecules, through the displacement by anions (method for anion detection);
- direct coordination of the antenna, targeting a chromophore capable of coordinating to the lanthanide, displacing other species;
- varying the energy difference between the triplet state and the ^5D lanthanide emissive state, which is made possible through chemical modifications of the antenna, whereby a selective with a certain analyte, modulates the energy of the triplet state of the antenna itself;
- via a photoinduced electron transfer switch, a reactive moiety capable of quenching the excited state of the antenna, but deactivable by binding with a specific analyte.

Among the most studied compounds, fulfilling all the requirements expressed above, there are the cyclen core based lanthanide complexes, comprehensively studied by Parker and coworkers (Figure 4.5).[29]

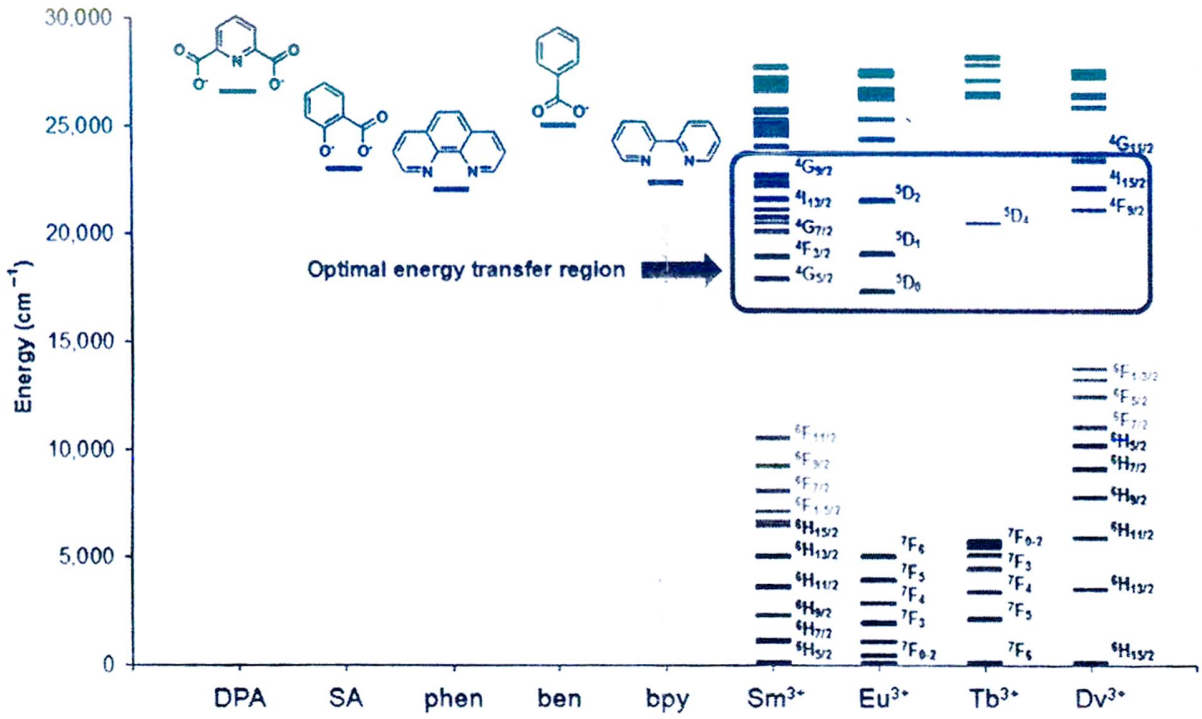

Figure 4.4 Energy level diagram depicting the triplet excited states of various aromatic ligands (left) along with the excited and ground states of the four luminescent lanthanides (right). Ground states that do not contribuite to luminescence are shown in gray. The area highlighted in the box illustrates the region where the energy gap between the ligand triplet state and the lanthanide excited state is optimal for efficient energy transfer. Aromatic ligands: dipicolinic acid, salicyclic acid, 1,10-phenantroline, benzoate and 2,2'-bypiridine.

Also for lanthanide luminescent probes, it could be necessary to fit the system with adequate functionalities able to couple with biological material, for cellular or bioimaging. The coupling is achieved either directly, e.g., in immunoassays in which the lanthanide probe is linked to a monoclonal antibody mAb, or indirectly, with the chelate being covalently bound to avidin (or biotin), and the resulting duplex being then fixed onto a biotinylated (or avidin-derivatized) mAb via the strong avidin-biotin interaction (log K ≈ 15).[31] Alternatively, avidin may be substituted by streptavidin[32] or bovine serum albumin (BSA).[33]

Another interesting series of systems developed is based on polylanthanide complexes, which give rise to self-assembly structure, like coordination bundles, helicates, successfully employable as probes.[34]

The mode of cellular uptake of the cyclen complexes showed in Fig. 4.5 was reported to be macropinocytosis.[35] The complexes have an interesting sub-cellular distribution, localizing, depending on their chemical functionalities, in lysosomes, nucleolus, mitochondria or in more organelles (Figure 4.6).[36]

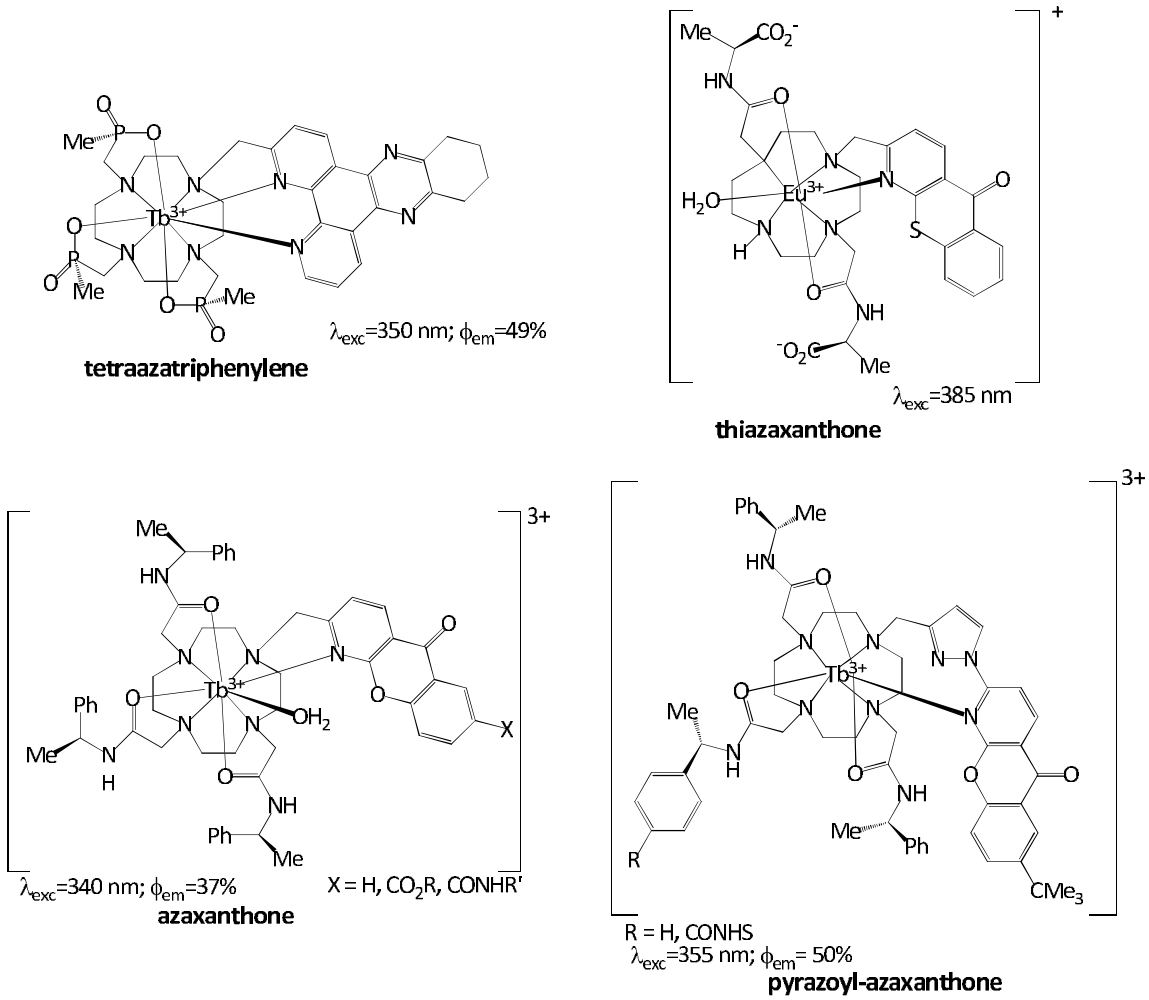

Figure 4.5 Structure of selected emissive Eu or Tb complexes with differing heterocyclic sensitizers, highlighting the sensitizer chemical moiety and the photophysical properties of the whole system (ϕ_{em} = quantum yield of emission).

4.2.1 Luminescent chiral Ln(III) complexes as potential biomolecular probes

Besides Circular Dichroism, another chiroptical technique, offering the chance of unique analysis, is Circular Polarization of Luminescence (from now on simply CPL). CPL measures the difference in the emission intensity of left vs. right circularly polarized light .

The considerable increase in the use of CPL most probably originated from the discovery that luminescence from intraconfigurational *f –f* transitions of the Ln(III) ions, obeying magnetic dipole selection rules, often showed large circular polarization, when the ion is embedded in a chiral, nonracemic environment.[38]

Transitions that satisfy the formal selection rules of ΔJ = 0, ±1 (except 0↔0) are magnetic-dipole allowed, where J stands for the total angular momentum quantum number found in the definition of the term symbol, ${}^{2S+1}L_J$, describing the electronic states of lanthanides.[14] It is common to report the degree of CPL in terms of the luminescence dissymmetry factor, $g_{lum}(\lambda) = 2\Delta I/I = 2(I_L - I_R)/(I_L + I_R)$, where I_L and I_R refer, respectively, to the intensity of left and right circularly polarized emissions. A value of 0 for g_{lum}corresponds to no circular polarization, while the maximum absolute value is 2.

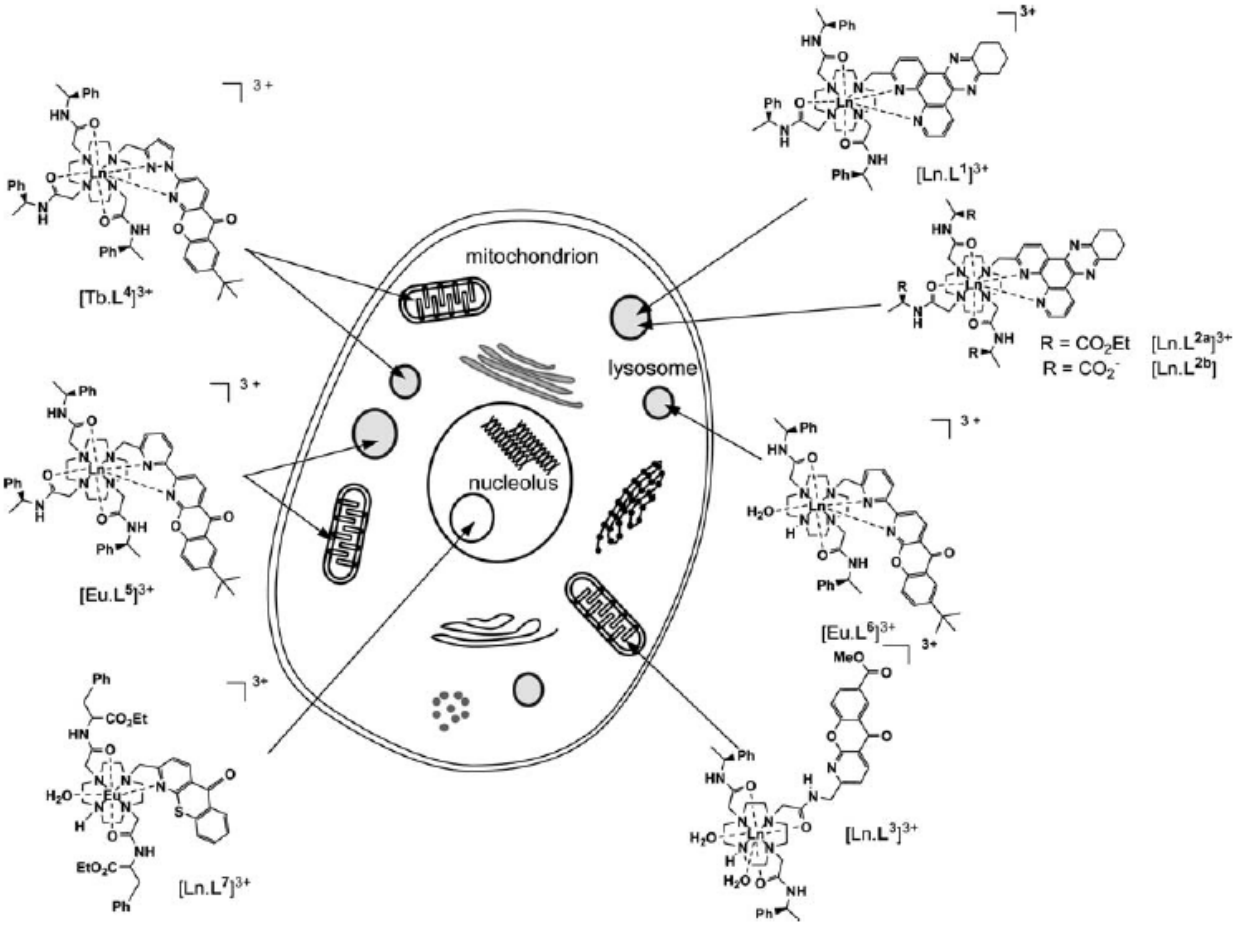

Figure 4.6 The four distinct sub-cellular localization profiles of luminescent lanthanide complexes: lysosomal, mitochondrial, nucleolar and mitochondrial-lysosomal. For each category one or two representative examples are shown.

For selected transitions of Ln(III) compounds larger g_{lum}—as high as 1.38— have been reported, compared to chiral organic molecules for which the extent of circular polarization is almost always less than $1 \cdot 10^{-2}$.[37]

CPL became increasingly useful as a probe of luminescent Ln(III) complexes as responsive systems for anion binding in aqueous media and as a test for the existence of chiral Ln(III) structures (i.e. predominant isomer in solution or if the solution of a complex containing an achiral ligand is indeed a racemic mixture).[36] It is also an indicator of changes in chiral structure (i.e. importance of the helical wrapping of the ligand strand contribution, and therefore its influence on the diastereomeric induction). In addition, information concerning metal-ion environments and the associated chiral structures of metal-containing biological systems could be obtained through CPL measurements. This information complements data obtained using CD spectroscopy.

Luminescent Ln(III) complexes can be used as chiral probes for biomolecules, taking advantage of different strategies, using either chiral or achiral ligands. In the latter case a racemate resolution must occur, e.g. through selective interaction with chiral biomolecules. In the presence of octahedral or square antiprismatic coordination (both possibly distorted) the use of achiral ligands commonly leads to the formation of Ln(III) complexes, existing as racemic mixtures of complexes with Δ and Λ coordination, which in solution are in dynamic equilibrium (see Section 5.2.4 and Chapter 7). A chiral species coordinating to the lanthanide centre could shift the equilibrium, due to the different diastereomeric relationship between the two forms, favoring one stereoisomer of the two. This leads to an enantiomeric excess in the ground state η, defined as follow:

$$\eta = \frac{[\Lambda] - [\Delta]}{[\Lambda] + [\Delta]} \tag{4.3}$$

These differences can be detected by measurement of CPL. Muller *et al.* showed that the CPL sign and its magnitude are dependent upon several factors and not only on the chirality of the perturber.[39] They observed that (i) simple modifications in the chiral molecules added to the racemic system did not change the sign of the CPL signal (the same enantiomeric form of the complex was favored), and (ii) the magnitude of the CPL signal was influenced by the presence of additional aromatic groups in the chiral molecules. Another possibility is to use a chiral quencher, that silence the luminescence of the enantiomer for which it has higher affinity, therefore the other enantiomer is highlighted and CPL is selectively induced. Through enantioselective quenching by an added chiral quencher molecule, it is possible to have a situation in which the non-racemic emitting state is the result of a time-dependent optically enriched excited state. Although this is commonly referred to as an enantioselective quenching process, a more appropriate description of it would be a diastereomeric interaction. The discriminatory interactions between the excited enantiomers of a racemic Ln(III) complex and a chiral quencher molecule results in a difference in excited state populations due to the quenching of one enantiomer over the other by the added chiral quencher. In terms of the experimental procedure, an unpolarized beam excites the racemic mixture to an emitting state leading to the presence of equal concentrations of the two excited enantiomers. Then, the chiral quencher, also present in the solution, interacts with the excited enantiomers in such a way that one of the enantiomers is quenched at a faster rate than the other. The result of this differential excited-state quenching process is that the excited state becomes chiral (or a non-racemic emitting state) over time, which can be analyzed using the time-resolved feature of the CPL instrumentation.[40]

Lanthanide complexes containing chiral ligands have been successfully employed in anion and cation recognition, taking advantage of chiroptical detection. Mainly two approaches have been used: sensing through coordination to the metal centre or to the antenna/receptor group, basically the same strategies tested for achiral systems as well.

References

[1] S. Mannson, A. Bjørnerud, in: *The Chemistry of Contrast Agents in Medical Magnetic Resonance Imaging,* A. E. Merbach, E. Toth Eds. **2001**, Wiley: Chichester; pp. 1-44.

[2] M.F. Tweedle, in: J.-C.G. Bünzli, G.R. Choppin (Eds.), *Lanthanide Probes in Life, Chemical and Earth Sciences: Theory and Practice*, **1989**, Elsevier: Amsterdam, p. 127.

[3] E. Brücher, A.D. Sherry, in: A.E. Merbach, E. Toth (Eds.), *The Chemistry of Contrast Agents in Medical Magnetic Resonance Imaging*, **2001**, Wiley: Chichester, p. 243.

[4] H.J. Weinmann, A. Mühler, B. Radüchel, in: I.R. Young (Ed.), *Biomedical Magnetic Resonance Imaging and Spectroscopy*, **2000**, John Wiley & Sons Ltd.: Chichester, p. 705.

[5] P. Caravan, J.J. Ellison, T.J. McMurry, R.B. Lauffer, *Chem. Rev.* **1999**, *99*, 2293.

[6] C. Bozigues, T. Gacoin, A. Alexandrou, *ACS Nano,* **2011**, *11*, 8488 and references therein.

[7] L. Banci, I. Bertini, C. Luchinat, *Nuclear and Electronic Relaxation*, VCH, Weinheim, **1991**, p. 91.

[8] G. Cucinotta, M. Perfetti, J. Luzon, M. Etienne, P.-E. Car, A. Caneschi, G. Calvez, K. Bernot, and R. Sessoli, *Angew. Chem. Int. Ed.* **2012**, *51*, 1606.

[9] M. Botta, *Eur. J. Inorg. Chem*. **2000**, *3*, 399.

[10] S. Aime, E. Gianolio, E. Terreno, *et al. J. Biol. Inorg. Chem.* **2000**, *5*, 488.

[11] S. Hajela, M. Botta, S. Giraudo, J. Xu, K. N. Raymond, S. Aime, *J. Am. Chem. Soc.* **2000**, *122*, 11228.

[12] S. Aime, M. Botta, L. Frullano, S. Geninatti Crich, G.B. Giovenzana, R. Pagliarin, G. Palmisano, M. Sisti, *J. Med. Chem.* **2000**, *43*, 4017.

[13] S. Aime, L. Calabi, C. Cavallotti, E. Gianolio, G. V. Giovenzana, P. Losi, A. Maiocchi, G. Palmisano and M. Sisti, *Inorg. Chem.* **2004**, *43*, 7588.

[14] S. Aime, M. Botta, M. Fasano, E. Terreno, in: A.E. Merbach, E. Toth (Eds.), *The Chemistry of Contrast Agents in Medical Magnetic Resonance Imaging*, **2001**, John Wiley & Sons Ltd.: Chichester, p. 193.

[15] R.B. Lauffer, D.J. Parmalee, S. U. Dunham, H. S. Ouelett, R. P. Dolan,. S. Witte, T. J. McMurry, R. C. Walcovitch, *Radiology,* **1998,** *207*, 529.

[16] a) S. Aime, M. Chiaussa, G. Digilio, E. Gianiolo, E. Terrano, *J. Biol. Inorg. Chem.* **1999**, *4*, 766. b) For an exhaustive review about the relaxation enhancement in Gd CAs, through the formation of adducts with macromolecular systems, see: M. Botta, L. Tei, *Eur. J. Inorg. Chem.* **2012**, 1945. C) For a review about the employment of zeolites, in this case both in the development of T_1 agents and T_2 agents, see: J. A. Peters, K. Djanashvili, *Eur. J. Inorg. Chem.* **2012**, 1961. d) D. A. Fulton, M. O'Halloran, D. Parker, K. Senanayake, M. Botta, S. Aime, *Chem. Comm.* **2005**, 474. e) D. A. Fulton, E. M. Elemento, S. Aime, L. Chaabane, M. Botta, D. Parker, *Chem. Comm*. **2006**, 1064.

[17] S. Aime, C. Cabella, S. Colombatto, S. Geninatti Crich, E. Gianolio and F. Maggioni, *J. Magn. Reson. Imag.* **2002**, *16*, 394.

[18] S. Aime, L. Frullano, S. Geninatti Crich, *Angew. Chem. Int. Ed.* **2002**, *41*, 1017.

[19] Z.M. Bhujwalla, D. Artemov, N. Mori, R. Ravi, *Cancer Res.* **2003**, *63*, 2723.

[20] (a) S. Zhang, P. Winter, K. Wu, A. D. Sherry, *J. Am. Chem. Soc.* **2001**, *123*, 1517; (b) S. J. Ratnakar, S. Viswanathan, Z. Kovacs, A. K. Jindal, K. N. Green, A. D. Sherry, *J. Am. Chem. Soc.* **2012**, *134*, 5798.

[21] S. Aime, D. Delli Castelli, E. Terreno, *Angew. Chem. Int. Ed.* **2005**, *44*, 5513.

[22] W. L. Scaff, D. L. Dyer, K. Mori, *J. Bacteriol.* **1969**, *98*, 246.

[23] S. I. Weissman, *J. Chem. Phys.* **1942**, *10*, 214.

[24] R. S. Dickins, J. I. Bruce, D. Parker, D. J. Tozer, *Dalton Trans.* **2003**, 1264.

[25] S. U. Pandya, J. Yu, D. Parker, *Dalton Trans.* **2006**, 2757.

[26] J. Yuan, G. Wang, *Anal. Chem.* **2006**, *25*, 490.

[27] J.-C.G. Bünzli, C. Piguet, *Chem. Soc. Rev.* **2005,** *34*, 1048.

[28] M. S. Tremblay, M. Halim, D. Sames, *J. Am. Chem. Soc.* **2007**, *129*, 7570.

[29] C. P. Montgomery, B. S. Murray, E. J. New, R. Pal, D. Parker, **2009**, *42*, 925.

[30] A. Thibon, V. C. Pierre, *Anal. Bioanal. Chem.* **2009**, *394*, 107.

[31] N. M. Green, *Biochem. J.* **1963**, *89*, 585.

[32] O. Prat, E. Lopez, G. Mathis, *Anal. Biochem.* **1991**, *195*, 283.

[33] S. P. Claudel-Gillet, J. Steibel, N. Weibel, T. Chauvin, M. Port, I. Raynal, E. Tóth,. R. F. Ziessel and L. J. Charbonniere, *Eur. J. Inorg. Chem.* **2008**, 2856.

[34] C. Lincheneau, F. Stomeo, S. Comby, T. Gunnlaugsson, *Aust. J. Chem.* **2011**, *64*, 1315.

[35] (a) W. A. Dunn, A. L. Hubbard and N. N. Aronson Jr. *J. Biol. Chem.* **1980**, *255*, 5971–5978; (b) S. Kessner, A. Krause, U. Rothe and G. Bendas, *Biochim. Biophys. Acta*, **2001**, *1514*, 177–190.

[36] E. J. New, A. Congreve, D. Parker, *Chem. Sci.* **2010**, *1*, 111.

[37] J. P. Riehl and G. Muller, in *Handbook on the Physics and Chemistry of Rare Earths*, ed. K. A. Gschneidner, Jr., J.-C. G. Buenzli and V. K. Pecharsky, **2005**, North-Holland Publishing Company: Amsterdam, vol. 34, pp. 289–357.

[38] C. K. Luk and F. S. Richardson, *J. Am. Chem. Soc.* **1975**, *97*, 6666.

[39] G. Muller and J. P. Riehl, *J. Fluorescence*, **2005**, *15*, 553.

[40] T. A. Hopkins, D. H. Metcalf and F. S. Richardson, *Chirality*, **2008**, *20*, 511.

Chapter 5

Pseudocontact shifts in lanthanide complexes with variable crystal field parameters and their application in solution structure determination: a close-up on the DOTMA case

Paramagnetic NMR provides some of the most sensitive and accurate experimental parameters for structural determinations in solution.[1,2] As seen in depth in Chapter 2, paramagnetism enhances relaxation rates and induces remarkable shifts of nuclear resonances: this is true for all the paramagnetic systems, offering interesting application in metal containing complexes. Both *d*- and *f*- metals have been fruitfully applied, where the formers have been very largely used in the context of biomolecular NMR,[1] while the latter have widespread interest for small or medium-size molecules,[3,4] although their use in proteins and nucleic acids has also gained increasing interest.[5,6]

Due to very similar ionic radius and identical structure of the frontier orbitals, lanthanide (III) ions are usually considered to provide isostructural complexes throughout the series, likely with a higher degree of homogeneity within the elements at the beginning or at the end of the series.[7] This fact is the basis for extracting contributions containing structural information from experimental observables, because one is able to compare the values of observables, measured on complexes having the same geometrical and electronic structure but different magnetic properties. A very relevant case is provided by the extraction of **pseudocontact shifts** (PCS), which are valuable pieces of geometrical information.[8] This is because they display a marked dependence on the polar coordinates of the observed nucleus in a reference system based on the magnetic anisotropy tensor. Thus, they offer the basis for accurate geometry determination in solution, provided they are reliably extracted from the observed shifts. To this end, several approaches were developed, some of them are based on structural models, other ones, like the Reilley's method,[9] are on the contrary are model free.

The existence of an exchangeable coordination site is a key feature for functional systems. As seen in the previous Chapters, applications such as: molecular recognition,[10] enantiomer discrimination,[11] substrate activation,[12] luminescence quenching,[13] water nuclear relaxation (T_1-contrast in MRI),[14] and saturation transfer contrast enhancement,[15] are all dependent on the dynamic binding of a ligand (most often water) to Ln^{3+}. As a consequence, most complexes are designed with a good chelating agent (often macrocyclic), leaving at least one position (hereafter called axial) open to dynamic coordination. This feature is associated with a variable coordination number (CN) along the series, whereby early lanthanides tend to bind ancillary ligands, which may be absent in the complexes of the late ions.[16] This has a negative effect on the separation of PCS because one cannot treat simultaneously data of complexes with different CN (usually before or after the so-called 'gadolinium break ').[17,18]

A simple set of equations, directly derived from the standard Reilley treatment, for achieving the isolation of PCS, in cases with variable CN was developed by us in a recent paper,[19] the same treatment was extended to other cases, where the properties of the main chelating agent are modulated, because of polarizability effects,

as in heterobimetallic systems or because of a peculiar conformational feature, typical of DOTA derivatives. In all these cases, we took advantage of a large set of data and extracted reliable PCS with a brand-new approach.

This alternative procedure for achieving separation of **Fermi contact** (FC) shifts from PCS is independent of crystal field parameters and provides reliable results even in cases of variable (possibly fractional) occupancy of the axial coordination site. It may be regarded as an extension of the 'two nuclei ' method,[20] that will be briefly described in Section 5.1.1.2 and its power resides in two points: (1) it is very straightforward to use and may be easily implemented on spreadsheets set up for the standard Reilley procedure and (2) it does not depend on the choice of nuclei nearby in the transition, but uses all the available set of experimental data. In its present form, our theory is addressed to complexes endowed with axial symmetry, i.e. containing a C_n-axis, with $n \geq 3$. Although one can observe that fast geometric rearrangements and ligand exchange often render effective axial symmetry much more common than expected.[20,21]

Before describing our new separation method, the standard procedures , both the model based and the model-free approaches, will be briefly recapitulated in the following Sections.

5.1 Separation of contact and pseudo-contact contributions in paramagnetic lanthanide complexes

Going back to Chapter 2, and substituting eq. (2.44) and (2.29) in the general eq. (2.6) for the paramagnetic shift contribution, we get the following expression for the lanthanide Ln and the nucleus *i*

$$\begin{aligned}\delta_{Ln}^{para}(i) &= \delta_{Ln}^{con}(i) + \delta_{Ln}^{pc}(i) \\ &= -\frac{A_i}{\hbar\gamma_I B_o}\langle S_z\rangle_{Ln} \\ &+ \frac{1}{12\pi r_i^3}\left[\left(\chi_{zz}^{Ln} - \frac{\chi_{yy}^{Ln} + \chi_{xx}^{Ln}}{2}\right)(3\cos^2\theta_i - 1) + \frac{3}{2}\left(\chi_{yy}^{Ln} - \chi_{xx}^{Ln}\right)(\sin^2\theta_i\ \cos 2\gamma_i)\right]\end{aligned} \tag{5.1}$$

Defining the contact term *F(i)* and the *geometrical factors G(i)* and *H(i)* as

$$F(i) = -\frac{A_i}{\hbar\gamma_I B_o} \tag{5.2}$$

$$G(i) = \frac{3\cos^2\theta - 1}{r_i^3} \tag{5.3}$$

$$H(i) = \frac{\sin^2\theta\ \cos 2\gamma}{r_i^3} \tag{5.4}$$

And going back to the $D_{Ln,1}$ and $D_{Ln,2}$ coefficient definition in Section 2.1.2, the equation simplifies

$$\delta_{Ln}^{para}(i) = \delta_{Ln}^{con}(i) + \delta_{Ln}^{pc}(i) = F(i)\langle S_z\rangle_{Ln} + D_{Ln,1}G(i) + D_{Ln,2}H(i) \tag{5.5}$$

The FC and the PCS contributions are constituted by the product of two terms depending respectively on the lanthanide ($\langle S_z\rangle_{Ln}$) and on the nucleus *i* ($F(i)$, $G(i)$ and $H(i)$). Since $\langle S_z\rangle_{Ln}$ is poorly affected by crystal-field

effects, the values tabulated for the free ions [23] hold for all complexes and the contact term is easily factorized. On the other hand, χ^{Ln} depends on the specific electronic structure of the lanthanide ion ($4f^n$ configuration) combined with specific crystal-field potentials produced by the surrounding ligands. Except for Bleaney's approach (see section 2.3.1 and the following ones in this Chapter), no straightforward *a priori* prediction can be made for χ^{Ln} and the treatment of pseudo-contact terms requires an initial assumption of the molecular structures in order to calculate a set of $G(i)$and $H(i)$ which are then used to extract the anisotropic part of the paramagnetic susceptibility tensor ($\chi_{zz}^{Ln} - \frac{\chi_{yy}^{Ln}+\chi_{xx}^{Ln}}{2}$, $\chi_{yy}^{Ln} - \chi_{xx}^{Ln}$) and consequently the dipolar constants *D via* least-squares fitting processes.[24] Non-linear least-square fits may be further applied in order to simultaneously refine the geometrical factors and the components of the magnetic tensor.[3,24]

Table 5.1 C_{Ln} are recalculated according to Bleaney,[17] except for Eu, whose value is taken from [20]; $\langle S_z \rangle_{Ln}$ are taken from [16]. The $\langle S_z \rangle$ value for Sm is affected by a high variability.

	Ce	Pr	Nd	Sm	Eu	Tb	Dy	Ho	Er	Tm	Yb
C_{Ln}	-6.48	-11.41	-4.46	0.52	4.00	-86.84	-100.00	-39.25	32.40	52.53	21.64
$\langle S_z \rangle_{Ln}$	0.98	2.97	4.49	-0.06	-10.68	-31.82	-28.54	-22.63	-15.37	-8.21	-2.59
$C_{Ln} / \langle S_z \rangle_{Ln}$	-6.61	-3.84	-0.99	-8.68	-0.37	2.73	3.50	1.73	-2.11	-6.40	-8.36

5.1.1 Calculation of the anisotropic part of the magnetic susceptibility tensor with structural models

In the absence of contact contribution ($F(i) = 0$), the paramagnetic shift purely reflects the PCS contributions and Eq. (2.29) is ideally suited for extracting the experimental anisotropic part of the magnetic susceptibility tensor as long as a reasonable structural model is available. Kemple *et al.* [25] reported a detailed ^{1}H-NMR study of lanthanide complexes: with an unambiguous proton assignment through NMR experiments, using an arbitrary Cartesian frame (*x*,*y*,*z* axes) with Ln(III) at the origin, the geometrical factors $G(i)$and $H(i)$ were calculated from the polar coordinates (r_i, θ_i and ϕ_i, see Fig. 2.3).

The quality of the fitting process for the complex of a lanthanide *Ln* is measured by the agreement factor AF_{Ln} defined in eq. (5.6) [26]

$$AF_{Ln} = \sqrt{\frac{\sum_i \left(\delta_{Ln}^{obs}(i) - \delta_{Ln}^{calc}(i)\right)^2}{\sum_i \left(\delta_{Ln}^{obs}(i)\right)^2}} \qquad (5.6)$$

The unsatisfying agreement factors required correction for the contact contributions of protons close to the metal center, adding the correcting term $\delta_{Ln}^{con}(i) = F_i \langle S_z \rangle_{Ln}$. However the reliability of the method requires a vanishing FC contribution for most of the protons, in order to create a solid structural model. The procedure works very well with low-symmetry complexes and has been applied successfully also for extracting the anisotropic part of the magnetic susceptibility tensor of proteins.[27]

Forsberg *et al.*[28] developed a computer program which allows the systematic permutation of the observed pseudo-contact shifts $\left(\delta_{Ln}^{pc}(i)\right)$ to different sets of protons when assignment is problematic. Basically following the procedure of Kemple *et al.* a structural model (from molecular mechanics) is used for calculating the magnetic susceptibility tensor according to eq. (2.29) for each possible permutation. The associated agreement factors AF_{Ln}, eq. (5.6) are then used as criteria for selecting the most probable assignment which minimizes AF_{Ln}. Subsequent diagonalisation or reorientation of the magnetic axes provides the anisotropic part of the magnetic susceptibility tensor in the principal magnetic axes system. Further refinements of molecular geometry were developed in order to take into account the FC contribution and obtain better *AF*s. The method has been successfully applied to ^{13}C and ^{31}P, as well.[29]

The direct experimental determination of the anisotropic part of the magnetic susceptibility tensor from a set of pure PCS shifts according to eq. (2.29) has the considerable advantage of requiring no assumption on the symmetry of the magnetic susceptibility tensor. Paramagnetic shifts for axial and rhombic complexes can be satisfyingly modeled. The estimation of the FC contributions either by simultaneous fitting processes [25] or by comparison with experimental LIS [29] allows a reliable separation of contact and pseudocontact contributions. However, this approach requires (i) a large number of nuclei displaying pure PCs contributions and (ii) an accurate *a priori* structural model for the complex in solution, two conditions which are often limiting when considering bigger scale systems, like for instance supramolecular lanthanide complexes of intermediate size.

5.1.2 The model-free methods

When no assumption is made on the solution structure, the determination of the desired geometrical factors $G(i)$ and $H(i)$ requires the *a priori* separation of the FC and PCS contributions to the shift. As already seen in section 2.3.1, Bleaney approach limited to the T^{-2} term and summarized by eqs. (2.45-46) (see sect. 2.3.1) is well-suited for this purpose since the anisotropic part of the magnetic susceptibility tensor can be modeled by a judicious combination of an electronic factor depending only on the electronic configuration of the Ln(III) ion and the crystal-field parameters of rank two for the complexes. Defining B_k^q parameters related to the crystal field coefficients A_k^q introduced in section 2.3.1 according to the following equations

$$B_0^2 = 2A_0^2\langle r^2\rangle \tag{5.7}$$

$$B_2^2 = \sqrt{\frac{2}{3}}A_2^2\langle r^2\rangle \tag{5.8}$$

Defining the *C* parameters as Bleaney factor[19] as

$$C = -\frac{\mu_0}{4\pi}\frac{g_j^2\mu_B^2 J(J+1)(2J-1)(2J+3)}{120(kT)^2}\langle J\|\alpha\|J\rangle \tag{5.9}$$

[19] Their values are defined scaled to Dysprosium, to which is attributed the arbitrary value of -100. The relative values are reported in Table 5.1

Substituting these constants in eq (2.46) and the PCS contribution expression derived in (5.5) gives eq. (5.10)

$$\delta_{Ln}^{para}(i) = \delta_{Ln}^{con}(i) + \delta_{Ln}^{pc}(i) = F(i)\langle S_z\rangle_{Ln} + C_{Ln}\left(B_0^2 G(i) + \sqrt{6}B_2^2 H(i)\right) \quad (5.10)$$

For axial symmetry, the equation further simplifies [9] to

$$\delta_{Ln}^{para}(i) = F(i)\langle S_z\rangle_{Ln} + C_{Ln}B_0^2 G(i) \quad (5.11)$$

5.1.2.1 Reilley method

Since $\langle S_z\rangle_{Ln}$and C_{Ln} do not depend on the crystal-field splitting (see sect. 2.2 and 2.3.1), Reilley *et al.*[9] first proposed to rearrange eq. (5.10) into two linear forms, eqs. (5.12-13), for testing isostructurality along the lanthanide series.

$$\frac{\delta_{Ln}^{para}(i)}{\langle S_z\rangle_{Ln}} = F(i) + \frac{C_{Ln}\left(B_0^2 G(i) + \sqrt{6}B_2^2 H(i)\right)}{\langle S_z\rangle_{Ln}} \quad (5.12)$$

$$\frac{\delta_{Ln}^{para}(i)}{C_{Ln}} = \left(B_0^2 G(i) + \sqrt{6}B_2^2 H(i)\right) + F(i)\frac{\langle S_z\rangle_{Ln}}{C_{Ln}} \quad (5.13)$$

Although these two equations are mathematically identical, eq. (5.12) should be used when $\delta_{Ln}^{para}(i)$ is dominated by the PCS contribution and eq. (5.13) should be used when FC is dominating, thus maximizing the slopes of the resulting straight lines.[30] Plots of $\delta_{Ln}^{para}(i)/\langle S_z\rangle_{Ln}$ vs. $C_{Ln}/\langle S_z\rangle_{Ln}$ or $\delta_{Ln}^{para}(i)/C_{Ln}$ vs. $\langle S_z\rangle_{Ln}/C_{Ln}$ along the lanthanide series at a fixed temperature are expected to give straight lines and any deviations point to structural changes affecting the 'structural term' $B_0^2 G(i) + \sqrt{6}B_2^2 H(i)$.[9, 31]

For the PCS extraction the slope and the intercept are

$$M^{Reilley} = B \cdot G(i) \quad (5.14)$$

$$Q^{Reilley} = F(i) \quad (5.15)$$

Accordingly, the PCS and FC factors can be calculated for any lanthanide as

$$\delta_{Ln}^{PC,Reilley}(i) = M^{Reilley}(i) \cdot C_{Ln} \quad (5.16)$$

$$\delta_{Ln}^{con,Reilley}(i) = Q^{Reilley}(i) \cdot \langle S_z\rangle_{Ln} \quad (5.17)$$

Analogously, the same thing can be done in case of prevailing FC contribution.

However this simple interpretation assumes that (i) the hyperfine constant ($A(i)$ and hence the $F(i)$ term) and the crystal-field parameters B_0^2 and B_2^2 do not vary along the lanthanide series, (ii) the T^{-2} term is sufficient for describing the molecular magnetic anisotropy and (iii) the stepwise lanthanide contraction occurring when going from R = Ce to Yb has negligible effects on the structural term. Peters [3] has theoretically addressed the latter point and geometrical $G(i)$ factors for axial complexes modeled with molecular mechanics have been computed. The smooth contraction of the Ln-ligand distances often results in a

minor break occurring between R = Eu and R = Tb in the plot of $\delta_{Ln}^{para}(i)/\langle S_z\rangle_{Ln}$ vs. $C_{Ln}/\langle S_z\rangle_{Ln}$ because the monotonous change in $G(i)$ is amplified by the large values of C_{Ln} characterizing the second part of the lanthanide series (Table 5.1). It is thus concluded that both linear plots should simultaneously display a break along the lanthanide series to be indicative of a significant structural change.

5.1.2.2 Crystal-field independent methods

The invariance of crystal-field parameters is more problematic since the experimental B_k^q parameters of lanthanide complexes in the solid state usually exhibit significant variations along the lanthanide series resulting from the contraction of the *4f* orbitals.[32,33] Moreover, an abrupt change around the middle of the series, sometimes referred to as the '*gadolinium break*' effect has been evidenced for various systems in the literature.[34] Related effects are thus expected for lanthanide complexes in solution and efforts have been made to remove the influence of crystal-field parameters.[8,36] In axial complexes, the simultaneous consideration of the chemical shifts of two nuclei *i* and *k* provides two equations (5.11) and (5.18), from which Bleaney's factor C_{Ln} and the crystal field parameter B_0^2 can be removed by a judicious mathematical substitution in order to give eq. (5.19) [20,36]

$$\delta_{Ln}^{para}(k) = F(k)\langle S_z\rangle_{Ln} + C_{Ln}B_0^2G(k) \tag{5.18}$$

$$\frac{\delta_{Ln}^{para}(i)}{\langle S_z\rangle_{Ln}} = \left(F(i) - F(k)\frac{G(i)}{G(k)}\right) + \frac{G(i)}{G(k)}\cdot\frac{\delta_{Ln}^{para}(k)}{\langle S_z\rangle_{Ln}} \tag{5.19}$$

Plots of $\delta_{Ln}^{para}(i)/\langle S_z\rangle_{Ln}$ vs $\delta_{Ln}^{para}(k)/\langle S_z\rangle_{Ln}$ are ideally suited for testing structural changes occurring along the lanthanide series in axial complexes because straight lines are expected as long as the slope and the intercept do not vary. Structural changes affect the slope $G(i)/G(k) = (3\cos^2\theta_i - 1)/(3\cos^2\theta_k - 1)\cdot r_k^3/r_i^3$ and can be easily detected, but crystal-field changes which are not associated with significant structural variations have no effect. Changes in the intercept are more difficult to interpret since the value depends both on geometrical factors, as the slope, and hyperfine constants (*via* $F(i)$ and $F(k)$). In favourable cases, the prior analysis of the slope allows to draw reliable conclusions concerning possible variations of the hyperfine constants along the lanthanide series.[18,20] Although $\langle S_z\rangle_{Ln}$ is relatively independent of crystal-field effects around room temperature (see sect. 2.3.1), Geraldes *et al.* [37] proposed to remove it by solving simultaneously eqs. (5.11), (5.18) and (5.20) for three different nuclei *i*, *k*, *l* in the same lanthanide complex. Straightforward algebraic substitutions and transformations give eq. (5.21) where $R_{ik} = G(i)/G(k)$ and $S_{ik} = F(i)/F(k)$.

$$\delta_{Ln}^{para}(l) = F(l)\langle S_z\rangle_{Ln} + C_{Ln}B_0^2G(l) \tag{5.20}$$

$$\frac{\delta_{Ln}^{para}(i)}{\delta_{Ln}^{para}(k)} = \frac{(S_{lk}R_{ik} - S_{ik}S_{lk})}{(S_{lk} - R_{lk})} + \frac{(S_{ik} - R_{ik})}{(S_{lk} - R_{lk})}\cdot\frac{\delta_{Ln}^{para}(l)}{\delta_{Ln}^{para}(k)} \tag{5.21}$$

Since only experimental paramagnetic shift data are required for testing isostructurality, the use of eq. (5.21) seems promising as long as three different NMR-active nuclei are available in the complex. However, both the slope and the intercept are complicated non-linear combinations of geometrical factors and contact terms.

Deviations from linearity are difficult to interpret and accidental compensation effects cannot be ruled out when strict linear behaviours are observed.[38]

5.1.2.3 The case of rhombic systems

The removal of crystal-field parameters according to the two-nuclei, eq. (5.19), and the three-nuclei, eq. (5.21), methods is strictly limited to axial complexes for which eq. (5.11) holds (*i.e.* possessing at least a C_3 axis). The explicit consideration of the rhombic term in Bleaney's approach, eq. (5.22) below, significantly complicates the derivation of crystal-field independent equations which requires at least three different nuclei. To the best of our knowledge, no analytical form has been reported in the literature for rhombic systems. Reuben and Elgavish [30] suggested that eq. (5.10) is only a poor approximation for rhombic systems and a better modeling of the pseudo-contact contribution requires two factors C_{Ln}^{axial} and C_{Ln}^{rombic}, eq. (5.22).

$$\delta^{pc}(i) = C_{Ln}^{axial} G(i) + C_{Ln}^{rhombic} H(i) \tag{5.22}$$

Since C_{Ln}^{axial} is proportional to $\chi_{zz}^{Ln} - 1/3\mathrm{Tr}\chi$ and $C_{Ln}^{rhombic}$ is proportional to $\chi_{yy}^{Ln} - \chi_{xx}^{Ln}$ in the principal magnetic axes system, eq. (2.29), Reuben and Elgavish [30] used the experimental diagonalised magnetic susceptibility tensors reported by Horrocks and Sipe [31] for a solid-state system in order to compute the proportionality factors C_{Ln}^{axial} and $C_{Ln}^{rhombic}$ scaled to $C_{Dy}^{axial} = -100$. Interestingly they notice that the axial factors C_{Ln}^{axial} satisfyingly match original Bleaney's C_{Ln} factors, but $C_{Ln}^{rhombic}$ have only poor correlations with C_{Ln} pointing to the limit of theoretical Bleaney's approach which predicts a single factor ($C_{Ln}^{axial} = C_{Ln}^{rhombic}$, eq. 5.10, Table 5.1). Two linear forms, eqs. (5.23-24) can be derived from eq. (5.22) for nuclei displaying no contact contributions ($F(i) = 0$).

$$\frac{\delta^{pc}(i)}{C_{Ln}^{axial}} = G(i) + H(i)\frac{C_{Ln}^{rhombic}}{C_{Ln}^{axial}} \tag{5.23}$$

$$\frac{\delta^{pc}(i)}{C_{Ln}^{rhombic}} = H(i) + G(i)\frac{C_{Ln}^{axial}}{C_{Ln}^{rhombic}} \tag{5.24}$$

Plots of $\delta^{pc}(i)/C_{Ln}^{axial}$ vs $C_{Ln}^{rhombic}/C_{Ln}^{axial}$ (eq.) or $\delta^{pc}(i)/C_{Ln}^{rhombic}$ vs $C_{Ln}^{axial}/C_{Ln}^{rhombic}$ (eq.) are expected to be linear within an isostructural series. The fitting process has been applied to non-axial lanthanide shift reagents and leads to improved linear correlations,[30] but the origin of the deviation from the strict T^{-n} terms was not addressed. One can infer that the different behaviours of C_{Ln}^{axial} and $C_{Ln}^{rhombic}$ along the lanthanide series result from higher-order T^{n} terms ($n \geq 3$) which are neglected in original Bleaney's approach, but which are required to reliably model complexes possessing large crystal-field splittings ($\Delta E_{CF}/kT \geq 1$). Since the $C_{Ln}^{rhombic}$ factor proposed by Reuben and Elgavish originates from the specific crystal-field splitting of one reference complex, [Ln(dipivolymethane)$_3$(4-picoline)$_2$], their systematic use for all lanthanide complexes is doubtful and this approach, to the best of our knowledge, has not been applied again for the structure-independent analysis of lanthanide induced shift data.

Recently model-free and crystal-free methods have been used [40] also for the analysis of the solution structure of rhombic complexes, with fairly good results.

5.2 Pseudocontact shifts in lanthanide complexes with variable crystal field parameters

As seen in section 5.1.2.1, discrepancies in the Reilley method may be due to lanthanide contraction, besides that, another cause is water coordination. Axial coordination of water or of some other ancillary ligand introduces a much greater source of variation of the crystal-field parameters *B*s. In systems endowed with a C_n axis with n≥3, the crystal field terms B_k^m with k≠0 vanish, included B_0^0 and the contribution of an axial ligand, B^{ax}, is limited to the terms B_0^n and is additive to those stemming from the other (non axial) ligands B^{lig}. [41] We can thus write the following partition

$$B = B^{lig} + B^{ax} \tag{5.25}$$

Consequently the magnetic anisotropy term can be written as the sum [41,42]

$$D_{Ln} = C_{Ln}\left(B^{lig} + B^{ax}\right) = D_{Ln}^{lig} + D_{Ln}^{ax} \tag{5.26}$$

It is very common that for a given ligand early lanthanides yield hydrated complexes on account of their preference for higher coordination numbers, while late lanthanides provide anhydrous complexes. Thus, instead of being constant or following a regular trend over the series, B may display a more or less abrupt change, which often occurs around the middle of the transition and is called gadolinium break.[18] This corresponds to a rigid picture, where the complex is either totally hydrated (viz. fully occupied at the axial coordination site) or totally anhydrous, which is unfit to represent a dynamic situation.

The axial coordination site is often labile and this is a key feature of lanthanide complexes. Indeed, dynamic axial coordination is at the basis of functional systems, such as those quoted in the introduction which must exchange axial ligands very rapidly. From the point of view of NMR spectroscopy, this means that the hydrated (H) and anhydrous (A) forms (plus water or in general any other ancillary ligand, W) must be in *fast exchange*, that is, the rate of the equilibrium

$$H \underset{k_-}{\overset{k_+}{\rightleftarrows}} A + W \tag{5.27}$$

is likely to be great compared to the shift difference (in Hz) between the corresponding nuclei in H and A. In this situation the spectra of the individual forms cannot be observed, but one set of resonances, at shifts

$$\delta_{Ln}^{obs}(i) = x_{Ln}^{H} \cdot \delta_{Ln}^{H}(i) + x_{Ln}^{A} \cdot \delta_{Ln}^{A}(i) = x_{Ln} \cdot \delta_{Ln}^{H}(i) + (1 - x_{Ln}) \cdot \delta_{Ln}^{A}(i) \tag{5.28}$$

where $x^A = (1 - x)$ and $x^H = x$ are the mole fractions of A and H for the complex with Ln.

It is thus reasonable to assume that to a first approximation PCS display the greatest sensitivity to the occupancy of the axial site, because they respond to the total charge distribution through *D*, while the diamagnetic shift and FC are mostly local properties, depending primarily on the electron density and on unpaired electron delocalization. Therefore we shall write

$$\delta_{Ln}^{obs}(i) = \delta_{Ln}^{dia}(i) + \delta_{Ln}^{con}(i) + \left[x_{Ln} \cdot \delta_{Ln}^{pc,H}(i) + (1 - x_{Ln}) \cdot \delta_{Ln}^{pc,A}(i)\right] \tag{5.29}$$

and

$$\delta_{Ln}^{para}(i) = \delta_{Ln}^{con}(i) + \left[x_{Ln} \cdot \delta_{Ln}^{pc,H}(i) + (1 - x_{Ln}) \cdot \delta_{Ln}^{pc,A}(i)\right] \tag{5.30}$$

Taking advantage of eq. (5.26), we can write

$$\delta_{Ln}^{pc,H}(i) = [D_{Ln}^{lig} + D_{Ln}^{ax}]G(i) \tag{5.31}$$

$$\delta_{Ln}^{pc,A}(i) = D_{Ln}^{lig}G(i) \tag{5.32}$$

which combine in the term in square parentheses of eq. (5.30) to

$$\delta_{Ln}^{pc,tot}(i) = x_{Ln} \cdot \delta_{Ln}^{pc,H}(i) + \left(1 - x_{Ln}\right) \cdot \delta_{Ln}^{pc,A}(i) = \left[D_{Ln}^{lig} + x_{Ln}D_{Ln}^{ax}\right]G(i) = D_{Ln}^{tot}G(i) \tag{5.33}$$

with

$$D_{Ln}^{tot} = D_{Ln}^{lig} + x_{Ln}D_{Ln}^{ax} \tag{5.34}$$

This demonstrates that D_{Ln}^{tot} is a function of the lanthanide not only through Bleaney's constant C_{Ln} but also because of variable occupancy of the axial site through x_{Ln}. Consequently, D_{Ln}^{tot} may not follow the expected trend and Reilley method for separating Fermi contact and pseudocontact shifts may fail.

The so-called two-nuclei method for separating FC and PCS terms is designed to take care of the variation in crystal-field parameters along the series (Sec. 5.1.1.2).[17] It has been proposed for the small variations in *B* induced by lanthanide contraction, but may very well serve to eliminate the problem of variable coordination number outlined above.

5.2.1 Two-lanthanides method

If we could neglect Fermi contact shifts altogether, by plotting $\delta_{Ln1}^{para}(i)$ vs. $\delta_{Ln2}^{para}(i)$ for two different isostructural complexes with lanthanides Ln1 and Ln2, we would obtain a straight line passing through the origin (which is rigorously true for PCS). The slope of this line is equal to the ratio

$$m = \frac{D_{Ln1}}{D_{Ln2}} \tag{5.35}$$

In the case of no variation in axial coordination (i.e. with the identity $x_{Ln1} = x_{Ln2}$) or in the crystal field parameters *B*, the above equation would reduce to the predictable constant

$$m_{ideal} = \frac{C_{Ln1}}{C_{Ln2}} \tag{5.36}$$

But this is not the case if $x_{Ln1} \neq x_{Ln2}$ with reference to eq. (5.29) (or in general if $B_{Ln1} \neq B_{Ln2}$).

We can now take advantage of the following facts regarding Fermi contact shifts:

(1) they are usually scattered in sign and magnitude;

(2) they are usually small for nuclei distant more than 4 bonds from Ln^{3+};

(3) for nuclei closer than 4 bonds from Ln^{3+}, FC may be large, but most often PCS are also very large (because of the short distance).

These three points concur in determining that plots of $\delta_{Ln}^{para}(i)$ for Ln1 and Ln2 are often linear to a very good approximation, possibly with the exception of small and highly conjugated ligands. The slope *m* provides the ratio of the *D* parameters given in eq. (5.35), while taking into account any variation in the crystal field parameters *B*, notably the part due to variable axial coordination. Now, we can recall eq. (5.12), simplified for axial systems, and substitute mD_{Ln2} for D_{Ln1}

$$\frac{\delta_{Ln1}^{para}(i)}{\langle S_z\rangle_{Ln1}} = F(i) + \frac{mD_{Ln2}}{\langle S_z\rangle_{Ln1}}G(i) \tag{5.37}$$

$$\frac{\delta_{Ln2}^{para}(i)}{\langle S_z\rangle_{Ln2}} = F(i) + \frac{D_{Ln2}}{\langle S_z\rangle_{Ln2}}G(i) \tag{5.38}$$

These two can be combined to yield the modified Reilley equation

$$\frac{\delta_{Ln2}^{para}(i)}{\langle S_z\rangle_{Ln2}} - \frac{\delta_{Ln1}^{para}(i)}{\langle S_z\rangle_{Ln1}} = D_{Ln2}G(i)\left(\frac{1}{\langle S_z\rangle_{Ln2}} - \frac{m}{\langle S_z\rangle_{Ln1}}\right) \tag{5.39}$$

The final equations for calculating FC and PCS for the nucleus *i* in the complexes with Ln1 and Ln2 are

$$\delta_{Ln1}^{pc}(i) = D_{Ln1}G(i) = mD_{Ln2}G(i) = m\left(\frac{(\delta_{Ln2}^{para}(i)/\langle S_z\rangle_{Ln2}) - (\delta_{Ln1}^{para}(i)/\langle S_z\rangle_{Ln1})}{(1/\langle S_z\rangle_{Ln2}) - (m/\langle S_z\rangle_{Ln1})}\right) \tag{5.40}$$

$$\delta_{Ln1}^{con}(i) = \delta_{Ln1}^{para}(i) - \delta_{Ln1}^{pc}(i) \tag{5.41}$$

We must note that this procedure does not rely on any assumption regarding the geometry of the complex (it falls into the category of the '*model free methods*'), provided they are axially symmetrical,[17,42] and moreover does not use any hypothesis on the degree of hydration (or bond to any other axial ligand) in the two complexes.

5.2.2 The 'all lanthanides' method

As an alternative and an extension to the method outlined above, we can take advantage of a set of Ln^{3+} complexes simultaneously.

(1) We select a reference compound, which must be chosen for being the best characterized one (with the largest set of unambiguously assigned resonances) and that is endowed with a large C_{Ln} and $C_{Ln}/\langle S_z\rangle_{Ln}$ ratio (see Table 5.1): the best choices may be in this order, Yb, Pr, and Ce. From now on, this reference lanthanide will be called ref. We must plot all the $\delta_{Ln}^{para}(i)$ vs. the $\delta_{ref}^{para}(i)$, and fit them to lines passing through the origin, with slopes m_{Ln}. Any significant deviation from linearity means that: (a) the complexes with Ln and ref are not

isostructural and (b) if this occurs more or less systematically, then large contact contributions must be envisaged. In both cases, the method cannot be applied.

(2) We build modified Reilley plots for each nucleus *i* as a function of Ln, by plotting

$$\frac{\delta_{Ln}^{para}(i)}{\langle S_z \rangle_{Ln}} \text{ vs. } \frac{m}{\langle S_z \rangle_{Ln}} \tag{5.42}$$

This must yield straight lines, because, by analogy with what was seen in the previous section,

$$\frac{\delta_{Ln}^{para}(i)}{\langle S_z \rangle_{Ln}} = F(i) + G(i) \cdot B \cdot C_{ref} \frac{m_{Ln}}{\langle S_z \rangle_{Ln}} \tag{5.43}$$

(3) The slope and intercept of these straight lines are for each nucleus

$$M_i = B \cdot C_{ref} \cdot G(i) \tag{5.44}$$

$$Q = F(i) \tag{5.45}$$

(4) We are now able to identify the PCS for each nucleus in each Ln-complex, by the simple operation

$$\delta_{Ln}^{pc}(i) = m_{Ln} \cdot M_i \tag{5.46}$$

and

$$\delta_{ref}^{pc}(i) = M_i \tag{5.47}$$

while the contact terms can be obtained again through eq. (5.17).

As we shall see in the case of cryptate below, the choice of the reference compound affects the results of the procedure to a very moderate extent for the PCS.

5.2.3 Applications

We shall discuss below a few practical cases, mostly taken from the literature, which will hopefully clarify the above outlined procedures and show their scope, their merit and their limitations.

It should be stressed that our approach is only applicable to systems with a set of pseudocontact-shifted signals, because only this ensures a good linear fitting for deriving the slopes m which must substitute the C_{Ln} in the standard Reilley treatment. Consequently, some small-size traditional ligands for Ln^{3+}, such as acetylacetonates or 1,3-oxydiacetate are not amenable to our procedure.

5.2.3.1 N,N-*diethyl-DOTAM*

In spite of the enormous interest towards DOTA and its derivatives, mostly due to their applications in MRI,[20] it is hard to find a complete set of experimental shifts throughout the series. In their comprehensive paper on the structure of Yb DOTA in solution, Aime, Botta and Ermondi showed the ^{1}H spectra of most Ln DOTA but did not provide figures for the shifts or their assignment.[44] The diethylamide derivative of DOTA, called *N,N*-diethyl-DOTAM (1,4,7,10-tetrakis(*N,N*-diethylacetamido)-1,4,7,10-tetraazacyclododecane, Figure 5.1) was thoroughly studied by Forsberg *et al.* in a paper containing the most complete separation of FC and PCS of this whole family of compounds.[21][28]

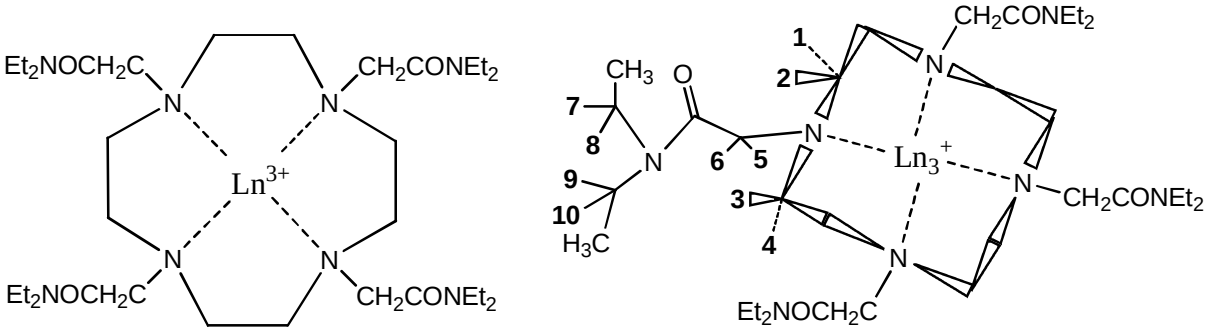

Figure 5.1

A standard Reilley analysis of the paramagnetic shifts consisting of the plots of $\delta_{Ln}^{para}(i)/\langle S_z\rangle_{Ln}$ vs. $C_{Ln}/\langle S_z\rangle_{Ln}$ is reported in Fig. 5.2. This shows that there is a reasonably good linearity, with the gross exception of Sm and Tm. The former element is characterized by very small paramagnetic shifts (see C_{Sm} and $\langle S_z\rangle_{Sm}$ in Table 5.1), whose exact quantification is consequently rather error-prone. Moreover, $\langle S_z\rangle_{Sm}$ is poorly estimated because it depends on a multiplet of energy levels very close to the fundamental one. The fact that this parameter is very small and that it is at the denominator of the quantities to be plotted in Reilley method has the effect of amplifying any uncertainty.

To our understanding, there is no obvious reason for a deviation in Tm shifts, although they do often show exceptional behavior, as observed e.g. in Piguet and Geraldes review.[17]

By discarding the values for Tm and Sm, one can apply a linear fit to the Reilley plot for all protons in Ln *N,N*-diethyl-DOTAM, obtaining the parameters shown in Table 5.2. Thereafter, one can achieve the separation of PCS and FC by means of Eqs. (5.16) and (5.17).

We can take two parameters to assess the quality of the Reilley method: the correlation coefficients *R(i)* of the linear fit and the differences

$$diff(i) = \delta_{Yb}^{para}(i) - \left(\delta_{Yb}^{pc,Reilley}(i) + \delta_{Yb}^{con,Reilley}(i)\right) \tag{5.48}$$

[20] Recently Sessoli *et al.*[43] described a new application for Dy DOTA as Single Molecule Magnet.

[21] Proton 1 corresponds to the 'axial at side proton' (ax@s), proton 2 corresponds to the 'equatorial at side' proton (eq@s), proton 3 corresponds to the 'axial at corner' proton (ax@c) and proton 4 corresponds to the 'equatorial at corner' proton (eq@c).

which should ideally be 0.

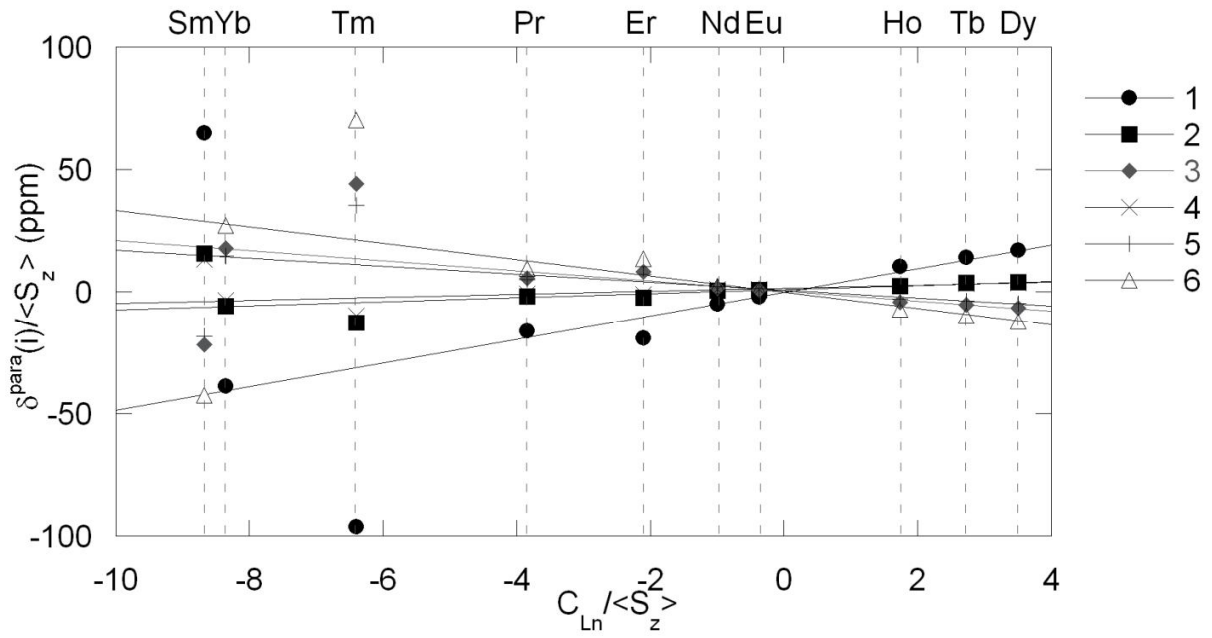

Figure 5.2 Reilley plots for a selection of protons in Ln *N,N*-diethyl-DOTAM. Data taken from Ref. [45]

We can appreciate that the quality of Reilley plots for this set of complexes is very good, as witnessed by the correlation coefficients, which are all above 0.97 with the sole exceptions of H9 and H10. These two protons are remote from Ln and experience a particularly small paramagnetic shift. Moreover, they are geminal and their assignment throughout the series may be less safe than in the other cases.

According to our method, we must take one complex as the reference and we choose Yb *N,N*-diethyl-DOTAM. We plot the paramagnetic shifts for all protons in Ln *N,N*-diethyl-DOTAM vs. those of the reference compound, obtaining plots as shown in Fig. 5.3, while the parameters of the linear fits (forced through the origin) are reported in Table 5.3.[22] The good linearity confirms that the complexes are isostructural and that the contributions of FC to the total paramagnetic shifts are small and scattered in sign and magnitude, as postulated in the previous sections. It is worth observing that also Tm provides a linear fit with Yb and it will be used in the following procedure, while it had to be arbitrarily discarded in the Reilley method.

We can now build plots of $\delta_{Ln}^{para}(i)/\langle S_z\rangle_{Ln}$ vs. $m_{Ln}/\langle S_z\rangle_{Ln}$ for each nucleus i, which yields the results shown in Fig. 5.4 and in Table 5.4.

[22] We can appreciate that the values of the slopes m_{Ln} follow the same trend of the constants C_{Ln}, apart for Sm and Tm. This is consistent with the previous observation that Reilley plots are linear.

Table 5.2 Slopes $M^{Reilley}$(i), intercepts $Q^{Reilley}$(i), and correlation coefficients $R^{Reilley}$(i) of a linear fit of Reilley plots for Ln *N,N*-diethyl-DOTAM, by excluding the data for Sm and Tm. The values of PCS and FC for Yb estimated through Eqs. (5.16) and (5.17) are reported in columns 5 and 6;the last column contains the difference defined in eq. (5.48). PCS, FC and diff values are in ppm units.

Protons	$M^{Reilley}$	$Q^{Reilley}$	$R^{Reilley}$	PCS	FC	diff
1	4.85	-0.22	0.98	104.93	0.57	-4.90
2	0.84	0.99	0.97	18.23	-2.55	-0.78
3	-2.07	0.30	0.98	-44.75	-0.78	-0.87
4	0.62	1.45	0.98	13.35	-3.76	-0.89
5	-1.62	0.78	0.98	-35.14	-2.03	-0.43
6	-3.35	-0.13	0.98	-72.58	0.35	2.03
7	-0.84	-0.06	0.98	-18.11	0.15	1.55
8	-0.56	-0.07	0.98	-12.15	0.19	1.66
9	0.17	0.15	0.53	3.72	-0.39	2.27
10	0.06	-0.17	0.29	1.34	0.44	2.62

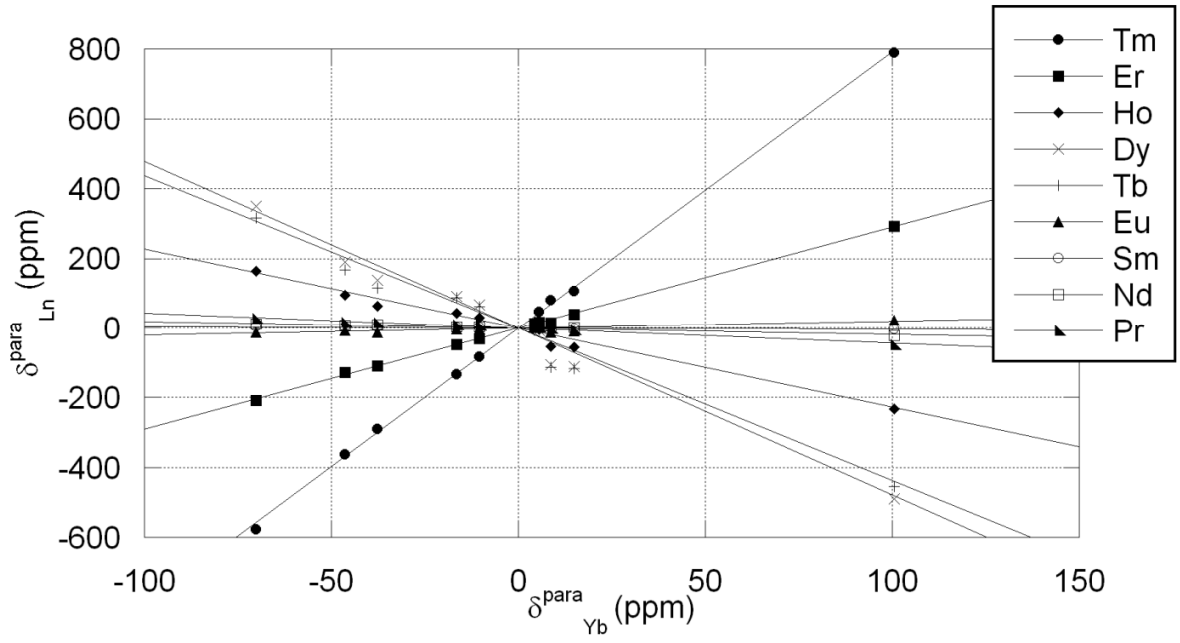

Figure 5.3 Plots of $\boldsymbol{\delta_{Ln}^{para}(i)}$ vs. $\boldsymbol{\delta_{Yb}^{para}(i)}$, for Ln *N,N*-diethyl-DOTAM.

In this case the slope *M* of our modified Reilley plots coincides by definition with the PCS of the reference compound (in this case Yb *N,N*-diethyl-DOTAM).

The improvement over the conventional Reilley method is apparent from both quality parameters (*R* and diff), although in the present case the gain is only marginal: we had already found excellent linearity in Reilley plots, which could hardly be improved.

Table 5.3 Slopes *m* and correlation coefficients *R* of the linear fits (forced through the origin) shown in Fig. 5.3.

Lanthanide	m_{Ln}	R
Pr	-0.435	0.99
Nd	-0.19	0.86
Sm	-0.036	0.98
Eu	0.20	0.78
Tb	-4.37	0.98
Dy	-4.79	0.99
Ho	-2.27	0.99
Er	2.90	0.99
Tm	7.93	0.99

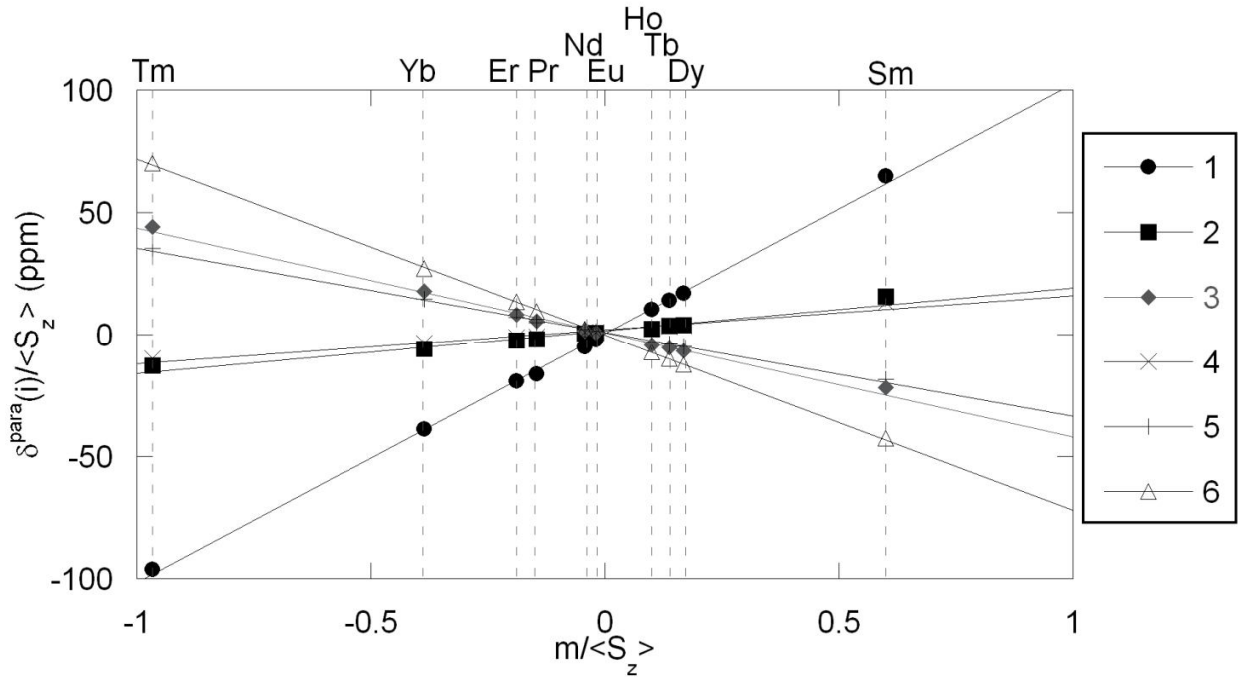

Figure 5.4 Plots of $\boldsymbol{\delta_{Ln}^{para}(i) / \langle S_z \rangle_{Ln}}$ vs. $\mathbf{m_{Ln} / \langle S_z \rangle_{Ln}}$ **for Ln *N,N*-diethyl-**DOTAM, having taken Yb ***N,N*-diethyl-**DOTAM as the reference compound for calculating m_{Ln}.

Table 5.4 Slopes (M_i), intercepts (Q_i) and correlation coefficients (R_i) of modified Reilley plots for Ln *N,N*-diethyl-DOTAM shown in Fig. 3. PCS and FC for the reference compound, Yb *N,N*-diethyl-DOTAM, were calculated from the values of M_i and Q_i, respectively, according to eqs. (5.46) and (5.17). The quality parameter diff is defined in Eq. (33). PCS, FC and diff values are in ppm units.

Protons	M	Q	R	PCS	FC	diff
1	102.21	0.54	1.00	102.21	-1.41	-0.20
2	17.60	1.73	0.98	17.60	-4.48	1.78
3	-42.80	0.09	1.00	-42.80	-0.24	-3.37
4	14.06	2.08	0.98	14.06	-5.39	0.03
5	-34.49	1.02	1.00	-34.49	-2.63	-0.48
6	-71.99	-0.09	1.00	-71.99	0.23	1.55
7	-17.57	-0.20	1.00	-17.57	0.53	0.65
8	-11.77	-0.32	0.99	-11.77	0.83	0.64
9	4.67	-0.08	0.87	4.67	0.21	0.72
10	-2.96	-1.27	0.47	-2.96	3.29	4.07

5.2.3.2 Cryptate

In 1999 Geraldes and coworkers reported a complete analysis of the paramagnetic shifts in a Ln cryptate derived from the condensation of tris(2-aminoethyl)amine and 2,6-diformylcresol,[20] shown in Figure 5.5. These authors highlighted a break in the Reilley plots, which was attributed to the presence of a coordinated water molecule in the first part of the transition, absent in the second part. This is particularly evident in the case of proton H3, as shown in Fig. 5.6.

In such a case it is clear that a conventional treatment through Reilley plots is only possible by treating separately early and late elements. This reduces the set of data and may worsen the quality of the analysis. Unfortunately, for the other protons in the very same molecule the situation is somewhat less evident, to the point that in some cases it would be difficult to put the break point to a specific lanthanide.[20]

To use our modified method, we follow the same steps outlined in the previous section. We choose Pr as the reference compound, because it has an optimal ratio $C_{Ln}/\langle S_z\rangle_{Ln}$ (Table 5.1) and it is completely characterized, unlike the Yb derivative. We plot $\delta_{Ln}^{para}(i)$ vs. the $\delta_{Pr}^{para}(i)$ and fit them with lines (passing through the origin), which leads to the results summarized in Table 5.5.

The correlation coefficients are satisfactory (although not always excellent), which demonstrates isostructurality through the series and small contributions of FC. The slopes m_{Ln} can be used to achieve the separation of PCS and FC following the sequence of operations described in eqs. (5.46) and (5.17) (Figures 5.7 and 5.8) with the results shown in Table 5.6.

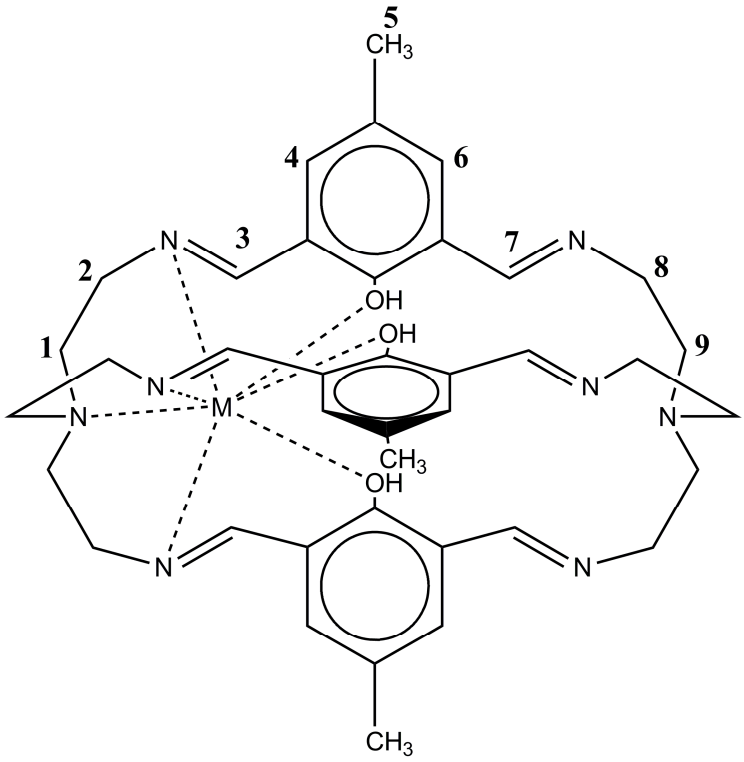

Figure 5.5

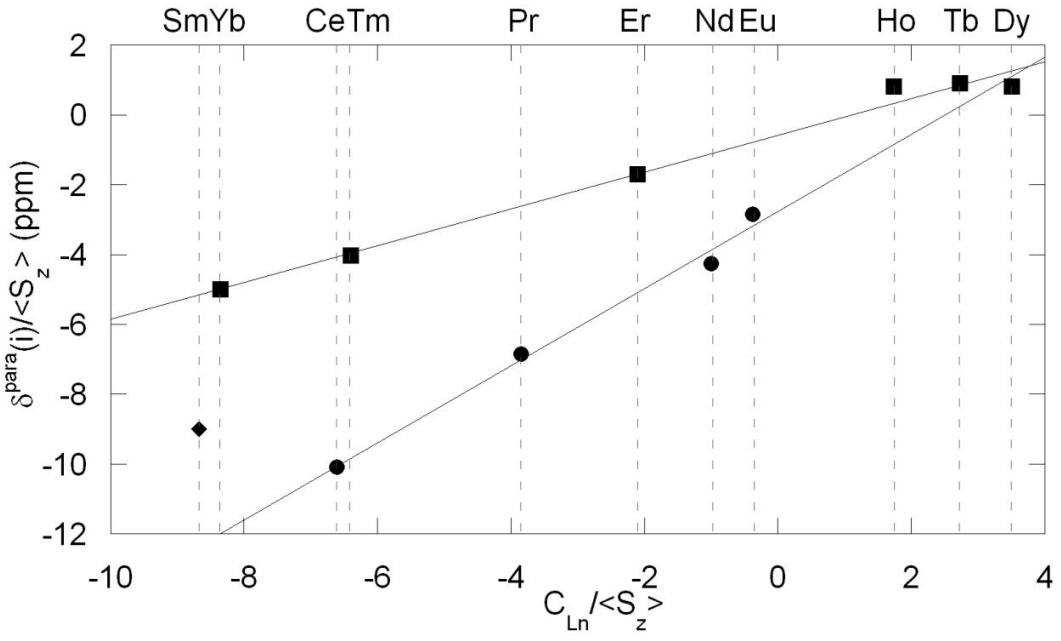

Figure 5.6 Reilley plot for H3 in the series of cryptates depicted in Scheme 2. Data taken from Ref. [20].

Table 5.5 Slopes m and correlation coefficients R of the linear fits (forced through the origin) relative to the set of Ln cryptates of Ref. [20].

Lanthanide	m_{Ln}	R
Ce	0.67	0.96
Nd	0.59	0.86
Sm	0.0014	0.16
Eu	-0.60	0.35
Tb	4.94	0.64
Dy	3.64	0.66
Ho	2.00	0.76
Er	-1.73	0.95
Tm	-2.40	0.91
Yb	-1.10	0.81

Interestingly, by choosing Ce instead of Pr as the reference compound, we obtain PCS values differing by less than 10%, as shown in Table 5.7.

Table 5.6 Slopes (M_i), intercepts (Q_i) and correlation coefficients (R_i) of modified Reilley plots for the Ln cryptates of Figure 5.5. PCS and FC for the reference Pr cryptate, were calculated from the values of M_i and Q_i, respectively, according to eqs. (5.46) and (5.17). The quality parameter diff is defined in Eq. (33). PCS, FC and diff values are in ppm units.

Protons	M	Q	R	PCS	FC	diff
H1ax	21.86	-1.23	0.94	21.86	-3.65	-5.22
H1eq	17.38	-1.24	0.98	17.38	-3.68	-0.67
H2ax	0.53	-0.72	0.36	0.53	-2.14	-0.17
H2eq	0.14	-0.38	0.13	0.14	-1.13	-0.70
H3	-10.79	-2.14	0.73	-10.79	-6.36	-3.23
H4	-8.84	2.16	0.45	-8.84	6.42	-3.22
H5	-2.18	0.36	0.65	-2.18	1.07	-0.68
H6	-1.71	0.03	0.94	-1.71	0.09	-0.21
H7[a]	8.24	-3.44	0.58	8.24	-10.22	2.96
H8ax	7.47	-0.45	0.99	7.47	-1.34	-0.46
H8eq	5.71	-0.36	0.99	5.71	-1.07	-0.32
H9ax	3.70	-0.24	0.99	3.70	-0.71	-0.17
H9eq	4.96	-0.31	0.99	4.96	-0.92	-0.35

[a] The values of δ^{para}(H7) are very small (below 1 ppm), consequently they are affected by a big error and should be considered unreliable

Proof of the quality of our results is provided in Fig. 5.9, where we show the modified-Reilley plot for H3. Moreover, in Fig. 5.10 we report PCS and FC for the Pr complex calculated with our method compared to those of the original paper. We can simultaneously use all the available data, without any more or less arbitrary partition due to the gadolinium break, which is at variance with what was reported in the original paper.

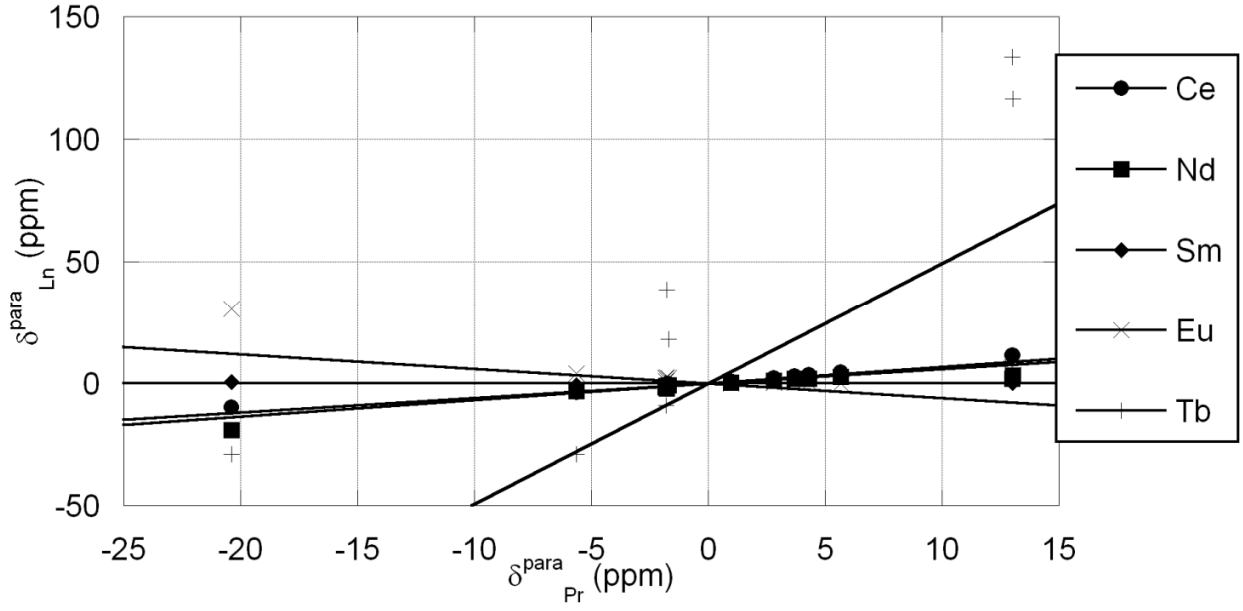

Figure 5.7 $\boldsymbol{\delta_{Ln}^{para}(i)}$ vs. $\boldsymbol{\delta_{Pr}^{para}(i)}$plot of the Cryptate protons for the Ce, Nd, Sm, Eu and Tb complexes.

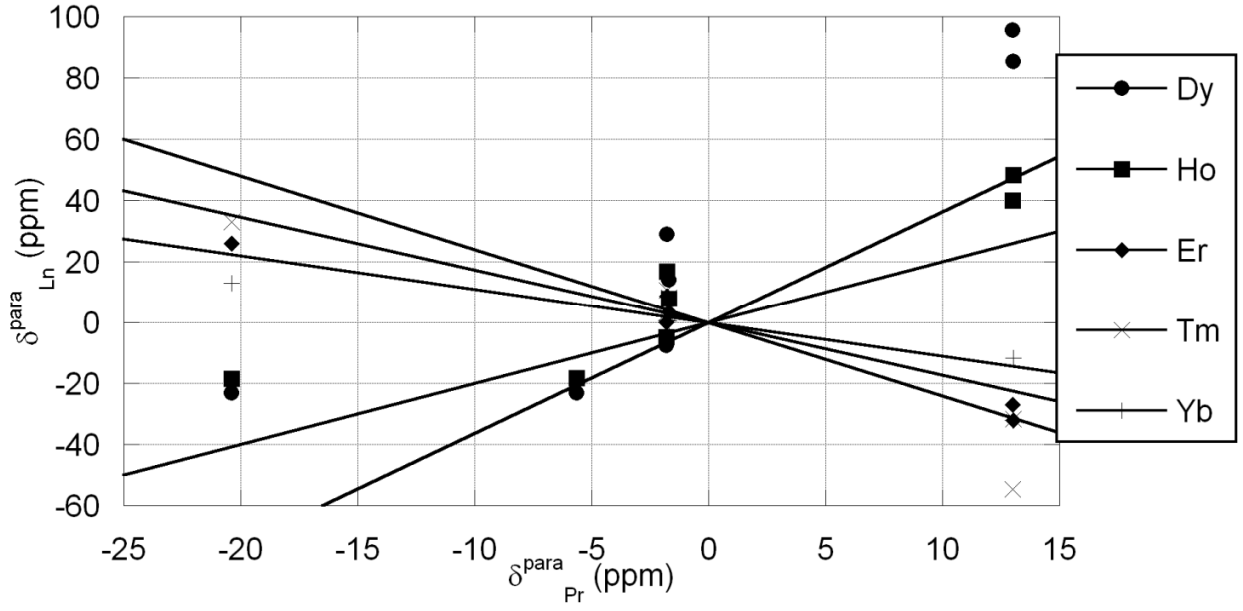

Figure 5.8 $\boldsymbol{\delta_{Ln}^{para}(i)}$ vs. $\boldsymbol{\delta_{Pr}^{para}(i)}$plot of the Cryptate protons for the Dy, Ho, Er, Tm and Yb complexes.

Although some of the correlation coefficients of the plots $\delta_{Ln}^{para}(i)$ vs. $\delta_{ref}^{para}(i)$ are unusually small compared to other cases, this does not prevent a satisfactory extraction of PCS, which are in close agreement with those found in Ref. [20].

Table 5.7 Differences between the PCS values of the Cryptate protons calculated with our methods taking as the reference compound the Ce or Pr derivatives.

	H1ax	H1eq	H2ax	H2eq	H3	H4	H5	H6	H7	H8ax	H8eq	H9ax	H9eq
Ce	-1.21	-1.42	-0.76	-0.40	-1.48	0.42	0.30	0.01	-3.55	-0.48	-0.38	-0.26	-0.34
Pr	-3.45	-3.37	-1.08	-0.56	-1.14	1.30	0.59	0.16	-5.54	-1.28	-0.99	-0.66	-0.87
Nd	-3.76	-3.30	-0.59	-0.29	0.44	1.47	0.50	0.24	-3.52	-1.33	-1.03	-0.67	-0.90
Sm	0.12	0.09	-0.01	0.00	-0.08	-0.05	-0.01	-0.01	0.01	NA	NA	NA	NA
Eu	6.80	5.62	0.51	0.23	-2.38	-2.72	-0.76	-0.49	4.02	2.36	1.81	1.18	1.57
Tb	8.00	2.38	-6.10	-3.33	-21.86	-3.85	0.73	NA	NA	NA	NA	NA	NA
Dy	5.37	1.35	-4.48	-2.44	-15.76	-2.62	0.58	NA	NA	NA	NA	NA	NA
Ho	1.17	-0.61	-2.41	-1.30	-7.51	-0.71	0.48	NA	NA	NA	NA	NA	NA
Er	3.14	3.69	1.96	1.03	3.80	ND	-0.77	NA	NA	NA	NA	NA	NA
Tm	3.54	4.50	2.74	1.45	5.80	ND	-1.00	NA	NA	NA	NA	NA	NA
Yb	0.66	1.33	1.29	0.69	3.28	ND	-0.37	NA	NA	NA	NA	NA	NA

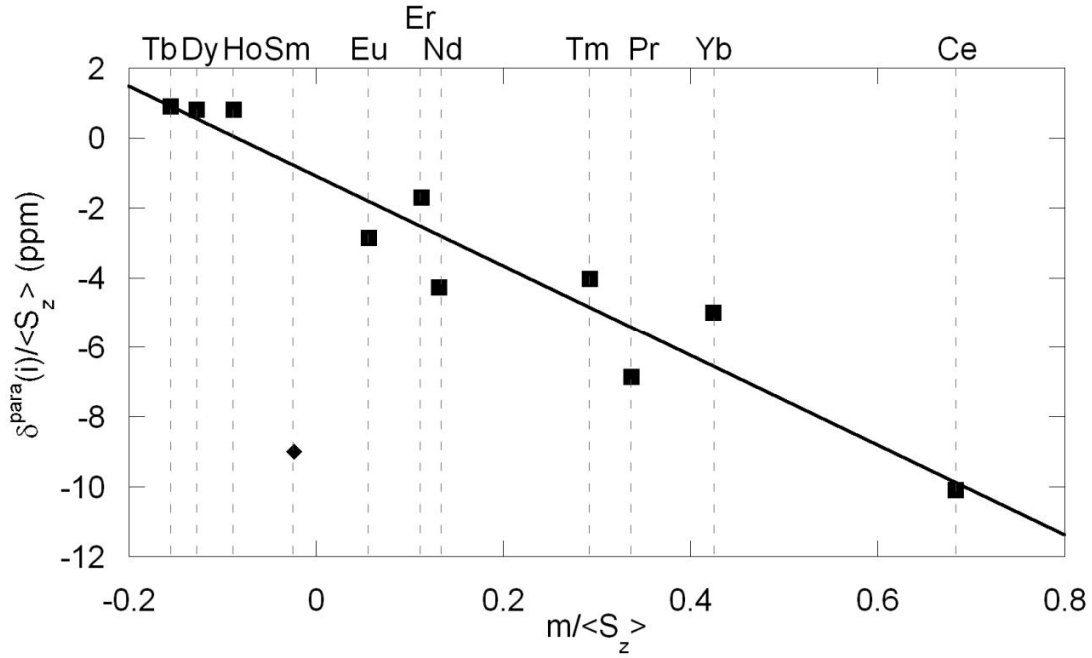

Figure 5.9 Modified Reilley plot for H3 in the series of cryptates depicted in Figure 5.5 after the treatment proposed.

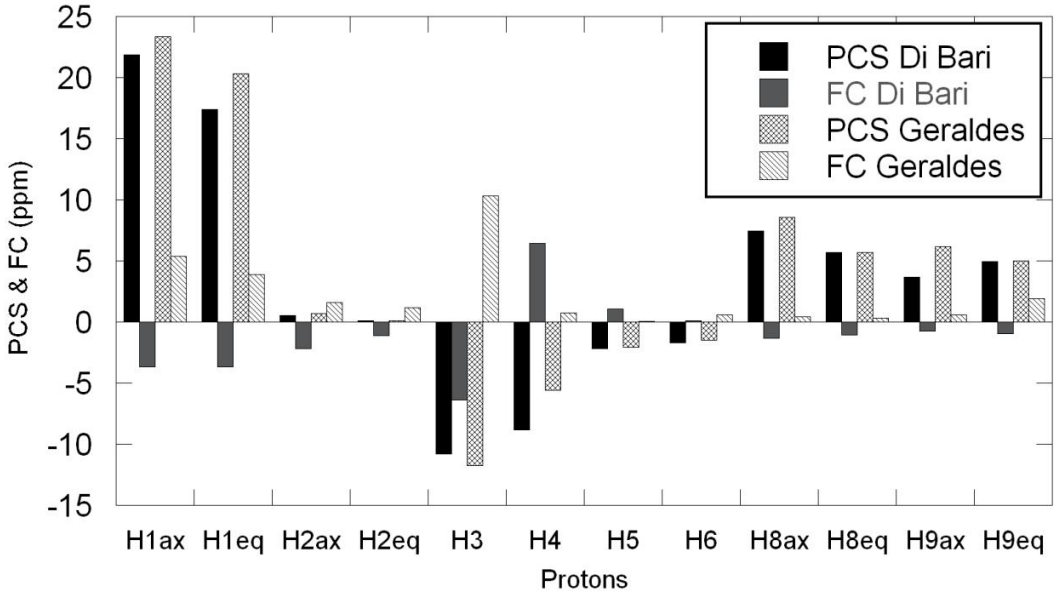

Figure 5.10 Comparison between PCS and FC for PR cryptate, calculated according to our method and extrapolated from the data of Ref. [20]

5.2.3.3 Saà's Binolam complexes

At first sight, the complexes shown in Figure 5.11, introduced by Saá,[30–33] are very similar to the well known Shibasaki's heterobimetallic systems treated below. The difference consists of the incorporation of a Brønsted base proximal to the naphthol hydroxyl. As a consequence, complex formation does not require the treatment with a base, which is a necessary step in Shibasaki's systems, and the result is a set of alkali metal-free (monometallic) compounds, displaying completely different structural and chemical properties.[33,46-47] The only system which led to crystals amenable for XRD was the Sc complex, while heavier elements were reluctant to crystallize.

The accurate analysis of paramagnetic shifts for Pr, Nd and Yb complexes unambiguously demonstrated isostructurality along the series, at least in the sense that the geometrical factors $G_{Ln}(i)$ are equal.[48] The existence of a dynamic hydration equilibrium becomes apparent through very simple experiments, where the sample water content is changed: the paramagnetic shifts of all nuclei are water sensitive to a more or less marked extent, as a function of Ln. One observes greater variations of the ^{1}H shifts for Pr and Nd Binolam, and much smaller for the Yb derivative. Thus, this system falls very obviously into the case depicted in Eq. (5.34), i.e. one set of $G_{Ln}(i)$, but water-dependent *D*.

Linearity of the plots $\delta_{Ln}^{para}(i)$ vs. $\delta_{Yb}^{para}(i)$ was already reported in Ref. [48], where it was also observed that the slopes m_{Ln} are very far from what was expected from Bleaney's factors. Accordingly, separation of FC and PCS cannot be attempted by means of the standard Reilley method but can be achieved successfully by our two-lanthanides method, through eqs. (5.40) and (5.41), with the results reported for the Pr–Nd pair in Table 5.8 and for the Pr–Yb one in Table 5.9.

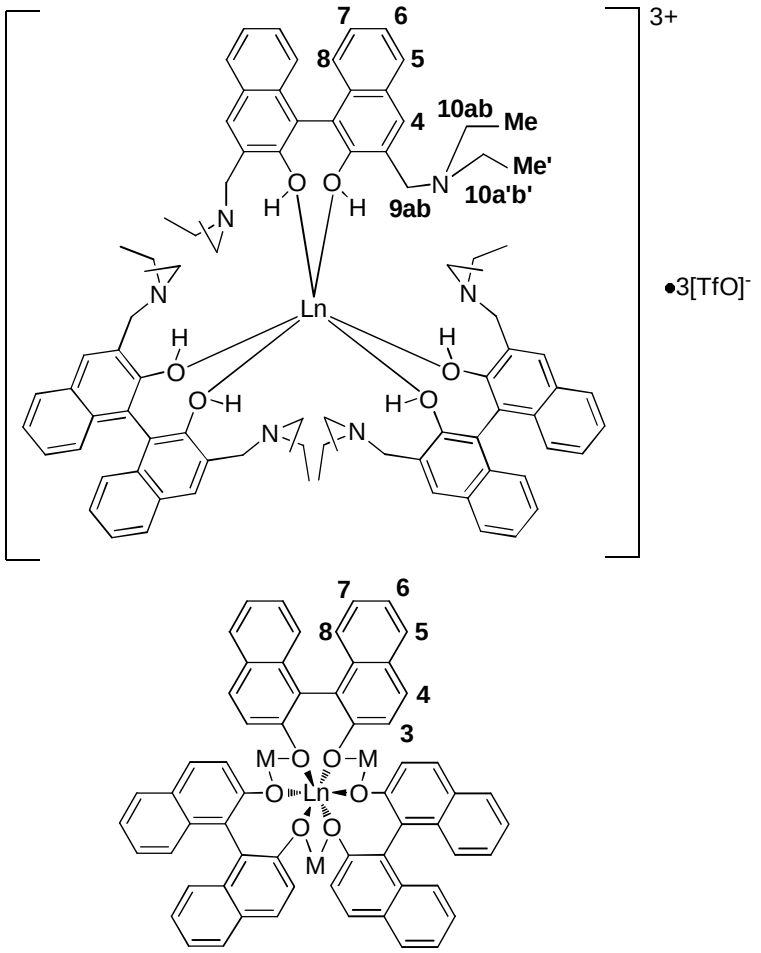

Figure 5.11

Table 5.8 Separation of PCS and FC according to the two-lanthanides method for Ln Binolam for the couple Pr–Nd. Para, PCS and FC values are in ppm units.

	Pr			Nd		
Protons	**Para**	**PCS**	**FC**	**para**	**PCS**	**FC**
4	-0.76	-0.81	0.05	1.05	0.97	0.08
5	-0.49	-0.44	-0.05	0.46	0.53	-0.07
6	-0.33	-0.25	-0.08	0.17	0.30	-0.13
7	-0.19	-0.27	0.08	0.45	0.33	0.12
8	-0.67	-0.76	0.09	1.04	0.91	0.13
9a	-1.12	0.03	-1.15	-1.77	-0.03	-1.74
9b	-2.06	-1.33	-0.73	0.49	1.59	-1.10
10a	1.84	1.89	-0.05	-2.35	-2.27	-0.08
10b	1.54	1.51	0.03	-1.78	-1.82	0.04
10a'	0.33	0.44	-0.11	-0.69	-0.53	-0.16
10b'	0.58	0.42	0.16	-0.26	-0.50	0.24
Me	0.72	0.59	0.13	-0.52	-0.71	0.19
Me'	0.54	0.57	-0.03	-0.73	-0.68	-0.05

Table 5.9 Separation of PCS and FC according to the two-lanthanides method for Ln Binolam for the couple Pr–Yb. Para, PCS and FC values are in ppm units.

	Pr			Yb		
Protons	**Para**	**PCS**	**FC**	**para**	**PCS**	**FC**
4	-0.76	-0.92	0.16	-4.52	-4.38	-0.14
5	-0.49	-0.52	0.03	-2.51	-2.48	-0.03
6	-0.33	-0.39	0.06	-1.92	-1.87	-0.05
7	-0.19	-0.31	0.12	-1.57	-1.47	-0.10
8	-0.67	-0.97	0.30	-4.88	-4.62	-0.26
9a	-1.12	-0.91	-0.21	-4.16	-4.34	0.18
9b	-2.06	-1.51	-0.55	-6.72	-7.20	0.48
10a	1.84	1.77	0.07	8.38	8.44	-0.06
10b	1.54	1.63	-0.09	7.82	7.74	0.08
10a'	0.33	0.64	-0.31	3.33	3.06	0.27
10b'	0.58	0.55	0.03	2.61	2.63	-0.02
Me	0.72	0.62	0.10	2.88	2.96	-0.08
Me'	0.54	0.82	-0.28	4.13	3.89	0.24

We can appreciate the consistency of the FC terms calculated for different Ln and also that they are small, on account of the limited possibility of delocalization of unpaired spin density over the moderately large ligand.

5.2.3.4 Shibasaki's heterobimetallic catalysts

Shibasaki introduced a class of C_3-symmetric Ln complexes based on binaphtholate (hereafter Binolate) as the ligand, which raised a great interest because of their properties as enantioselective catalysts in a number of organic reactions (Figure 5.11).[49] As for many other catalysts, the possibility of coordination of ancillary ligands is of prime importance, since this dynamic binding is at the basis of substrate activation.

The complexes of formula $M_3Ln(Binolate)_3$ (M = Li, Na, K) display a pinwheel structure, which has been investigated in great detail both in solution and in the solid state.[50] In the latter case, single crystal XRD demonstrates that early elements provide hydrated complexes, while late elements yield anhydrous ones. Notably, for Eu, both forms have been reported. In solution, the investigation into hydration number is more difficult and only indirect proofs have been provided. By two different synthetic procedures, Aspinall *et al*. [51] and Walsh *et al.* [52] obtained two completely different sets of ^{1}H NMR data for what is apparently the very same complex: $Li_3Eu(Binolate)_3$. This must be attributed to the different extents of hydration in the two compounds, since in only one case (Aspinall) was the sample obtained in rigorously water-free conditions. Interestingly, no-one reports on the existence of two sets of signals for hydrated and anhydrous forms: we must conclude that this system falls into the fast exchange regime, as envisaged in Eqs. (5.28)–(5.44) and that the Reilley analysis would lead to inconsistent results.

Unlike in the cases discussed above and notwithstanding the large interest and the numerous reports on heterobimetallic complexes, in the literature we were able to find ^{1}H shifts only for a limited number of

lanthanides. Usually the water content of the various samples is difficult to estimate and moreover, they refer to different alkali metals M.

As we said, Pr and Yb surely display opposite behaviour: one should mostly yield the water-capped complexes, the other should provide the anhydrous ones. We proceed through our modified method: first of all, we plot all the paramagnetic shifts for $Li_3Pr(Binolate)_3$vs. those of $Li_3Yb(Binolate)_3$, and we obtain the slope

$$m_{Pr,Yb} = -0.23 \tag{5.49}$$

which is far from the ideal value of $m^{ideal} = -0.52$ (see Eq. (5.34)), on account of the different hydration states of the two species. By application of Eqs. (5.40) and (5.41), we obtain the PCS and FC reported in Table 5.10. We can appreciate that the FC terms are small for most nuclei.

In the same way, we can treat both sets of data for $Li_3Eu(Binolate)_3$, as reported by Aspinall and Walsh, which are very different, comparing their paramagnetic shifts with those of $Li_3Yb(Binolate)_3$ method and we find

$$\begin{aligned} m_{Eu\ Aspinall,Yb} &= 0.07 \\ m_{Eu\ Welsh,Yb} &= 0.22 \end{aligned} \tag{5.50}$$

This allows us to use the two-lanthanides method and to obtain the PCS and FC reported in Table 5.11. A general comment for all these cases is that the FC terms are in any case small for most nuclei.

Table 5.10 Separation of PCS and FC according to the two-lanthanides method for $Li_3Pr(Binolate)_3$ vs. those of $Li_3Yb(Binolate)_3$. Para, PCS and FC values are in ppm units.

	Li_3 Pr (Binolate)$_3$			**Li_3 Yb (Binolate)$_3$**		
Protons	**para**	**PCS**	**FC**	**para**	**PCS**	**FC**
3	-18.51	-19.29	0.78	83.20	83.88	-0.68
4	-4.03	-3.68	-0.35	16.29	15.98	0.31
5	0.86	-0.58	1.44	1.26	2.51	-1.25
6	1.44	0.85	0.59	-4.21	-3.70	-0.51
7	2.97	1.66	1.31	-8.37	-7.23	-1.14
8	6.64	4.61	2.03	-21.82	-20.05	-1.77

These heterobimetallic systems feature another aspect, which is particularly interesting for our analysis. The alkali metal has the effect of modulating the charge on the Binolate oxygen atoms and consequently of changing the crystal field parameters, while leaving the overall geometry of the various complexes unchanged, as observed by Aspinall and subsequently confirmed.[50,51] This means that the corresponding nuclei on complexes with different M and/or different hydration numbers have the same set of $G(i)$. This observation prompted us to put forward another more adventurous attempt: using sets of data of heterogeneous systems, i.e. separate PCS and FC from systems which differ not only in the Ln but also in the alkali metal M. Accordingly, we pursued the two-lanthanides method on the data of $Li_3Pr(Binolate)_3$ vs. of $Na_3Yb(Binolate)_3$.[50] The results

are reported in Table 5.12 and compare very well to those of Table 5.10: the PCS and FC of $Li_3Pr(Binolate)_3$ separated taking the two Yb compounds as the reference are practically identical.

Table 5.11 Separation of PCS and FC according to the two-lanthanides method for the two sets of data relative to the formula $Li_3Eu(Binolate)_3$ taken from Ref. [52] (Walsh) and from Ref. [51] (Aspinall), vs. those of $Li_3Yb(Binolate)_3$. Para, PCS and FC values are in ppm units.

	Eu Walsh			Eu Aspinall		
Protons	**para**	**PCS**	**FC**	**para**	**PCS**	**FC**
3	17.91	18.33	-0.42	5.17	6.09	-0.92
4	3.10	3.61	-0.51	1.62	1.18	0.44
5	0.58	0.26	0.32	1.83	0.06	1.77
6	-0.72	-0.94	0.22	1.23	-0.34	1.57
7	-3.05	-1.77	-1.28	-0.92	-0.61	-0.31
8	-7.16	-4.67	-2.49	-4.66	-1.54	-3.12

Table 5.12 Results of the separation of PCS and FC according to the two-lanthanides method mixing data relative to two different alkali metals in heterobimetallic systems: $Li_3Pr(Binolate)_3$ vs. of $Na_3Yb(Binolate)_3$. Para, PCS and FC values are in ppm units.

	$Li_3Pr(Binolate)_3$			$Na_3Yb(Binolate)_3$		
Protons	**para**	**PCS**	**FC**	**para**	**PCS**	**FC**
3	-18.51	-19.87	1.36	36.3	37.48	-1.18
4	-4.03	-3.34	-0.69	6.9	6.30	0.60
5	0.86	-0.64	1.50	-0.1	1.21	-1.31
6	1.44	1.03	0.41	-2.3	-1.94	-0.36
7	2.97	1.00	1.97	-3.6	-1.88	-1.72
8	6.64	3.16	3.48	-9	-5.97	-3.03

5.2.4 The special case of DOTMA

The most involved system we wish to treat is a complete lanthanide series of Ln DOTMA,[53,54] a chiral DOTA analogue (DOTMA = 1,4,7,10-tetrakis(R)-methylacetic acid-1,4,7,10-tetraazacyclododecane), the all-R derivative structure is reported in Figure 5.12.

As seen in Chapter 4, Gd DOTA is one of the most widely used MRI contrast agents and this clearly demonstrates that hydration/dehydration equilibrium is a key feature. Water exchange has been studied with great accuracy for this parent compound and for a number of closely related ones.[55] The dynamical stereochemistry of the cyclen system is extremely fascinating: the macrocycle can easily invert, with the interconversion of the two types of carbon atoms (at the *corner*, or at the *side*, Figure 5.13). This equilibrium could be described as a $(\lambda\lambda\lambda\lambda) \rightleftarrows (\delta\delta\delta\delta)$ or a $g^- \rightleftarrows g^+$ interconversion. Moreover, the pendant arms,

involved in the metal center coordination as well, lean from the same side: this concerned arrangement is associated with a positive (clockwise) or a negative (anticlockwise) NCCO dihedral, which gives rise to Λ or Δ coordination (Figure 5.14).

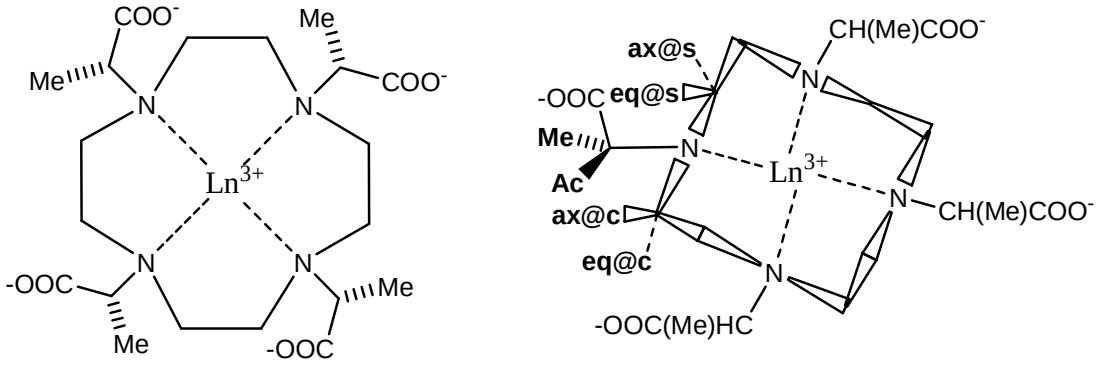

Figure 5.12

The two conformational chirality elements we found, namely, the macrocycle arrangement described through $(\lambda\lambda\lambda\lambda)/(\delta\delta\delta\delta)$ and the side arm orientation, leading to Λ/Δ metal coordination combine to provide four stereoisomers, which are two pairs of enantiomers and otherwise diastereomers. The complete picture of the dynamic processes occurring in Ln DOTA complexes is represented in Figure 5.15.[44,53,56-57] When the helicity of these two elements is the same then the coordination geometry is defined by a monocapped twisted square antiprism (TSAP), when they are opposed by a monocapped square antiprism (SAP). The most prominent structural difference between SA and TSA can be expressed by the angle ϕ between the two squares, defining the bases of the coordination polyhedron as shown in Figure 5.16.[58,59] It is interesting to observe that the degree of van der Waals interactions in the two conformations is comparable, and it would be hard to predict which one is most stable, on simple stereochemical arguments based on the ligand alone.

The structural readjustment, however, has a series of very relevant implication. The two squares (one above Ln, with oxygen atoms at the corner, one below Ln, defined by nitrogen atoms) are linked by the three bonds N-C-C-O, which determines a rigid geometry; consequently, the acetate is more bent for larger ϕ values and this lead these two bases of the antiprism to become nearer. We can deduce that the coordination polyhedron is relatively more compressed for SA and more extended for TSA, as represented in Figure 5.16 and 5.17, as indeed found by inspecting computer optimized and experimental structures for many DOTA-like complexes.[59,60] A further consequence of this geometry is that the bite angle, that is, O-Ln-O with reference to opposed oxygen atoms is wider in SA than in TSA and finally that the former is more open to axial coordination than the latter.[58] A more complete structural picture requires the definition of occupancy of the axial site by water, leading to the formation of 8- or 9-coordinated species. The position of these equilibria and their characteristic rate constants strongly depend on the Ln and on solvent composition and have relevant consequences, for instance in applications for MRI contrast.[15,55,61-63]

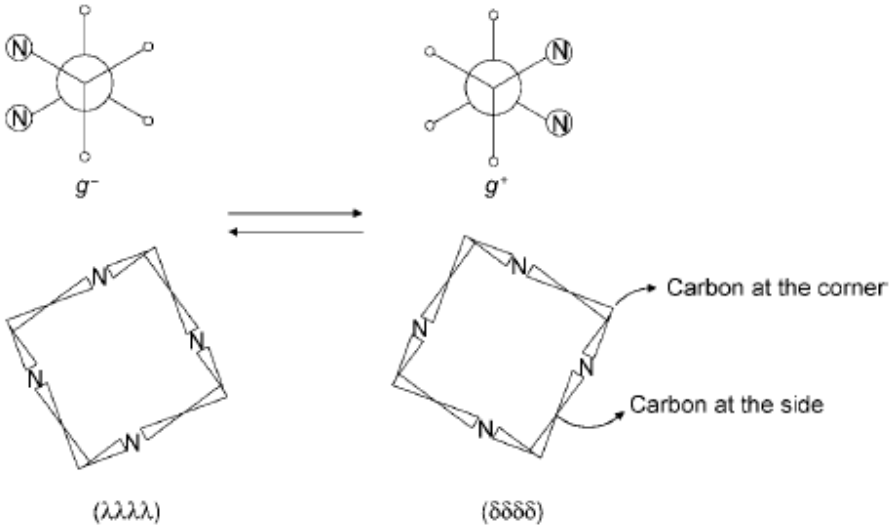

Figura 5.13 Enantiomeric cyclen [3333] ring conformations

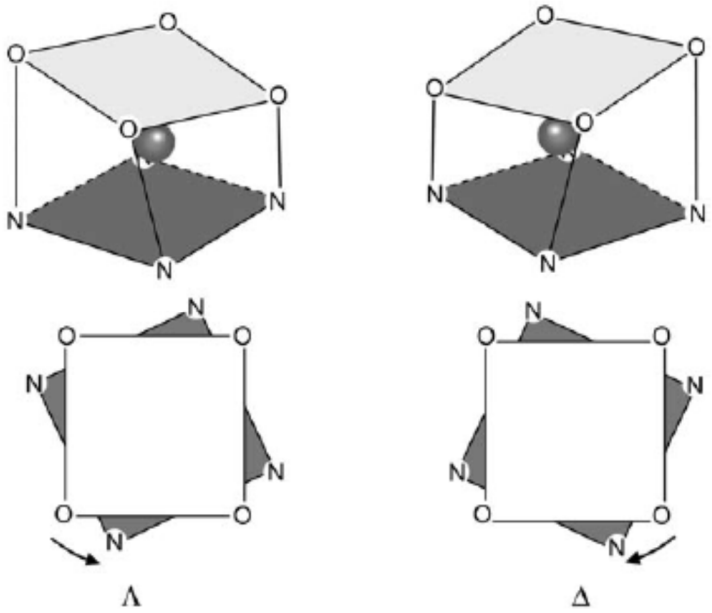

Figure 5.14 Λ and Δ metal coordination

By introducing further chirality elements, for example, through ring carbon substitution or with a chiral group attached at nitrogen, as in case on DOTMA, leads to the formation of diastereomers, where the configurational and conformational chirality elements combine. DOTA and DOTMA are formally very similar, the difference consisting of the fact that one hydrogen atom of the acetate arms of DOTA is substituted with a methyl group in DOTMA, which introduces a further element of chirality.

Although the possible diastereomers are four, just two species in slow exchange, on the paramagnetic NMR scale, are for DOTMA and other analogous derivatives.[53,64-67] From crystal structure and NIR data, it

became clear that the introduction of a substituent on the pendant arm of DOTA chelate introduces control over the orientation of the pendant arm, inhibiting its rotation (Figure 5.16).[65,66,68-69]

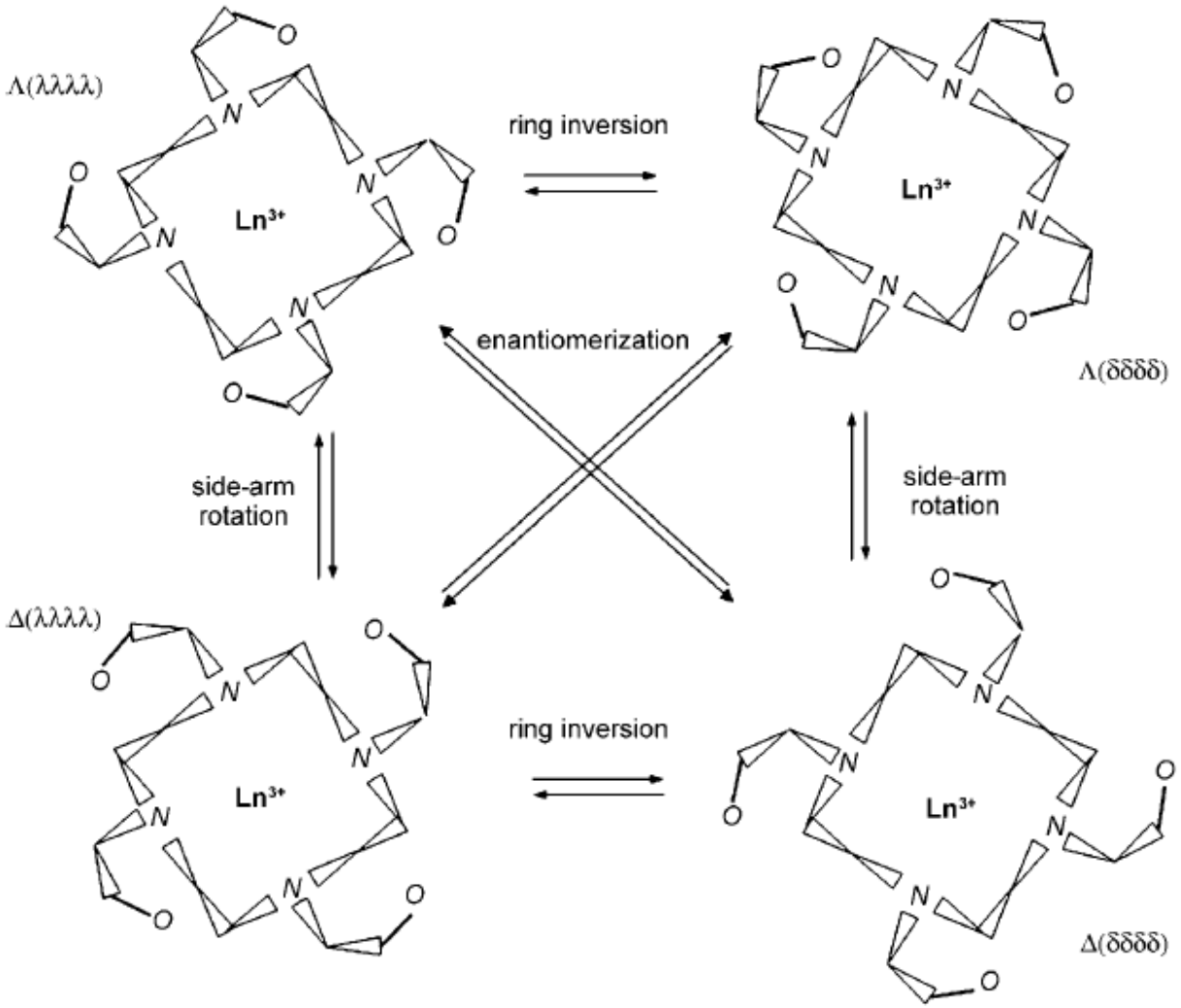

Figura 5.15 Stereochemistry of Ln DOTA. The species across the diagonals are enantiomers, while between top and bottom lines, and left and right columns, there is a conformational diastereomer relation.

The Gd DOTMA system has promising properties as contrast agent, paradoxically not investigated until very recently,[68] more favorable than those of its achiral analogous Gd DOTA. The crystal structure of Gd DOTMA demonstrates that the Gd OH_2 distance is longer in the TSAP isomer than in the SAP. Notably this elongation is not so pronounced in the crystal as in solution, presumably because of the dynamic nature of the solution state measurements. In terms of their use as the basis of MRI contrast agents the elongation of the Gd OH_2 results in water exchange kinetics that are more favorable for Gd DOTMA than Gd DOTA. Gd DOTMA does have one potential advantage over Gd DOTA as an MRI contrast agent, due to its higher kinetic inertness.

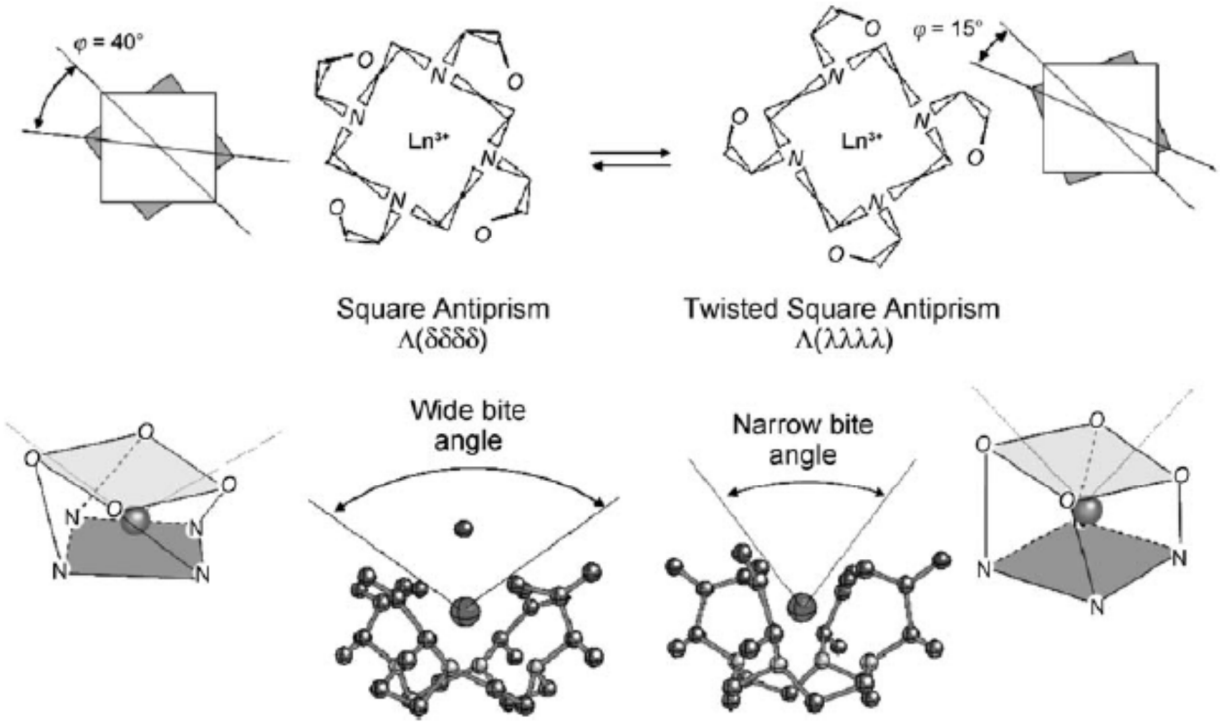

Figure 5.16 Regular and twisted square antiprismatic forms of Ln DOTA. In the bottom line, side views of the two conformations. The SA is more compressed than the TSA, which leads to a wider O-Ln-O angle (bite angle). Consequently, notice the axial coordinating water molecule in the SA form but absent in the TSA (tilt angles are referred to Yb DOTA case).

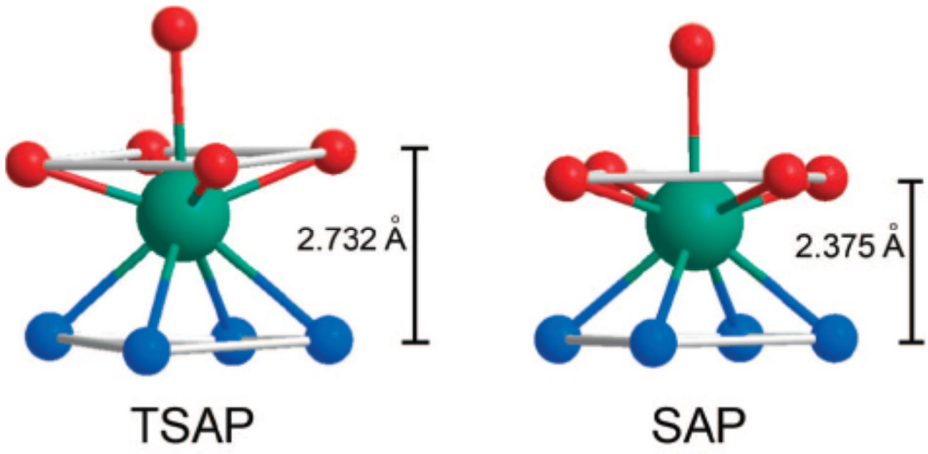

Figure 5.17 Schematic representation of the SAP and TSAP coordination geometries of Ln DOTA, showing only the atoms directly coordinating to the central lanthanide metal ion. The compactness of SAP in comparison to TSAP is pointed out.

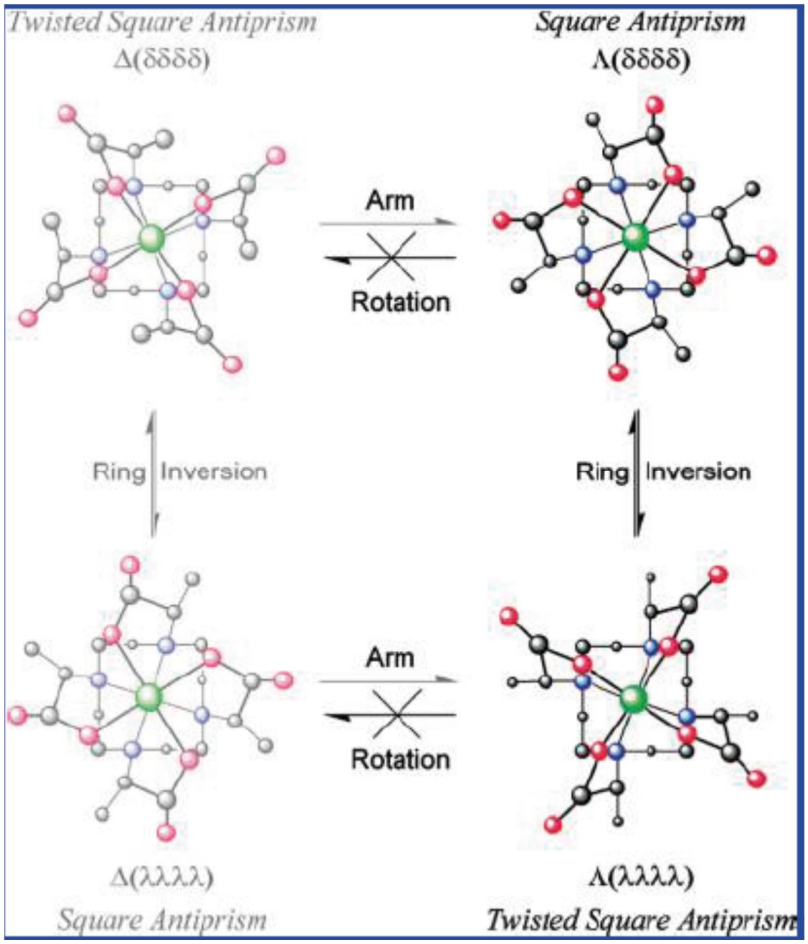

Figure 5.18 Structural isomerism in Gd DOTMA chelates. Four stereoisomeric structures are possible for Gd DOTA, but two of these structures are inaccessible to Gd DOTMA because the arm rotation motion by which they are accessed is 'frozen ' out in this chelate. These stereoisomers are represented by the washed out structure on the left.

Their mole proportion is variable throughout the series (Figure 5.19),[23][69] and also their affinity for water is changeable. The chelates of DOTMA with early Ln^{3+} ions adopt almost exclusively the TSAP isomer in solution. As with other analogous ligands, the SAP isomer becomes increasingly favored as the ionic radius decreases, but this trend reaches a maximum much earlier in the lanthanide series; between Tb^{3+} and Dy^{3+} (~117 pm ionic radius) with never more than ~42% of the chelate as a SAP isomer observed in solution. As the Ln^{3+} ionic radius decreases yet further the TSAP isomer again becomes increasingly. However, in the case of DOTMA by the time we reach the smallest Ln^{3+} ions Yb^{3+} and Lu^{3+} the TSAP isomer is almost the exclusive isomeric form of the chelate in solution. A very striking feature of these molecules is that the PCS of TSAP and of SAP forms are proportional, on account of the practical (accidental) identity of the geometrical factors $G(i)$ for all nuclei.[64, 70] This can be easily demonstrated by plotting the PCS (or even the paramagnetic shifts) of the two forms of the same Ln complex one against the other. Thus, in spite of the great geometrical detail attained by paramagnetic NMR, it may be difficult to recognize if one is dealing with one or the other form, for a new term of this family of compounds. On the other hand, TSAP and SAP feature relevant differences in their ability to

[23] Our data are in agreement with Aime *et al.* [69] although with a slight difference in molar fractions for some lanthanide complexes.

bind water in the first coordination sphere and also in the dynamic exchange of bound and bulk water, which has relevant consequences in MRI.[15,55,61] This is due to the different dihedral between the planes, influencing water coordination, due to the different sterical constriction, with the SAP conformer offering a wider coordination cage, in which the ninth site can be easily occupied by water, or the coordinating solvent. The TSAP conformer can have also a certain degree of hydratation, even though to a lesser extent in comparison to the other stereoisomer. However, due to the more hindered coordination cage of the TSAP conformer, the bond with water is significantly elongated, offering a faster water exchange and consequently higher relaxivity. An empirical correlation has been put forward, by which SA can be expected to give larger paramagnetic shifts compared to TSA: this is based on the empirical evidence of the optical emission band splittings in Eu DOTMA and analogous observed by Dickins *et al.* directly proportional to the B_0^2 term.[71][24] Therefore, very commonly it is enough to observe the difference in the most downfield-shifted signal, relative to the proton in the axial 'at corner ' position,[61,71-72] which amounts to saying that

$$|D^{TSAP}| < |D^{SAP}| \tag{5.51}$$

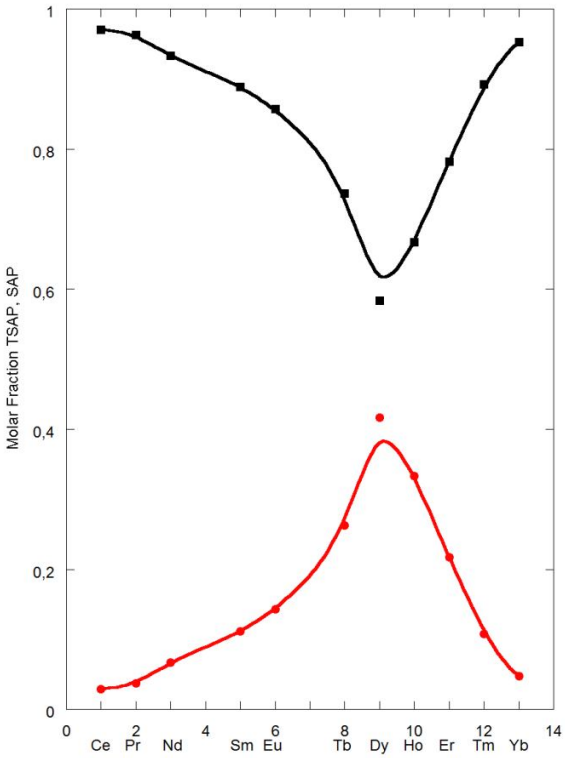

Figure 5.19 Mole fractions of the SAP (circles) and TSAP (squares) isomers of Ln DOTMA chelates as a function of the Ln^{3+} ion.

The only exceptions are Tm and Er DOTMA (Figure 5.20), for the former system an anomalous high crystal field parameter has already been observed in a similar structure complex in the literature.[74] Unfortunately, when only one set of signals is visible in the NMR spectrum the assignment may be less safe. Moreover, predicting

[24] Specifically, the splitting (cm^{-1}) of the magnetic dipole allowed emission transition ($\Delta J = 1$, not affected by the ligand environment) is equal to 0.3 B_0^2.

the prevalence for TSAP or SAP may be very difficult, because of a subtle enthalpy/entropy compensation effect,[56,64] and consequent interplay with even minor solvation or polarizability effects.[72] Even if water coordination in the DOTMA case has been profoundly studied and determined very recently.[69]

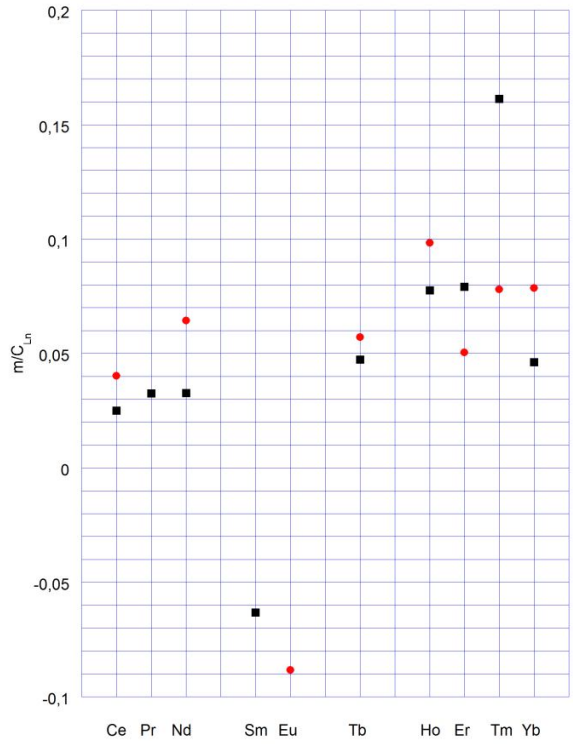

Figure 5.20 m/C_{Ln} ratio for Ln DOTMA, TSAP form (■) and SAP (●) are compared along the series. Data for Yb DOTMA SAP conformer are from ref. [64]

The linear relation between PCS for the two forms, in the context of the present work, calls for another property: to a large extent a plot of $\delta_{Ln1}^{para}(i)$ **vs.** $\delta_{Ln2}^{para}(i)$ will provide a good linear fit not only independent of Ln1 and Ln2, but also independent of the fact that we are dealing with a TSAP or a SAP form.

To some extent, we may say we are in a situation similar to that described above for heterobimetallic catalysts, where we could take advantage of data arising from complexes with different alkali metals.

Separating FC from PCS in DOTMA (as well as in DOTA) is hardly possible by means of the standard Reilley method, because of the combined effect of the SAP/TSAP and of the hydration/dehydration equilibria. Nonetheless, we obtained excellent results using our modified method.

First of all, we choose as the reference spectrum the major form of Yb DOTMA (which is TSAP) and we plot all the shifts of both major and minor forms of the various Ln DOTMA (Table 5.13) vs. this set of data (the plot is shown in Figure 5.21).

As we see from Table 5.14, the correlation coefficients are all fully satisfactory. The slopes of these linear fits can be used to build one modified Reilley plot for each proton (Figure 5.22), by taking into account simultaneously all of the available data for Ln DOTMA in both major and minor forms and to achieve separation of PCS and FC, as shown in Table 5.15.

Table 5.13 Experimental ^{1}H NMR shifts (ppm) of Ln DOTMA (major and minor forms).

	La	Lu	Ce		Pr	Nd		Sm	Eu		Tb		Ho		Er		Tm		Yb
Protons			**MAJ**	**min**	**MAJ**	**MAJ**	**min**	**MAJ**	**MAJ**	**min**	**MAJ**	**min**	**MAJ**	**min**	**MAJ**	**min**	**MAJ**	**min**	**MAJ**
Ax@s	2.83	3.01	-13.35	-23.74	-33.00	-12.70	-26.70	-0.21	20.00	40.75	-367.20	-464.60	ND	ND	211.00	122.00	ND	327.00	96.43
Eq@s	2.54	2.69	0.91	ND	1.14	4.46	1.70	ND	-3.50	1.14	-85.60	-101.30	-39.22	-60.73	21.00	18.70	69.40	61.80	17.68
Eq@c	2.78	2.69	0.17	-2.37	-1.44	7.02	ND	ND	-8.83	-23.83	-88.00	-108.50	-43.39	-62.70	40.80	32.70	93.80	82.00	11.98
M	1.25	1.20	3.60	ND	6.69	3.70	ND	1.75	-1.74	-3.95	61.60	67.77	35.77	42.46	-43.70	-28.00	-104.00	-67.00	-14.68
Ax@c	3.38	3.01	7.80	10.43	14.59	8.11	10.30	3.39	-4.01	-5.53	136.09	154.60	82.14	96.11	-106.50	-69.30	-255.90	-163.00	-21.53
Ac	3.91	3.91	14.83	21.72	29.17	13.41	23.65	6.63	-8.41	-10.40	301.60	344.10	ND	ND	-211.00	-148.00	ND	-346.00	-69.94

We can appreciate that the quality of this separation is excellent, as measured by the diff parameter of Eq. (5.48) for Yb DOTMA and also by the fact that the trend of FC follows reasonably closely the one found for the correspondent protons in Ln *N,N*-diethyl-DOTAM.

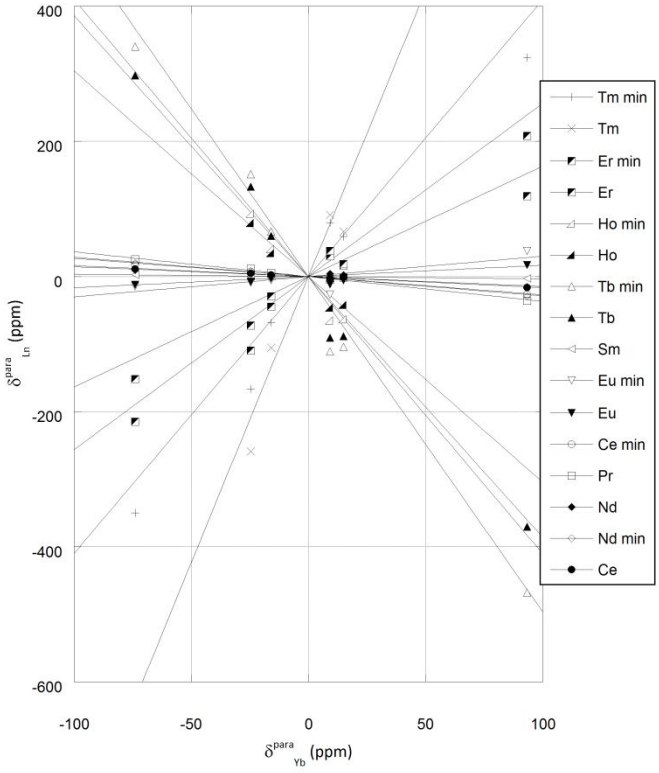

Figura 5.21 $\boldsymbol{\delta^{para}_{Ln}(i)}$ vs. $\boldsymbol{\delta^{para}_{Yb}(i)}$ plot of the DOTMA protons for the Ln complexes.

Table 5.15 Slopes (equal to the PCS of Yb DOTMA), intercepts and correlation coefficients of modified Reilley plots for all protons in Ln DOTMA, obtained by taking the major form of Yb DOTMA as the reference spectrum; FC terms for Yb DOTMA calculated according to Eq. (5.17). The last column displays the quality parameters diff as in Eq. (5.48) for Yb DOTMA. PCS, FC and diff values are in ppm units.

Protons	M	Q	R	diff
Ax@s	89.12	0.23	0.99	4.90
Eq@s	10.655	0.51	0.94	5.66
Eq@c	13.14	0.23	0.95	-3.25
M	-13.65	0.18	0.99	-1.76
Ax@c	-30.83	0.34	0.98	7.17
Ac	-79.54	-0.40	0.99	4.65

Table 5.14 Slopes and correlation coefficients for linear fits (forced through the origin) for $\delta^{para}_{Ln1\ maj/min}(i)$ vs. $\delta^{para}_{Yb\ maj}(i)$

Lanthanide	m	R
Ce	-0.16	0.99
Ce min	-0.26	0.97
Pr	-0.37	0.99
Nd	-0.15	0.92
Nd min	-0.29	0.98
Sm	-0.03	0.98
Eu	0.17	0.74
Eu min	0.30	0.75
Tb	-4.10	0.99
Tb min	-4.96	0.99
Ho	-3.04	0.98
Ho min	-3.86	0.96
Er	1.63	0.98
Er min	2.56	0.96
Tm	8.47	0.98
Tm min	4.10	0.95

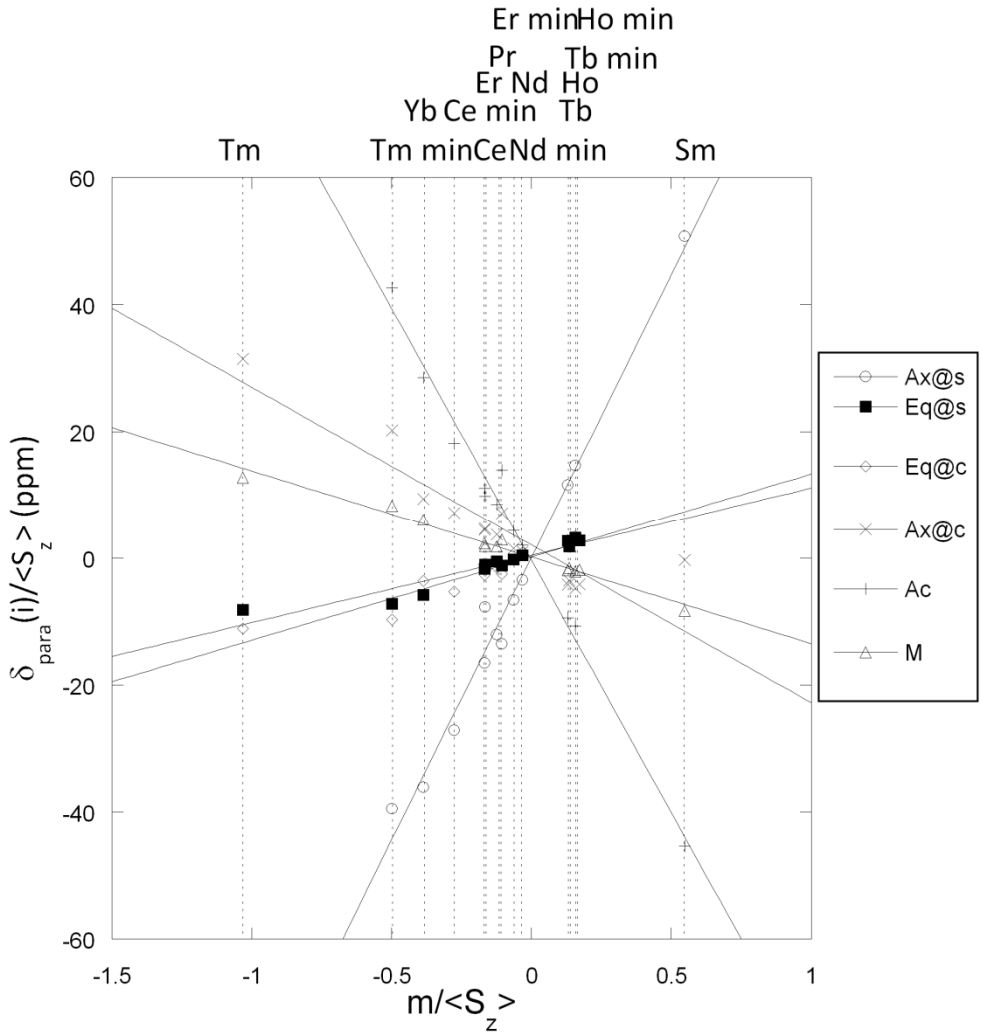

Figure 5.22 Plots of $\boldsymbol{\delta_{Ln}^{para}(i)/\langle S_z\rangle_{Ln}}$ vs. $\mathbf{m_{Ln}/\langle S_z\rangle_{Ln}}$ for Ln DOTMA, having taken Yb DOTMA as the reference compound for calculating m_{Ln}.

References

[1] I. Bertini, C. Luchinat, G. Parigi, R. Pierattelli, *Dalton Trans.* **2008**, 3782.

[2] I. Bertini, C. Luchinat, *Coord. Chem. Rev.* **1996**, *150*, 1.

[3] J.A. Peters, J. Huskens, D.J. Raber, *Prog. NMR. Spectrosc.* **1996**, *28*, 283.

[4] L. Di Bari, P. Salvadori, *Coord. Chem. Rev.* **2005**, *249*, 2854.

[5] G. Pintacuda, M. John, X.C. Su, G. Otting, *Acc. Chem. Res.* **2007**, *40*, 206.

[6] X.C. Su, G. Otting, *J. Biomol. NMR,* **2010**, *46*, 101.

[7] S. Cotton, *Lanthanide and Actinide Chemistry*, **2006,** John Wiley & Sons Ltd.: Chichester.

[8] J. Reuben, *J. Magn. Reson.* **1982**, *50*, 233.

[9] C.N. Reilley, B.W. Good, *Anal. Chem.* **1975**, *47*, 2110.

[10] R.S. Dickins, S. Aime, A.S. Batsanov *et al. J. Am. Chem. Soc.* **2002**, *124*, 12697.

[11] R.S. Dickins, A. Badari, *Dalton Trans.* **2006**, 3088.

[12] M. Shibasaki, N. Yoshikawa, *Chem. Rev.* **2002**, *102,* 2187.

[13] J.-C.G. Bünzli, C. Piguet, *Chem. Soc. Rev.* **2005**, *34*, 1048.

[14] P. Caravan, *Chem. Soc. Rev.* **2006**, *35*, 512.

[15] M. Woods, E.W.C. Donald, A.D. Sherry, *Chem. Soc. Rev.* **2006**, *35,* 500.

[16] I. Persson, P. D'Angelo, S. De Panfilis, M. Sandstrom, L. Eriksson, *Chem.-Eur. J.* **2008**, *14*, 3056.

[17] J. K. A. Geschneidner, J.C.G. Bünzli, V.K. Pecharsky (Eds.) *Handbook on the Physics and Chemistry of Rare Earths*, **2003**, Elsevier:Amsterdam, pp. 353.

[18] S. Rigault, C. Piguet, *J. Am. Chem. Soc.* **2000**, *122*, 9304.

[19] S. Di Pietro, S. Lo Piano, L. Di Bari, *Coord. Chem. Rev.* **2011**, *255*, 2810.

[20] C. Platas, F. Avecilla, A. de Blas *et al. Inorg. Chem.* **1999**, *38*, 3190.

[21] R.J. Abraham, R. Koniotou, F. Sancassan, *J. Chem. Soc. Perkin Trans. 2,* **2002**, 2025.

[22] L. Di Bari, M. Lelli, P. Salvadori, *Chem. Eur. J.* **2004**, *10*, 4594.

[23] R. M. Golding and M. P. Halton, *Aust. J. Chem.* **1972**, *25*, 2577.

[24] J. H. Forsberg, Gschneidner, K. A., and L. Eyring, Eds. *Handbook on the Physics and Chemistry of Rare Earths*, **1996**, Elsevier:Amsterdam, p 1.

[25] M. D. Kemple, B. D. Ray, K. B. Lipkowitz *et al. J. Am. Chem. Soc.* **1988**, *110*, 8275.

[26] M. R. Wilcott, R. E. Lenkinski and R. E. Davis, *J. Am. Chem. Soc.* **1972**, *94*, 1742.

[27] I. Bertini, M. B. L. Janik, Y-.M. Lee, C. Luchinat, A. Rosato, *J. Am. Chem. Soc.* **2001**, *123*, 4181.

[28] J. H. Forsberg, R. M. Delaney, Q. Zhao, G. Harakas and. R. Chandran, *Inorg. Chem.* **1995**, *34*, 3705.

[29] J. Lisowski, J. L. Sessler and T. D. Mody, *Inorg. Chem.* **1995**, *34*, 4336.

[30] J. Reuben and G. A. Elgavish, *J. Magn. Res.* **1980**, *39*, 421.

[31] W. deW. Horrocks Jr. and J. P. Sipe, *Science*, **1972**, *177*, 994.

[32] A. D. Sherry, C. F. G. C. Geraldes, J.-C. G. Bünzli and G. Choppin, Eds. *Lanthanide Probes in Life, Chemical and Earth Sciences, Theory and Practice*, **1989**, Elsevier:Amsterdam, Ch. 4.

[33] A. J. Freeman, R. E. Watson, *Phys. Rev. B.* **1962**, *127*, 2058.

[34] C. Görller-Walrand and K. Binnemans; K. A. Gschneidner, and L. Eyring, Eds. *Handbook on the Physics and Chemistry of Rare Earths*, **1996**, Elsevier:Amsterdam, ch. 155, p 121.

[35] (a) T. A. Hopkins, J. P. Bolender, D. H. Metcalf and F. S. Richardson, *Inorg. Chem.* **1996**, *35*, 5356 and references therein. (b) T. A. Hopkins, D. H. Metcalf and F. S. Richardson, *Inorg. Chem.* **1998**, *37*, 1401 and references therein.

[36] S. Spiliadis, and A. A. Pinkerton, *J. Chem. Soc. Dalton Trans.* **1982**, p. 1815.

[37] C. F. G. C. Geraldes, , S. Zhang, C. Platas *et al. J. Alloys and Compds* **2001**, *323-324*, 824.

[38] N. Ouali, B. Bocquet, S. Rigault, P.-Y. Morgantini, J. Weber and C. Piguet*, Inorg. Chem.* **2002**, *41*, 1436.

[39] Jr. W. deW. Horrocks, J. P. Sipe, *Science*, **1972**, *177*, 994.

[40] (a) N. Ouali, J.-P. Rivera, N. Chapon, *Inorg. Chem.* **2004**, *43*, 1517; (b) E. Terrazzi, J.-P. Rivera, N. Ouali, *Magn. Res. Chem.* **2006**, *44*, 539.

[41] L. Di Bari, G. Pintacuda, P. Salvadori, R.S. Dickins, D. Parker, *J. Am. Chem. Soc.* **2000**, *122*, 9257.

[42] A.G. Martynov, Y.G. Gorbunova, *Polyhedron* **2010**, *29*, 391.

[43] G. Cucinotta, M. Perfetti, J. Luzon, M. Etienne, P.-E. Car, A. Caneschi, G. Calvez, K. Bernot, and R. Sessoli, *Angew. Chem. Int. Ed.* **2012**, *51*, 1606.

[44] S. Aime, M. Botta, G. Ermondi, *Inorg. Chem.* **1992**, *31*, 4291.

[45] J.M. Saá, F. Tur, J. Gonzalez, M. Vega, *Tetrahedron Asymmetr.* **2006**, *17*, 99.

[46] F. Tur, J.M. Saá, *Org. Lett.* **2007**, *9*, 5079.

[47] J.M. Saá, F. Tur, J. González, *Chirality* **2009**, *21*, 836.

[48] L. Di Bari, S. Di Pietro, G. Pescitelli, F. Tur, J. Mansilla, J. M. Saa*, Chem. Eur. J.* **2010**, *16*, 14190.

[49] M. Shibasaki, H. Sasai, T. Arai, *Angew. Chem. Int. Ed. Engl.* **1997**, *36*, 1236.

[50] L. Di Bari, M. Lelli, G. Pintacuda, G. Pescitelli, F. Marchetti, P. Salvadori, *J. Am. Chem. Soc.* **2003**, *125*, 5549.

[51] H.C. Aspinall, J.F. Bickley, J.L.M. Dwyer, N. Greeves, R. V. Kelly and A. Steiner, *Organometallics* **2000**, *19*, 5416.

[52] A.J. Wooten, P.J. Carroll, P.J. Walsh, *J. Am. Chem. Soc.* **2008**, *130*, 7407.

[53] H.G. Brittain, J.F. Desreux, *Inorg. Chem.* **1984**, *23*, 4459.

[54] L. Di Bari, G. Pintacuda, P. Salvadori, *Eur. J. Inorg. Chem.* **2000**, 75.

[55] A. Borel, J.F. Bean, R.B. Clarkson, L. Helm, L. Moriggi, A. D. Sherry and M. Woods*, Chem. Eur. J.* **2008**, *14*, 2658.

[56] S. Aime, M. Botta, M. Fasano *et al. Inorg. Chem.* **1997**, *36*, 2059.

[57] S. Hoeft, K. Roth, *Chem. Ber.* **1993**, *126*, 869.

[58] P. Hermann, J. Kotek, V. Kubicek, I. Lukes, *Dalton Trans.* **2008**, 3027.

[59] F. Benetollo, G. Bombieri, L. Calabi, S. Aime, M. Botta, *Inorg. Chem.* **2003**, *42*, 148.

[60] U. Cosentino, A. Villa, D. Pitea, G. Moro, V. Barone, A. Maiocchi, *J. Am. Chem. Soc.* **2002**, *124*, 4901.

[61] R. E. Mewis, S. J. Archibald, *Coord. Chem. Rev.* **2010**, *254*, 1686.

[62] S. Zhang, M. Merritt, D. E. Woessner, R. E. Lenkinski, A. D. Sherry, *Acc. Chem. Res.* **2003**, *36*, 783.

[63] F.A. Dunand, R.S. Dickins, D. Parker, A.E. Merbach, *Chem. Eur. J.* **2001**, *7*, 5160.

[64] L. Di Bari, G. Pintacuda, P. Salvadori, *Eur. J. Inorg. Chem.* **2000**, *1*, 75.

[65] J. A. K. Howard, A. M. Kenwright, J. M. Moloney, D. Parker, M. Navet and O. Rousseau, *Chem. Commun.* **1998**, *13*, 1381.

[66] M. Woods, S. Aime, M. Botta, *J. Am. Chem. Soc.* **2000**, *122*, 9781.

[67] M. Woods, Z. Kovacs, R. Kiraly, E. Brucher, S. R. Zhang, A. D. Sherry, *Inorg. Chem.* **2004**, *43*, 2845.

[68] M. Lelli, G. Pintacuda, A. Cuzzola, L. Di Bari, *Chirality* **2005**, *17*, 201.

[69] S. Aime, M. Botta, Z. Garda, B. E. Kucera, G. Tircso, V. G. Young, M. Woods, *Inorg. Chem.* **2011**, *50*, 7955.

[70] L. Di Bari, G. Pintacuda, P. Salvadori, *J. Am. Chem. Soc.* **2000**, *122*, 5557.

[71] R. S. Dickins, D. Parker, J. I. Bruce, D. Tozer, *Dalt. Trans.* **2003**, 1264.

[72] T. Mani, G. Tircso, P.Y. Zhao, A. D. Sherry and M. Woods, *Inorg. Chem.* **2009**, *48*, 10338.

[73] L. Di Bari, G. Pescitelli, A.D. Sherry, M. Woods, *Inorg. Chem.* **2005**, *44*, 8391.

[74] J. Ren, A. D. Sherry, *J. Magn. Res.* **1996**, *B111*, 178.

Chapter 6

LIVE: Lanthanide-Induced Vibrational Circular Dichroism (VCD) Enhancement, in solution and solid state

Transition metal containing chiral complexes exhibit some peculiar VCD behaviours which have fascinated researchers in inorganic chemistry and in spectroscopy, due to the presence of low lying electronic states (LLES). In the following Section we will briefly recall the examples in the literature, before starting to analyze the case of lanthanide complexes (Section 6.2).

6.1 VCD Intensity Enhancement in Transition Metal Containing Chiral Complexes

The first case of a VCD spectrum of *d*-transition metal complexes where anomalous intensity were reported are Ni^{2+} and Co^{2+} spartein complexes: Barnett *et al.* found that the C-H stretching region of open-electron shell *d*-spartein complexes, Co(II) and Ni(II), in spite of having a conserved absorption spectrum in comparison to the corresponding close-shell Zn(II) complex, displays an IR-CD spectrum, consisting of an extremely broad feature attributed to ECD, which covers the whole field 3500-2500 cm^{-1} (actually, extending well beyond the upper limit) and of (relatively) strong bands corresponding to C-H vibrational transitions, with an increase of at least one order of magnitude in the VCD intensity.[1] This effect is attributed to a resonance phenomenon, due to the degeneracy of the two processes: a set of discrete vibrational transitions and a very broad electronic one, constituting a quasi continuum. Such a coupling is known as a *Fano*-type mechanism.[2] The VCD spectra of Co and Ni-spartein complexes are *not* correlated to each other, neither to the Zn-analogue (which lacks electronic transitions in the IR).

About 20 years later, Nafie *et al.* [3] re-examined the same case, extending the observation to the mid-IR region below 1000 cm^{-1}, where Co^{2+} and Ni^{2+} ECD can be neglected. In this range, VCD effects are much larger than usual and lose the dispersive character, displaying conventional absorption lineshapes. Once more, there is no correlation between the various VCD spectra, albeit the absorption one is well reproduced for all of them.[3] This result questions the direct *Fano*-type mechanism interpretation, in fact there is no close energy match between low-energy electronic transitions, endowed with large magnetic dipole character called LLES (Low Lying Electronic States) to vibrational states, with electric dipole transition moments. Consequently, Nafie developed a more complete theoretical framework to deal with this coupling also in non-resonant cases, i.e. when the energies of the electronic and vibrational transitions are rather different.

Following Nafie, Eq. 6.1,[4] a magnetic-dipole electronic transition of at the angular frequency Ω will contribute to the total rotational strength of a VCD transition at angular frequency ω with a term weighted by

$$\frac{(\omega + i\gamma)^2}{(\Omega + i\Gamma)^2 - (\omega + i\gamma)^2} \tag{6.1}$$

where γ is the damping factor of the vibrational state while Γ refers to the electronic state.

Eq. (6.1) has the functional form of a complex Lorentzian with both dispersive (real) and non-dispersive (imaginary) parts. It accounts for the enhancement of the magnetic dipole transition moment. Its contribution decreases on increasing the difference $|\Omega - \omega|$, while the damping factors Γ and γ modulate how far the two frequencies can be apart in order to provide observable effects. The LLES of Co^{2+} and Ni^{2+} have very large damping factors Γ, which explains why they extend their effects with $|\Omega - \omega| \gg 1000$ cm^{-1}.

Further examples of transition metal complexes with enhanced VCD involve small ligands, such as azide and cyanide, in metalloproteins, like myoglobin and hemoglobin. VCD associated with the stretching vibrations of these ligands gives rise to enhanced VCD with a ratio of VCD to IR intensity of approximately of 10^{-3}. These vibrational modes gain VCD intensity from their chiral environment and borrow intensity from low-lying *d-d* transitions in the low-spin Fe(II) center of these heme proteins.[5,6]

Also for other *d*-transition metal complexes the effect has been observed, in particular, in a bis-(biuretato) cobaltate (III) coordination compound, Johannessen *et al.* observed VCD a 5-10 fold signal magnitude increase, both in solution and in the solid state.[7] The phenomenon interpretation by the authors is the same as the one developed by Nafie.[4]

6.2 VCD Intensity Enhancement in Lanthanide Containing Chiral Complexes

Despite the potential advantages of the interference mechanism in LLES *d*-transition metal complexes, above all the signal intensity enhancement in VCD acquisitions[25], it has been completely unexploited so far. The reasons for this apartness may be: 1) the enhanced VCD spectra may display dispersive lineshapes[1] and are still poorly amenable to interpretation tools; 2) a precise knowledge of the geometry of paramagnetic *d*-metal adducts in solution may be extremely difficult to achieve; 3) finding an isostructural pair of an 'enhanced' and a 'reference' compound could be not trivial.

Lanthanide chemistry offers a completely different picture. First, as we shall see and discuss in the following, the enhanced VCD spectra display absorptive lineshapes and moreover have Cotton effects which are identical in sign (and to some extent in relative amplitudes) to the reference compound. Second, there are NMR techniques to solve solution structures of paramagnetic Ln complexes with extremely high accuracy.[8,9] Third, lanthanide compounds are generally isostructural throughout the series, possibly with a variation in the coordination of an ancillary ligand like water (see Chapter 5).[9,10] Thus, La^{3+}, Gd^{3+}, Lu^{3+} offer ideal reference compounds in the present context, because they lack LLES.

On the contrary, several lanthanide ions have LLES in the IR. Following Fields and Carnall, we collected the lowest lying ones in Table 6.1. Taking for example Eu^{3+}, we expect the $^7F_1$ state at 360, the $^7F_2$ at 1020 and the $^7F_3$ at 1890 cm^{-1} above the fundamental state $^7F_0$. Consequently we have the electronic transition $^7F_0 \rightarrow {}^7F_2$ at about 1000 cm^{-1}, the $^7F_0 \rightarrow {}^7F_3$ at about 1900 cm^{-1} and the $^7F_1 \rightarrow {}^7F_3$ at 1500 cm^{-1} (approximating

[25] As already seen in Chapter 3, the technique suffers of a certain low S/N ratio, due to the phenomenon weakness (usually below 10^{-4} of absorption), therefore a signal enhancement would be very useful in order to offset this limitation.

wavenumbers to 100 cm^{-1}). Crystal field removes the degeneracy of *J*-multiplets and this gives rise to manifolds of lines around the above mentioned frequencies. The 4*f*-orbitals are very efficiently shielded by the frontier orbitals of Ln^{3+}, with principal quantum numbers 6 and 5, to which they are poorly mixed. This ensures that: 1) crystal field interaction is small; 2) the lifetimes of excited states are long and consequently the electronic damping factors are small, due also to the fact that *f-f* transitions are forbidden according to *Laporte* rules (See Chapter 1).

Table 6.1 Energy levels (cm^{-1}) of the first excited states of Ln^{3+} ions

Lanthanide	Ce[1]	Pr[2]	Nd[2]	Sm[2]	Eu[3]	Tb[4]	Dy[2]	Ho[2]	Er[2]	Tm[2]	Yb[1]
E_1 (cm^{-1})	2250	2160	1880	1040	380	2115	3465	5020	6490	5730	10140
E_2 (cm^{-1})		4300	3900	2250	1040	3270					
E_3 (cm^{-1})		5000		3570	1880	4415					
E_4 (cm^{-1})				4960	2870	4950					
E_5 (cm^{-1})					3910						
E_6 (cm^{-1})					4980						

(1) F. S. Richardson, M. S. Reid, J. J. Dallara, R. D. Smith, *J. Chem. Phys.* **1985**, *83*, 3813. (2) W. T. Carnall, P. R. Fields, K. Rajnak, *J. Chem. Phys.* **1968**, *49,* 4424. (3) W. T. Carnall, P. R. Fields, K. Rajnak, *J. Chem. Phys.* **1968**, *49,* 4447. (4) W. T. Carnall, P. R. Fields, K. Rajnak, *J. Chem. Phys.* **1968**, *49,* 4450.

We shall describe a Lanthanide Induced VCD Enhancement and dub it by the acronym LIVE.

At least a couple of precedents can be found in the literature. In the first comprehensive report on VCD, a remarkable intensity difference was observed on the C-H stretching for Pr and Eu camphorate complexes ($Ln(tfc)_3$). Unfortunately, the phenomenon was not interpreted in depth.[11] More recently, a VCD variation on the specific nucleus (Ln=La, Eu, Yb) in another set of camphorates was observed, but once again not explained.[12]

In the following Sections the LIVE phenomenon will be examined for series of well-characterized complexes: Ln DOTMA (whose solution structures have been described in detail in Section 5.2.4), Ln DOPhA and the heterobimetallic system $Cs[Ln(hbfc)_4]$, shown in Figure 6.1, all endowed with C_4-symmetry. Some features of the VCD of the hbfc complexes have already been described by Kaizaki *et al*.[12]

6.2.1 Lanthanide-Induced VCD Enhancement in Ln DOTMA

With all the above premises, we can now face the analysis of the IR CD of the set of Ln DOTMA complexes in D_2O.[13,14] The individual spectra can be found in the Appendix 1 pp.120-126, with the corresponding absorption spectra, while in the main text we shall deal only with a selection of the most significant ones. The complete series of spectra is represented in Figure 6.2 (with L is labelled the spectrum of the free ligand).

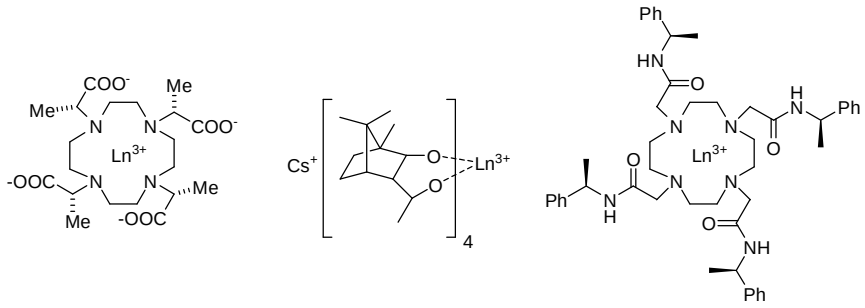

(*R*,*R*,*R*,*R*)-Ln DOTMA (*S*,*S*,*S*,*S*)-Ln DOPhA

1 **2** 3

Figure 6.1

The much lower intensity of the spectrum of the free ligand is due to its floppy conformation in solution, in contrast with the well defined one, adopted by Ln DOTMAs, as confirmed by NMR experiments (see Section 5.2.4) as well.

La^{3+}, Lu^{3+} and Gd^{3+} lack LLES, because they have empty, full and semiempty *f*-shell, respectively, and may be regarded as reference elements in the present context. Figure 6.3 compares the VCD of their DOTMA complexes which are indeed closely similar. This ensures that they are practically isostructural, an important prerequisite for any further speculation and is also in agreement with NMR findings.[11,15]

These VCD spectra have some dominating features, but display many more small signals, which would be easily confused with noise or artefacts, if they were not well reproduced in all the spectra of the series (but absent in the baseline or the spectrum of the free ligand).

We shall now discuss a case of a peculiar Fano-type mechanism, by considering Sm DOTMA (Figure 6.4). According to Richardson's selection rules,[16] the 1040 cm^{-1} transition of Sm^{3+} ($^6H_{5/2} \rightarrow {}^6H_{7/2}$) should be expected to give a (relatively) strong ECD, because it belongs to the *R I* class (ΔJ=1). Around this wavenumber, the mid-IR spectrum of Sm DOTMA consists of a series of relatively strong bands, which are poorly correlated to any other spectrum in the series. This feature should be regarded as due to intrinsically mixed electronic and vibrational states, where one cannot disentangle the two contributions, which provide a rather unusual case of vibrational/electronic CD which is neither VCD nor ECD and is not related to the common notion of vibronic coupling. What makes it very different from what we recalled above concerning to C-H stretchings for Co and Ni-spartein is the fact that, the $^6H_{5/2} \rightarrow {}^6H_{7/2}$ transition of Sm^{3+} *per se* should consist of a multiplet of up to 12 sharp lines and not just of one broad band.

It is tempting to gain some insight about the order of magnitude of rotational strength which one can assign (somewhat arbitrarily) to ECD. One cannot transfer easily the information about the intensity of ECD bands from one lanthanide to another one, because this relies on several effects, difficult to correctly take into account,[17] but we may recall that for the 10000 cm^{-1} $^7F_{7/2} \rightarrow {}^7F_{5/2}$ transition of Yb DOTMA, belonging to *R I* class, like the $^6H_{5/2} \rightarrow {}^6H_{7/2}$ of Sm^{3+}, but lacking significant vibrational contributions, the maximum excursion of the ECD spectrum is of the order of magnitude $\Delta\Delta\varepsilon \approx 1$.[14] This figure compares well with what we can observe in the region 980-1120 cm^{-1} of Sm DOTMA shown in Figure 6.4.

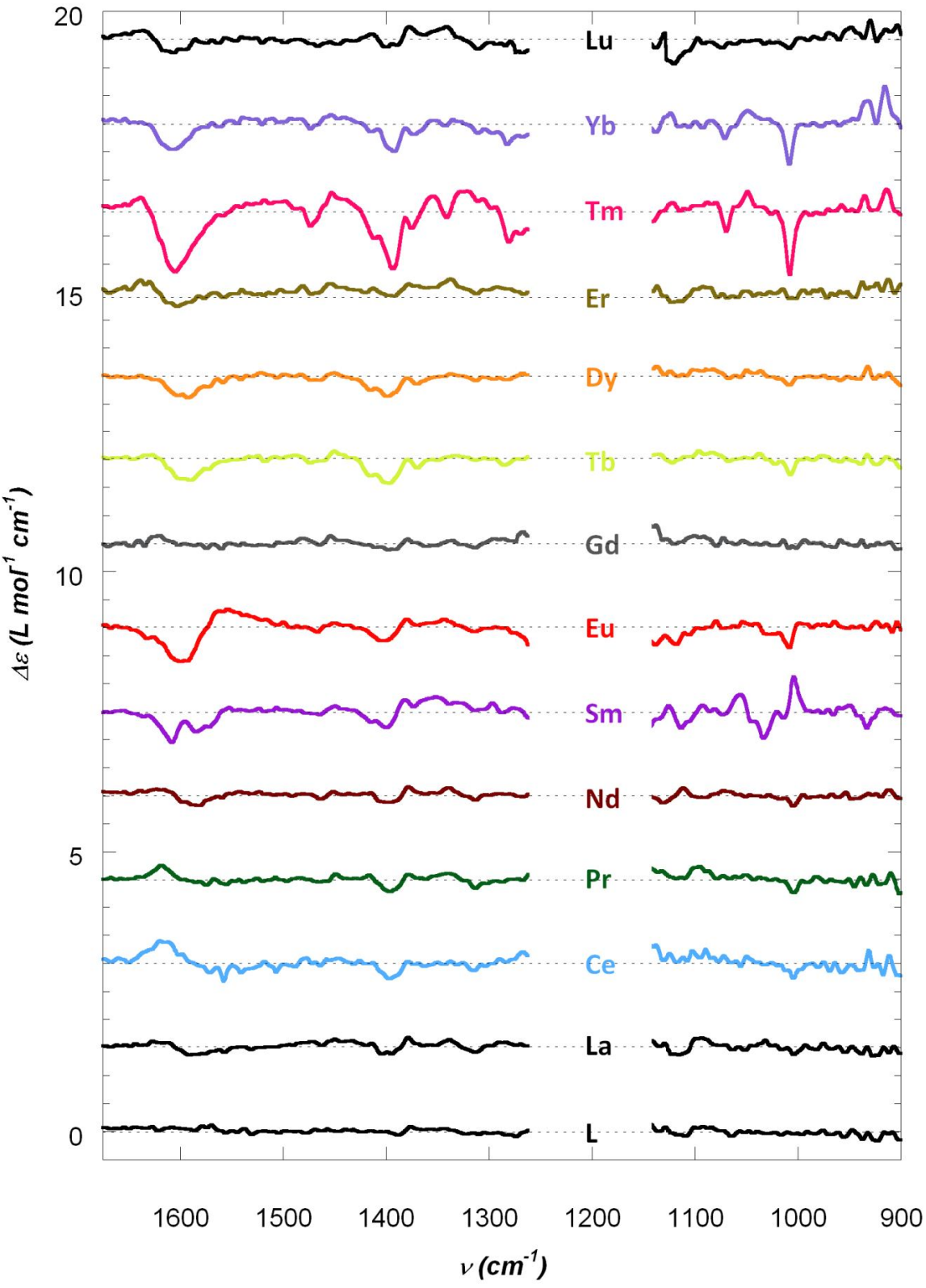

Figure 6.2 VCD spectra in D_2O solution (0.05 M) of the reference compounds for Ln DOTMAs and the free ligand (L) in solution. The region between 1280 and 1160 cm^{-1} was erased because obscured by the D_2O signal. The data have been vertically offset.

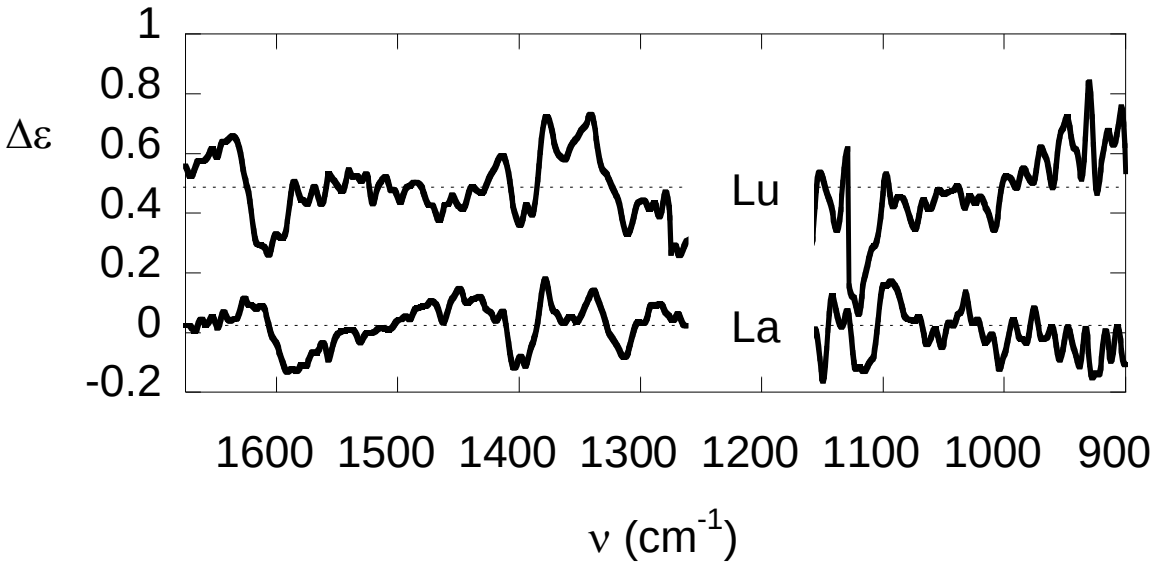

Figure 6.3 VCD spectra in D_2O solution (0.1M) of the reference compounds for Ln DOTMA (Ln = La, Lu), with f^0 and f^{14} electronic configurations, which lack LLES. The region between 1280 and 1160 cm^{-1} was erased because obscured by the D_2O signal. The data have been vertically offset.

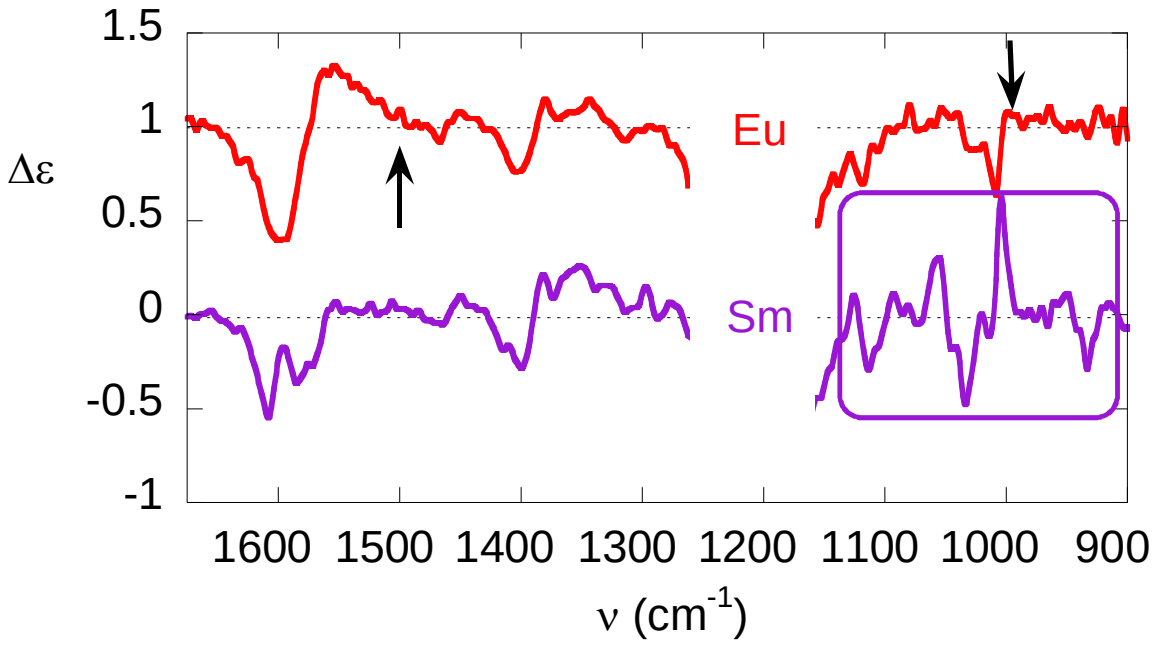

Figure 6.4 Mid-IR CD spectra of Sm DOTMA and Eu DOTMA. The region where strong electronic contribution to circular dichroism can be expected for Sm^{3+} is enclosed in the rectangular shape. In the case of Eu DOTMA, we mostly deal with pure VCD, although three electronic transitions fall near the wavenumbers indicated by the arrows (the low energy one corresponds to two electroning transitions, having almost the same frequency). The region between 1280 and 1160 cm^{-1} was erased because obscured by the D_2O signal. The data have been vertically offset.

As we saw in the previous section, Eu^{3+} has at least 3 electronic transitions in the mid-IR, namely, $^7F_0 \rightarrow {}^7F_2$, $^7F_1 \rightarrow {}^7F_3$ and $^7F_0 \rightarrow {}^7F_3$ at about 1000, 1500 and 1900 cm^{-1}, respectively. All these transitions belong to *R II* class ($\Delta J \geq 2$) and have much weaker electronic rotational strengths compared to *R I*.[16] Consequently, Eu^{3+} cannot provide much ECD contribution to the mid-IR spectrum of Eu DOTMA, unlike Sm^{3+}. Moreover,

since these three transitions are magnetic-dipole forbidden, they cannot provide interference terms, therefore the enhancement mechanism predicted by Nafie is not possible for them.[4] The spectrum shown in Figure 6.4 displays modest enhancements of the VCD bands at 1008 and 1405 cm^{-1} in comparison to La DOTMA, i.e. close to the three LLES, with approximately a doubling of the *g*-factor[26] (See Appendix 1, pp. 124, 125). Interestingly, the sign of these bands is the same as for the reference spectra of Figure 6.3.

Inspection of Table 6.1 reveals that there are no other occurrences of exact matching of electronic and vibrational frequencies, because our spectral window is limited to 1700 cm^{-1}. Rather near to this upper limit, there are the lowest lying transitions of Ce^{3+} ($^2F_{5/2} \rightarrow {}^2F_{7/2}$), Pr^{3+} ($^3H_4 \rightarrow {}^3H_5$), Nd^{3+}($^4I_{9/2} \rightarrow {}^4I_{11/2}$), and Tb^{3+}($^7F_6 \rightarrow {}^7F_5$). All of them are $\Delta J = \pm 1$ and therefore are magnetic-dipole permitted.

The high-energy end of the mid-IR VCD spectra of the corresponding DOTMA complexes (Figure 6.5) displays the very same overall features of the reference compounds, with somewhat increased intensities.

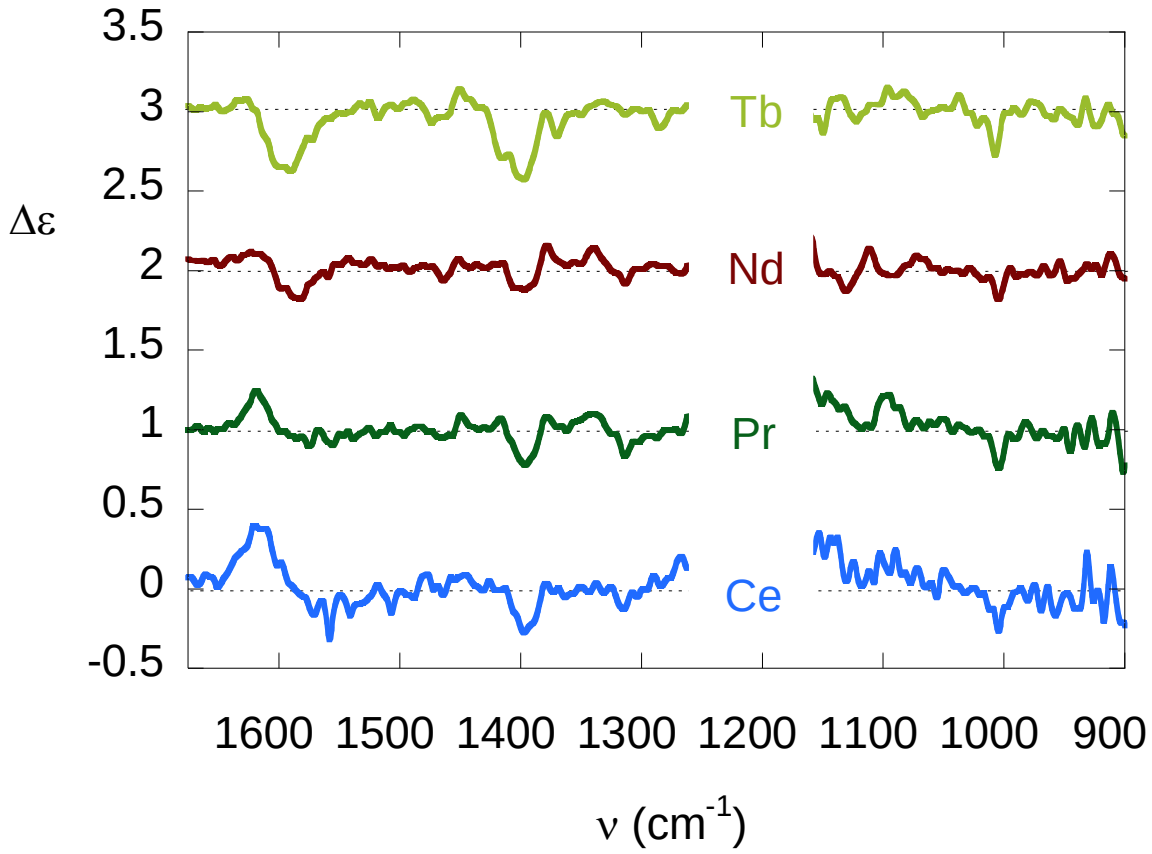

Figure 6.5 VCD spectra of Ce, Pr, Nd and Tb DOTMA. The region between 1280 and 1160 cm^{-1} was erased because obscured by the D_2O signal. The data have been vertically offset.

More in detail, we can observe that concerning the strongest VCD bands, for Ce and Pr the positive component at 1620 cm^{-1} becomes so intense to cancel the flanking negative band at 1605 cm^{-1}, while the opposite is true for Nd and Tb; the cluster of unresolved negative bands around 1400 cm^{-1} are enhanced in

[26] The *g*-factor is defined as VCD/VA. A useful operational trick is to modify slightly this definition, by adding a small constant value to the absorbance at the denominator. This ensures that *g* is defined over the whole spectrum and that it becomes numerically smoother also when the absorbance is very small. The error introduced through this stratagem is negligible as soon as the absorbance becomes sizeable.

all cases but Pr[27] (see Appendix 1, pp. 123-126). The enhancement factor is four for Tb, two for Ce and around 1.5 for Nd). At the same time, we must also observe that very many tiny lines become evident especially for Ce and to a minor extent for Pr and Tb, while they were *almost unnoticed* for the reference spectra. We underlined the word unnoticed, because once spotted out in the Ce spectrum, these lines could be recognized also for the other compounds, which is a first nice feature of the LIVE effect.

In the same spectral region (left of the deuterated water signal), we should also record a strongly enhanced activity of Sm DOTMA, which may be ascribed to the effect of the lower lying 1040 cm^{-1} electronic transition, discussed above.

Far more surprising is the fact that also the lower-energy part of VCD spectra of Ce, Pr and Tb DOTMA displays enhanced lines, in spite of the fact that the frequency difference $|\Omega - \omega| >> 1000\ cm^{-1}$.

Let us now look at the spectra of late elements (from Dy to Yb)[28], which have their lowest-lying electronic state well above mid-IR and indeed they are rather in the near IR.

Figure 6.6 demonstrates that in particular Tm and Yb feature very strong enhancements producing intense VCD lines, up to one order of magnitude larger than the reference spectrum of Lu DOTMA. Once more the sequence of signs and the gross appearance of the spectra are closely similar and one can immediately recognize that one deals with related compounds. One more remarkable point is that the low-energy end of the VCD spectrum experiences a particularly strong enhancement especially for Yb, which is extremely far from the energy of the spectroscopic term-to-term transition indicated in Table 6.1 (10000 cm^{-1}). A similar argument holds for Tm or Dy, with an increase of *g*-factor of even more than one order of magnitude for some transitions in comparison to Lu, which all seem to lack appropriate electronic transitions to couple effectively with the vibrational ones. This paradox will be the object of Section 6.2.4.

6.2.2 Enhancement of C=O stretchings in Lanthanide-Cesium heterobimetallic camphorates

The VCD spectra of some elements of the series $M[Ln(hfbc)_4]$, where M is an alkali metal, were reported by Kaizaki et al.[12] We shall presently focus only on M = Cs, which is the only alkali metal leading to a a tetrakis coordination (for the others, also the tricoordinated species is present in solution, hence potentially affecting the VCD spectra of the samples).[29] We performed a detailed NMR analysis of the paramagnetic shifts of these systems, to demonstrate isostructurality, which holds at least from Pr to Yb (the Ce-induced PCS are small and the diamagnetic La and Lu obviously lack completely this effect). The published crystallographic structure[18] is a poor model for the solution state, where the complexes undergo a rearrangement leading to a complete C_4-symmetry (as demonstrated by NMR).[29] It is worth observing that C_4 symmetry implies that there is complete selection for *fac*-type isomers, i.e. the 4 camphorate moieties are similarly oriented with respect to the unique C_4 axis.

[27] Since Pr DOTMA has nitrate as counterion, the anion absorption in the range is pretty intense, this causes an underestimation of the enhancement effect.
[28] We must acknowledge that the spectrum of Ho DOTMA in our hands is particularly dull and structureless and will be discarded in the discussion.
[29] S. Di Pietro et al. *in press*.

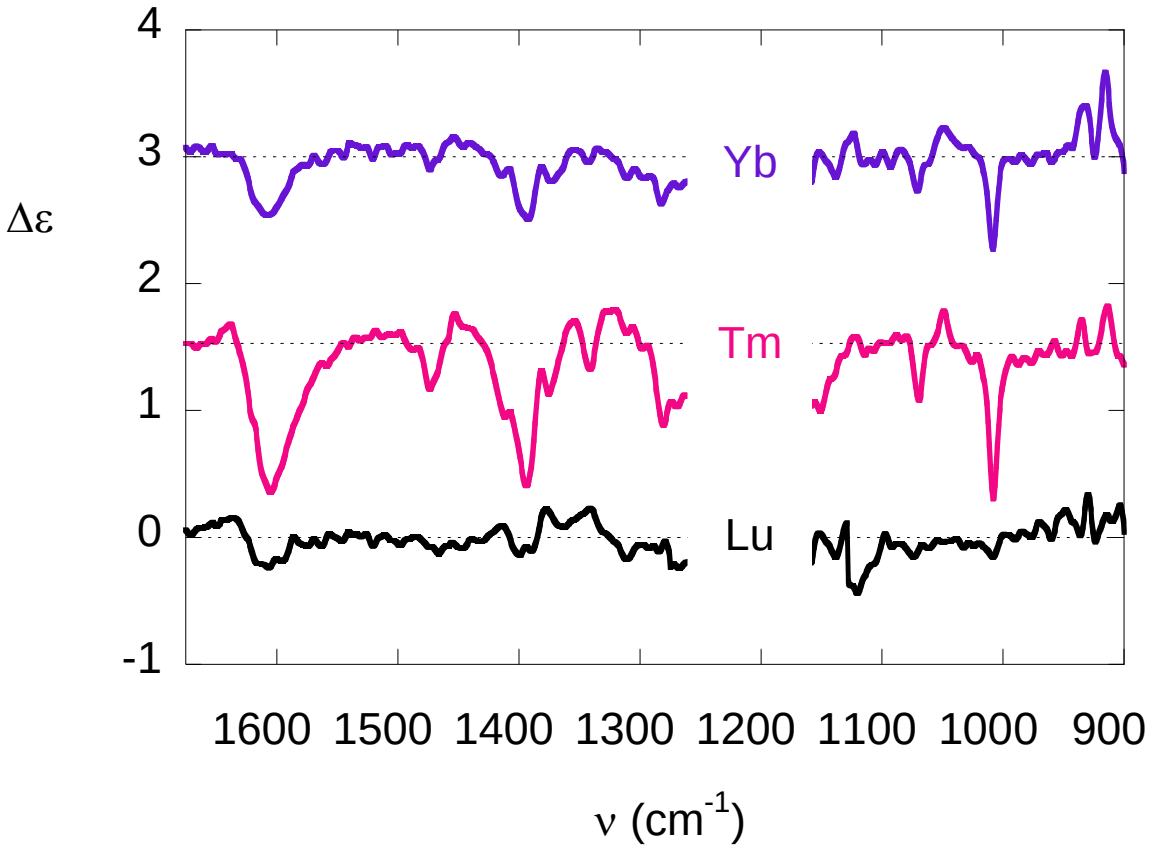

Figure 6.6 VCD spectra of Tm, Yb and Lu DOTMA. The region between 1280 and 1160 cm^{-1} was erased because obscured by the D_2O signal. The data have been vertically offset.

The mid-IR spectra and VCD of Cs[Ln(hfbc)$_4$]are dominated by the diketonate vibrations, more specifically C=O and C-C stretching modes, in close similarity to other metal diketonates complexes (we include in this class also systems with different symmetries and ligand-to-metal ratios),[19-22] and we shall primarily limit our analysis to these ones.

Figure 6.7 demonstrates that the spectra of the reference compounds (La, Gd and Lu complexes) display a strong couplet (negative for (+)-hfbc), which can be attributed to the coupled oscillations of the diketonates moieties in a Δ-square antiprismatic (SAP) coordination, following a mechanism which is explained in detail in the literature.[19,21]

Another important normal mode involving $\nu_{C=O}$ alone consists of a single band and normally falls at higher energy to this couplet. It can be easily recognized in the IR absorption spectrum (see Appendix 1, pp. 127-131) at about 1655 cm^{-1}, but apparently it does not produce any detectable VCD signal. This is in contrast with *tris*-acetylacetonates of various *d*-metals (ranging from Cr(III) to Ir(III)).[19]

The situation becomes dramatically different for several other late lanthanides, namely Eu, Tb, Er, Tm and Yb (Figure 6.8).

In the first place, the bisignate couplet takes the shape of two intense bands of the same sign, close to 1547 and 1527 cm^{-1};[30] the solitary transition at 1655 cm^{-1} also provides a strong positive VCD band. As a consequence the skyline of the VCD spectrum is deeply modified and becomes characterized by three intense positive transitions when using (+)-hfbc, which leads to Δ-square antiprismatic coordination (SAP). Of course, the reverse is true for the enantiomeric compounds (see Appendix 1, pp. 127-131). It is worth remarking that for all of these compounds the enhanced VCD spectra are very similar, once more in great contrast to Ni and Co spartein or to the other cases reported in the literature for *d*-metals.

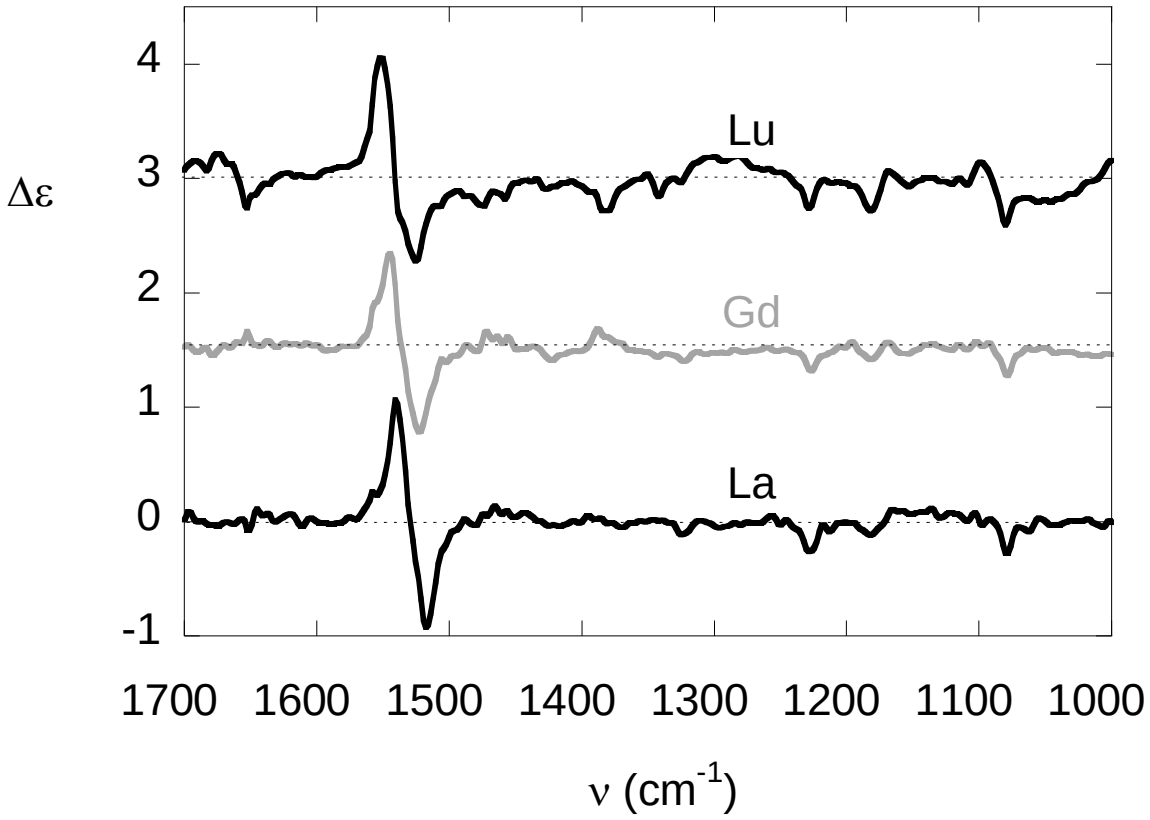

Figure 6.7 VCD spectra of $Cs[Ln(hfbc)_4]$ (with Ln= La, Gd, or Lu), which can be considered the reference compounds for the present investigation because they lack LLES. The data have been vertically offset.

It should be borne in mind that because of isostructurality and also of equal charge distribution of the complexes, other mechanisms accounting for vibrational optical activities should be equally active throughout the Ln-series. This is true in particular for the enhancement due ring currents and consequent Magnetic Dynamic Field (MDF) theory. Therefore, they do play a role in determining the intensity of the VCD bands, but they cannot explain why e.g. the 1655 cm^{-1} is practically inactive in the reference compounds (or for Dy and Pr), characterized by the coupling of the diketonate moieties oscillations, but becomes a prominent landmark for Tb, Tm and Yb.

The exciton coupling model which has been invoked to explain the negative-positive feature around 1540 cm^{-1} *per se* predicts that the two lines have equal and opposite rotational strengths. As customary in this

[30] In the case of the Eu derivative, the lower energy component at about 1527 cm^{-1} appears as a shoulder of the 1547 cm^{-1} band.

mechanism, a closure relation implies that if two transitions are coupled by a strong electric dipole-dipole interaction, which overrides other interactions with the environment, the total rotational strength integrated over the two transitions should vanish (hence the bisignate feature of a typical exciton couplet). In some *tris*-diketonate compounds of *d*-metals, MDF has been demonstrated to account for the unbalance in the intensity of the two components of the couplet, because it provides an effective coupling to the environment. In the present case, for Cs[Ln(hfbc)$_4$] compounds with Ln = Eu, Tb, Tm and Yb, the very marked gain of total rotational strength in the region 1520-1560 cm^{-1} demonstrates that an important magnetic dipole moment is coupled to the electric-dipole C-C and C=O oscillators responsible for this part of the vibrational spectrum. Clearly, this must be sought in LLES of the Ln^{3+} ions, as will be further discussed below.

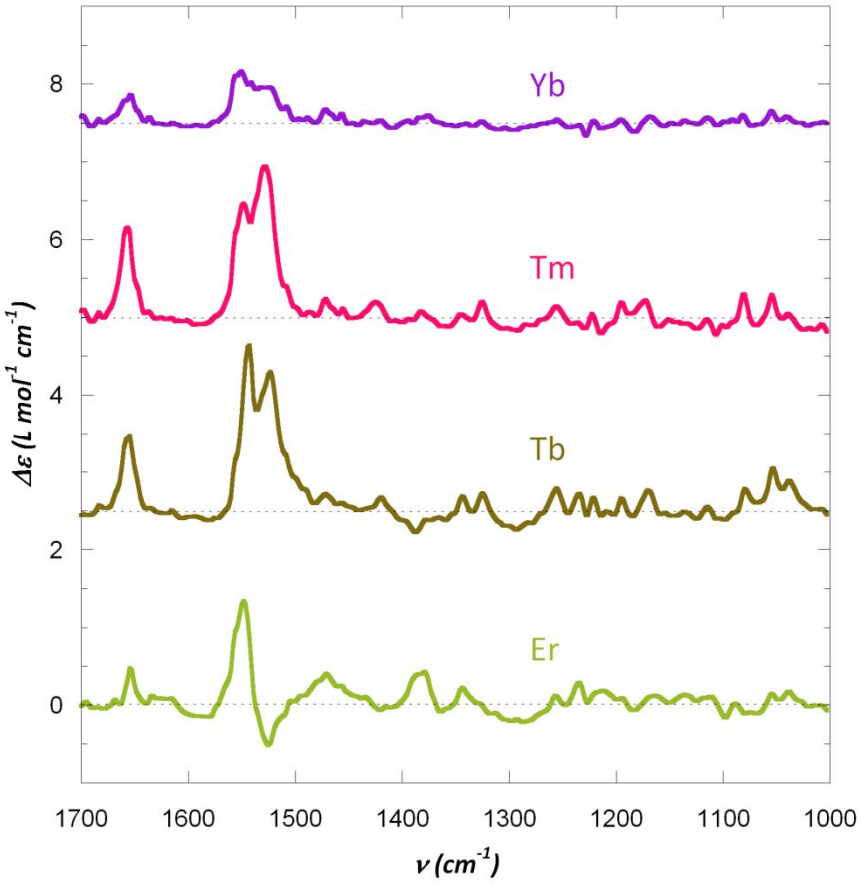

Figure 6.8 VCD spectra of Cs[Ln(hfbc)$_4$] (with Ln = Tb, Er, Tm or Yb). The data have been vertically offset.

The rest of the VCD spectrum is made of a multitude of smaller bands, which undergo relevant changes according to the central ion, not very differently from what we have discussed for Ln DOTMA.

6.2.3 Enhancement of the amide modes in Ln DOPhA

Ln DOPhA are obviously correlated to Ln DOTA: the four carboxylate groups on the side arms are formally substituted with amide bonds with (*S*)-methyl benzylamine.[23-25] The four exocyclic chiral centers are symmetry-related and enforce one chiral conformation of the whole lanthanide complex, which is in fact

structurally homogeneous.[24,26] Like in the case of Ln DOTMA discussed above, there are several stereogenic elements, viz. Δ-metal coordination, *G*⁻-conformation of the ethylene bonds (also referred to as λ) and finally the (*S*)-centers.[26] The VCD spectra of a selection of lanthanide complexes of this ligand are reported in Figure 6.9, where one can immediately appreciate that all of them are moderately intense if compared to Ln DOTMA.[31] Even the reference compound Lu DOPhA displays many bands with a *g*-factor above 0.001 (see Appendix 1, page 135), which may be the effect of the conformational homogeneity and possibly also of a role of other VCD enhancement effects, like MDF. This may explain why the differences between the various Ln-complexes are much less marked here than in the cases discussed above.

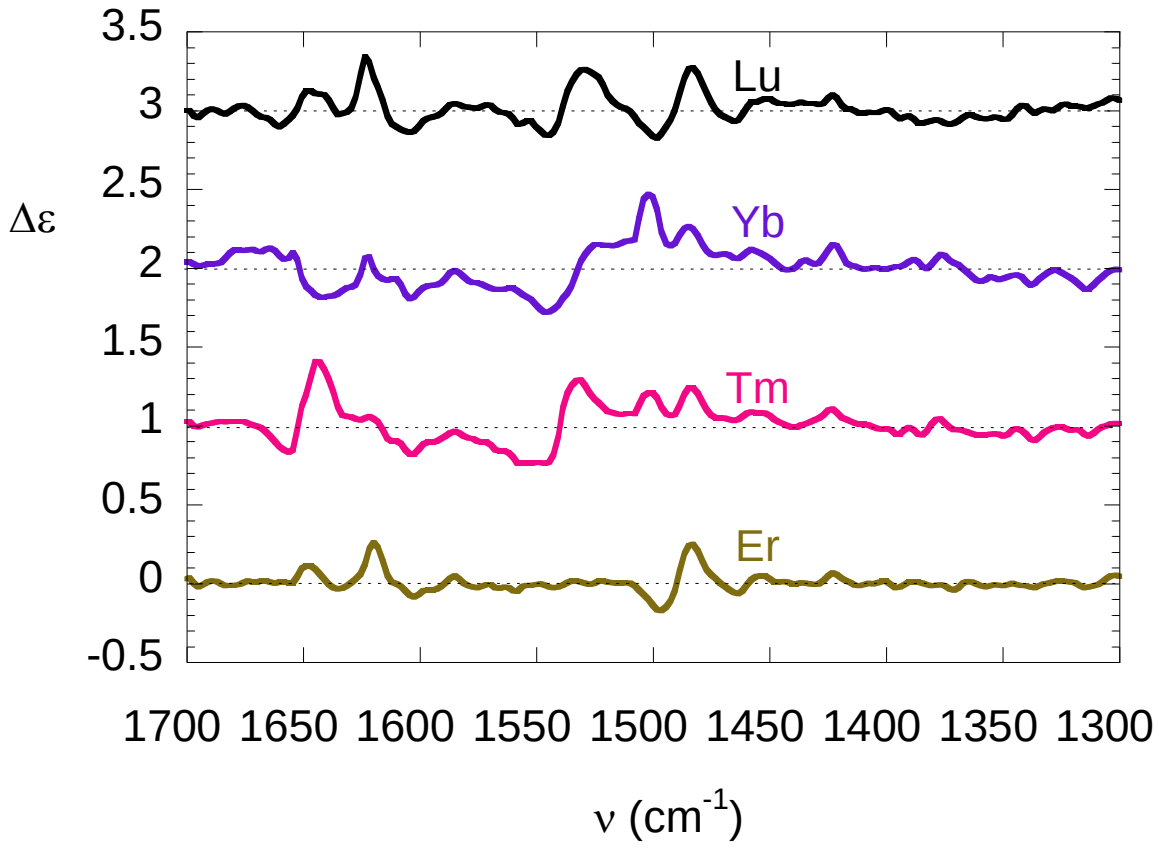

Figure 6.9 VCD spectra of Er, Tm and Yb and Lu DOPhA. The data have been vertically offset.

Nonetheless, a few normal modes stand out for particularly large *g*-values: the couplets at 1651 cm^{-1} and at 1538 cm^{-1} for Tm, and the bands at 1422 and 1314 cm^{-1} for Yb (as well as the second couplet, although to a lesser extent, just for the negative part) are definitely enhanced with respect to Lu (or even to Er) DOPhA. Interestingly, the former two frequencies correspond to amide I and II modes, having the highest g-values among the transitions: $g_{Tm}^{1656} = 1.1 \cdot 10^{-3}$, $g_{Tm}^{1546} = 6.1 \cdot 10^{-3}$, $g_{Tm}^{1533} = -5.7 \cdot 10^{-3}$, $g_{Tm}^{1313} = 1.4 \cdot 10^{-3}$, $g_{Yb}^{1546} = -2.0 \cdot 10^{-3}$, $g_{Yb}^{1537} = -2.0 \cdot 10^{-3}$, $g_{Yb}^{1527} = 1.3 \cdot 10^{-3}$, $g_{Yb}^{1423} = 1.1 \cdot 10^{-3}$, $g_{Yb}^{1313} = -2.4 \cdot 10^{-3}$.

[31] Spectra have been acquired in the range 2000-1300 cm^{-1}, due to CD_3OD high absorption in the lower energy region.

6.2.4 Geometric and spectroscopic factors of the LIVE effect

In the three cases presented above we saw that:

1) Some lanthanides induce enhancements of certain VCD bands. This is particularly noticeable for late elements and especially Tm and Yb.
2) The enhanced lines display mostly the same sign on passing from a complex to another one, in spite of any difference in the electronic configuration of the Ln^{3+} ion.
3) At a first sight, this effect is not immediately related to a Fano-type mechanism, whereby one should expect a match between electronic (metal centred) and vibrational (ligand centred) transitions. This situation is encountered for Sm and Eu DOTMA and leads to features very different from the ones attributed to LIVE.
4) Certain normal modes are more sensitive than other ones to LIVE. This is particularly true for those involving C=O vibrations.
5) Tm appears particularly active in enhancing effects around 1400-1600 cm^{-1}, while Yb is somewhat more active at lower frequencies.

Using perturbation theory, Nafie demonstrated that the wavefunctions relevant to VCD spectra in the presence of LLES result from an admixture of electronic and vibrational states, formally localized on the metal and on the ligand.[4] At least two factors intervene in this mixing: a) the involvement of the metal in the normal mode responsible for the VCD band; b) the energy matching between the two transitions.

Condition a) can be seen as a geometrical or structural constraint, whereby among the multitude of vibrations falling in the fingerprint region of the IR spectrum, those involving the donor atoms directly bonded to the metal ion and those due to ring-modes embedding Ln^{3+} are the foremost candidates. This aspect is particularly well appreciated for the Ln camphorates described above. The modes which undergo the strongest enhancements are those which involve the asymmetric C=O stretchings. According to the assignment of ref.s [12,21,22], $\nu_{C=O}$ is responsible for the band 1640 cm^{-1} and, in combination with the diketonates C-C vibrations, it participates in the region 1550-1520 cm^{-1}. In all these cases, we deal with a transition with strong electric dipole character, but practically lacking any magnetic dipole. This explains why $\nu_{C=O}$ is not associated to any prominent VCD feature in the reference compounds (La, Gd, Lu). The couplet centered at 1530 cm^{-1} is due to the concerted in-phase and out-of-phase oscillations of the diketonate carbon backbones of two different ligands,[21] which involves the Ln^{3+} ion to a much lesser extent than $\nu_{C=O}$. As a consequence, we may put forward that metal centered LLES bringing about a strong magnetic dipole character couple very strongly with $\nu_{C=O}$, but much less to ν_{C-C}. Thus, $\nu_{C=O}$ gives rise to a large rotational strength, which is negative for Δ-Cs[Ln((+)-hfbc)$_4$]in all the transitions where it contributes (1645, 1545, 1520 cm^{-1}), to the point that the couplet feature around 1530 cm^{-1} is obscured by two large positive VCD effects.

The fact that LIVE is a strongly local effect may be particularly desirable, because it has the effect of lighting up a molecular moiety, where the Ln ion binds, practically leaving the rest of the VCD in the twilight. We

are currently studying metal-binding biological molecules, where only a few spectral features undergo LIVE and must consequently be associated to the pocket hosting Ln^{3+}.

Point b) above regards the spectroscopic conditions necessary for LIVE. In the section dedicated to Ln DOTMA above, we have already presented the fact that we observe the strongest enhancements for late lanthanides and that according to the frequencies listed in Table 6.1 they apparently do *not* possess the necessary LLES, which is at first sight quite puzzling.

Some time ago, we made a detailed investigation of the electronic circular dichroism (ECD) spectrum of Yb DOTMA, in the NIR around 10200 cm^{-1}, and we proposed the first assignment of all the crystal field-splitted sublevels of Yb^{3+}.[14] Both the TSAP and SAP coordinations lift the degeneracy of the $^2F_{7/2}$ and $^2F_{5/2}$ (ground and excited) electronic states into 4 and 3 Kramers doublets, respectively, which is responsible for 12 electronic transitions visible in the NIR ECD spectrum of this complex. The four sublevels of $^2F_{7/2}$ lie within about 1000 cm^{-1} and are interconnected by low lying transitions with $\Delta J = 0$ and $\Delta M_J \neq 0$, which is one of the conditions for a large magnetic dipole character.

This may justify the particularly strong enhancements of the low frequency bands, at 915 (where *g* reaches the incredible value of $4.3\ 10^{-3}$), 935 and 1009 cm^{-1}.

Unfortunately this enhancement interpretation is questionable, since no significant variations, for different lanthanide ions, have been obtained in the preliminary calculations of low-lying electronic states energy, in the case of DOTMA complexes.[27] The hypothetical intraconfigurational transitions have very similar energy values, both for the enhancing lanthanides and the silent ones. However the low calculation precision leaves room enough for further investigations, which are currently in progress in our research group.

References

[1] C. J. Barnett, A. F. Drake, R. Kuroda, S. F. Mason, S. Savage, *Chem. Phys. Lett.* **1980**, *70*, 8.

[2] U. Fano, *Phys. Rev.* **1961**, *124*, 1866.

[3] Y. N. He, X. L. Cao, L. A. Nafie, T. B. Freedman, *J. Am. Chem. Soc.* **2001**, *123*, 11320.

[4] L. A. Nafie, *J. Phys. Chem. A,* **2004,** *108,* 7222.

[5] P. J. Stephens, *J. Phys. Chem.* **1985**, *89*, 748.

[6] A. D. Buckingham, P. W. Fowler, P. A. Galwas, P. A. *Chem. Phys.* **1987**, 112.

[7] C. Johannessen, P. W. Thulstrup, *Dalt. Trans.* **2007**, 1028.

[8] L. Di Bari, P. Salvadori, *Coord. Chem. Rev.* **2005**, *249*, 2854.

[9] C. Piguet, C. F. G. C. Geraldes, in *Handbook on the Physics and Chemistry of Rare Earths, Vol. Volume 33* (Eds.: J. K. A. Gschneidner, J. C. G. Bünzli, V. K. Pecharsky), **2003**, Elsevier: Amsterdam, pp. 353.

[10] S. Di Pietro, S. Lo Piano, L. Di Bari, *Coord. Chem. Rev.* **2011**, *255*, 2810.

[11] L. A. Nafie, T. A. Keiderling, P. J. Stephens, *J. Am. Chem. Soc.* **1976**, *98*, 2715.

[12] a) H. Sato, D. Shirotani, K. Yamanari, S. Kaizaki, *Inorg. Chem.* **2010**, *49*, 356. b) D. Shirotani, T. Suzuki, S. Kaizaki, *Inorg. Chem.* **2006**, *45*, 6111.

[13] H. G. Brittain, J. F. Desreux, *Inorg. Chem.* **1984**, *23*, 4459.

[14] L. Di Bari, G. Pintacuda, P. Salvadori, *J. Am. Chem. Soc.* **2000**, *122*, 5557.

[15] S. Aime, M. Botta, Z. Garda, B. E. Kucera, G. Tircso, V. G. Young, M. Woods, *Inorg. Chem.* **2011**, *50*, 7955.

[16] F. S. Richardson, *Inorg. Chem* **1980**, *19*, 2806.

[17] L. Di Bari, G. Pescitelli, in *Computational Spectroscopy* (Ed. J. Grunenberg), **2010**, Wiley-WHC: Weinheim, pp. 241.

[18] D. Shirotani, T. Suzuki, K. Yamanari, S. Kaizaki, *J. Alloy. Compd.* **2008**, *451*, 325.

[19] H. Sato, T. Taniguchi, A. Nakahashi, K. Monde, A. Yamagishi, *Inorg. Chem.* **2007**, *46*, 6755.

[20] T. B. Freedman, G. A. Balukjian, L. A. Nafie, *J. Am. Chem. Soc.* **1985**, *107*, 6213.

[21] D. A. Young, E. D. Lipp, L. A. Nafie, *J. Am. Chem. Soc.* **1985**, *107*, 6205.

[22] I. Diaz-Acosta, J. Baker, W. Cordes, P. Pulay, *J. Phys. Chem. A* **2001**, *105*, 238.

[23] R. S. Dickins, D. Parker, J. I. Bruce, D. J. Tozer, *Dalton Transactions* **2003**, 1264.

[24] L. Di Bari, G. Pintacuda, P. Salvadori, R. S. Dickins, D. Parker, *J. Am. Chem. Soc.* **2000**, *122*, 9257.

[25] R. Dickins, S.J. Howard, A.K.C. Lehmann, W.J. Moloney, D.Parker, D. Peacock Robert, *Ang. Chem. Int. Ed.* **1997**, *36*, 521.

[26] L. Di Bari, P. Salvadori, *ChemPhysChem* **2011**, *12*, 1490.

[27] R. Berardozzi, Master Thesis, unpublished results.

Chapter 7

Development of a chiral probe for the acute phase proteins alpha-1-acid glycoprotein and alpha-1-antitrypsin based on europium luminescence

In Chapter 4, the employment of lanthanides complexes as MRI CAs or as luminescent bioprobes has been briefly reviewed. In this Chapter, a new specific probe for a peculiar application to target specifically two acute phase proteins is described.

Acute phase proteins have plasma concentrations that increase (positive) or decrease (negative) by more than 25% in response to inflammation. Alpha-1-acid glycoprotein (α_1-AGP) is an important protein in the blood, that is normally present in the concentration range 12 to 32 μM. It has a molecular weight of about 42 kDa, a pI of 2.7 and exists in several isoforms that differ in their degree of glycosylation,[1] typically varying the sialic acid content. It is one of the most important 'acute-phase' proteins[2] and gives negative feedback on an inflammatory response. The plasma concentration quickly rises by a factor of three to four as a result of inflammation in several disease states, for example that induced by tumor growth.[3] The change typically involves a 3 to 4-fold increase in concentration. The plasma concentration of α_1-antitrypsin (α_1-AAT) is also up regulated in response to inflammation. For example, inflammatory conditions such as rheumatoid arthritis have been associated with up to a 4-fold increase in serum levels of this in non-deficient subjects.[2b] In contrast to α_1-AAT, α_1-AGP is a known drug-binder: It binds strongly (K_d typically 1 to 10 μM) to a large number of apolar and basic drugs, e.g. methadone, warfarin, progesterone, imatinib [Glivec], regulating their pharmacokinetics and pharmacodynamics.[4] Recently, the X-ray crystal structures of certain isoforms, both free and when bound to selected basic drugs (e.g. chlorpromazine, amitryptyline and disopyramide), have been reported.[5,6] These studies revealed the presence of a drug binding pocket located within an eightstranded β-barrel, in which several aromatic residues, e.g. Trp-25, line the hydrophobic pocket; a proximate Glu residue (Glu-64), was also implicated in electrostatic binding. The protein has been immobilised on silica microspheres and functions as a versatile and widely used chiral stationary phase in HPLC analysis.[7]

Recently, studies into the creation of chiral probes based on well-defined, emissive lanthanide complexes have been undertaken.[8,9] In principle, these complexes may interact with a protein in two main ways: first, at the metal centre, where a protein residue (e.g. an Asp or Glu carboxylate) displaces solvent or a weakly coordinated ligand donor,[10] and second via a non-covalent binding interaction between the sensitising moiety and a protein binding pocket.[11-13] The latter interaction is much more common, and has been examined frequently in related relaxivity studies with gadolinium complexes, almost exclusively targeting the binding of the most abundant serum protein, albumin.[14] An example of a chiral optical probe for albumin was recently described, in which reversible binding to the protein was signalled by a switch in the circular polarisation of the luminescence (CPL), associated with dynamic helicity inversion (Δ to Λ) of the enantiopure lanthanide complex.[9]

In the following section, the first example of an optical probe for the acute phase proteins α_1-AGP and α_1-AAT, in which binding involves both metal coordination and a non-covalent interaction of the integral sensitising moiety. Reversible protein binding is characterised by unprecedented, large induced ECD and CPL signals, and a significant change in the europium total emission spectrum, associated with the change in the metal coordination environment.[15]

7.1 A chiral probe for alpha-1-acid glycoprotein based on europium luminescence

The europium (III) complex, $[EuL^1(OH_2)]^+$ (Figure 7.1), recently has been demonstrated to bind to serum albumin and cause a change in the form and relative intensity of the observed europium emission.[16] As a consequence, it was decided to study its binding to six of the most common proteins found in human serum, examining associated spectral changes and assessing relative affinity.[32] The constitutionally isomeric complex, $[EuL^1(OH_2)]^+$ [17] and the neutral mono-azaxanthone complex $EuL^3(OH_2)$ [18] were used as controls. In the former case, the constitution of the tricyclic sensitising group minimizes the steric demand about the metal centre compared to $[EuL^1(OH_2)]^+$, where the pyridyl nitrogen is flanked by the σ-polarising α-oxygen, reducing its donor ability.

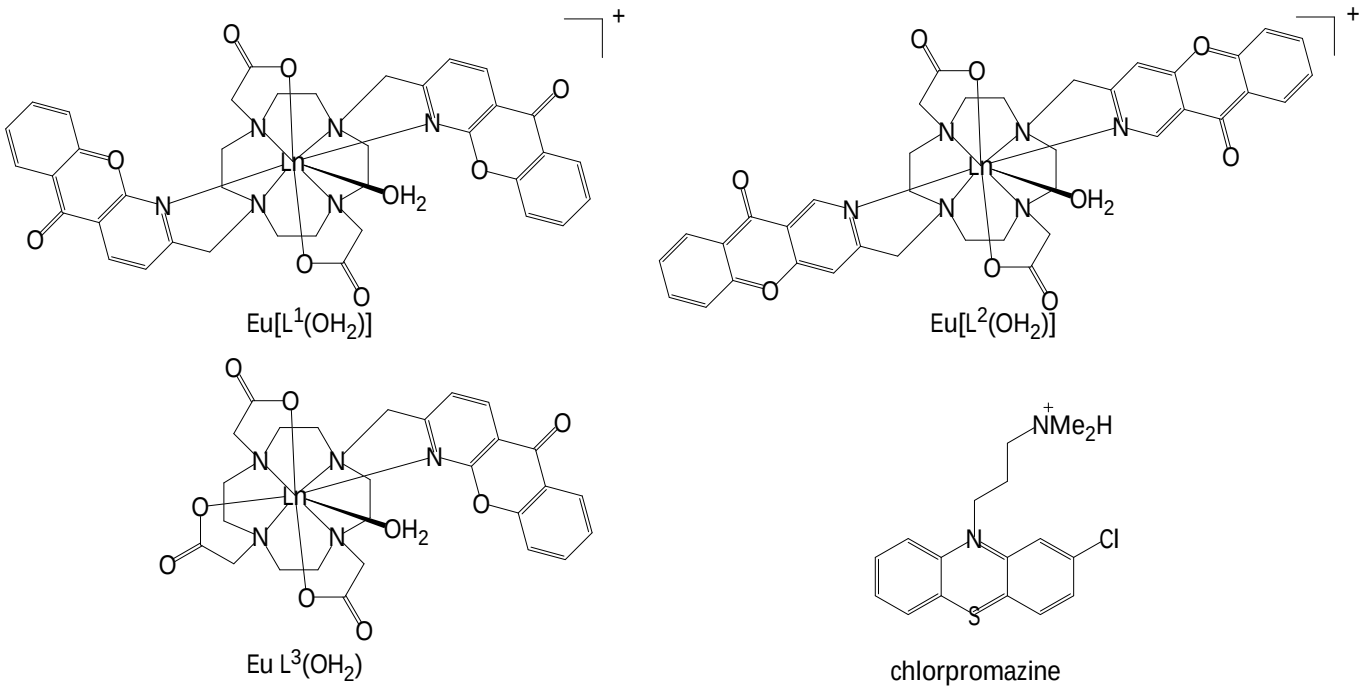

Figure 7.1

Incremental addition of human α_1-AGP to $[EuL^1(OH_2)]^+$ (20 μM) at pH 7.4 (0.1 M NaCl) gave rise to pronounced changes in the relative intensity and form of the Eu emission bands, Fig.7.2. In the limiting spectrum of the bound species, one major emissive species was apparent (ϕ_{em} = 8%, vs 4 (±1)% for the parent complex), as defined by the single $\Delta J = 0$ transition at 579 nm and the occurrence of 3 components in the $\Delta J = 1$ manifold around 590 to 600 nm. The intensity of the hypersensitive transition centred at 620 nm more than doubled. Measurements of the radiative rate constants characterising Eu emission (586 nm) for the protein bound species in H_2O and D_2O were 1.29 and 0.84 ms^{-1} respectively (compared to 2.08 and 0.61 ms^{-1} for $[EuL^1(OH_2)]^+$), establishing the displacement of the coordinated water (q^{Eu} ~ 0.2 for the bound species). Parallel experiments with $[EuL^2(OH_2)]^+$ and $[EuL^3(OH_2)]$ showed no changes in spectral form and a slight reduction in overall emission intensity, consistent with no variation in the metal coordination environment and some quenching of the chromophore excited state. Excitation spectra for $[EuL^1(OH_2)]^+$, both free and when bound to α^1-AGP gave similar spectral profiles, that closely matched the absorption spectrum of the free complex. Iterative, non-linear least squares data fitting of the spectral changes

[32] See Appendix 2 for details of emission spectral titrations.

associated with α_1-AGP binding to $[Eu\ L^1(OH_2)]^+$allowed estimation of a 'global' association constant, K_D = 1.5 μM, assuming a 1:1 binding stoichiometry, Table 7.1.

Parallel experiments were undertaken with human serum albumin, γ-immunoglobulin (γ-Ig-G), fibrinogen, apo-transferrin and α_1-antitrypsin.[33] In every case, much weaker binding was observed. Considerable quenching of emission was noted for addition of fibrinogen and more than one emissive Eu species was evident in limiting spectra for HSA, apo-transferrin, fibrinogen and γ-immunoglobulin. Interestingly, addition of α_1-antitrypsin gave rise to a Eu-bound species that had an identical emission spectrum to that observed with α_1-AGP, notwithstanding a protein affinity that was an order of magnitude lower. Adding sialic acid in 2.5 fold excess to $[EuL^1(OH_2)]^+$caused no change in the form of the Eu emission spectrum (Appendix 2, Figure A2.10).

Both α_1-AGP and α_1-antitrypsin are positive acute-phase proteins,[2] exhibiting similar increases in concentration, following an inflammatory response. Analysis of DNA sequence homology in genes coding for α_1-AGP and α_1-antitrypsin revealed a conserved region, but only within the 5'-untranslated region.[19] It is therefore unsurprising that an examination of the amino-acid sequence in each protein reveals little homology. However, protein structural alignment using FATCAT[20] (see Figure A2.1) revealed some common features. This was most apparent in the location of the glutamate residues 35 and 36 that lie over the binding pocket in α_1-AGP, *vs* Glu-151 and Glu-152 in the superposed structure with α_1-antitrypsin. In addition, Glu-64 in α_1-AGP lay close to Glu-206 in α_1-antitrypsin, in the superposed structure (see Appendix 2, Fig A2.1).

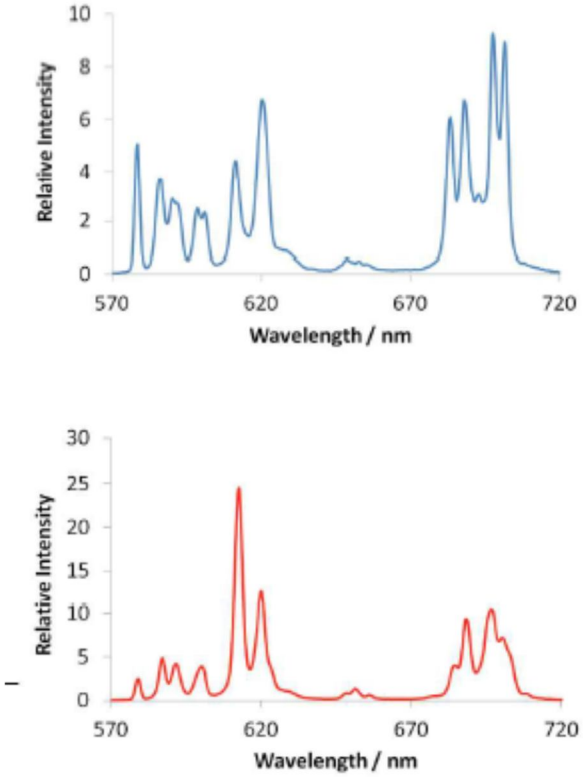

Figure 7.2 Total emission spectra for $[EuL^1(OH_2)]^+$ in solution (20 μM, 0.1 M NaCl, pH 7.4) and, *lower*, in the presence of 50 μM of human α_1-AGP.

[33] See Appendix 2 for details of emission spectral tritations.

The complex $[EuL^1(OH_2)]^+$ exists in solution as a racemic mixture of Δ and Λ stereoisomers. Protein binding to the metal centre was indicated by the change in spectral form and hydration state. Accordingly, ECD probing in absorption the chiral environment of the azaxanthone chromophore, and CPL spectroscopy examining in emission the local chirality at Eu, were used to study each protein-bound complex. As expected, no ECD or CPL signal was observed for the unbound complex; neither was any for the complexes $[EuL^2(OH_2)]^+$and $[EuL^3]$ in the presence of either α_1-AGP or HSA.

Table 7.1 Abundance and relative affinity constants with [Eu ·L^1]OAc (295 K, pH 7.4, I = 0.1 M NaCl) for the six most abundant serum proteins.

Protein / pI	Normal Range/μM[(a)]	K_D μM[(b)]	Comment
α_1-AGP 2.7 to 3	12-32	1.5	Emission intensity increases.
α_1-Antitrypsin 4.9 - 5.1	40-80	20	Bound species has same spectrum as with AGP.
Albumin 4.7 to 5.1	500-750	125	More than one Eu species evident.
Fibrinogen 5.6	6-14	(16)	Considerable quenching occurs.
apo-Transferrin 6.5	25-40	(c)	Minor spectral change only evident.
γ-Ig-G 6.4 to 9	50-120	250	Quenched; > 1 species found.

(a) Normal range in human serum; in inflammation, the concentration of α_1-AGP and α_1-antitrypsin is raised by up to 400%, while that of serum albumin and transferrin is reduced; (b) a global affinity constant, (± 0.1) assuming a 1:1 binding stoichiometry; (c) 30 spectral changes were insufficiently well-defined to allow reliable estimates of logK to be made.

The UV-visible absorption and electronic circular dichroism (ECD) spectra of $[Eu\ L^1(OH_2)]^+$ (41 μM) in the absence and presence of one equivalent of α_1-AGP revealed two main bands around 290 and 340 nm, (Figure 7.3). The mere existence of an ECD signal confirms the formation of a well-defined adduct between protein and complex. It consists of two negative Cotton effects (g_{abs}: -4.6×10^{-4} (340) and -1.4×10^{-4} (285)) with partially resolved fine structure, typical of a relatively rigid environment with no solvation dynamics, associated with the two main transitions of the azaxanthone chromophore.

The appearance of two partially resolved CD bands in each transition ($\Delta\lambda \sim 6$ nm) suggests that each azaxanthone groups is in a moderately different local chiral environment, consistent with a model in which one remains bound to europium, whilst the other is not coordinated but is included in the apolar protein cavity.[5,6] Prior CD studies examining the binding of small drug molecules to α_1-AGP, such as chlorpromazine,[21] suggested that exciton coupling with the electric-dipole allowed transitions of a proximate tryptophan (Trp-25) accounts for the observed ECD.

A dissociation constant of the order of $K_D = 1$ μM were estimated for chlorpromazine association, based on competitive binding assays. Incremental addition of chlorpromazine (0 to 1.25 eqs) to the AGP-bound europium complex (1:1, 21 μM) led to a progressive diminution of the induced CD for the azaxanthone chromophore, consistent with reversible binding and competitive displacement.

A tentative model for the protein-bound complex can be postulated (Figure 7.4), that is consistent with the emission and CD spectral changes and prior structural analyses.[5,6] It involves axial coordination of a Glu carboxylate (e.g. Glu 64) with one azaxanthone moiety included by the drug binding site.

The CPL spectra of $[EuL^1(OH_2)]^+$bound to human α_1-AGP and α_1-antitrypsin (Fig. 7.5) were identical but differed considerably from those associated with γ-immunoglobulin or HSA binding. In each case, a characteristic CPL fingerprint was found for the protein-bound species. Much larger emission dissymmetry values (g_{em}) values were observed for α_1-AGP binding {g_{em}: -0.19 (597 nm); -0.27 (618 nm); +0.29 (624 nm); +0.01 (694 nm); -0.02 (702)}, compared to values measured for the HSA adduct {g_{em}: - 0.13 (598); +0.03 (619); -0083 (624)}. No CPL was observed for the complex in the presence of fibrinogen or apo-transferrin.

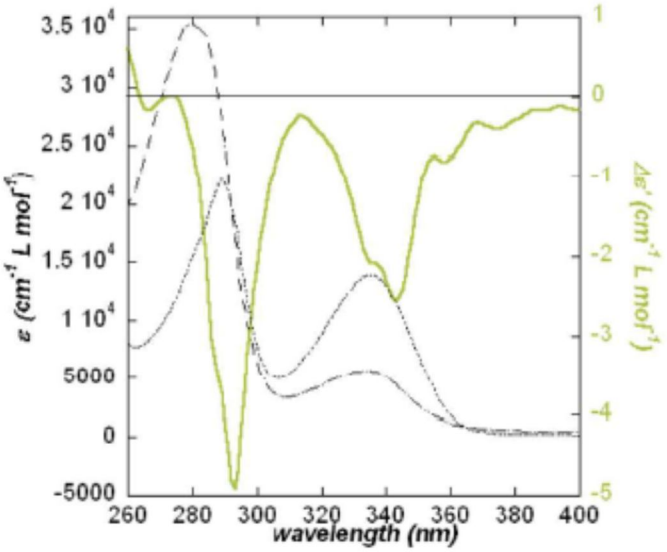

Figure 7.3 UV-Absorption and ECD spectra of $[Eu\ L^1(OH_2)]^+$ (41 μM, pH 7.4) (dotted line) and in a 1:1 mixture with α_1-AGP (absorption-dashed line; ECD-continuous line). The ECD spectra were normalised ($\Delta\varepsilon'$) to the total concentration of complex.

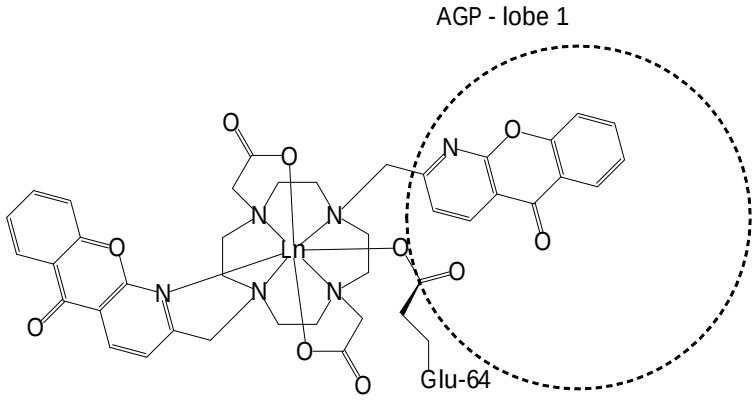

Figure 7.4 Model of the interaction between the complex $[EuL^1(OH_2)]^+$ and the protein binding-site.

Finally, the total emission and CPL spectra of $[EuL^1(OH_2)]^+$ (20 μM) were recorded in human serum solution. Initial spectral analysis suggested the presence of a mixture of Eu species, in which a major HSA-bound species was present. Incremental addition of α_1-AGP led to progressive formation of the spectral signature

of the α_1-AGP-bound species. The initial concentration of α_1-AGP in the serum sample was estimated using a commercial ELISA assay and was found to 16(±2) μM. Up to 50 μM of protein was added, reflecting a four-fold increase from the normal serum value, in order to simulate an inflammatory response. The final concentration of α_1-AGP was also measured by the ELISA assay to be 65(±3) μM, consistent with the amount of protein added. By measuring the intensity ratio of the $\Delta J = 1/\Delta J = 2$ emission bands, or by assessing the g_{em} increases (see Appendix 2 for both of the data), the spectral response could be calibrated and is independent of complex concentration (Fig. 7.6). Hence, analysis of the intensity ratio can be used directly and quickly to assess the extent of α_1-AGP elevation in serum. Luminescence analyses of the concentration of urate, citrate and lactate (<3 minutes in total) have been reported recently using related ratiometric europium emission methods.[22]

Control experiments were undertaken with α_1-AAT. Its concentration also rises up to 4-fold in inflammation, and it too gave rise to an increase in the emission intensity that was very similar to that induced by added AGP.[2] Thus, the elevation of serum levels of either protein will give rise to the observed in the Eu emission increase, signalling the onset of inflammation in each case.

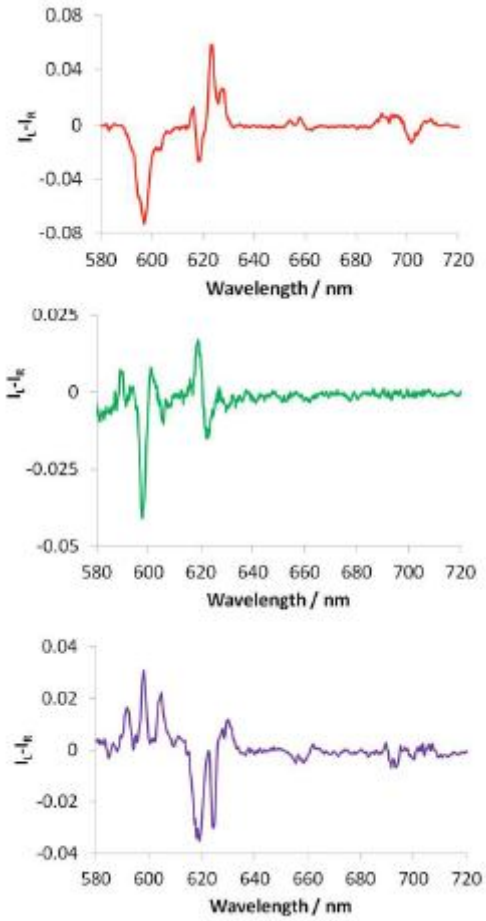

Figure 7.5 Circularly polarised luminescence (CPL) spectra of $[EuL^1(OH_2)]^+$ (20 μM) in the presence of: *top*, α_1-AGP (50 μM); *centre*, HSA (0.7 mM); *lower,* γ-immunoglobulins (0.3 mM).

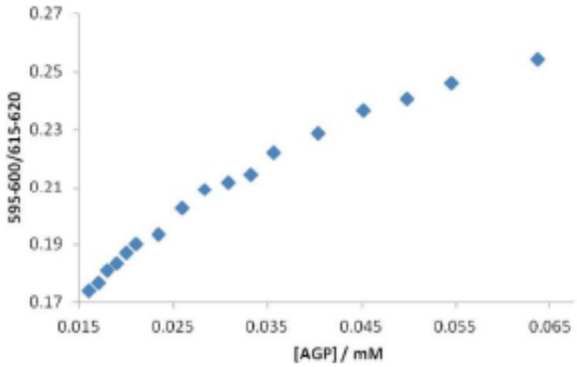

Figure 7.6 Variation of the emission intensity ratio of the Eu emission bands (620 vs 592 nm) as a function of *added* α_1-AGP for $[Eu\ L^1(OH_2)]^+$ (20μM, pH 7.4) in human serum solution (295K). The initial and final [α_1-AGP] concentration were measured to be 16μM and 65μM by an independent ELISA assay.

References

[1] a) H. Yoshima, A. Matsumoto, T. Mizuochi, T. Kawasaki, A. Kobata, J. Biol. Chem., **1981**, 256, 8476. b) T. Hochepied, F. G. Berger, H. Baumann, C. Libert, *Cytokine Growth Factor Rev.* **2003**, *14*, 25. c) T. Fournier, N. N. Medjaubi, D. Porquet, *Biochim. Biophys. Acta*, **2000**, *1482*, 157.

[2] a) F. Ceciliani, V. Pocacqua, *Curr. Protein Pept. Sci.* **2007**, *8*, 91. b) For the use of α_1-antitrypsin as a diagnostic tool: B. Lisowska-Myjak, *Clin. Chim. Acta* **2005**, *352*, 1.

[3] a) L. Budai, O. Ozohanics, K. Ludanyi, L. Drahos, T. Kremmer, I. Krenyacz, K. Vekey, *Anal. Bioanal. Chem.* **2009**, *393*, 991. b) H. H. Petersen, J. P. Nielsen, P. M. Heegard, *Vet. Res.* **2004**, *35*, 163.

[4] a) G. L. Trainor, *Expert Opin. Drug Discov.* **2007**, *2*, 51. b) K. M. Wasan, D. R. Brocks, S. D. Lee, K. Sachs-Barrable, S.J. Thornton, *Nat. Rev. Drug Discov.* **2008**, *7*, 84. c) F Herve, G. Caron, J-C. Duche, P. Gaillard, N. Abd. Rahman, A. Tsantili-Kakoulidou, P-A. d'Athis, P. Tillement, B. Testa, *Molec. Pharmacol.* **1998**, *54*, 129.

[5] D. L. Schonfeld, R. B. G. Ravelli, U. Mueller, A. Skera, *J. Mol. Biol.* **2008**, *384*, 393.

[6] K. Nishi, T. Ono, T. Nakamura, N. Fukunaga, M. Izumi, H. Watanabe, A. Suenaga, T. Maruyama, Y. Yamagata, S. Curry, M. Otagiri, *J. Biol. Chem.* **2011**, *286*, 14427.

[7] a) D. S. Hage, A. Jackson, M. R. Sobansky, J. E. Schiel, M. J. Yoo, K.S. Joseph, *J. Sep. Sci.* **2009**, *32*, 835. b) H. Matsunaga and J. Hoginaka, *J. Chromatogr. A*, **2006**, *1106*, 124.

[8] J. I. Bruce, S. Lopinski, D. Parker, R. D. Peacock, *Chirality*, **2002**, *14*, 562.

[9] a) C. P. Montgomery, E. J. New, D. Parker, R. D. Peacock, *Chem. Commun.* **2008**, 4261. b) D. M. Dias, J. M. C. Teixeira, I. Kuprov, E. J. New, D. Parker, C.F.G.C. Geraldes, *Org. Biomol. Chem.* **2011**, *9*, 5047.

[10] a) S. Aime, E. Gianolio, E. Terreno, R. Pagliarin, G. B. Giovenzana, M. P. Lowe, D. Parker, M. Sisti, G. Palmisano, M. Botta, *J. Biol. Inorg. Chem.* **2000**, *5*, 488. b) Y. O. Fung, W. Q. Wu, C. T. Yeung, H. K. Kong, K. K. C. Wong, W. S. Lo, G-L. Law, K. L. Wong, C. K. Lau, C. S. Lee, W. T. Wong, *Inorg. Chem.* **2011**, *50*, 5517. c) J. H. Tang, N. Lian, *Anal. Sci.* **2009**, *25*, 1237. d) C.P. Montgomery, E.J. New, L-O. Palsson, D. Parker, A.S. Batsanov, L. Lamarque, *Helv. Chim. Acta*, **2009**, *92*, 2186.

[11] a) J. Yu, R. Pal, D. Parker, R. A. Poole, M. J. Cann, *J. Am. Chem. Soc.* **2006**, *128*, 2294. b) B. S. Murray, E.J. New, R. Pal, D. Parker, *Org. Biomol. Chem.* **2008**, *6*, 2085. c) F. Kielar, E.J. New, G-L. Law, D. Parker, *Org. Biomol. Chem.* **2008**, *6*, 2256.

[12] a) E. J. New, D. Parker, *Chem. Sci.* **2010**, *1***,** 111. b) C. P. Montgomery, B. S. Murray, E. J. New, D. Parker, *Acc. Chem. Res.* **2009**, *42*, 925.

[13] X. Wang, X. Wang, Y. Wang, Z. Guo, *Chem. Commun.* **2011**, *47*, 8127.

[14] a) S. Dumas, V. Jacques, W.C. Sun, J.S. Troughton, J.T. Welch, J. M. Chasse, H. Schmitt-Willich, P. Caravan, *Invest. Radiol.* **2010**, *45*, 600. b) P. Caravan, *Acc. Chem. Res.,* **2009**, *42*, 851. c) P. Caravan, G. Parigi, J. M. Chasse, N. J. Cloutier, J. J. Ellison, R. B. Lauffer, C. Luchinat, S. A. McDermid, M. Spiller, T.J. McMurry, *Inorg. Chem.* **2007**, *46*, 6632. d) E. Gianolio, G. B. Giovenzana, D. Lango, I. Lango, I. Menegotto, S. Aime, *Chem. Eur. J.* **2007**, *13*, 5785. e) M. Botta, S. Avedano, G. B. Giovenzana, A. Lambardi, D. Longo, C. Cassino, L. Tei, S. Aime, *Eur. J. Inorg. Chem.* **2011**, *6*, 802.

[15] R. Carr, L. Di Bari, S. Lo Piano, D. Parker, R. D. Peacock and J. M Sanderson, *Dalton Trans.* **2012**, *41*, 13154.

[16] G-L. Law, C. Man, D. Parker, J. W. Walton, *Chem. Commun.* **2010**, *46*, 2391.

[17] J. W. Walton, L. Lamarque, D. Parker, J. Zwier, *Eur. J. Inorg. Chem.* **2010**, 3691.

[18] P. Atkinson, K.S. Findlay, F. Kielar, R. Pal, R.A. Poole, H. Puschmann, S.L. Richardson, P.A. Stenson, A.L. Thompson, J. Yu, *Org. Biomol. Chem.* **2006**, *4*, 1707.

[19] L. Dente, G. Ciliberto, R. Cortese, *Nucl. Acids Res.* **1985**, *13*, 3941.

[20] Y. Ye, A Godzik, *Protein Sci*. **2004**, *13*, 1841.

[21] F. Zsila, Y. Iwao, *Biochim Biophys. Acta.,* **2007**, *1770*, 797.

[22] Citrate and lactate analyses in serum or seminal fluid: a) R. Pal, A. Beeby, D. Parker *J. Pharmaceut. Biomed. Anal,* **2011**, *56*, 352. b) R. Pal, L. C Costello, D. Parker, *Org. Biomol. Chem*. **2009**, *7*, 1525. c) For urate analysis in urine or serum: R. A. Poole, F. Kielar, D. Parker, S. L. Richardson, P. A. Stenson, *Chem. Commun*. **2006**, 4084.

[23] The only reports of 'chiral' CPL probes for macromolecules have been based on enantioselective quenching of racemic complexes: a) S. C. J. Meskers, H.P.J.M. Dekkers, *J. Phys. Chem. A* **2001**, *105*, 4589; b) G. Muller, *Dalton Trans*. **2009**, 9692. c) CPL has also been used to probe local coordination in calcium binding sites of various proteins, following addition of the aqua lanthanide ion, e.g., N. Coruh, J. P. Riehl, *Biochemistry*, **1992**, *31*, 7970.

Conclusion

The work developed in this thesis was based on the correlation between lanthanide complexes structural and chiroptical properties. In order to have reliable geometrical information in solution, a new method for the separation of contact and pseudocontact shifts has been elaborated. During VCD spectra acquisition, a new enhancement mechanism of signals intensity in lanthanide containing complexes, for some specific elements, has been discovered. Finally, through fine ligand structural screening, a new chiral emissive Europium complex, specific for alpha-glycoprotein targeting, has been developed.

In particular, In Chapter 5, a modification of the Reilley protocol for pseudocontact separation in axial symmetric lanthanide complexes was proposed, in order to compensate for any variation in crystal field parameters. We discussed the standard and modified protocols on four sets of NMR data taken from the literature and on an unreported set for a chiral derivative of Ln DOTA, Ln DOTMA. We discussed the main limitation of the standard protocol, consisting of the necessity to restrict the analysis to some lanthanides characterized by similar crystal field parameter(s). In many cases, the change in these parameters may be not trivial and sometimes even unpredictable, which introduces a certain degree of arbitrariness. This is especially true in cases of significant axial ligand dynamics, where capped and non-capped forms may coexist and freely exchange, as notably found in catalytic systems and in MRI contrast agents. The proposed analysis offers a new 'lens', to extract the PCS from the total paramagnetic shifts. It has the merit of avoiding any more or less arbitrary partition into early and late lanthanides (or the notion of 'gadolinium break') and can effortlessly and seamlessly cope with changes in crystal field parameters arising e.g. from axial dynamics or from lanthanide contraction. We cannot and do not claim that the PCS extracted in this way are more accurate than any other, because their 'true' values are only experimentally accessible through a more or less questionable separation protocol. We only can say that they compare well with sets of geometrical factors arising from a structural optimization. In any case there is some degree of self-reference which invalidates the comparison.

Our procedure can be classified in the context of 'model free' methods, because it makes no assumption on a specific geometrical model and also avoids reference to Bleaney's constants. It can be used even if only a few (two) Ln derivatives of a certain complex are characterized, independent of the position of the elements in the series, i.e. early and late lanthanides can be analyzed simultaneously. One of the most interesting features of this new method is that we can even mix and treat together heterogeneous data, which is especially relevant in some specific cases where it may be difficult to know for sure the nature of the species observed in solution, as in the case of the binaphtholate heterobimetallic systems or in the presence of different structural forms such as in the DOTA derivatives.

In Chapter 6 we discussed in detail three cases of stable lanthanide chelates of C_4 –symmetry, where one can observe enhancement of VCD bands as a function of the nature of the normal mode and of the specific lanthanide ion. We demonstrated that, in the cases we studied so far, late lanthanides, and in particular Tm and Yb, provide the largest enhancements, which must be attributed to metal-centered low-lying electronic states with large magnetic dipole character. There are some features which make this effect attractive for further applications:

1) the enhanced VCD bands have in the large majority of cases the same sign independent of the lanthanide ion;
2) all the bands have regular absorption lineshapes;
3) different lanthanides may be more effective in different mid-IR regions allowing one to focus on specific spectroscopic features;
4) there is a wide literature concerning lanthanide complexes, and paramagnetic NMR provides the necessary complementary structural information;
5) lanthanides have been used as structural probes in protein and biomolecular NMR.

Likely it will possible to be able to take advantage of these points and use them in a more quantitative way, with potential interesting application in structure elucidation for the LIVE effect.

In Chapter 7 we discussed the development of the first chiroptical probe for the important protein, α_1-AGP. The Eu^{3+} complex binds α_1-AGP reversibly in aqueous solution. It exhibits a selectivity for α_1-AGP over α_1-AAT and the other major serum proteins of at least 12:1, as defined by the order of dissociation constants. The protein bound adduct apparently involves displacement of water, possibly via a glutamate side chain, leading to a more strongly emissive species with a distinctive spectral fingerprint. Chiroptical spectroscopy studies are indicative of formation of a protein-bound adduct that possesses a large induced CD and a characteristic CPL signal. It is hypothesised that in this adduct, one azaxanthone group remains coordinated to Eu via the pyridyl ring *N*, whilst the other is included into the same deep binding cavity that is used to bind to a variety of tricyclic heteroaromatic drugs. Binding to α_1-antitrypsin is identical at the metal coordination centre but is an order of magnitude weaker, possibly due to a less favourable hydrophobic interaction with the azaxanthone groups.

Using emission spectroscopy, it allows a direct and rapid assessment of increases in serum levels of the positive 'acute phase' proteins, α_1-AGP and α_1-antitrypsin, that accompany an acute response to inflammation.

Related publications

- Sebastiano Di Pietro, Samuele Lo Piano, Lorenzo Di Bari, ***'Pseudocontact shifts in lanthanide complexes with variable crystal field parameters'***, *Coordination Chemistry Reviews*, **2011**, *255*, 2810.

- Samuele Lo Piano, Sebastiano Di Pietro, Lorenzo Di Bari, ***'Shape-conserving enhancement of vibrational circular dichroism in lanthanide complexes'***, *Chemical Communications*, **2012**, *48*, 11996.

- Rachel Carr, Lorenzo Di Bari, Samuele Lo Piano, David Parker, Robert D. Peacock and John M. Sanderson, ***'A chiral probe for the acute phase proteins alpha-1-acid glycoprotein and alpha-1-antitrypsin based on europium luminescence'***, *Dalton Transactions*, **2012**, *41*, 13154.

Experimental Part

Materials and Methods

Instrumentation and measurements

All **VCD** spectra were acquired with a JASCO FVS-4000 instrument using BaF_2 cells and were baseline subtracted with spectra of the cell filled with blank solvent, using the same acquisition parameters and recorded immediately after, or immediately before, the sample. In all cases 6000 or 8000 scans were accumulated in the 2000-900 cm^{-1}, 2000-950 cm^{-1}, or 2000-1300 cm^{-1} wavenumber range.

The Ln DOTMA spectra (2000-900 cm^{-1}) were acquired as 0.05 M D_2O solutions in 50 μm BaF_2 cells.

The $Cs[Ln(hfbc)_4]$ spectra (2000-950 cm^{-1}) were acquired as 0.01 M $CDCl_3$ in 150 μm BaF_2 cells (in this case, the samples were sonicated for 20 minutes to assure a perfect solubilization).

The Ln DOPhA spectra (2000-1300 cm^{-1}) were acquired as 0.01 M CD_3OD solutions, in 150 μm cell.

^{1}H NMR (Varian Inova 600 operating at 14.1 T, and 25° C, in D_2O, $CDCl_3$ and CD_3OD) were collected for all compounds, with the exception of Gd-complexes.

Circularly polarised luminescence spectra (I_L-I_R) for $[EuL^1(OH_2)]^+$ were measured using a homebuilt CPL spectrometer (Glasgow University, UK) based on a Spex-Fluoromax-2-spectrofluorimeter. Samples were prepared using aqueous solutions containing 0.1 M NaCl in disposable UV-grade methacrylate cuvettes. The samples were pH adjusted to 7.4 using c. HCl and c. NaOH and then lyophilised for transportation. Samples were redissolved in D_2O and run at room temperature using indirect excitation at 340 nm. The measured wavelength range was 400-800 nm.

Absorption UV/vis. and **ECD** spectra were acquired on a JASCO V650 spectrophotometer and a JASCO J715 spectropolarimeter respectively. Samples were run in cylindrical quartz cells at room temperature. The band width was set to 2.0 nm, response to 1 sec and scan speed to 50 nm/min. Up to 4 accumulations were averaged to improve S/N. The total concentration of $[EuL^1(OH_2)]^+$ alone and in a 1:1 (mol/mol) mixture with α_1-AGP was 41.3 μM. In all cases the absorbance and dichroism data were scaled for the total concentration of $[EuL^1(OH_2)]^+$ to yield ε' and Δε' (the prime indicates that the real concentration of the ECD-active species is uncertain).

Emission spectra were recorded on an ISA Joblin-Yvon Spex Fluorolog-3 luminescence spectrometer (Durham University, UK). Quartz cuvettes with a pathlength of 1 cm were used to contain all samples. Luminescence titrations were carried out at pH 7.4 using aqueous solutions containing 0.1 M NaCl in order to maintain a constant ionic background. For α_1-AGP, Fibrinogen, apo-Transferrin and α_1-antitrypsin, volumetric addition of stock solutions was carried out. In the case of HSA and γ-Ig-G, the protein was added directly to the solution as a lyophilised solid. In each case, the pH was adjusted following protein addition. Data were analysed as described in reference 22, Chapter 7.

Synthesis and materials

Lanthanides salts were used as received from Aldrich and stored in a desiccators with P_2O_5. All the solvents were reagent or HPLC grade. Triethyl amine was freshly distilled and stored on KOH pellets. All proteins were purchased from Sigma.

Preparation of Na[Ln(DOTMA)]

Na[Ln(DOTMA)] were synthetized according to a described procedure.[34]

A stoichiometric amount of 0.1 M lanthanide chloride, or triflate (La, Sm), or nitrate (Pr), aqueous solution was added to solid DOTMA. The resulting mixtures were heated up to 80°C and kept stirring for 24 h. Diluted NaOH solution was then added in each case to pH 6.5 and finally water was removed by evaporation. The NMR characterization can be found elsewhere.[35]

Preparation of Ln[Cs(hfbc)$_4$]

Ln[Cs(hfbc)$_4$] complexes were prepared according to the literature procedure,[36] by shaking the hfbc ligand (100 μL, 3.5 10^{-4} mol) in chloroform (20 mL) with an aqueous solution (20 mL) of the lanthanide chloride or triflate in 3:1 ratio (ca. 70 mg for a Ln triflate or ca. 30 for a Ln chloride, 1.17 10^{-4} mol), in the presence of a slight molar excess (with respect to the ligand) of triethyl amine (ca. 50 μL, 3.5 10^{-4} mol). The organic phase was then treated with an aqueous solution of CsCl. The solution was evaporated and the solid solubilized with the minimum amount of hot acetonitrile. In a few days (1-4), almost colorless needle-like crystals of the complexes, that can be filtered and dried under vacuum. The yield of these preparations is low (less than 20%) and not quantified.

Cs[Lu((+)-hfbc)$_4$]: the complex is prepared using Luthetium(III) chloride and (+)-hfbc. ^{1}H-NMR (600MHz, $CDCl_3$, 25°C) δ = 0.80 (s, 3H), 0.82 (s, 3H), 0.89 (s, 3H), 1.12 (m, 1H), 1.26 (m, 1H), 1.45 (m, 1H), 1.89 (m, 1H), 2.60 (m, 1H).

Cs[Eu((+)-hfbc)$_4$]: the complex is prepared using Europium(III) triflate and (+)-hfbc. ^{1}H-NMR (600MHz, $CDCl_3$, 25°C) δ= -6.35 (br s, 1H), -4.55 (br s, 1H), -2.72 (br s, 4H), -1.66 (br s, 1H), -0.99 (br s, 1H), -0.89 (br s, 3H), 5.2 (br s, 3H).

Cs[Tb((+)-hfbc)$_4$]: the complex is prepared using Terbium(III) triflate and (+)-hfbc. ^{1}H-NMR (600MHz, $CDCl_3$, 25°C) δ= -76.04 (br s, 3H), 26.84 (br s, 3H), 49.76 (br s, 1H), 58.64 (br s, 3H), 60.55 (br s, 1H), 97.11 (br s, 1H), 98.54 (br s, 1H), 122.90 (br s, 1H).

[34] H. G. Brittain, J. F. Desreux, *Inorg. Chem.* **1984**, *23*, 4459.
[35] S. Di Pietro, S. Lo Piano, L. Di Bari, *Coord. Chem. Rev.* **2011**, *255*, 2810 and Table 5.13.
[36] H. Sato, T. Taniguchi, A. Nakahashi, K. Monde, A. Yamagishi, *Inorg. Chem.* **2007**, *46*, 6755.

Cs[Tm((+)-hfbc)$_4$]: the complex is prepared using Thulium(III) chloride and (+)-hfbc. ^{1}H-NMR (600MHz, $CDCl_3$, 25°C) δ= -146.45 (br s, 1H), -117.20 (br s, 1H), -109.31 (br s, 1H), -97.57 (br s, 3H), -67.79 (br s, 3H), -67.01 (br s, 1H), -55.69 (br s, 1H), 97.57 (br s, 3H).

Cs[Yb((+)-hfbc)$_4$]: the complex is prepared using Ytterbium(III) triflate and (+)-hfbc. ^{1}H-NMR (600MHz, $CDCl_3$, 25°C) δ= -25.09 (br s, 1H), -19.92 (br s, 1H), -17.20 (br s, 1H), -10.87 (br s, 3H), -10.37 (br s, 1H), -8.83 (br s, 1H), -4.70 (br s, 3H), 17.68 (br s, 3H).

Preparation of the Ln DOPhA complexes

Ligand DOPhA and Ln DOPhA complexes were synthetized according to a described procedure.[37]

1,4,7,10-Tetrakis-[(*S*)-1-(1-phenyl)ethylcarbamoylmethyl]-1,4,7,10-tetraazacyclododecane (*DOPhA*)*:*

Chloroacetylchloride (76.0 mmol) in dry diethyl ether (200 mL) was added dropwise to a stirred solution of (*S*)-α-methylbenzylamine (61.0 mmol) and triethylamine (61.0 mmol) in dry diethyl ether (30 mL) at -20°C. The reaction mixture was allowed to warm to room temperature and stirred for 1 h. The resulting white precipitate was dissolved in water (600 mL) and the organic layer washed with hydrochloric acid (0.1 M, 500 mL), water (3 x 300 mL), dried (K_2CO_3) and the solvent removed in vacuo to yield a white solid. Recrystallisation from diethyl ether yielded white needles, yield 35%. The NMR data were fully compatible with those reported in the cited literature.

A solution of *(S)-N*-2-chloroethanoyl-1-phenylethylamine (13.9 mmol) in dry *N,N*-dimethylformamide (2.5 mL) was added to a stirred mixture of 1,4,7,10-tetraazacyclododecane (2.8 mmol) and fine mesh anhydrous potassium carbonate (13.9 mmol) in dry *N,N*-dimethylformamide (25 mL) under a nitrogen atmosphere. The reaction mixture was heated at 60°C for 48 h. The solvent was removed by distillation in vacuo and the resulting brown oil was extracted into dichloromethane (20 mL), washed with water (3x20 mL) and brine (20 mL), dried (K_2CO_3) and the solvent removed in vacuo to yield a yellow oil. The product was purified by alumina column chromatography (gradient elution from dichloromethane to 2% methanoldichlorometha-ne). Recrystal-lization from acetonitrile adding hexane yielded white needles, 25%.

^{1}H-NMR (250 MHz, $CDCl_3$, 25°C): δ= 7.28 - 7.21 (m, 20H, Ar), 6.90 (d, ^3J=8.1 Hz, 4H, NH), 5.10 (br t, ^3J=7.5 Hz, 4H, CH), 2.86 (br s, 8H, CH_2CO), 2.50 (br s, 16H, ring-CH_2), 1.46 (br d, ^3J=6.9 Hz, 12H, CH_3).

Ln DOPhA: 0.080 mmol of lanthanium chloride (Er, Tm and Lu), or triflate (Yb) and trimethylorthoformate (0.85 mL) were heated at reflux in dry acetonitrile (0.85 mL) for 2 h. A stoichiometric amount of ligand in dry acetonitrile (0.43 mL) was added and the solution heated at reflux for further 18 h for triflate complexes, and 66 h for chloride ones. The solution was concentrated and added dropwise with stirring to diethyl ether (30 mL). The resulting solid was filtered, washed with acetonitrile and dried in vacuo.

[37] R. S. Dickins, J. A. K. Howard, C. L. Maupin, J. M. Moloney, D. Parker, J. P. Riehl, G. Siligardi, and J. A. G. Williams, *Chem. Eur. J.* **1999**, *5*, 1095.

[ErDOPhA]Cl_3 : This complex was prepared from Erbium(III) chloride (0.08 mmol) and ligand *DOPhA* (0.08 mmol) by the method described above. White solid, yield 53%. ^{1}H-NMR (300 MHz, CD_3OD, 25°C): δ=119 (br s, 4H, ring-H_{ax}), 14.6 (br s, 4H, ring-H_{eq}), 5.42 (br s, 4H, ring-H_{eq}), 4.60 ± 3.30 (m, 20H, Ar), -0.994 (s, 4H, CH), -4.26 (s, 12H, CH_3), -38.9 (s, 4H, CH_2CO), -42.7 (br s, 4H, ring-H_{ax}), -74.3 (br s, 4H, CH_2CO).

[TmDOPhA]Cl_3 : This complex was prepared from Thulium(III) chloride (0.08 mmol) and ligand *DOPhA* (0.08 mmol) by the method described above. White solid, yield 54%. ^{1}H-NMR (300 MHz, CD_3OD, 25°C): δ=280 (br s, 4H, ring-H_{ax}), 47.9 (br s, 4H, ring-H_{eq}), 36.9 (br s, 4H, ring-H_{eq}), 3.45 (s, 12H, CH_3), -2.91 (s, 4H, CH), -12.1 ± -13.6 (m, 20H, Ar), (m, 20H, Ar), -82.6 (s, 4H, CH_2CO), -95.5 (br s, 4H, ring-H_{ax}), -134 (br s, 4H, CH_2CO).

[YbDOPhA]$(CF_3SO_3)_3$: This complex was prepared from Ytterbium(III) triflate (0.08 mmol) and ligand *DOPhA* (0.08 mmol) by the method described above. Yellowish solid, yield 49%. ^{1}H-NMR (300 MHz, CD_3OD, 25°C): δ=109 (br s, 4H, ring-H_{ax}), 20.4 (br s, 4H, ring-H_{eq}), 17.0 (br s, 4H, ring-H_{eq}), 5.04 ±1.95 (m, 20H, Ar), -0.51 (s, 4H, CH), -3.78 (s, 12H, CH_3), -29.5 (s, 4H, CH_2CO), -35.7 (br s, 4H, ring-H_{ax}), -69.7 (br s, 4H, CH_2CO).

[LuDOPhA]Cl_3 : This complex was prepared from Luthetium(III) chloride (0.08 mmol) and ligand *DOPhA* (0.08 mmol) by the method described above. White solid, yield 56%. ^{1}H-NMR (300 MHz, CD_3OD, 25°C): δ=7.46 ± 7.24 (m, 20H, Ar), 4.62 (br s, 4H, CH), 3.18 (br tr, ^2J = 15 Hz, 8H, CH_2CO), 2.71 (d, ^2J = 15 Hz, 4H, ring-C*H*H), 2.40 (br d, ^2J = 12 Hz, 4H, ring-C*H*H), 2.15 (br d, ^2J = 15 Hz, 4H, ring-C*H*H), 1.67 (br d, ^2J = 15 Hz, 4H, ring-C*H*H) , 1.59 (d, ^3J = 6 Hz, 12H, CH_3).

Protein Structure Alignment

Flexible protein structure alignment was performed on representative PDB entries for α_1-AGP (3KQ0) and α_1-AAT (9API) using the FATCAT algorithm,[38] with the twist parameter *t* set to a maximum of 5.2.

Although globally the two structures were not significantly similar, local structure alignments yielded 126 equivalent positions with a root mean square deviation of 3.72 Å for a value of *t* = 4. Amongst these, the location of two sets of glutamates is striking.

The first involves the second glutamate in the sequence NEEY of α_1-AGP (residues 34–37), which lies over the entrance to the hydrophobic binding pocket and in close proximity in the modelled structure to the second glutamate of the sequence TEEA from α_1-AAT (residues 150–153, Fig. A2.1 A, B).

The second involves E64 of α_1-AGP, which lies on the face of the β-sheet in the hydrophobic binding pocket of this protein. In the modelled structure, E206 of α_1-AAT lies in close proximity to this residue, although there are differences in the side-chain orientations of these residues (Fig. A2.1 C).

[38] Y. Ye and A. Godzik, *Nucleic Acids Res.* **2004**, *32*, W582.

Appendix 1

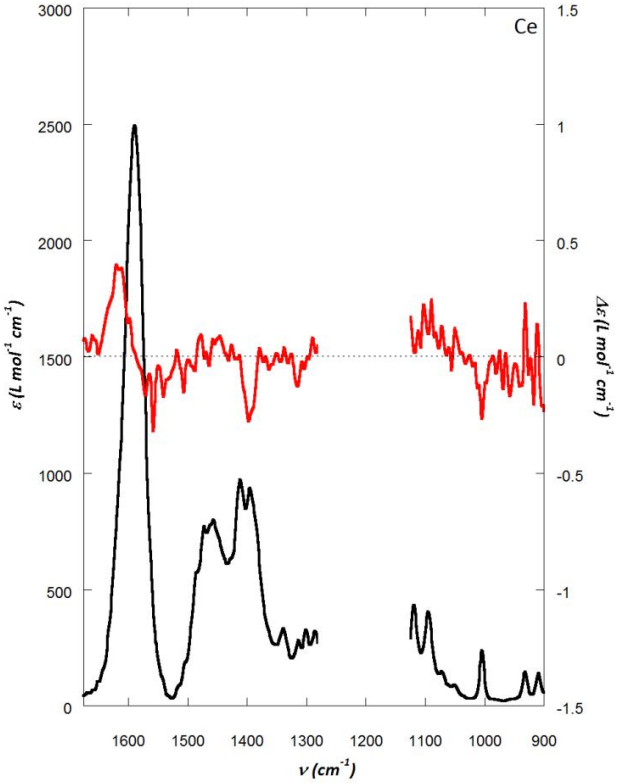
Ce
ε (L mol⁻¹ cm⁻¹)
Δε (L mol⁻¹ cm⁻¹)
ν (cm⁻¹)

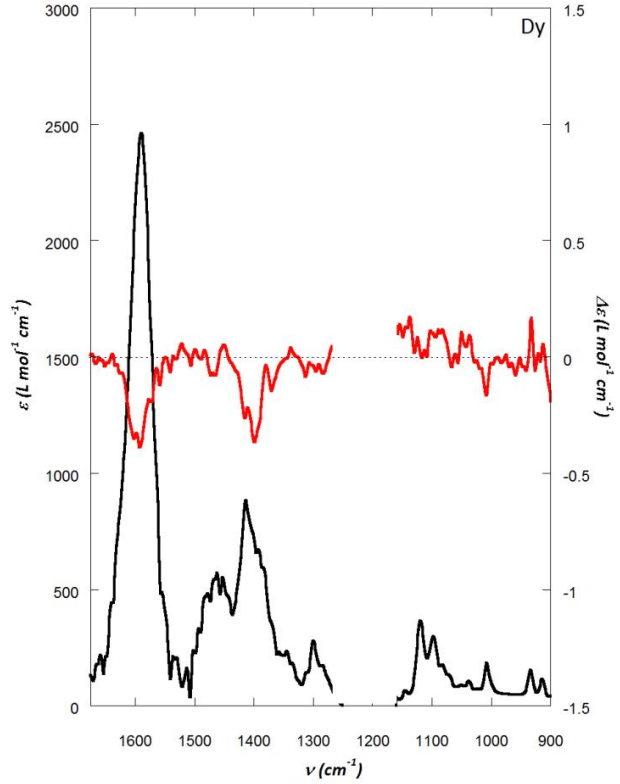
Dy
ε (L mol⁻¹ cm⁻¹)
Δε (L mol⁻¹ cm⁻¹)
ν (cm⁻¹)

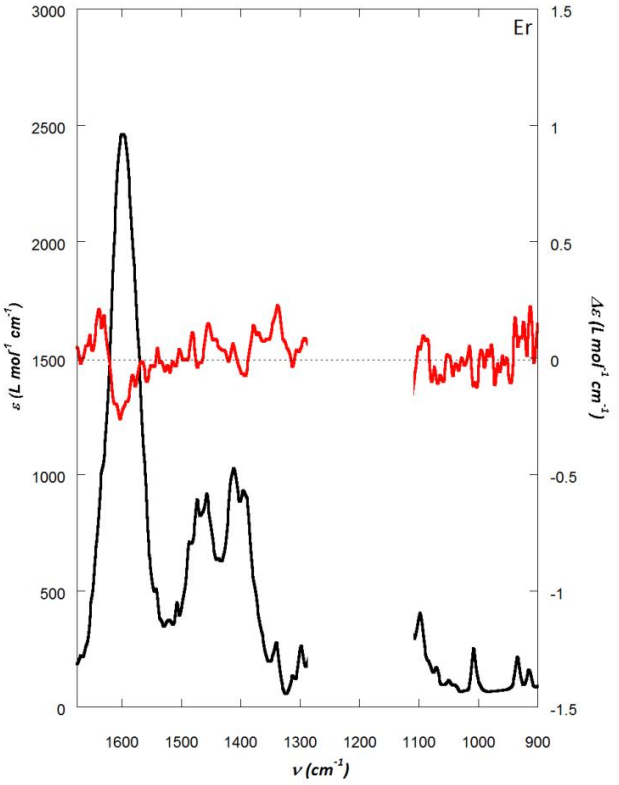
Er
ε (L mol⁻¹ cm⁻¹)
Δε (L mol⁻¹ cm⁻¹)
ν (cm⁻¹)

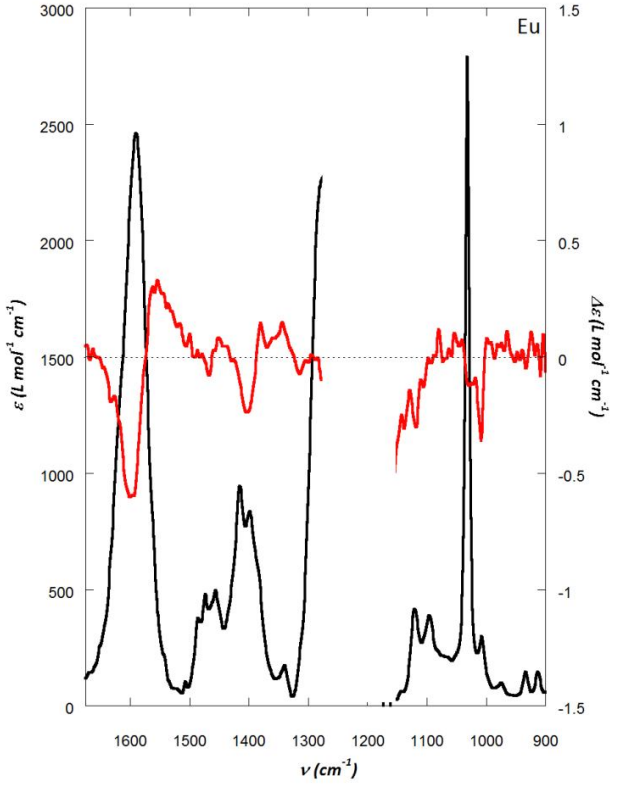
Eu
ε (L mol⁻¹ cm⁻¹)
Δε (L mol⁻¹ cm⁻¹)
ν (cm⁻¹)

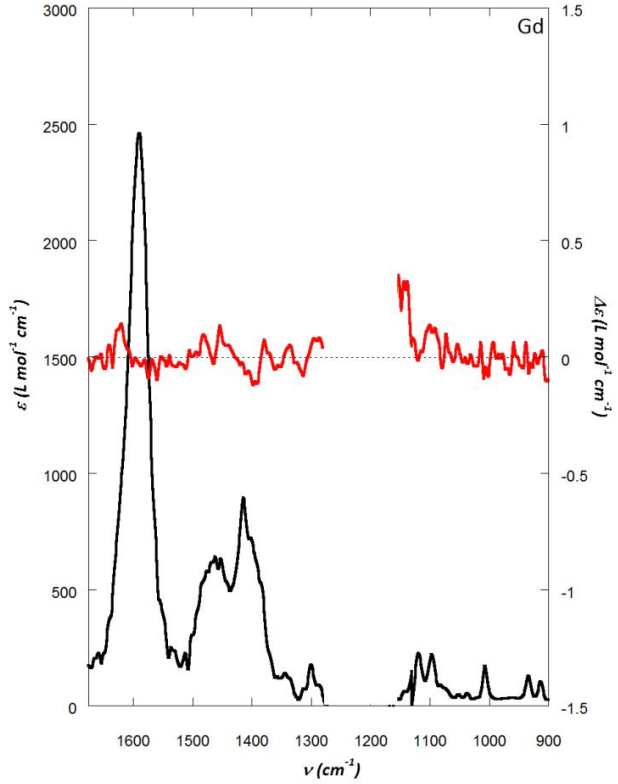
Gd
ε (L mol-1 cm-1)
Δε (L mol-1 cm-1)
ν (cm-1)

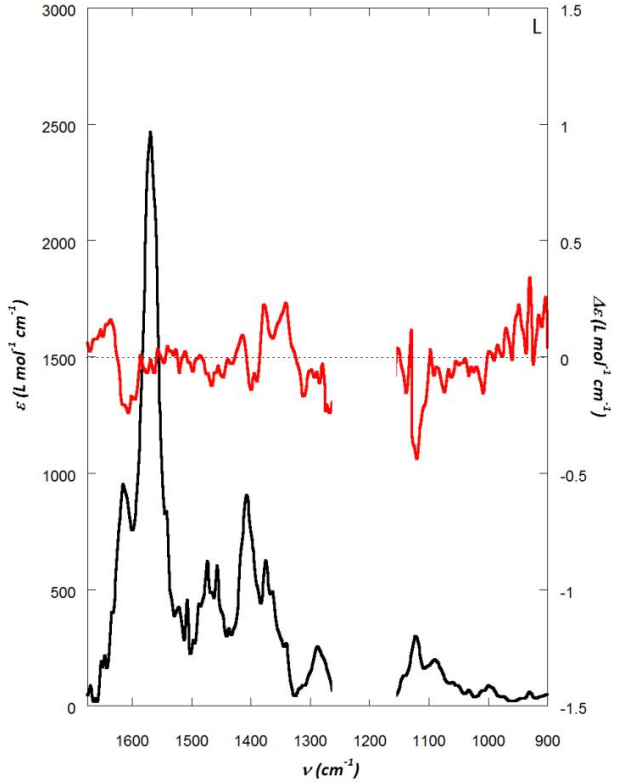
L
ε (L mol-1 cm-1)
Δε (L mol-1 cm-1)
ν (cm-1)

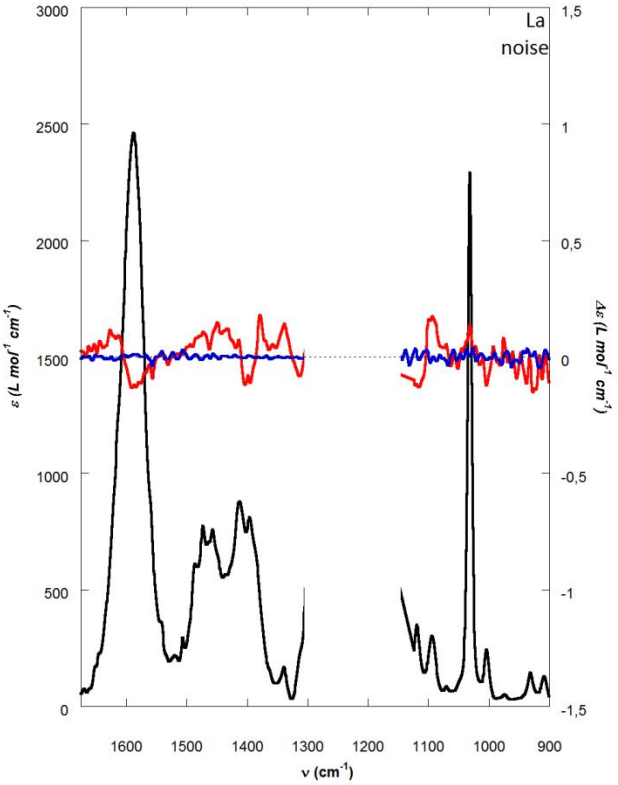
La
noise
ε (L mol-1 cm-1)
Δε (L mol-1 cm-1)
ν (cm-1)

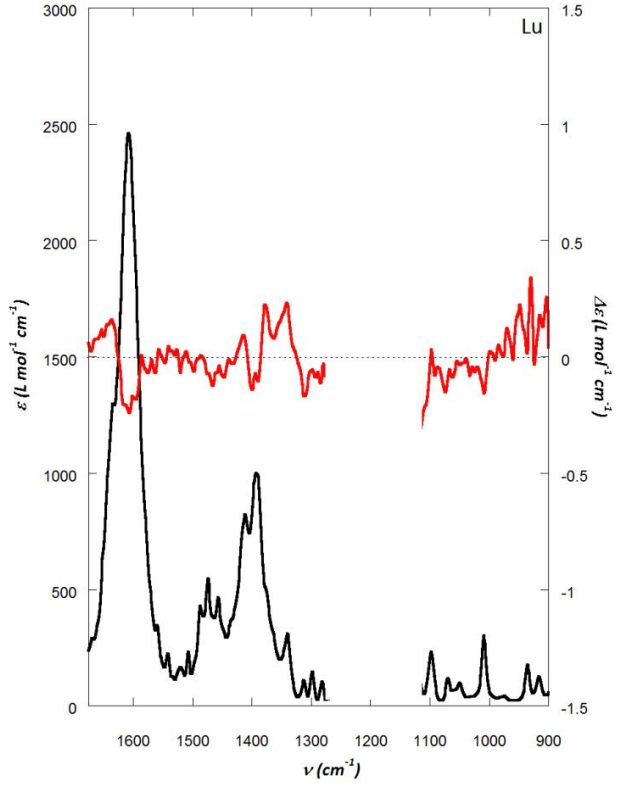
Lu
ε (L mol-1 cm-1)
Δε (L mol-1 cm-1)
ν (cm-1)

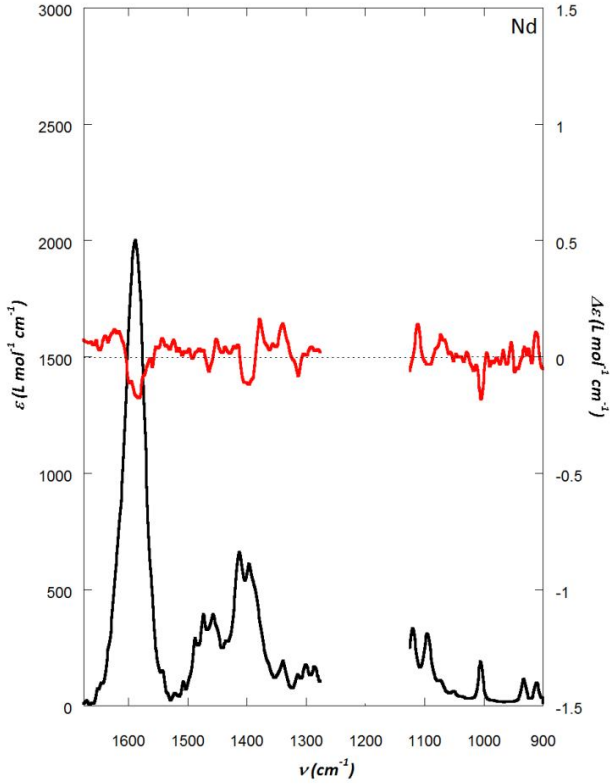
Nd
ε (L mol-1 cm-1)
Δε (L mol-1 cm-1)
ν (cm-1)

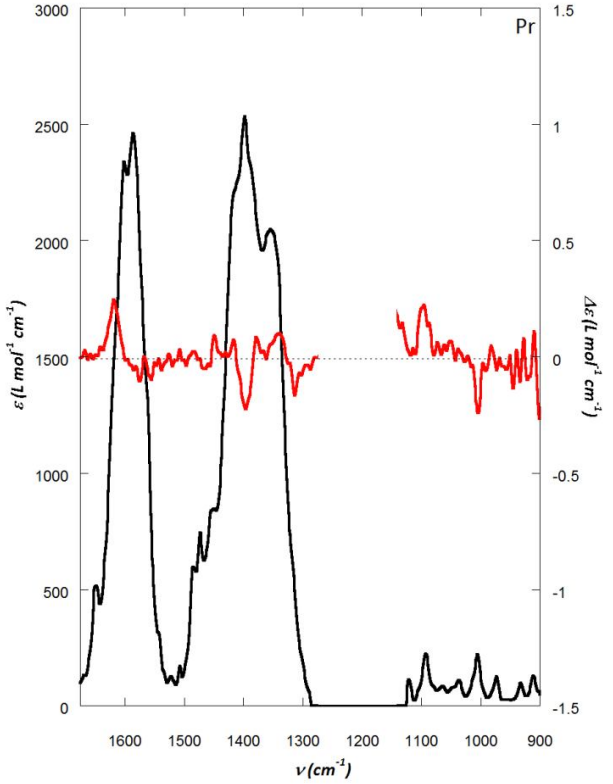
Pr
ε (L mol-1 cm-1)
Δε (L mol-1 cm-1)
ν (cm-1)

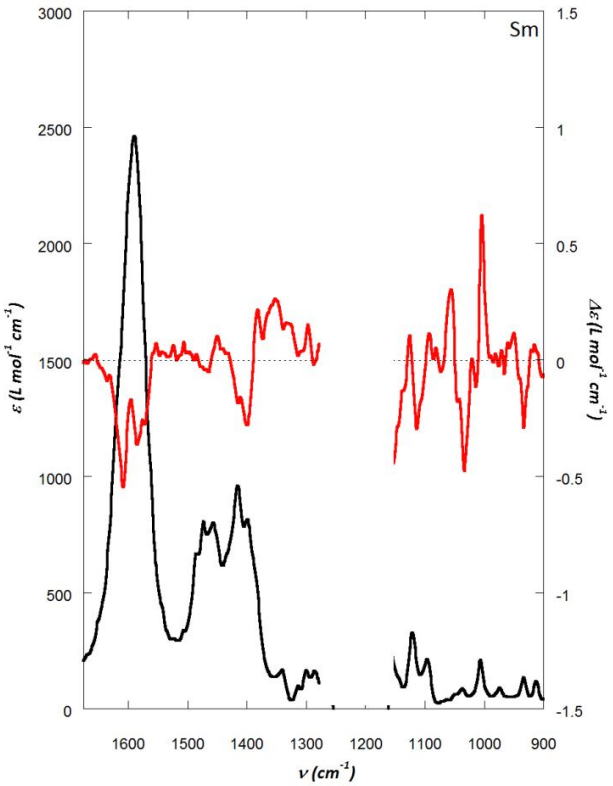
Sm
ε (L mol-1 cm-1)
Δε (L mol-1 cm-1)
ν (cm-1)

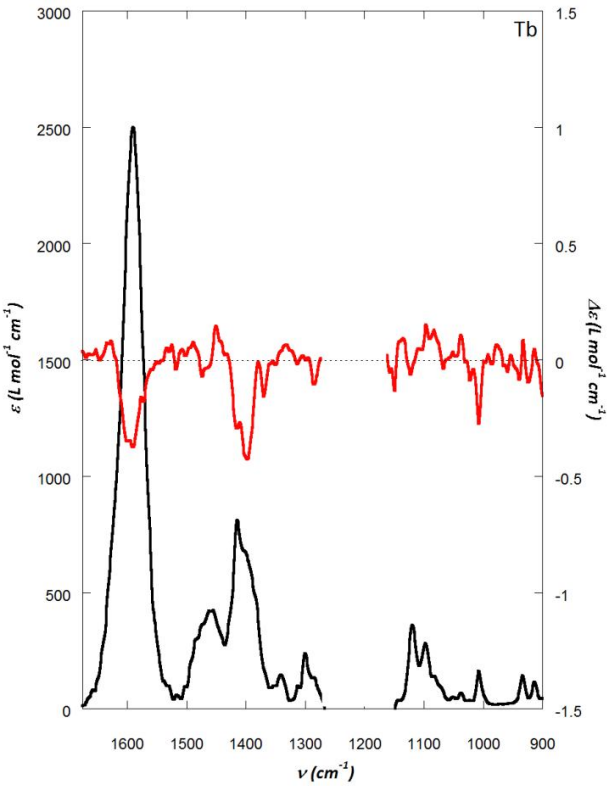
Tb
ε (L mol-1 cm-1)
Δε (L mol-1 cm-1)
ν (cm-1)

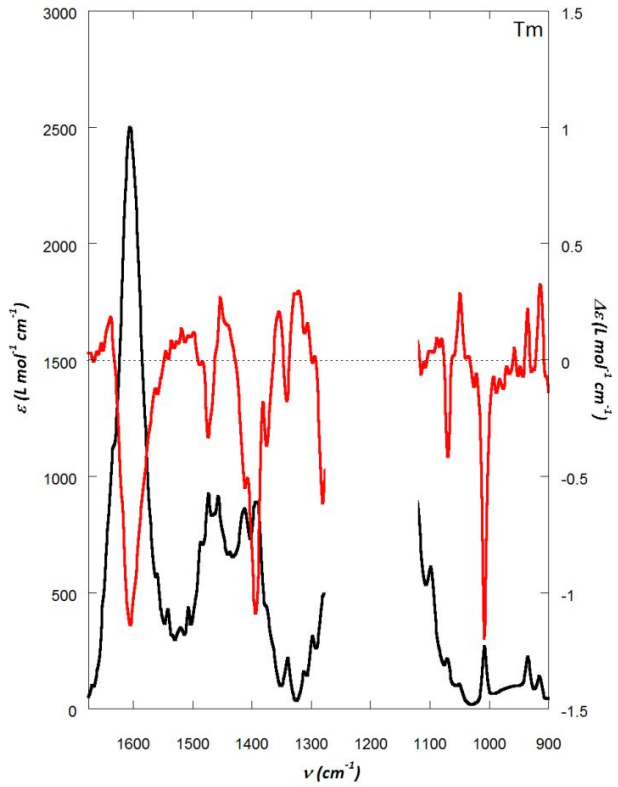
Tm
3000
2500
2000
1500
1000
500
0
1.5
1
0.5
0
-0.5
-1
-1.5
1600 1500 1400 1300 1200 1100 1000 900
ν (cm-1)
ε (L mol-1 cm-1)
Δε (L mol-1 cm-1)

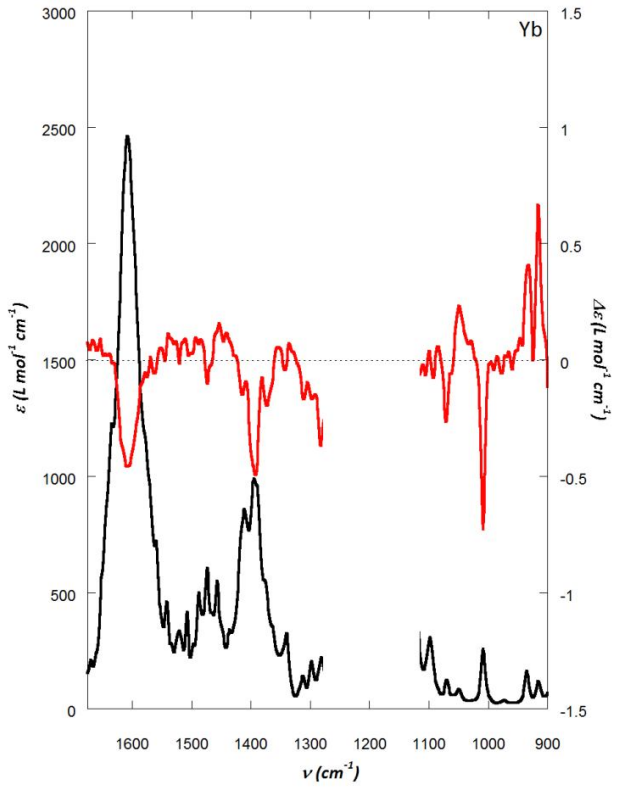
Yb
3000
2500
2000
1500
1000
500
0
1.5
1
0.5
0
-0.5
-1
-1.5
1600 1500 1400 1300 1200 1100 1000 900
ν (cm-1)
ε (L mol-1 cm-1)
Δε (L mol-1 cm-1)

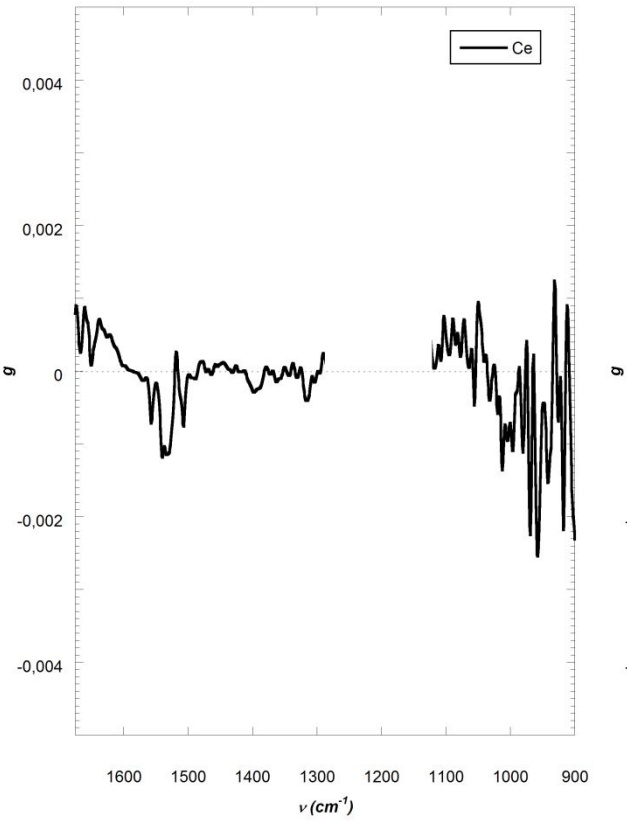
Ce
0,004
0,002
0
-0,002
-0,004
g
1600 1500 1400 1300 1200 1100 1000 900
ν (cm-1)

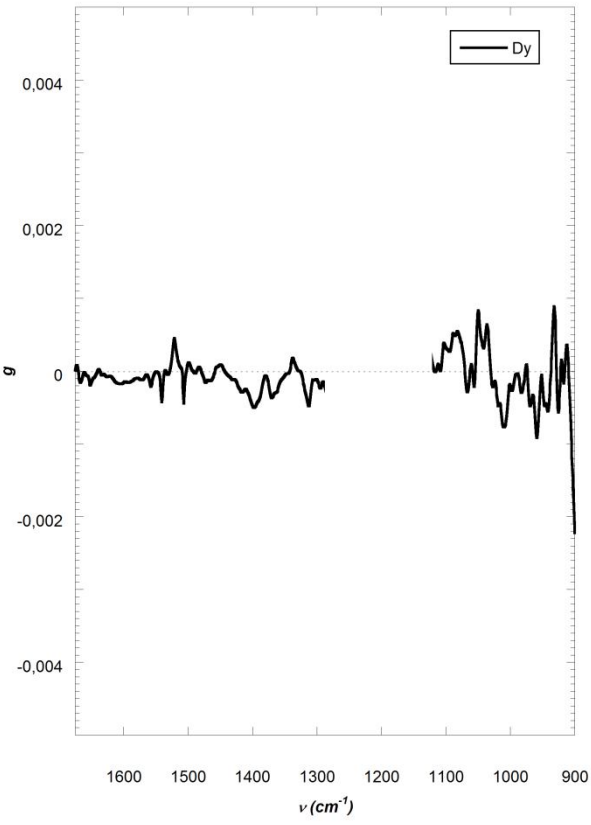
Dy
0,004
0,002
0
-0,002
-0,004
g
1600 1500 1400 1300 1200 1100 1000 900
ν (cm-1)

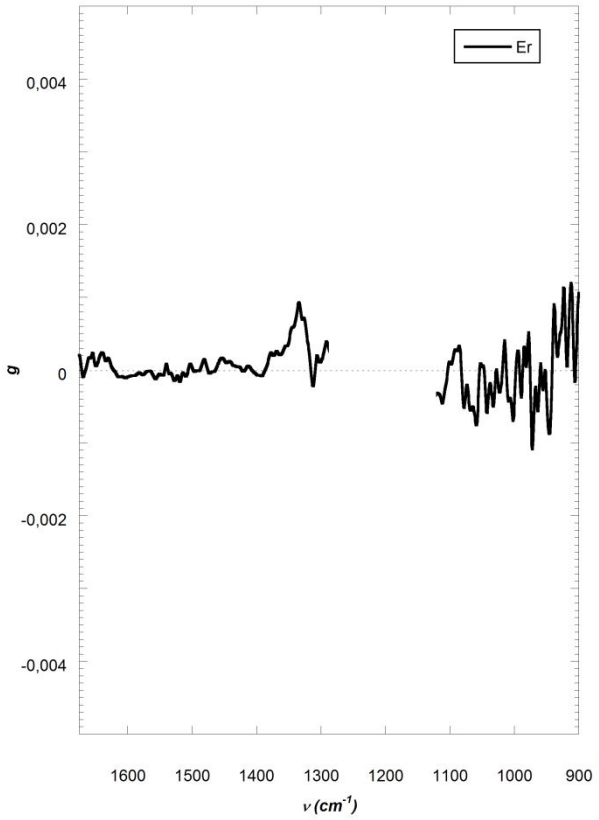
Er
0,004
0,002
0
-0,002
-0,004
g
1600 1500 1400 1300 1200 1100 1000 900
ν (cm-1)

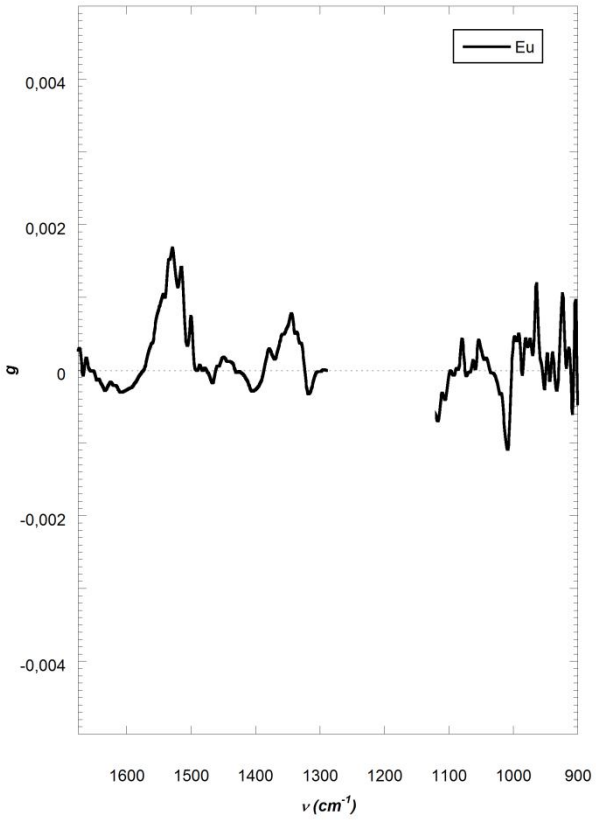
Eu
0,004
0,002
0
-0,002
-0,004
g
1600 1500 1400 1300 1200 1100 1000 900
ν (cm-1)

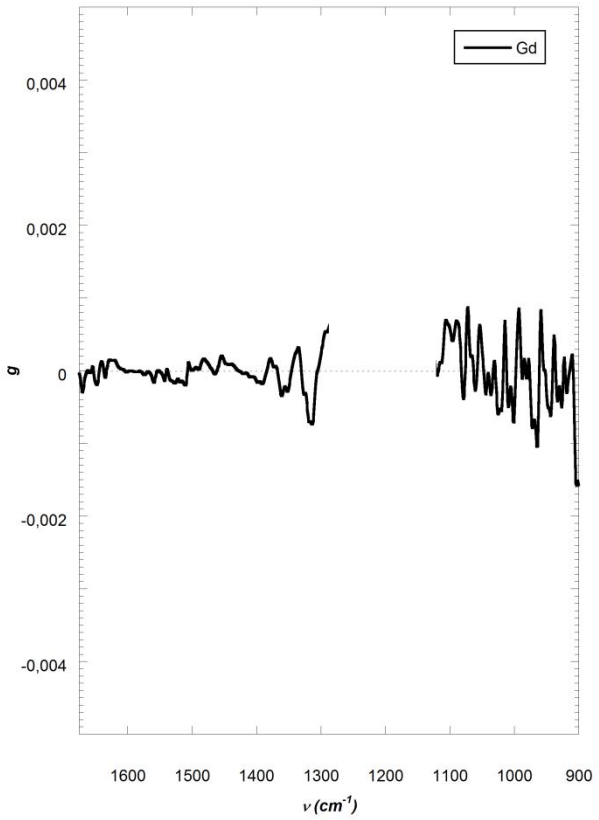
Gd
0,004
0,002
0
-0,002
-0,004
g
1600 1500 1400 1300 1200 1100 1000 900
ν (cm-1)

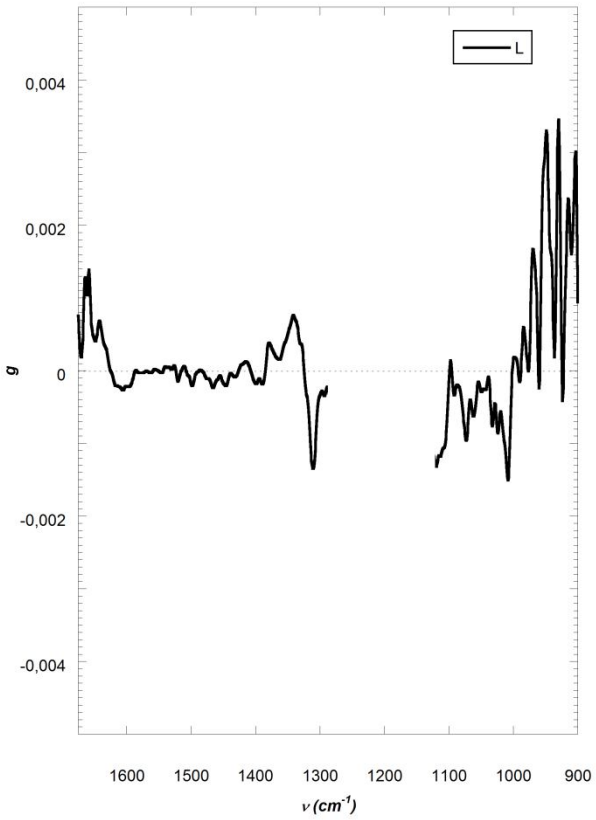
L
0,004
0,002
0
-0,002
-0,004
g
1600 1500 1400 1300 1200 1100 1000 900
ν (cm-1)

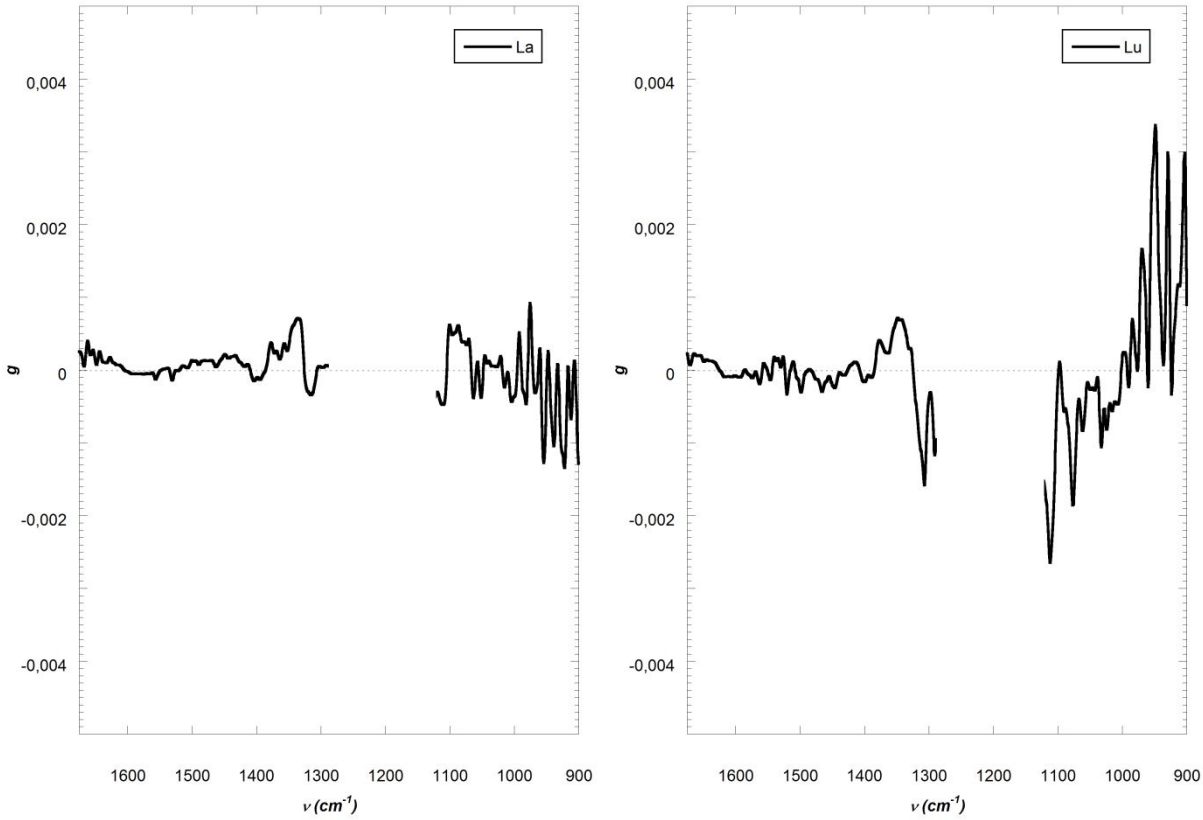
La
0,004
0,002
0
-0,002
-0,004
g
1600 1500 1400 1300 1200 1100 1000 900
ν (cm-1)

Lu
0,004
0,002
0
-0,002
-0,004
g
1600 1500 1400 1300 1200 1100 1000 900
ν (cm-1)

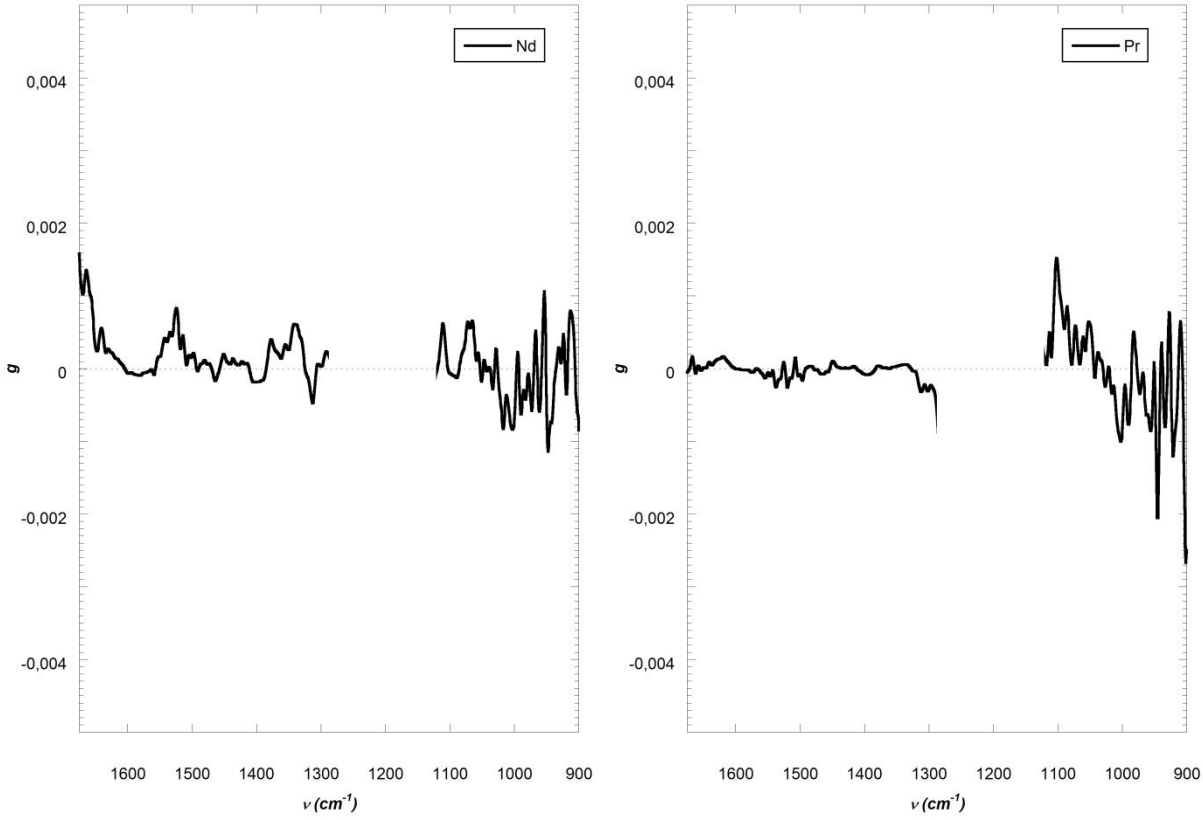
Nd
0,004
0,002
0
-0,002
-0,004
g
1600 1500 1400 1300 1200 1100 1000 900
ν (cm-1)

Pr
0,004
0,002
0
-0,002
-0,004
g
1600 1500 1400 1300 1200 1100 1000 900
ν (cm-1)

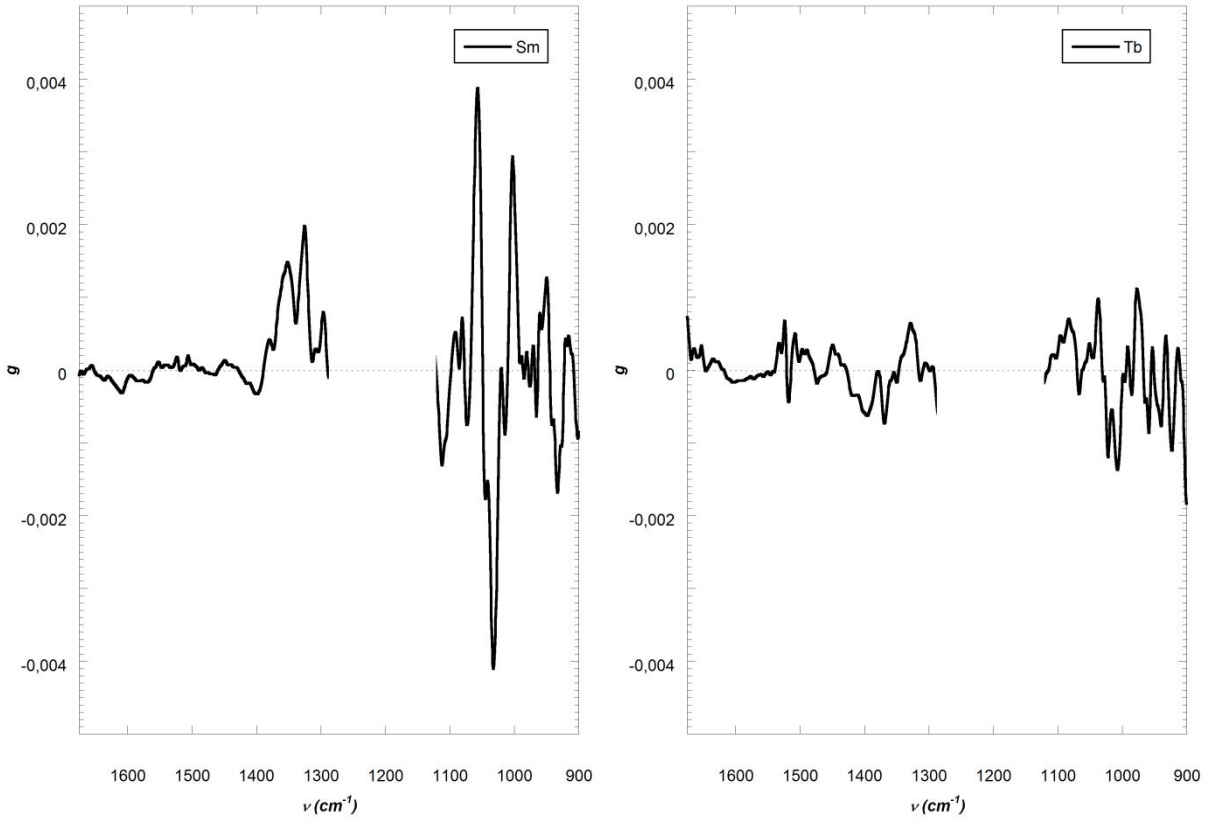
Sm
0,004
0,002
0
-0,002
-0,004
g
1600 1500 1400 1300 1200 1100 1000 900
ν (cm-1)

Tb
0,004
0,002
0
-0,002
-0,004
g
1600 1500 1400 1300 1200 1100 1000 900
ν (cm-1)

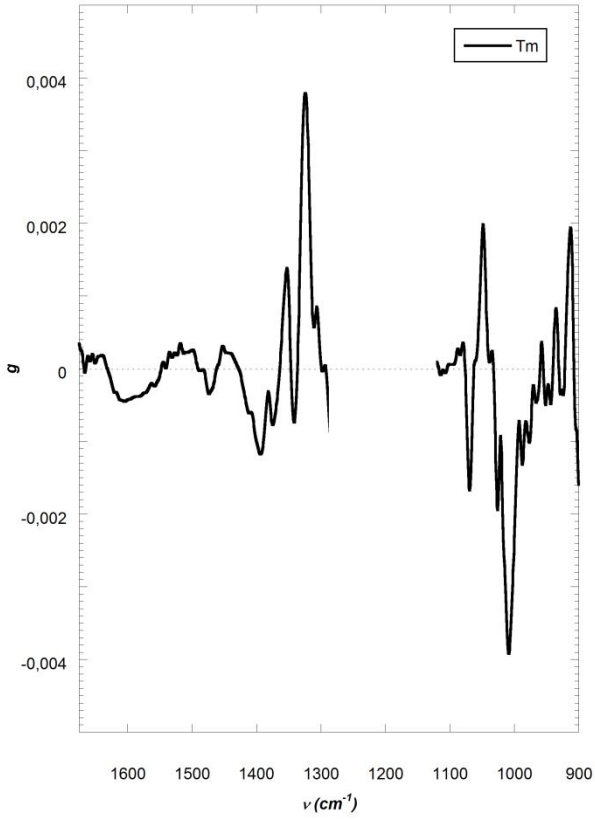
Tm
0,004
0,002
0
-0,002
-0,004
g
1600 1500 1400 1300 1200 1100 1000 900
ν (cm-1)

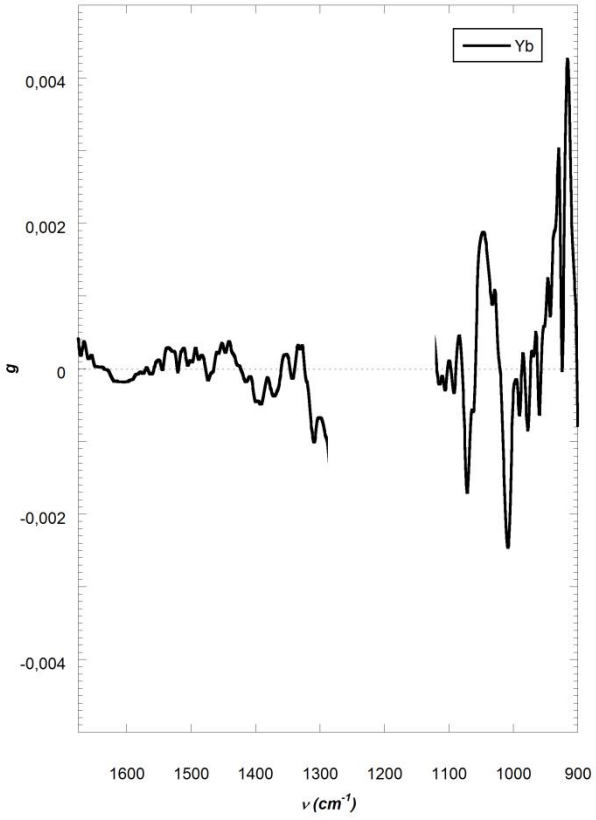
Yb
0,004
0,002
0
-0,002
-0,004
g
1600 1500 1400 1300 1200 1100 1000 900
ν (cm-1)

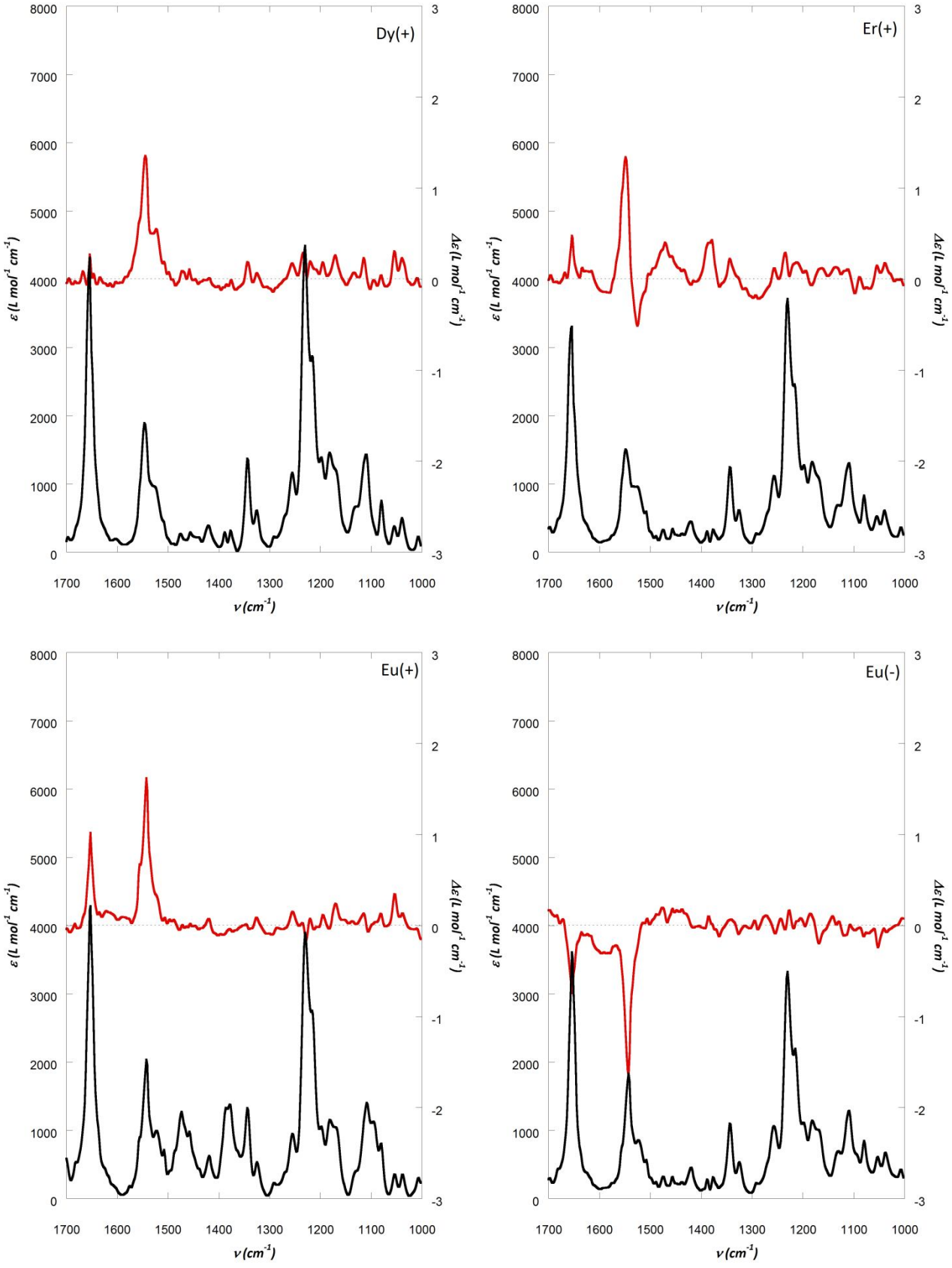
Dy(+)
Er(+)
Eu(+)
Eu(-)
ε (L mol-1 cm-1)
Δε (L mol-1 cm-1)
ν (cm-1)
8000
7000
6000
5000
4000
3000
2000
1000
0
3
2
1
0
-1
-2
-3
1700
1600
1500
1400
1300
1200
1100
1000

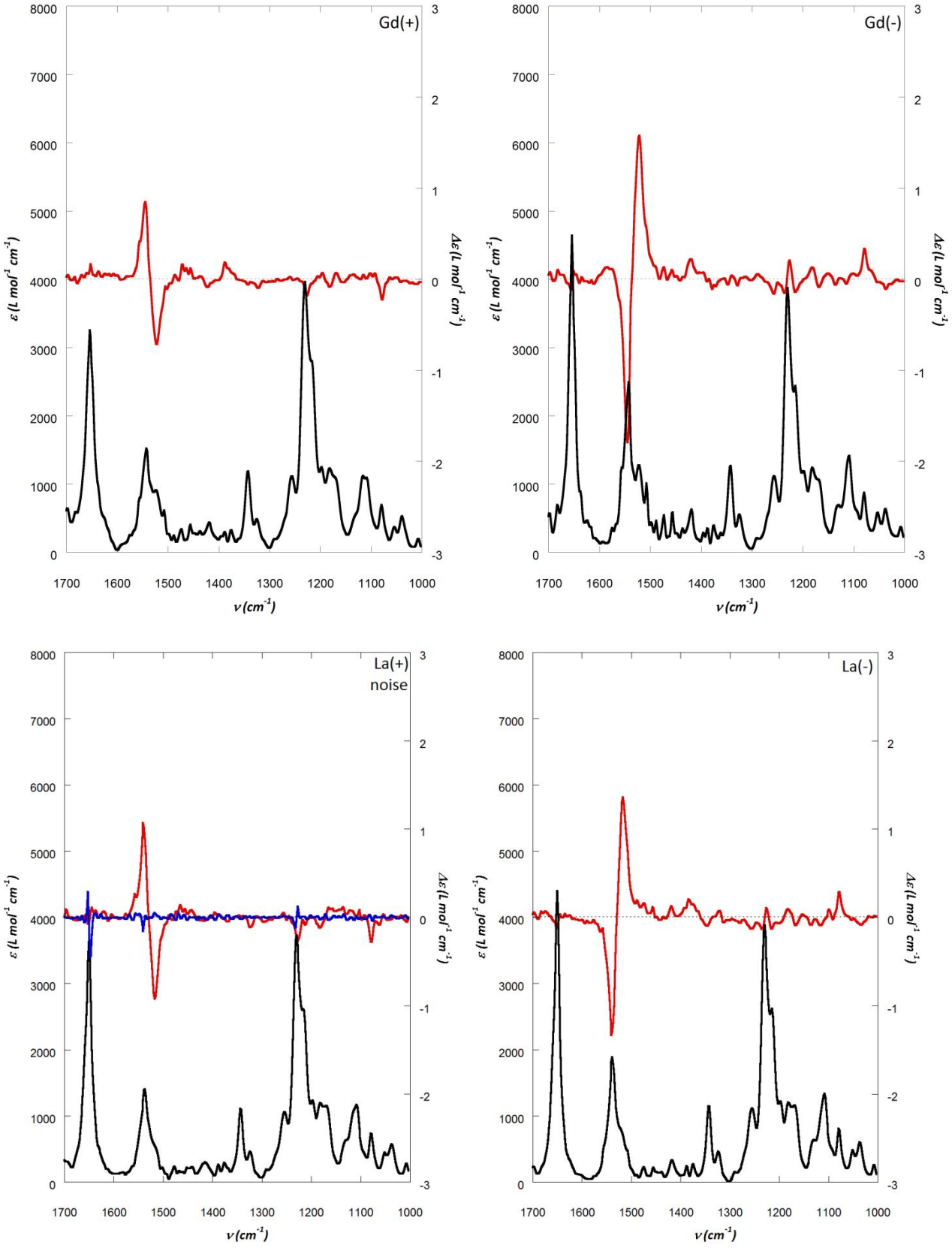
Gd(+)
Gd(-)
La(+)
noise
La(-)
ε (L mol-1 cm-1)
Δε (L mol-1 cm-1)
ν (cm-1)
8000
7000
6000
5000
4000
3000
2000
1000
0
3
2
1
0
-1
-2
-3
1700
1600
1500
1400
1300
1200
1100
1000

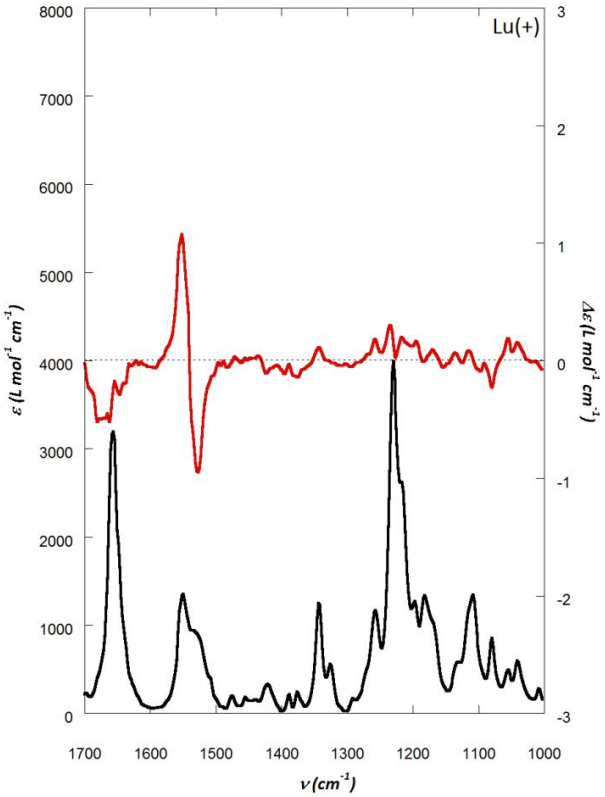
Lu(+)
ε (L mol-1 cm-1)
Δε (L mol-1 cm-1)
ν (cm-1)

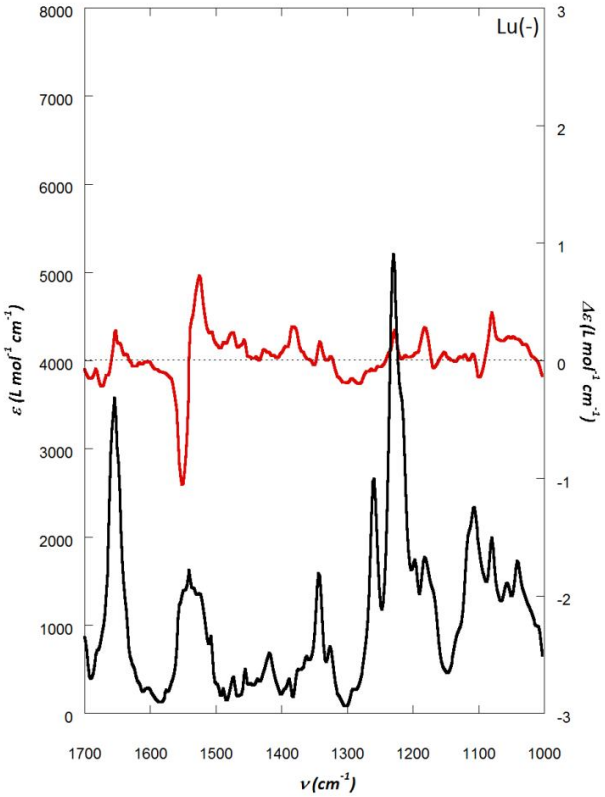
Lu(-)
ε (L mol-1 cm-1)
Δε (L mol-1 cm-1)
ν (cm-1)

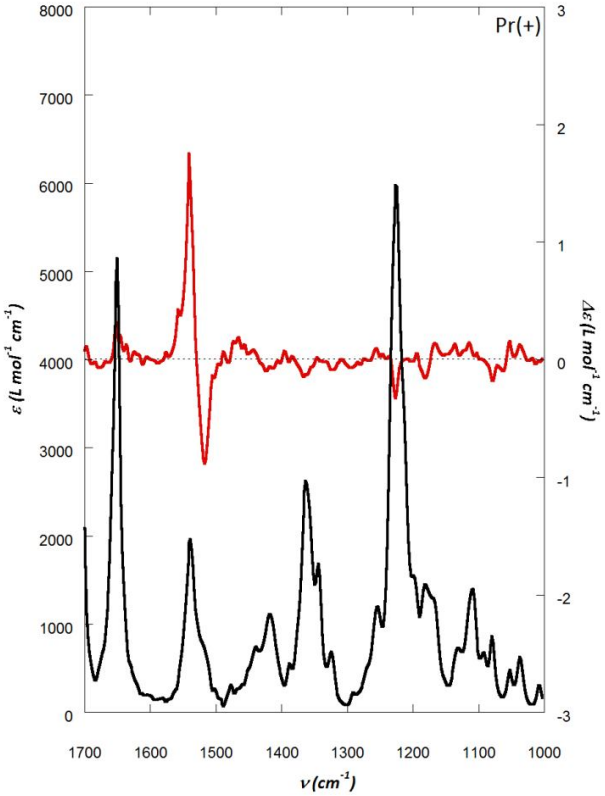
Pr(+)
ε (L mol-1 cm-1)
Δε (L mol-1 cm-1)
ν (cm-1)

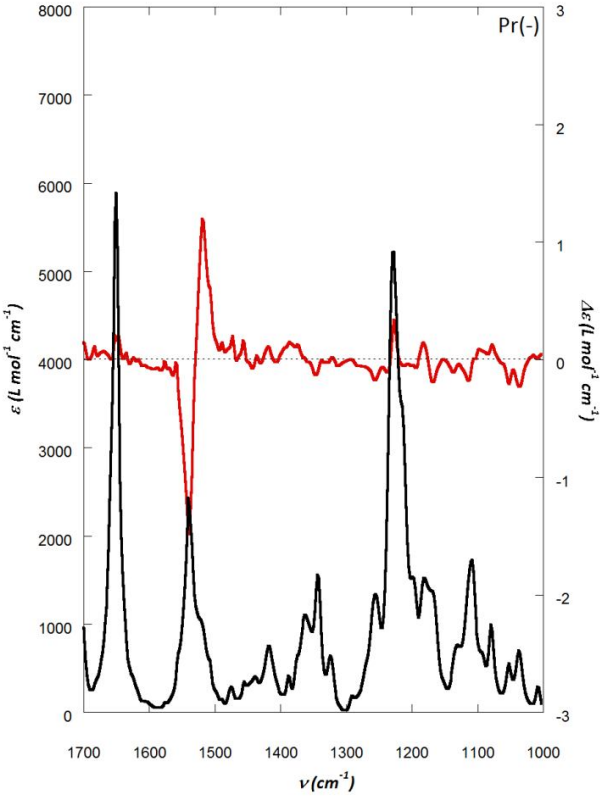
Pr(-)
ε (L mol-1 cm-1)
Δε (L mol-1 cm-1)
ν (cm-1)

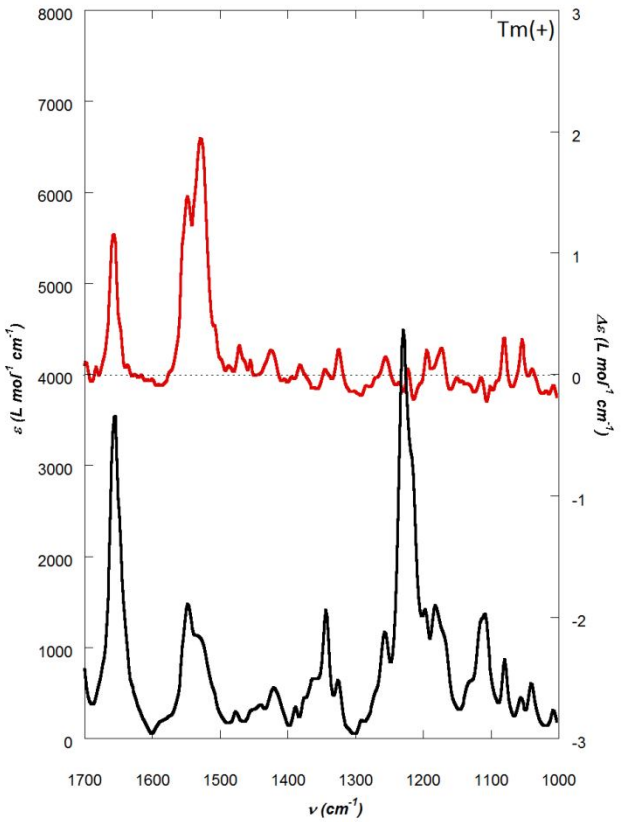
Tm(+)
ε (L mol-1 cm-1)
Δε (L mol-1 cm-1)
ν (cm-1)

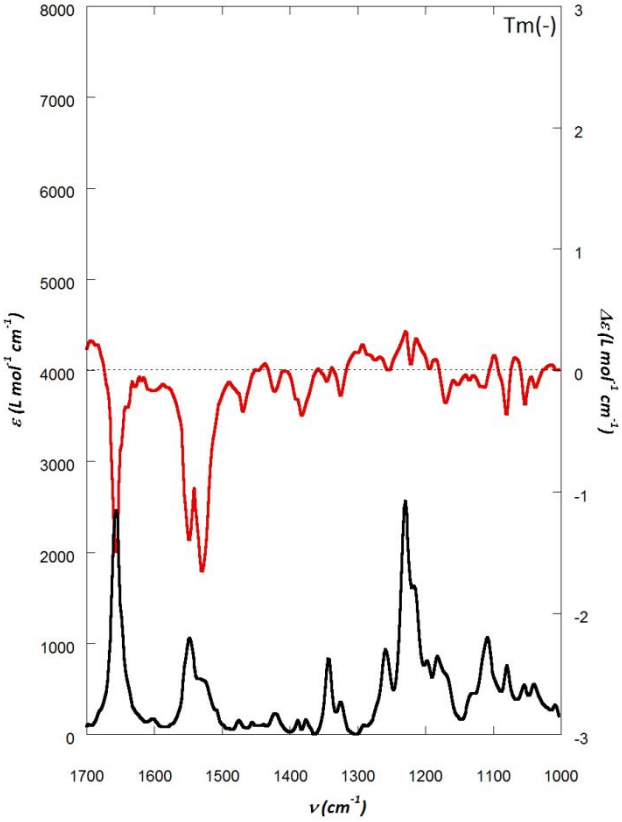
Tm(-)
ε (L mol-1 cm-1)
Δε (L mol-1 cm-1)
ν (cm-1)

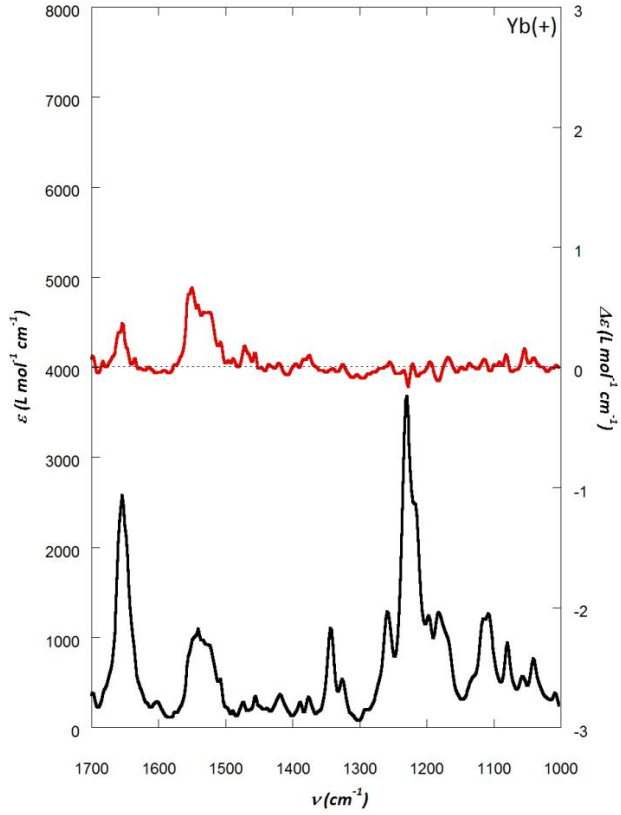
Yb(+)
ε (L mol-1 cm-1)
Δε (L mol-1 cm-1)
ν (cm-1)

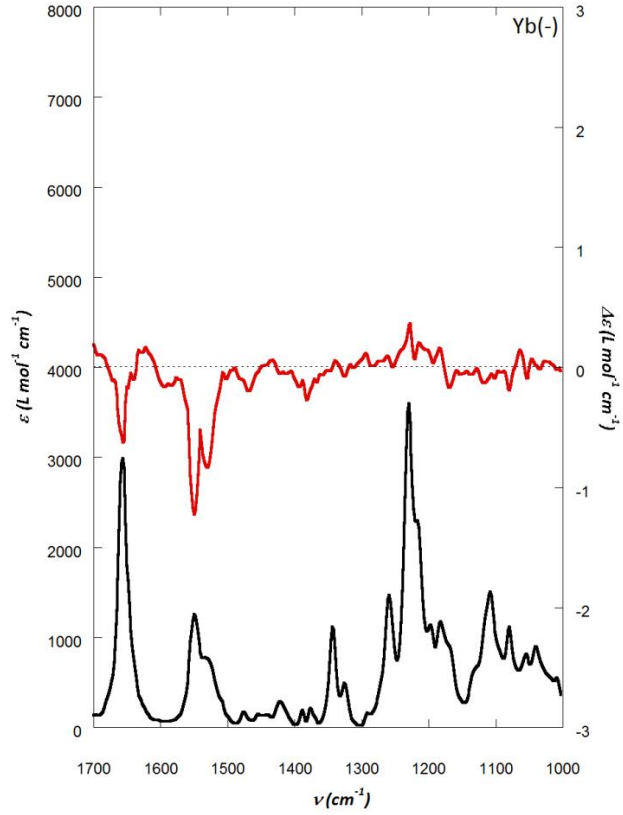
Yb(-)
ε (L mol-1 cm-1)
Δε (L mol-1 cm-1)
ν (cm-1)

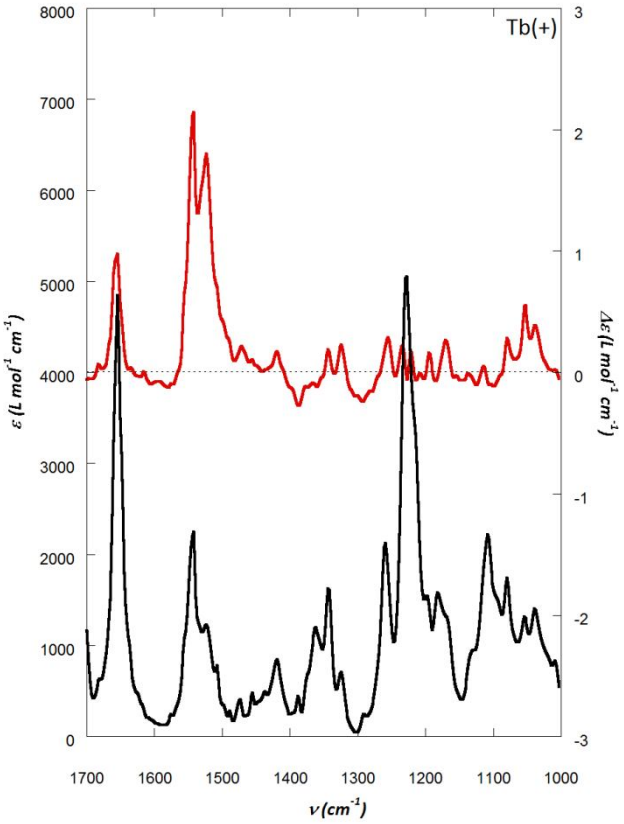
Tb(+)
8000
7000
6000
5000
4000
3000
2000
1000
0
3
2
1
0
-1
-2
-3
1700
1600
1500
1400
1300
1200
1100
1000
ν (cm-1)
ε (L mol-1 cm-1)
Δε (L mol-1 cm-1)

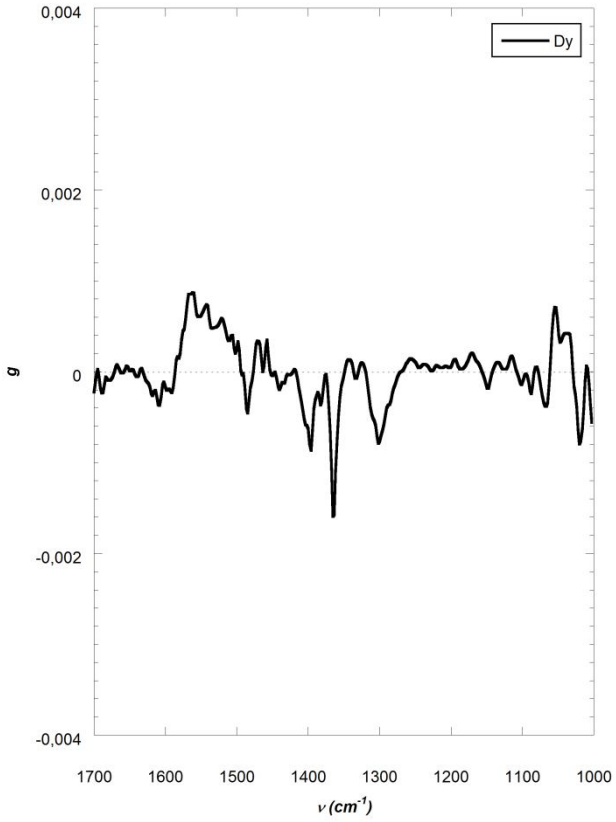
Dy
0,004
0,002
0
-0,002
-0,004
g
1700
1600
1500
1400
1300
1200
1100
1000
ν (cm-1)

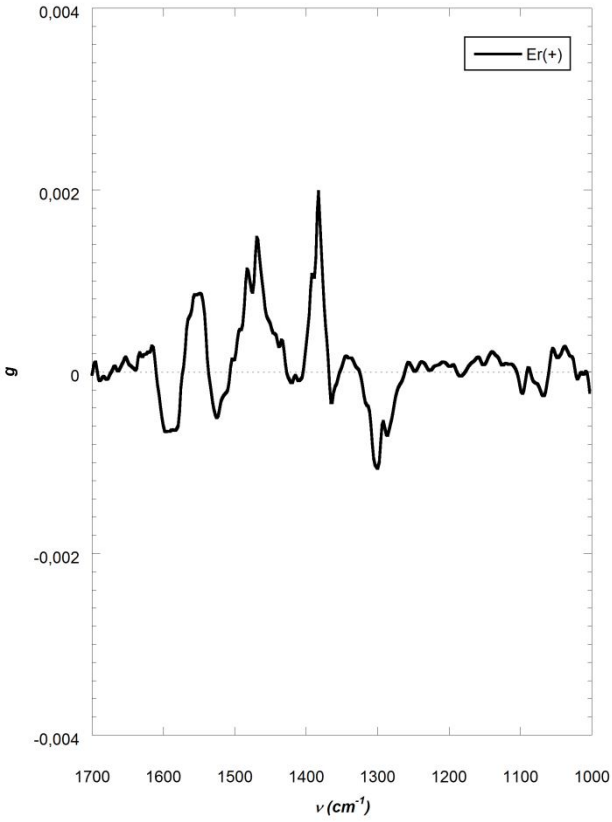
Er(+)
0,004
0,002
0
-0,002
-0,004
g
1700
1600
1500
1400
1300
1200
1100
1000
ν (cm-1)

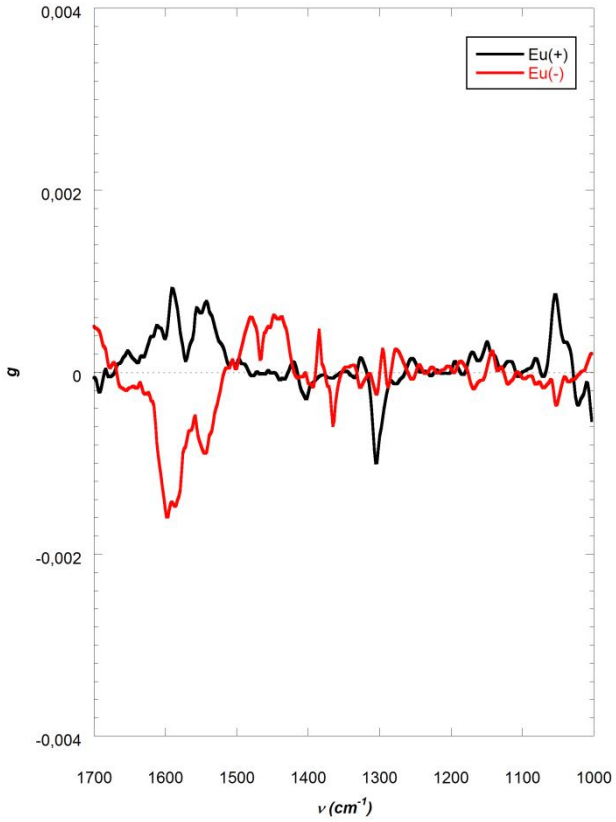
Eu(+)
Eu(-)
0,004
0,002
0
-0,002
-0,004
g
1700
1600
1500
1400
1300
1200
1100
1000
ν (cm-1)

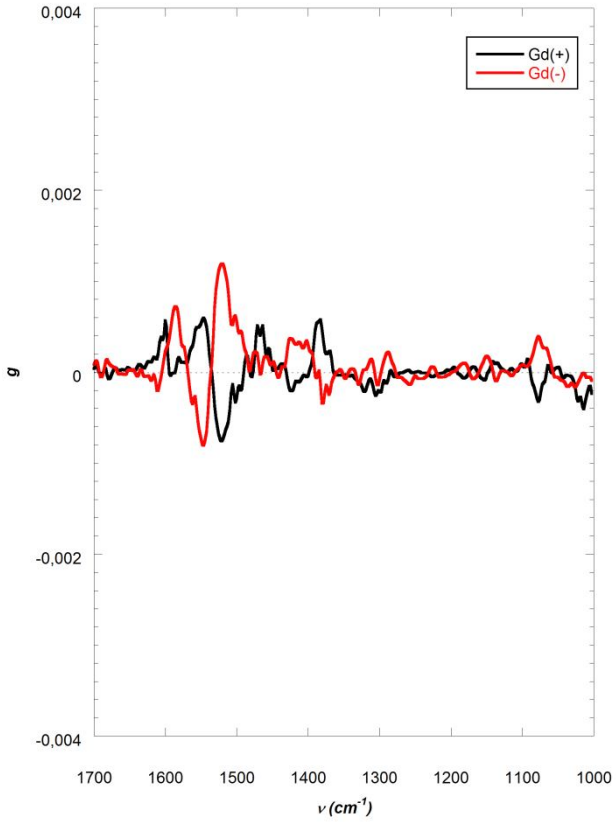
Gd(+)
Gd(-)
0,004
0,002
0
-0,002
-0,004
g
1700
1600
1500
1400
1300
1200
1100
1000
ν (cm-1)

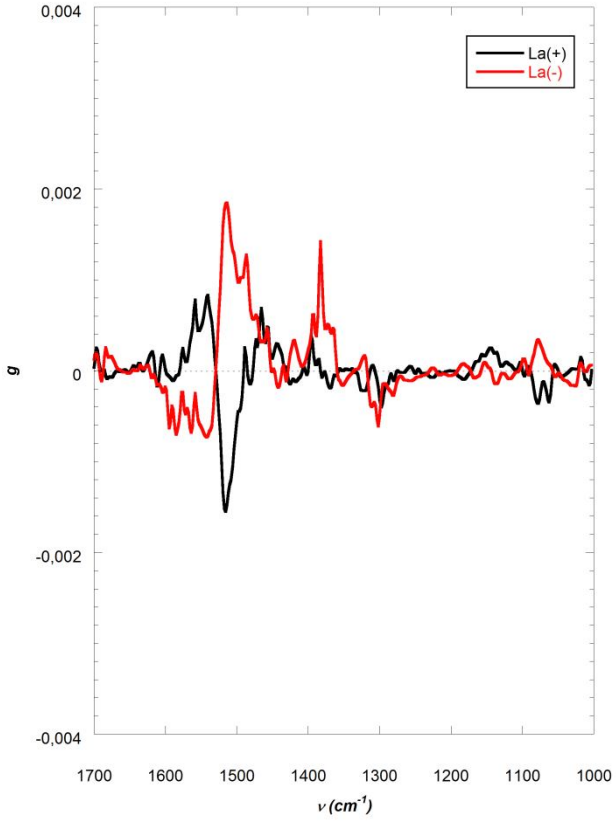
La(+)
La(-)
0,004
0,002
0
-0,002
-0,004
g
1700
1600
1500
1400
1300
1200
1100
1000
ν (cm-1)

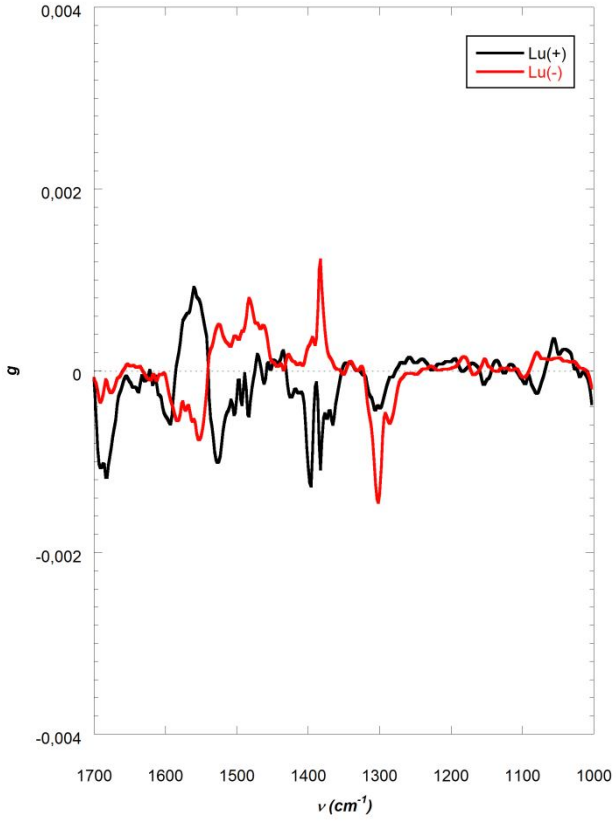
Lu(+)
Lu(-)
0,004
0,002
0
-0,002
-0,004
g
1700
1600
1500
1400
1300
1200
1100
1000
ν (cm-1)

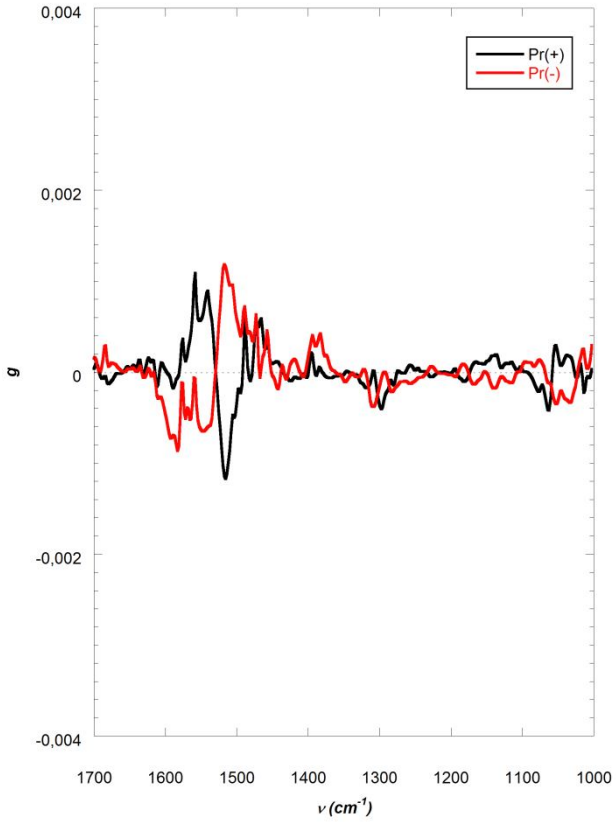
Pr(+)
Pr(-)
0,004
0,002
0
-0,002
-0,004
g
1700
1600
1500
1400
1300
1200
1100
1000
ν (cm-1)

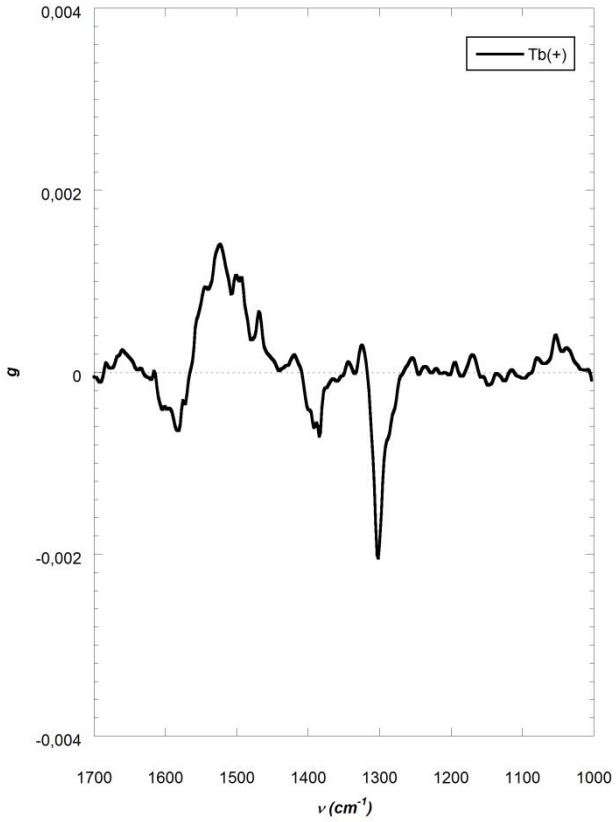
Tb(+)
0,004
0,002
0
-0,002
-0,004
g
1700
1600
1500
1400
1300
1200
1100
1000
ν (cm-1)

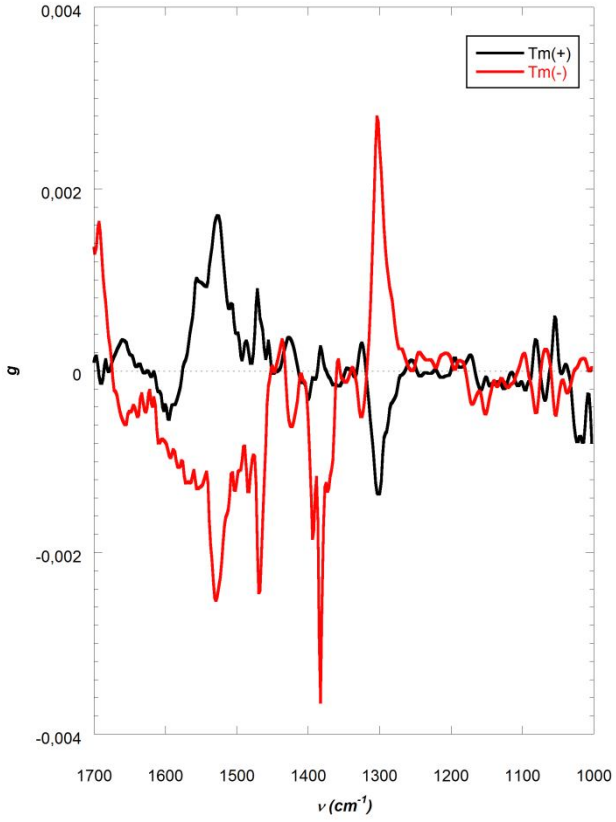
Tm(+)
Tm(-)
0,004
0,002
0
-0,002
-0,004
g
1700
1600
1500
1400
1300
1200
1100
1000
ν (cm-1)

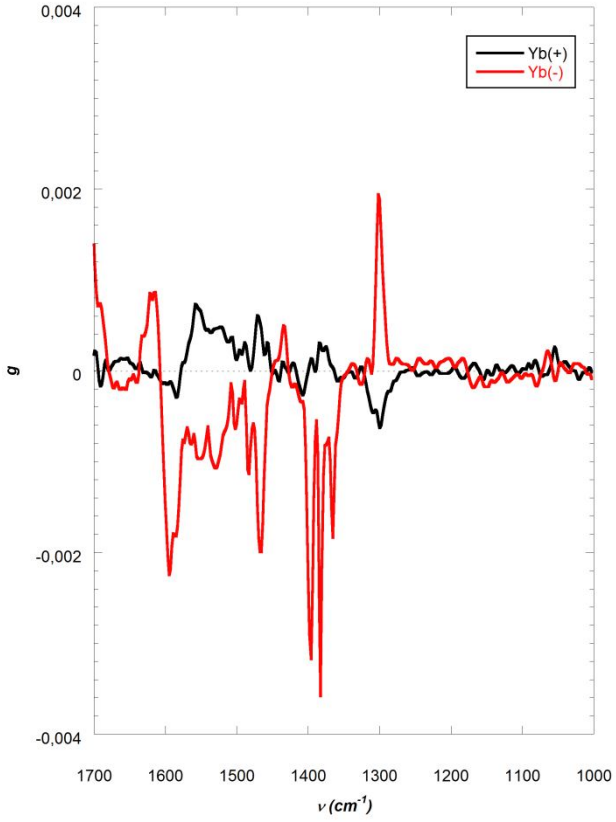
Yb(+)
Yb(-)
0,004
0,002
0
-0,002
-0,004
g
1700
1600
1500
1400
1300
1200
1100
1000
ν (cm-1)

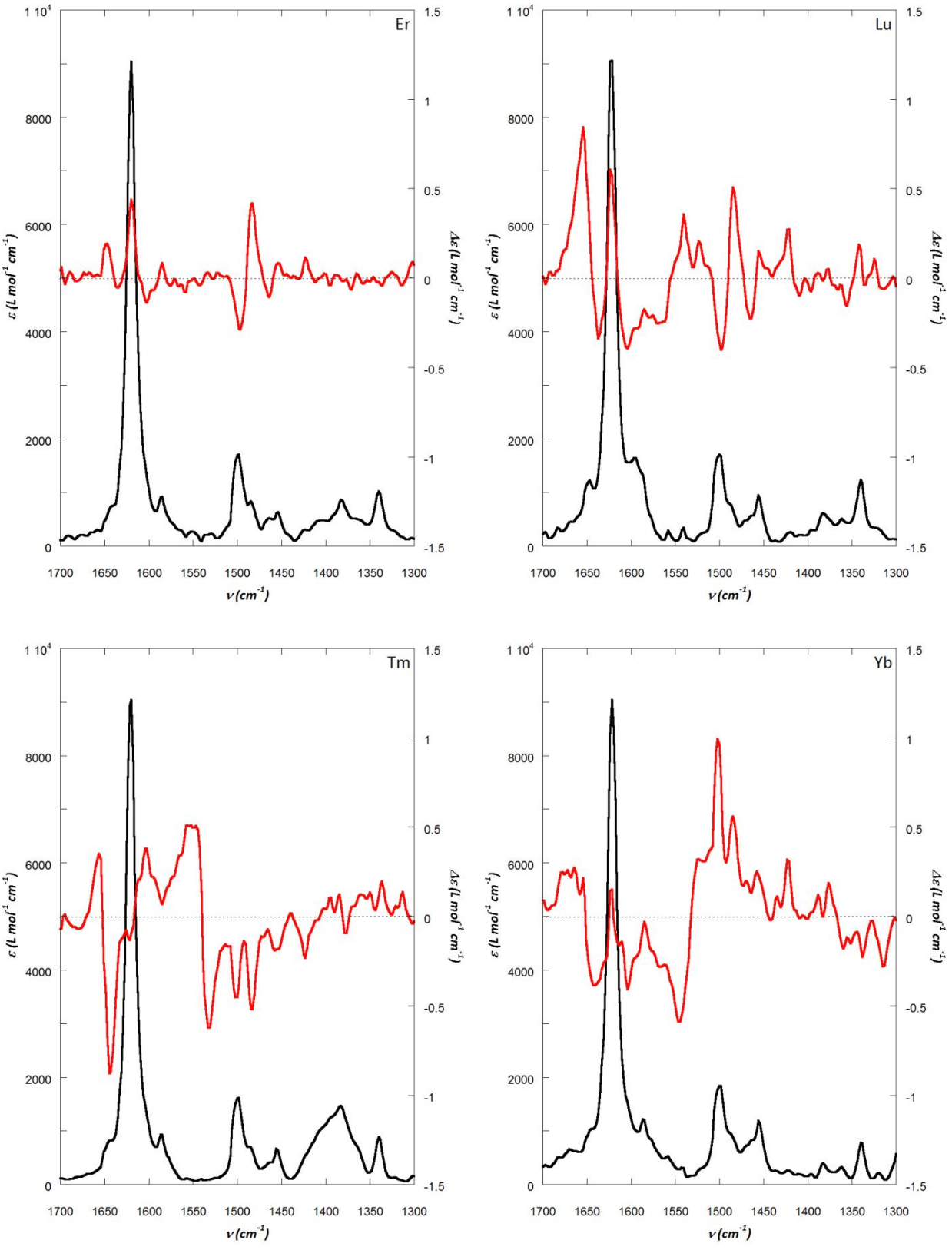
Er
Lu
Tm
Yb
1 10^4
8000
6000
4000
2000
0
1.5
1
0.5
0
-0.5
-1
-1.5
1700 1650 1600 1550 1500 1450 1400 1350 1300
ν (cm^-1)
ε (L mol^-1 cm^-1)
Δε (L mol^-1 cm^-1)

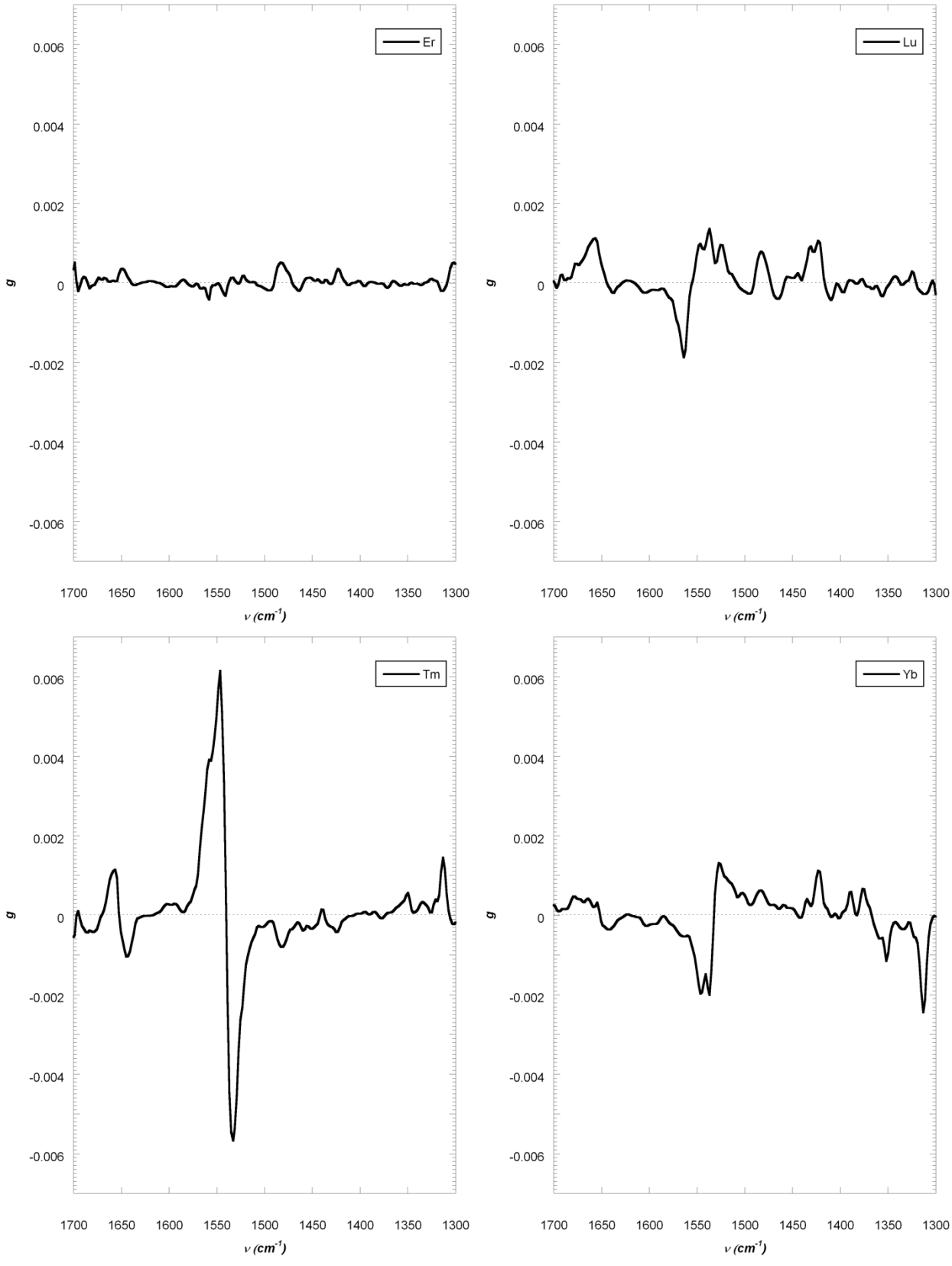
Er
Lu
Tm
Yb
g
0.006
0.004
0.002
0
-0.002
-0.004
-0.006
1700 1650 1600 1550 1500 1450 1400 1350 1300
ν (cm-1)

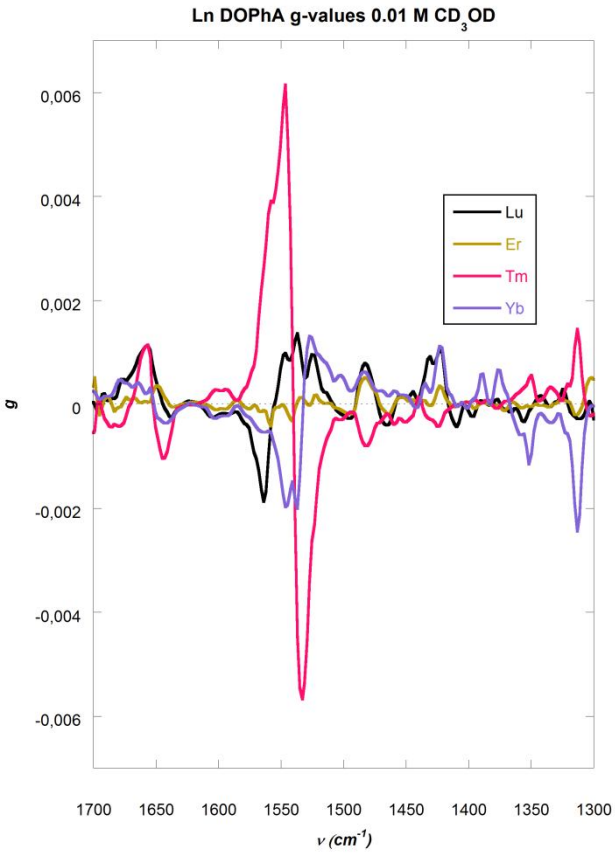
Ln DOPhA g-values 0.01 M CD3OD
0,006
0,004
0,002
0
-0,002
-0,004
-0,006
g
Lu
Er
Tm
Yb
1700
1650
1600
1550
1500
1450
1400
1350
1300
ν (cm-1)

Appendix 2

A2.1 Protein Structure Alignment

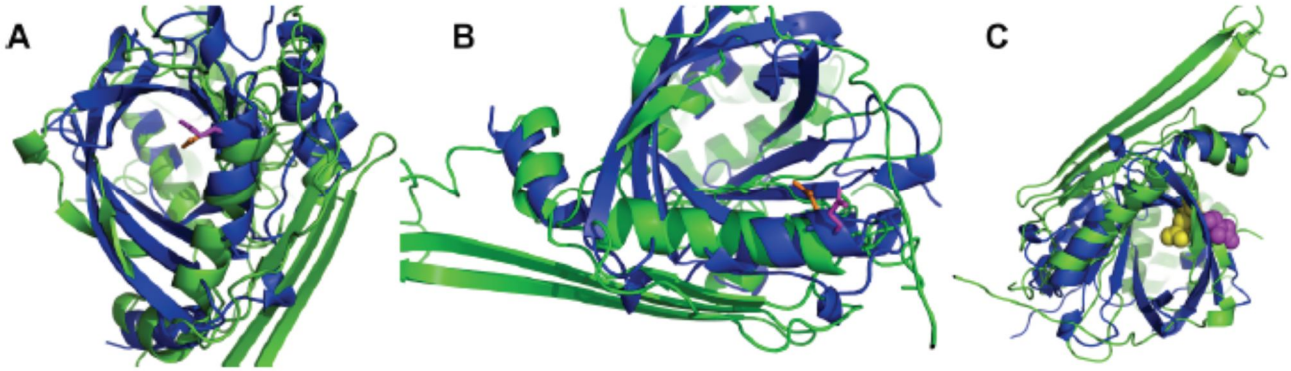

Figure A2.1 Structural superposition using FATCAT. In each case, α_1-AGP (3KQ0) is shown in blue, α_1-AAT (9API) is shown in green. (A) and (B), orthogonal views of the superposition of E36 of α_1-AGP (magenta) with E152 of α_1-AAT (orange); (C), showing the position of E64 of α_1-AGP (yellow) and E206 of α_1-AAT (purple).

A2.2 Europium emission spectral titrations and data analysis

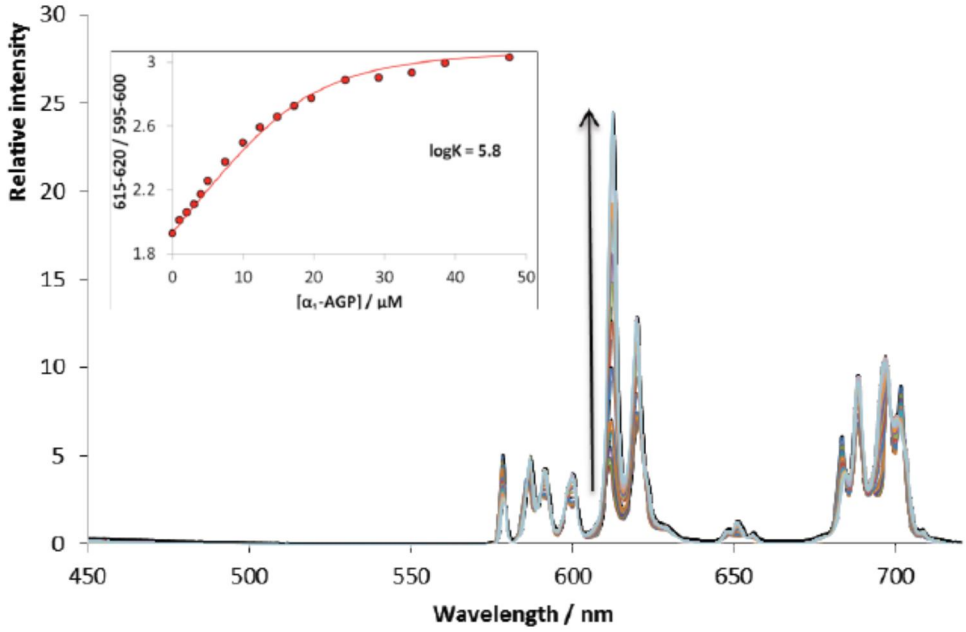

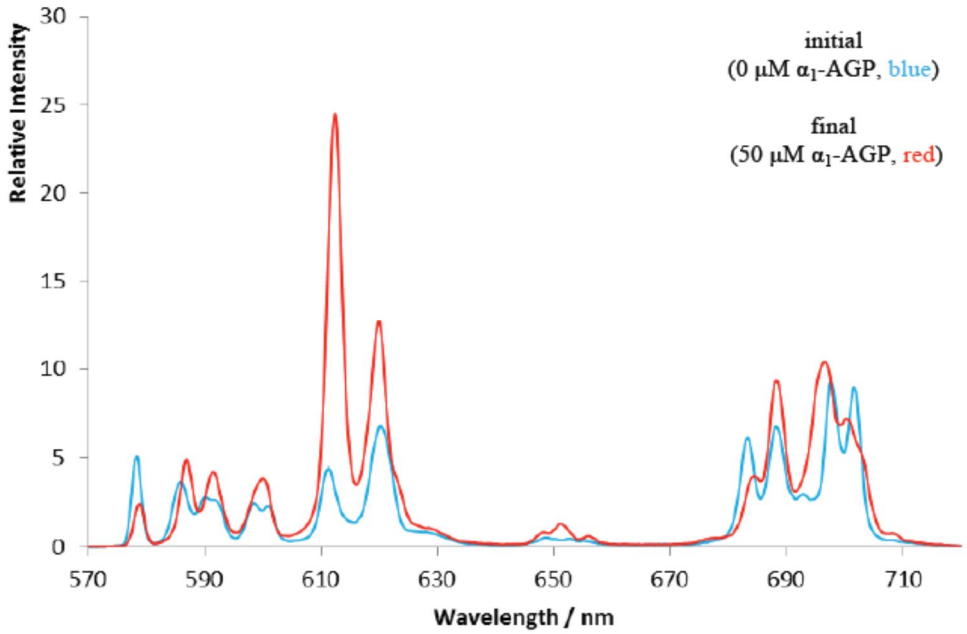

Figure A2.2 Europium emission spectral changes following addition of human α_1-AGP to $[EuL^1(OH_2)]^+$ (20 μM, 295 K, 0.1 M NaCl, pH 7.4).

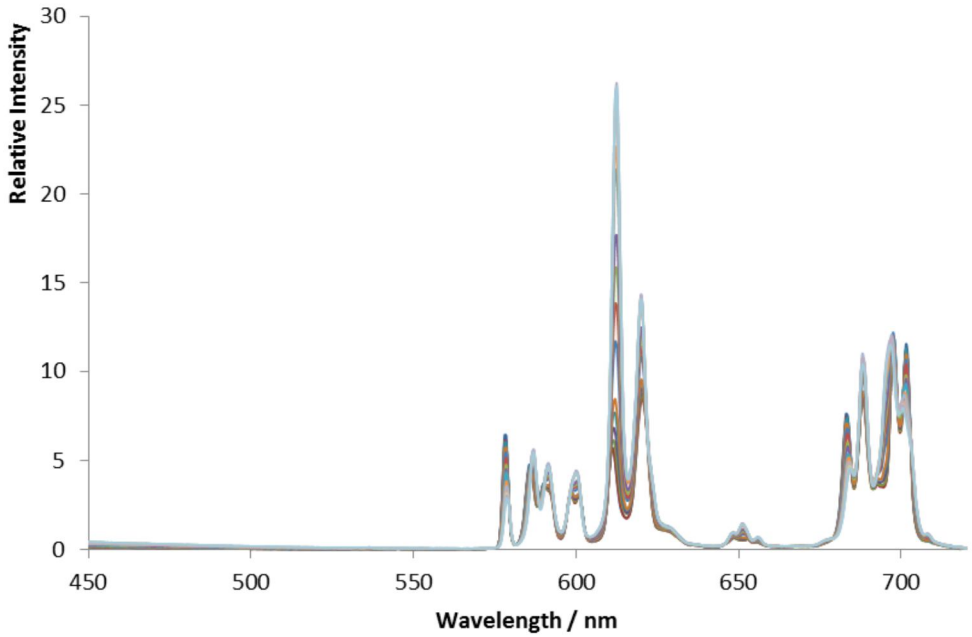

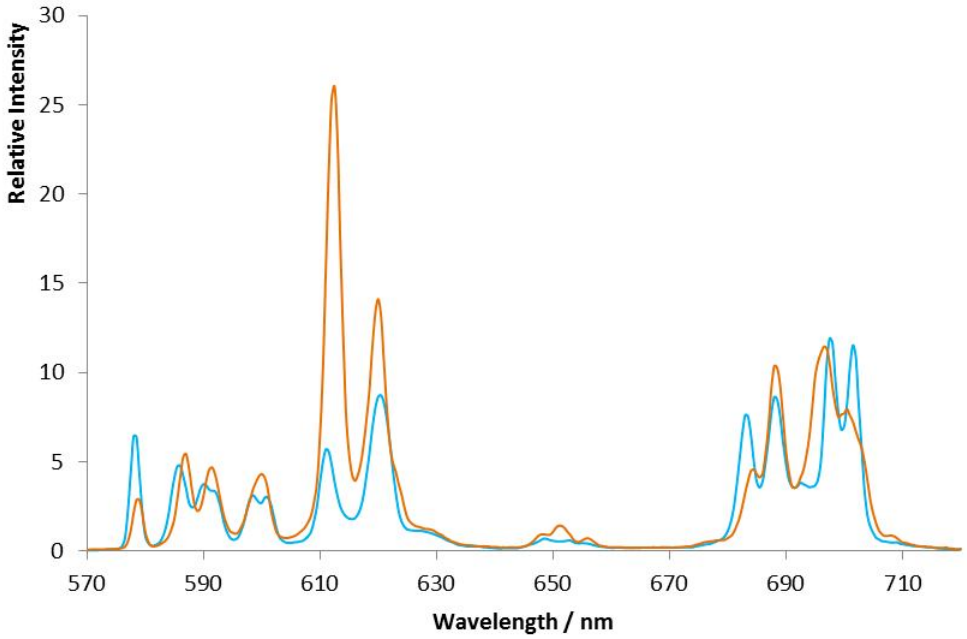

Figure A2.3 Europium emission spectral changes following addition of human α_1-antitrypsin to $[EuL^1(OH_2)]^+$ (20 μM, 295 K, 0.1 M NaCl, pH 7.4).

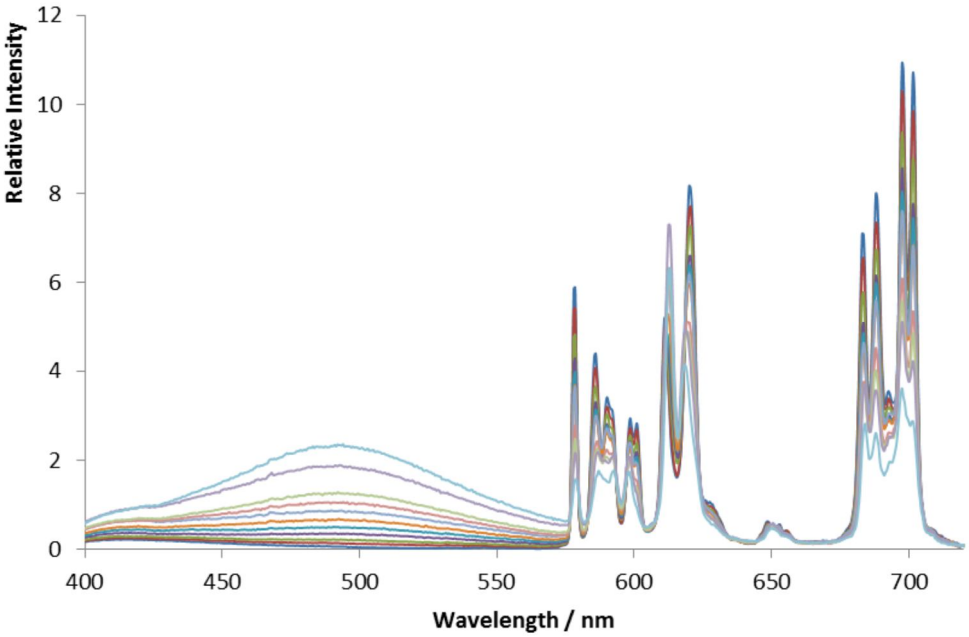

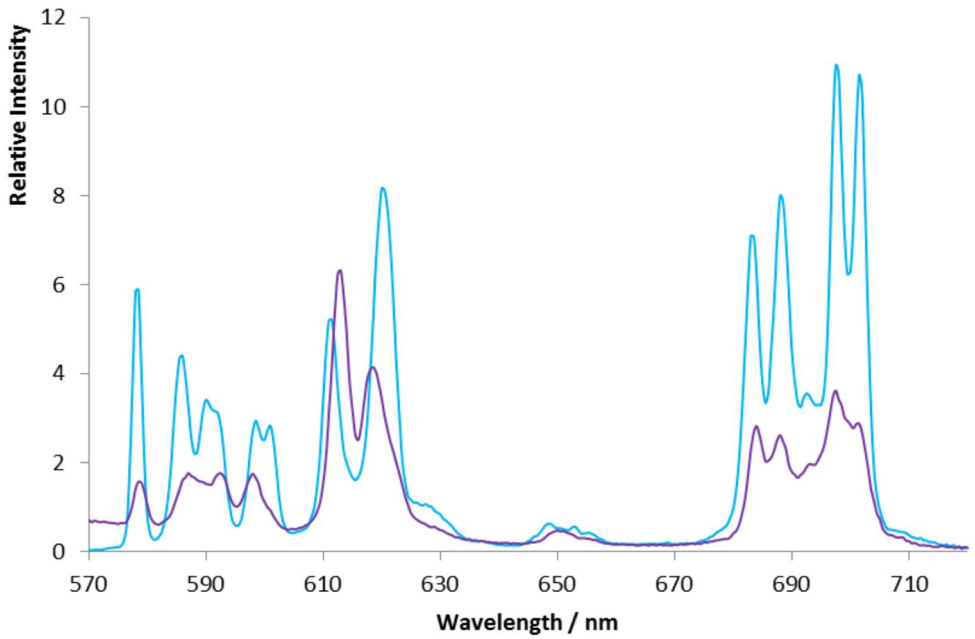

Figure A2.4 Europium emission spectral changes following addition of bovine γ-Ig-G to $[EuL^1(OH_2)]^+$ (20 μM, 295 K, 0.1 M NaCl, pH 7.4).

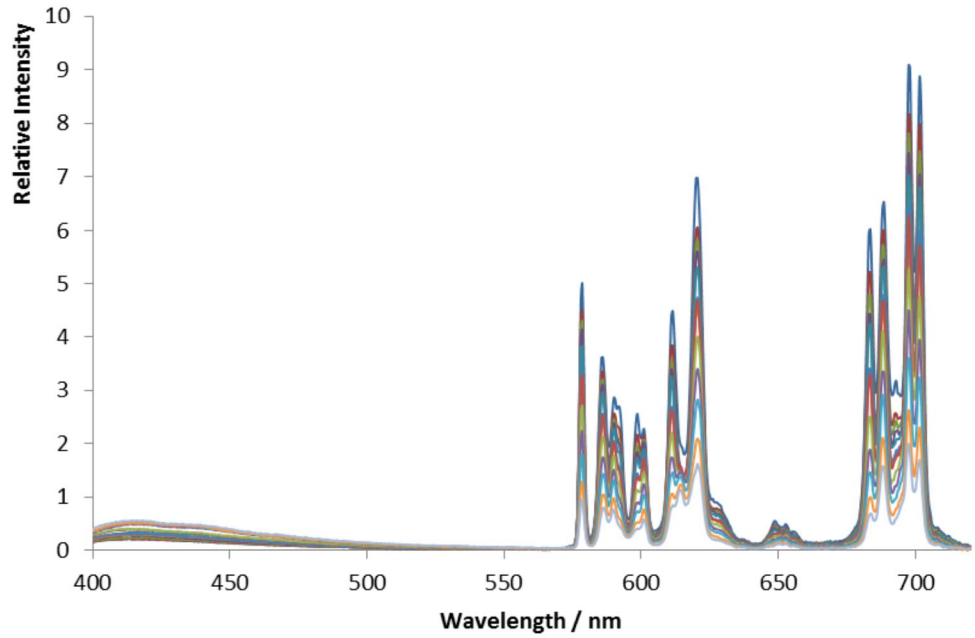

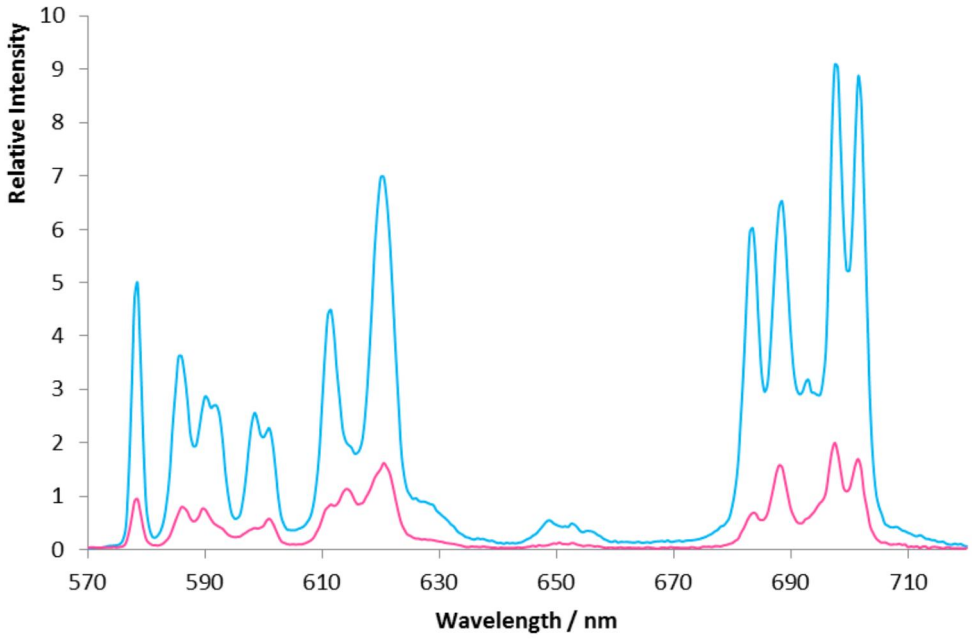

Figure A2.5 Europium emission spectral changes following addition of bovine fibrinogen to $[EuL^{1}(OH_2)]^{+}$ (20 μM, 295 K, 0.1 M NaCl, pH 7.4).

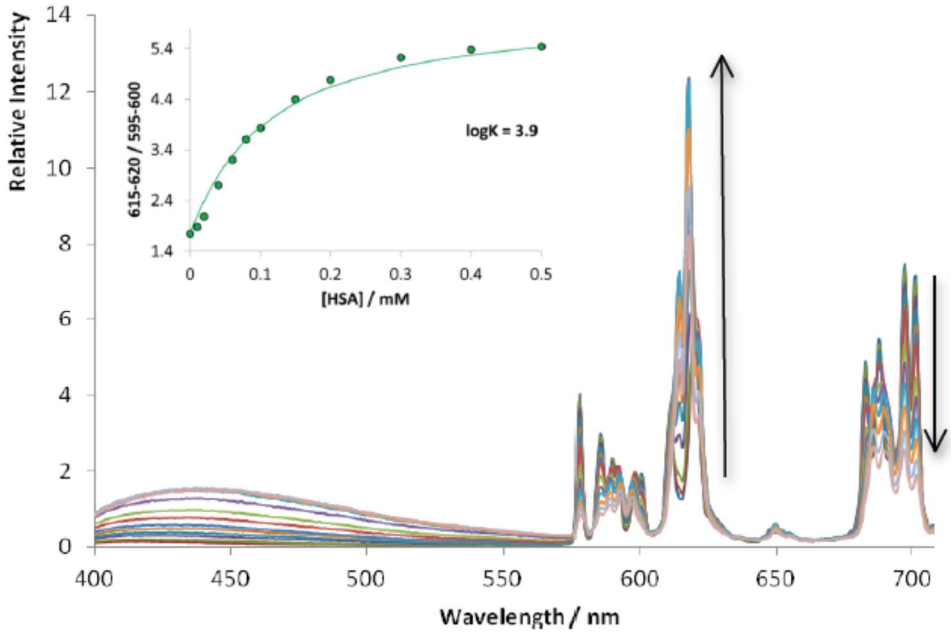

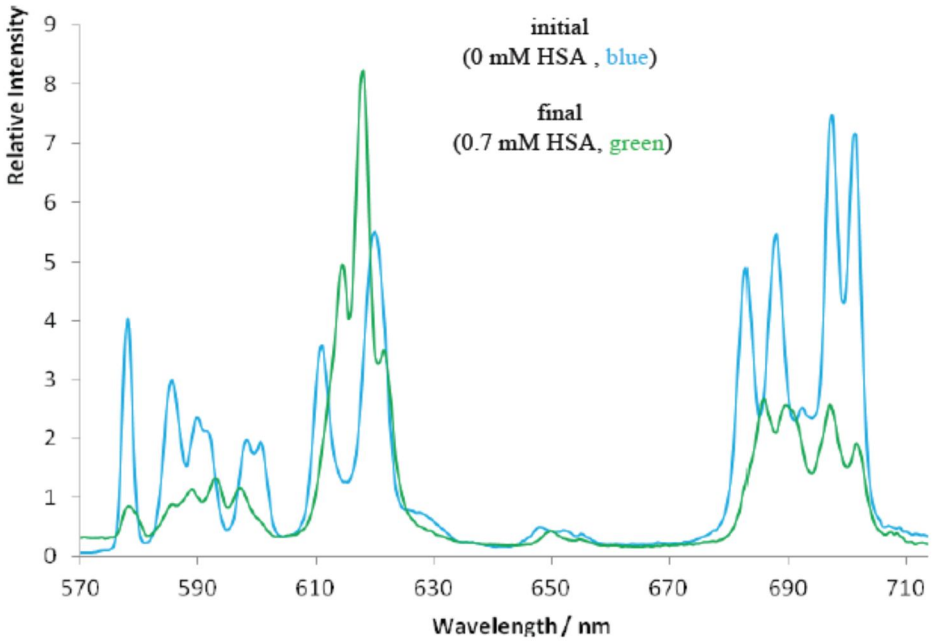

Figure A2.6 Europium emission spectral changes following addition of HSA to $[EuL^1(OH_2)]^+$ (20 μM, 295 K, 0.1 M NaCl, pH 7.4).

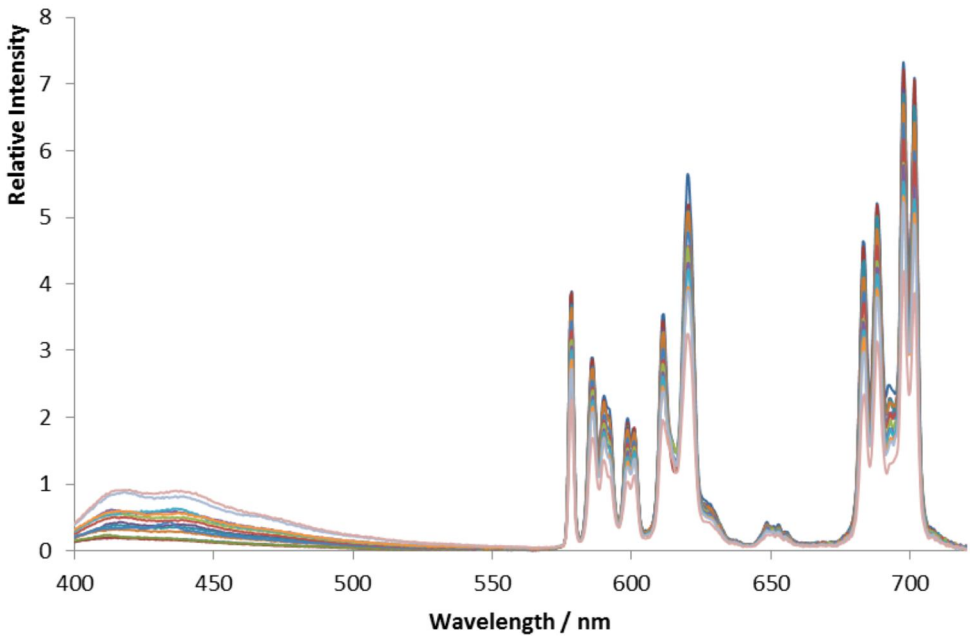

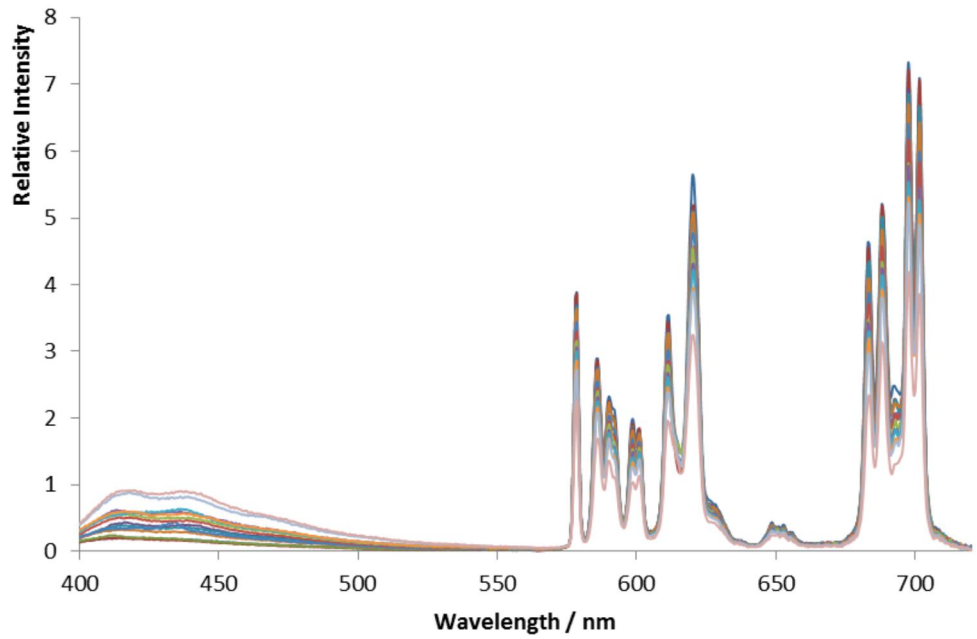

Figure A2.7 Europium emission spectral changes following addition of human apo-transferrin to $[EuL^1(OH_2)]^+$ (20 μM, 295 K, 0.1 M NaCl, pH 7.4).

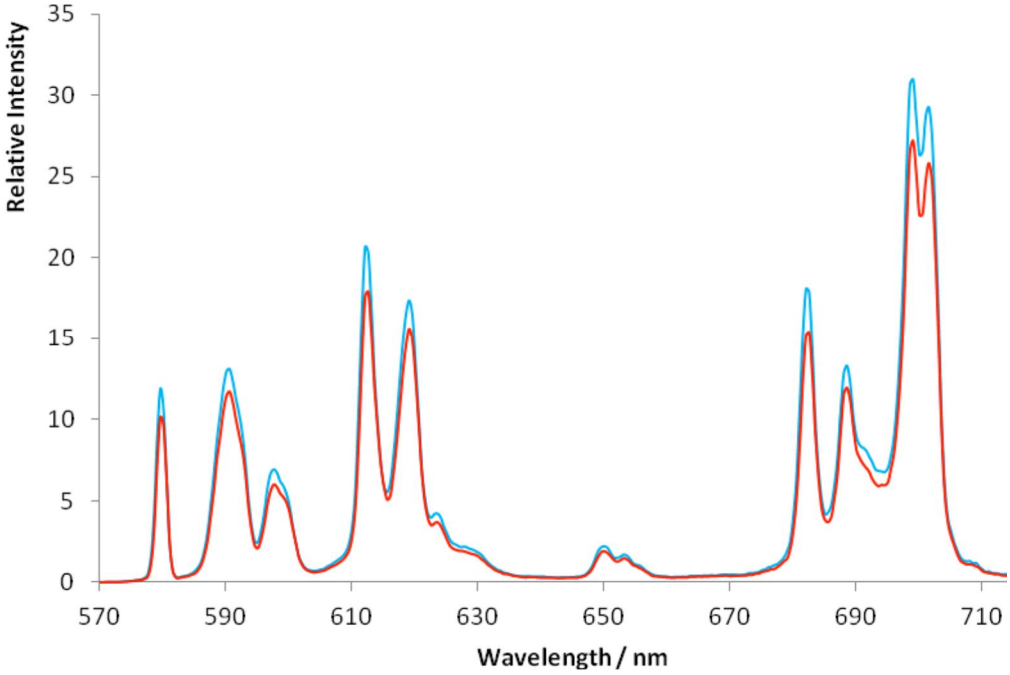

Figure A2.8 Europium emission spectral changes following addition of human α_1-AGP to $[EuL^2(OH_2)]^+$ (20 μM, 295 K, 0.1 M NaCl, pH 7.4).

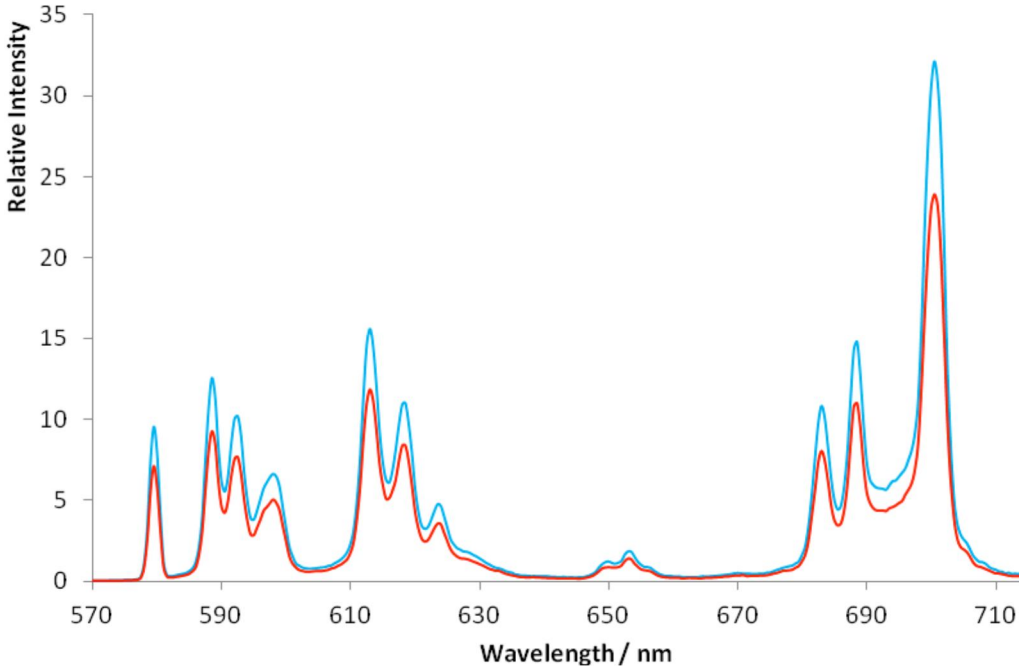

Figure A2.9 Europium emission spectral changes following addition of human α_1-AGP to $[EuL^3(OH_2)]$ (20 μM, 295 K, 0.1 M NaCl, pH 7.4).

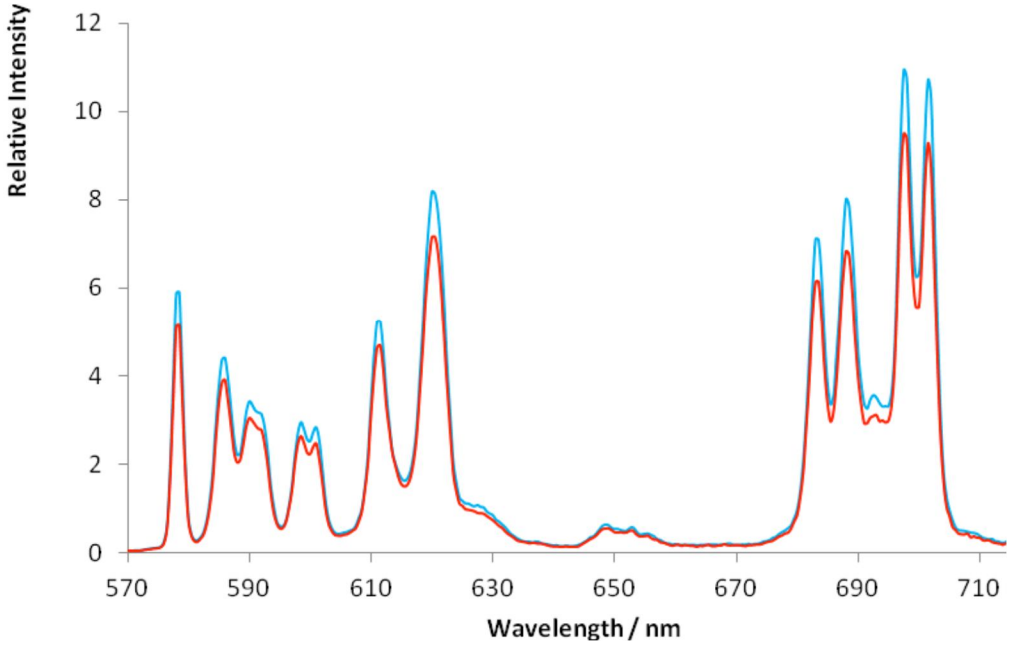

Figure A2.10 Europium emission spectral changes following addition of sialic acid to $[EuL^1(OH_2)]^+$ (20 μM, 295 K, 0.1 M NaCl, pH 7.4).

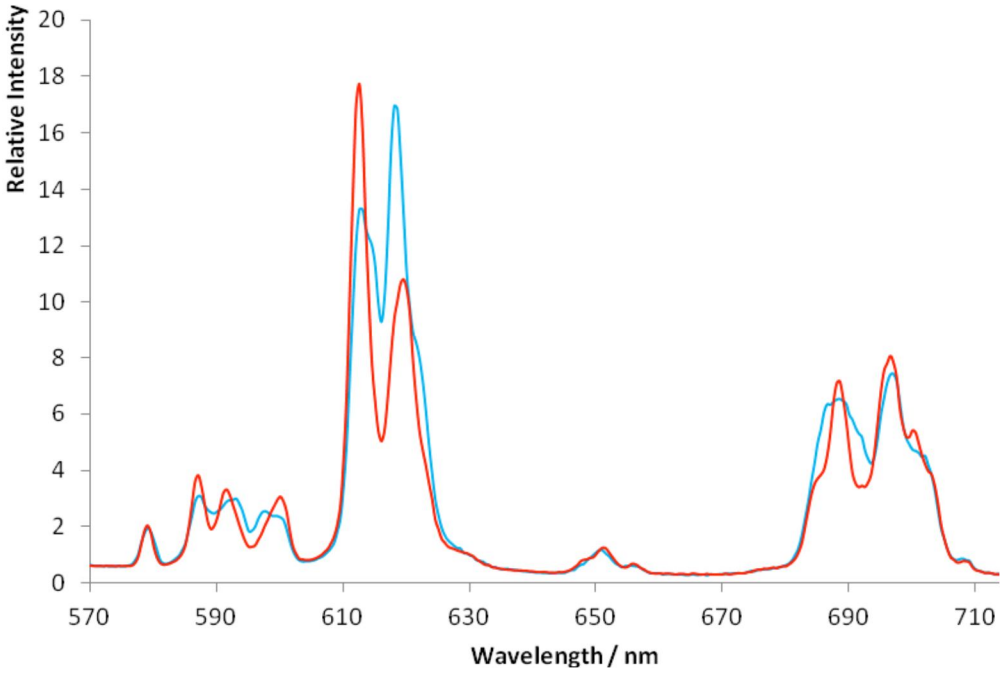

Figure A2.11 Europium emission spectral changes following addition of human α_1-AGP to $[EuL^1(OH_2)]^+$ in human serum (295 K, 0.1 M NaCl, pH 7.4).

A2.3 ECD and UV absorption spectra of humane α_1-AGP, $[EuL^1(OH_2)]$+ and their adduct tritation with CPZ

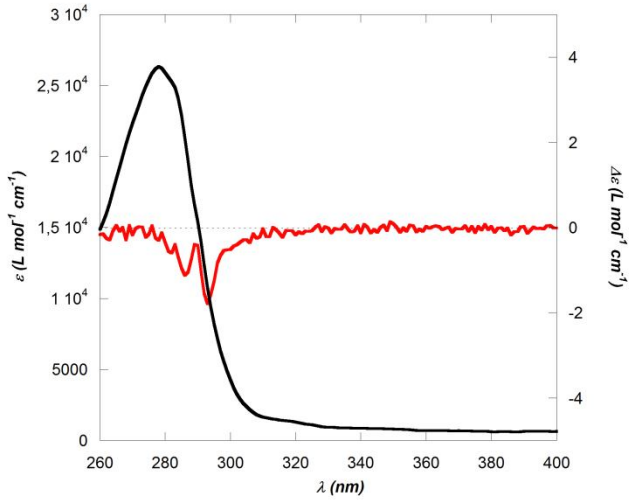

Figure A2.12 UV Absorption and ECD Spectra of humane α_1-AGP (0.0413 mM, water, 295 K, pH 7.0)

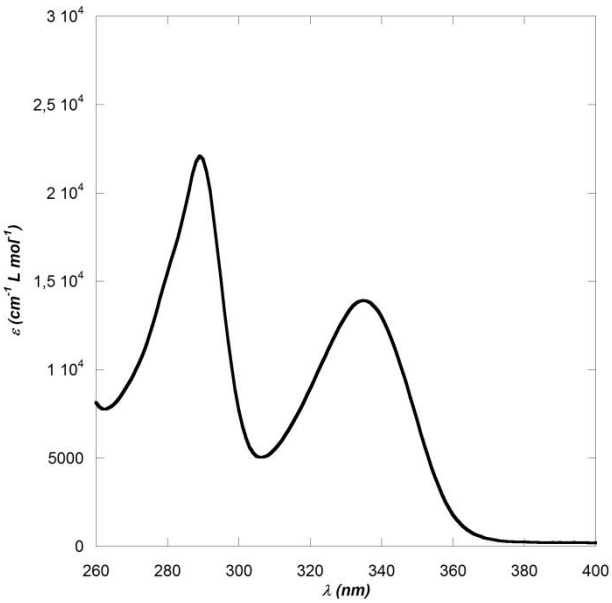

Figure A2.13 UV Absorption and ECD Spectra of complex $[EuL^1(OH_2)]^+$ (0.0413 mM, water, 295 K, pH 7.0)

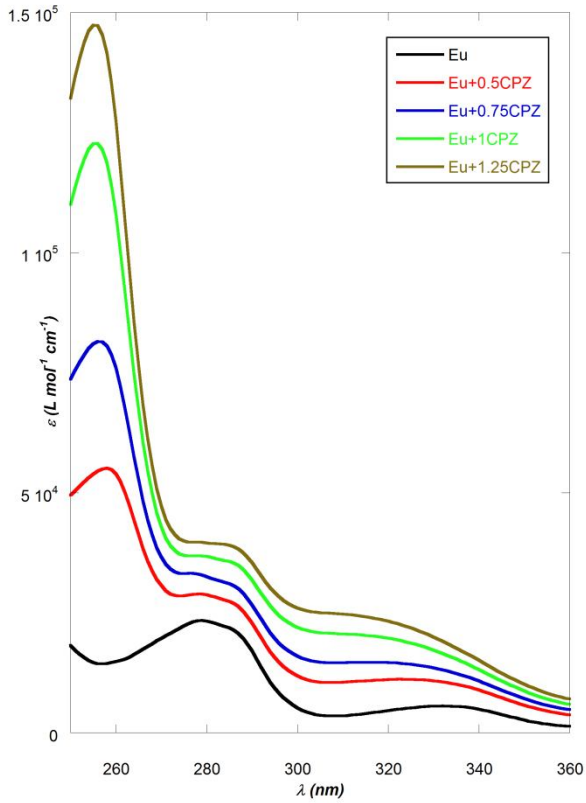

Figure A2.14 Tritation Absorption Spectra of humane α_1-AGP/$[EuL^1(OH_2)]^+$ 0.0413M with 0.0207M chlorpromazine (water, 295 K, pH 7.0)

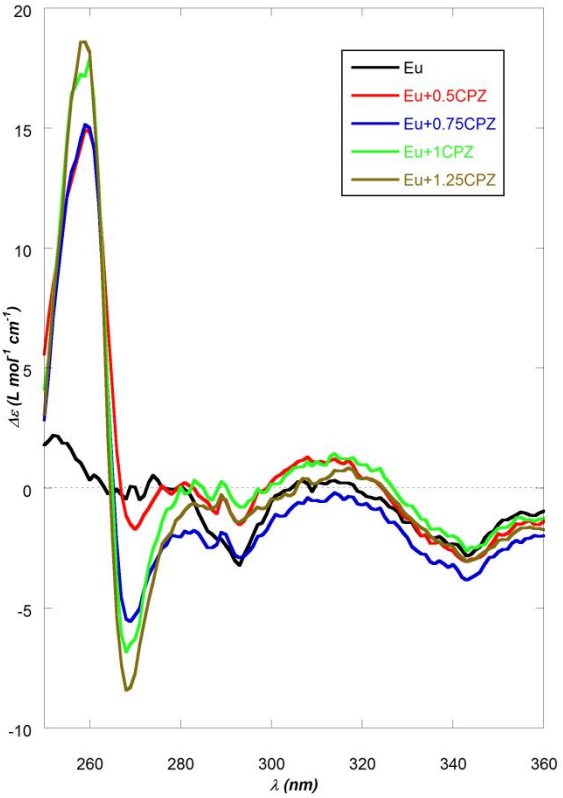

Figure A2.15 Tritation Absorption Spectra of humane α_1-AGP/$[EuL^1(OH_2)]^+$ 0.0413M with 0.0207M chlorpromazine (water, 295 K, pH 7.0)

A2.4 CPL spectra for protein bound complexes and CPL titration of bovine α_1-AGP in human serum

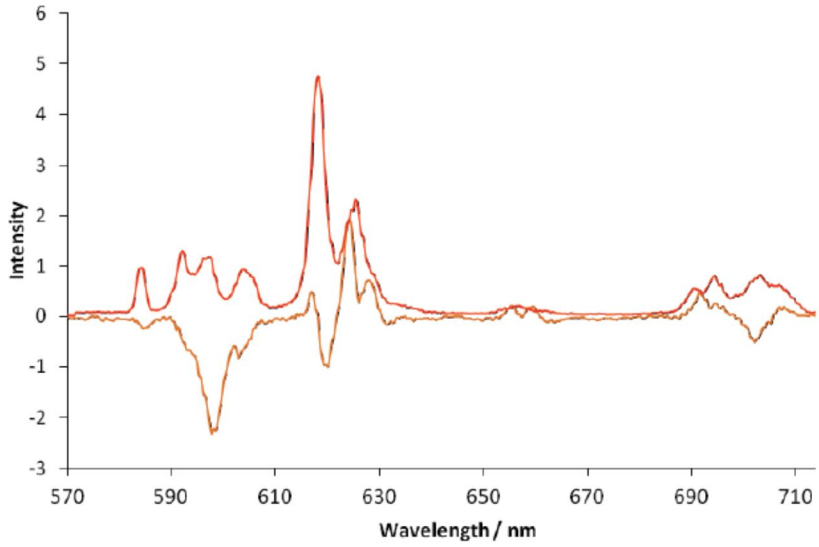

Figure A2.16 Europium emission spectrum and CPL spectrum of $[EuL^1(OH_2)]^+$ in the presence of 100 μM human α_1-antitrypsin (20 μM, 295 K, 0.1 M NaCl, pH 7.4). The scale used refers to (I_L-I_R) and is on a scale of x40 with respect to (I_L+I_R)

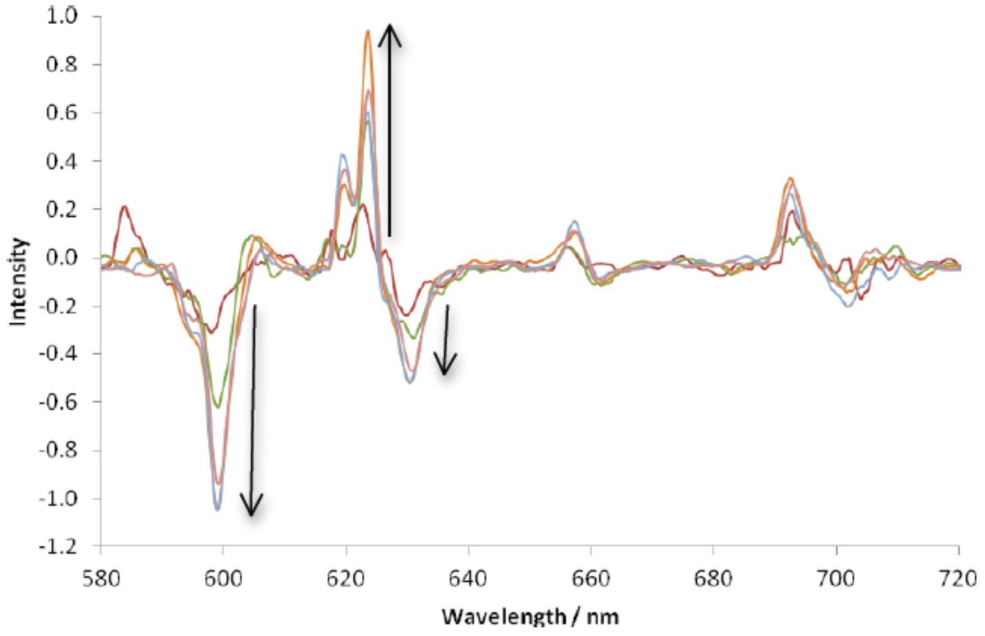

Figure A2.17 CPL spectral changes following addition of bovine α_1-AGP to $[EuL^1(OH_2)]^+$ (20 μM, 295 K, 0.1 M NaCl, pH 7.4).

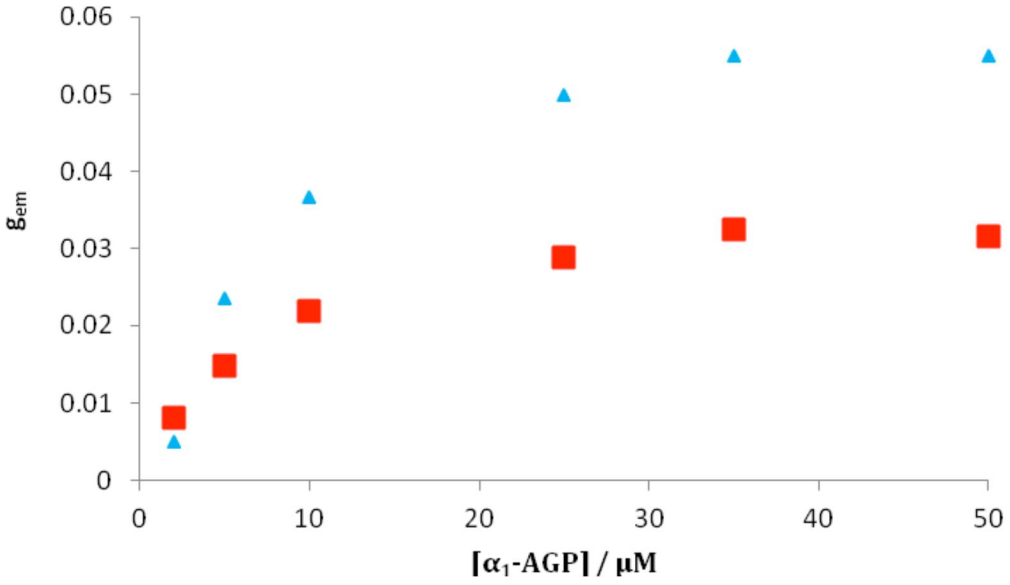

Figure A2.18 Variation of the observed dissymmetry factor, g_{em}, with added bovine α_1-AGP for $[EuL^1(OH_2)]^+$ (20 μM, 295 K, 0.1 M NaCl, pH 7.4); blue triangles = 600 nm, red squares = 630 nm.

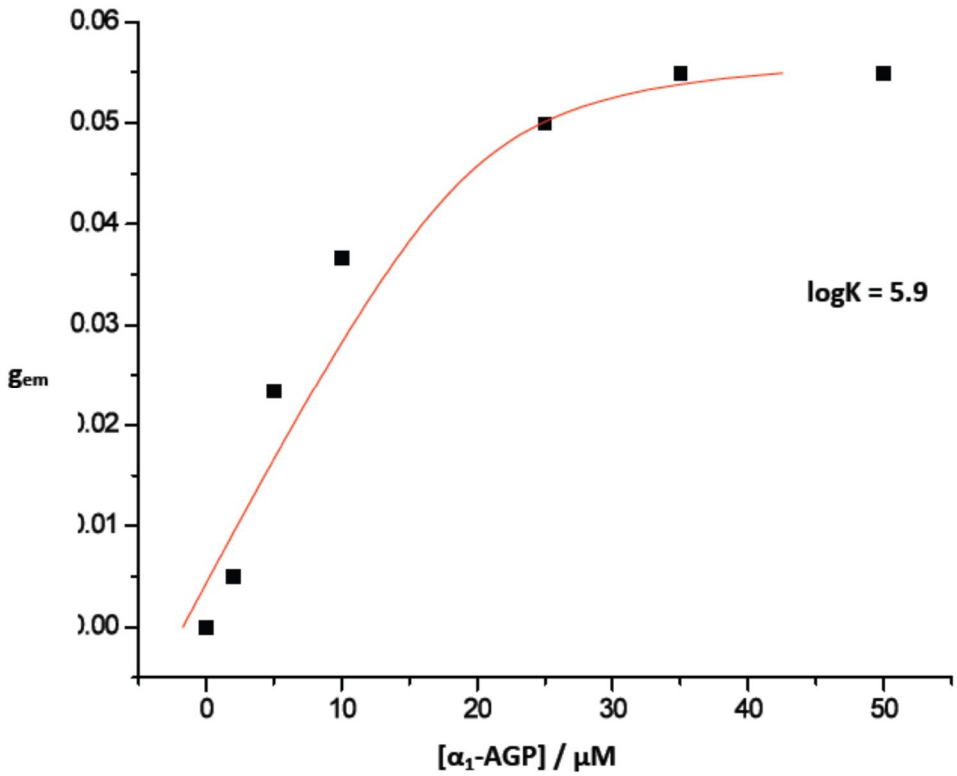

Figure A2.19 Variation of the observed dissymmetry factor, g_{em}, with added bovine α_1-AGP for $[EuL^1(OH_2)]^+$ (20 μM, 295 K, 0.1 M NaCl, pH 7.4) at 600 nm. Iterative, non-linear least squares data fitting allowed a 'global' association constant to be estimated, log K = 5.9 (±0.1).

List of Abbreviations

AAT	Antitrypsin
AGP	Acid Glycoprotein
BO	Born-Oppenheimer
CA	Contrast Agent
CD	Circular Dichroism
CEST	Chemical Exchange Saturation Transfer
CPL	Circular Polarization of Luminescence
CN	Coordination Number
DCTA	1,2-diaminocyclohexane-*N, N, N', N'* -tetraacetic acid
DFT	Density Functional Theory
DNA	Desoxyribonucleic Acid
DOPhA	1,4,7,10-Tetrakis-[(*S*)-1-(1-phenyl)ethylcarbamoylmethyl]-1,4,7,10-tetraazacyclododecane
DOTA	1,4,7,10-tetraazacyclododecane-1,4,7,10-tetraacetic acid
DOTMA	[(*1R,4R,7R,10R*)]-$\alpha,\alpha',\alpha'',\alpha'''$–tetramethyl-1,4,7,10-tetraazacyclododecane-1,4,7,10-tetraacetic acid
DPM	Dual Polarization Modulation
DTPA	diethylenetriamine-*N, N, N', N', N''*-pentaacetic acid
ECD	Electronic Circular Dichroism
EDTA	Ethylenediaminetetraacetic acid
ELISA	Enzyme-linked Immunosorbent Assay
FATCAT	Flexible structure AlignmenT by Chaining Aligned fragment pairs allowing Twists
FC	Fermi Contact
FTIR-VCD	Fourier transform Infrared Vibrational Circular Dichroism
FWHM	Full Width at Half Maximum
HEDTA	*N'*-hydroxyethylethylenediamine-*N, N, N'*-triacetic acid

hfbc	heptafluorobutyrylcamphorato
HSA	Human Serum Albumin
Ig-G	Immunoglobulin G
IR	Infrared
LIVE	Lanthanide Induced Vibrational Circular Dichroism Enhancement
LLES	Low Lying Electronic States
MCT	Mercury Cadmium Telluride (HgCdTe)
MDF	Magnetic Dynamic Field
MO	Molecular Orbital
MRI	Magnetic Resonance Imaging
NMR	Nuclear Magnetic Resonance
PCS	Pseudocontact Shift
PEM	Photoelastic Modulator
SAP	Square Antiprismatic
SPM	Single Polarization Modulation
ST	Saturation Transfer
Triflate	Trifluoromethansulfonate
TSAP	Twisted Square Antiprismatic
VA	Vibrational Absorption
VCD	Vibrational Circular Dichroism
VOA	Vibrational Optical Activity
XRD	X-Ray Diffraction